



January 2016

Understanding Addiction, Depression, And Autism Spectrum Disorder Through Structure-Function Analyses Of The Dopamine And Serotonin Transporters

Danielle Krout

Follow this and additional works at: <https://commons.und.edu/theses>

Recommended Citation

Krout, Danielle, "Understanding Addiction, Depression, And Autism Spectrum Disorder Through Structure-Function Analyses Of The Dopamine And Serotonin Transporters" (2016). *Theses and Dissertations*. 2037.
<https://commons.und.edu/theses/2037>

This Dissertation is brought to you for free and open access by the Theses, Dissertations, and Senior Projects at UND Scholarly Commons. It has been accepted for inclusion in Theses and Dissertations by an authorized administrator of UND Scholarly Commons. For more information, please contact zeinebyousif@library.und.edu.

UNDERSTANDING ADDICTION, DEPRESSION, AND AUTISM SPECTRUM DISORDER
THROUGH STRUCTURE-FUNCTION ANALYSES OF THE DOPAMINE AND
SEROTONIN TRANSPORTERS

by

Danielle Patricia Marie Krout
Bachelor of Arts, Concordia College, 2010

A Dissertation

submitted to the Graduate Faculty

of the

University of North Dakota

in partial fulfillment of the requirements

for the degree of

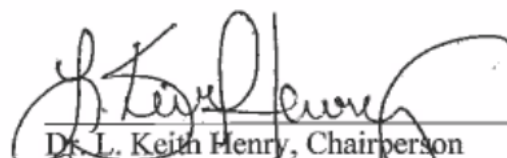
Doctor of Philosophy

Grand Forks, North Dakota

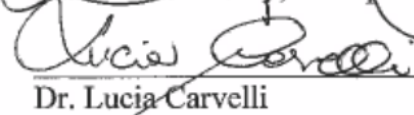
August
2016

Copyright 2016 Danielle Krout

This dissertation, submitted by Danielle Krout in partial fulfillment of the requirements for the Degree of Doctor of Philosophy from the University of North Dakota, has been read by the Faculty Advisory Committee under whom the work has been done and is hereby approved.




Dr. L. Keith Henry, Chairperson



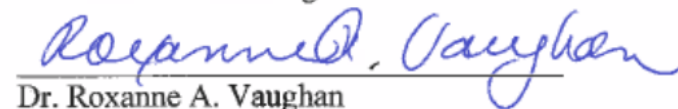
Dr. Lucia Carvelli



Dr. James D. Foster



Dr. Thad A. Rosenberger



Dr. Roxanne A. Vaughan

This dissertation is being submitted by the appointed advisory committee as having met all of the requirements of the School of Graduate Studies at the University of North Dakota and is hereby approved.



Dr. Grant McGimpsey
Dean of the School of Graduate Studies

July 22, 2016
Date

PERMISSION

Title Understanding Addiction, Depression, and Autism Spectrum Disorder through
 Structure-Function Analyses of the Dopamine and Serotonin Transporters

Department Pharmacology, Physiology, and Therapeutics

Degree Doctor of Philosophy

In presenting this dissertation in partial fulfillment of the requirements for a graduate degree from the University of North Dakota, I agree that the library of this University shall make it freely available for inspection. I further agree that permission for extensive copying for scholarly purposes may be granted by the professor who supervised my dissertation work or, in his absence, by the Chairperson of the department or the dean of the School of Graduate Studies. It is understood that any copying or publication or other use of this dissertation or part thereof for financial gain shall not be allowed without my written permission. It is also understood that due recognition shall be given to me and to the University of North Dakota in any scholarly use which may be made of any material in my dissertation.

Danielle Krout
August 5, 2016

TABLE OF CONTENTS

LIST OF FIGURES	xii
LIST OF TABLES	xv
ACKNOWLEDGMENTS	xvi
ABSTRACT	xvii
CHAPTER	
I. INTRODUCTION	1
Solute Carrier Superfamily of Transporters	1
Physiological Functions and Molecular Characteristics of MATs	2
NET	4
DAT	4
SERT	5
MAT Structure and Mechanism of Transport	5
S1 Binding Site	9
LeuT	9
MATs	10
S2 Binding Site	12
LeuT	12
MATs	14
Alternating Access Mechanism of Transport	17
MAT Pathophysiology and Polymorphisms	18

NET	19
DAT	20
SERT	21
MAT Pharmacology and Therapeutic Intervention	23
Antidepressants	23
Cocaine	24
II. COMPUTATIONAL AND BIOCHEMICAL DOCKING OF THE IRREVERSIBLE COCAINE ANALOG RTI 82 DIRECTLY DEMONSTRATES LIGAND POSITIONING IN THE DOPAMINE TRANSPORTER CENTRAL SUBSTRATE-BINDING SITE	27
Introduction	27
Methodology	32
Comparative DAT Homology Model Construction	32
RosettaLigand Docking	33
Induced Fit Docking	34
Molecular Dynamic Simulations	35
Cell Culture and Site-directed Mutagenesis	36
[³ H]Dopamine Uptake and [³ H]CFT Binding Assays	37
RTI 82 Synthesis and Radioiodination	38
Photoaffinity Labeling and CNBr Peptide Mapping	38
RTI 82 Potency in Phe-319 Mutants	39
SCAM Protection Analysis of S1-and S2-Binding Sites	40
Results	41
Computational Docking of RTI 82	41
RosettaLigand	41

	Induced Fit Docking	44
	MD Simulation of RL and IFD Docked RTI 82 Poses	44
	Analysis of 4'-Azido-3'-iodophenyl Moiety Interactions with Phe-319	48
	CNBr Peptide Mapping of [¹²⁵ I]RTI 82-Labeled TM6 Mutants	49
	Analysis of RTI 82 Protection of S2 Residues from the Inactivation by Methanethiosulfonate (MTS) Reagents	55
	Discussion	60
III.	IDENTIFYING THE ADDUCTION SITE OF THE PHOTOACTIVE AZIDE OF THE IRREVERSIBLE COCAINE ANALOG [¹²⁵ I]MFZ 2-24 FOR ELUCIDATING THE COCAINE BINDING SITE IN THE DOPAMINE TRANSPORTER	66
	Introduction	66
	Methodology	70
	Comparative DAT Homology Model Construction	70
	Molecular Dynamics Analysis of DAT in Complex with MFZ 2-24	70
	Synthesis and Radiolabeling of MFZ 2-24	70
	Chemicals and Materials	70
	Cell Culture and Site-directed Mutagenesis	71
	Photoaffinity Labeling and CNBr Peptide Mapping	71
	[³ H]CFT Binding	72
	[³ H]DA Uptake	73
	SCAM Protection Analysis of S1- and S2-binding Sites	73
	Results	74
	Computational Docking of MFZ 2-24 to rDAT Homology Models	74
	RosettaLigand Docking	74

	IFD Docking	75
	MD Simulation of RL and IFD Docked MFZ 2-24 Poses	77
	Peptide Mapping of Photoaffinity Labeled Site	79
	Analysis of MFZ 2-24 Protection of S1- and S2-binding Pockets from Cys-directed Biotinylation	83
	Discussion	85
IV.	ANTAGONISM OF THE DOPAMINE TRANSPORTER BY THE IRREVERSIBLE BENZTROPINE ANALOG [¹²⁵ I]GA II 34 OCCURS AT THE CENTRAL SUBSTRATE-BINDING SITE	89
	Introduction	89
	Methodology	93
	Cell Culture and Site-directed Mutagenesis	93
	GA II 34 Synthesis and Radioiodination	94
	Photoaffinity Labeling and In Situ Proteolysis of Native DAT	94
	Photoaffinity Labeling of Expressed DAT	95
	CNBr Peptide Mapping	95
	SCAM Protection Analysis of S1- and S2-binding Sites	96
	Results	96
	Proteolytic Peptide Mapping of [¹²⁵ I]GA II 34	96
	CNBr Mapping of [¹²⁵ I]GA II 34 Attachment	98
	Localizing [¹²⁵ I]GA II 34 Adduction to TM1 in DAT	100
	Analysis of GA II 34 Protection of S1- and S2-binding Pockets from Cys-Directed Biotinylation	101
	Discussion	104
V.	MEMBRANE POTENTIAL SHAPES REGULATION OF DOPAMINE TRANSPORTER TRAFFICKING AT THE PLASMA MEMBRANE	106

Introduction	106
Methodology	108
Cell Culture	108
Cell lines	108
Midbrain primary neuron culture	109
Plasmid Constructs	110
Electrophysiology	111
Microscopy	112
TIRFM	112
Confocal microscopy and JHC 1-064 labeling of DAT	114
Depolarization-induced Ca ²⁺ influx	116
Biotinylation Assay	116
Drug/Solution Application and Optical Stimulation	117
Data Analysis	118
Results	118
MP Depolarization Reduces Membrane DAT Levels	118
Membrane DAT Reduction is CaMKII α and Dynamin Dependent	123
MP Depolarization Internalizes JHC 1-064/DAT Complexes	126
MP Depolarization Redistributes DAT into Early Endosomes	127
Change in MP State Alters Cell Surface Membrane DAT Levels	129
Change in MP State Alters DAT-Mediated Current	131
Neuronal MP Changes Alter Surface-Membrane DAT Levels	133
Discussion	137

VI.	INHIBITION OF SEROTONIN TRANSPORT IS ALTERED BY METABOLITES OF SELECTIVE SEROTONIN AND NOREPINEPHRINE REUPTAKE INHIBITORS AND REPRESENTS A CAUTION TO ACUTE OR CHRONIC TREATMENT PARADIGMS	142
	Introduction	142
	Methodology	144
	Animals	144
	Synaptosome and Platelet-rich Plasma Preparations	145
	5-HT Competition Uptake Assays	146
	Animal Injections and Measurement of Brain and Serum Drug Concentrations	146
	Brain Tissue and Serum Preparations	146
	UPLC-MS/MS Analysis for Citalopram and Desmethylcitalopram	147
	Results and Discussion	148
VII.	AUTISM-LINKED MUTATIONS IN THE HUMAN SEROTONIN TRANSPORTER INDUCE DISTINCT STRUCTURAL CHANGES THAT MAY ACCOUNT FOR THE ALTERED FUNCTION OF THE TRANSPORTER ...	156
	Introduction	156
	Methodology	159
	Cell Culture and Site-directed Mutagenesis	159
	Cysteine Accessibility Analysis	159
	Conformational changes assessed by rate of inactivation	159
	Antagonist- or substrate-induced protection of Cys-277	160
	Cys-277 accessibility in mimicked hyper- or de-phosphorylated SERT	160
	Protein Expression Analysis	161
	Results	161

Sensitivity of Cys Probes to MTS Reagents	161
MTS Reactivity is Cation Dependent	165
Effect of 5-HT and Cocaine on MTSEA Inactivation	168
PKG-mimicked SERT Phosphorylation Alters MTSEA Reactivity	169
Discussion	172
REFERENCES	176

LIST OF FIGURES

Figure	Page
1. Role of MATs in synaptic transmission	3
2. Structure and topology of MATs	6
3. Architecture of the LeuT fold	8
4. DA occupies the central, S1 binding site	11
5. S1 accommodates high- and low-affinity interactions with various ligands	12
6. Location of the LeuT S2 binding site in relation to S1	13
7. Allosteric modulation of inhibitor binding	14
8. hSERT allosteric binding site	15
9. Alignment of SERT and DAT	16
10. LeuT alternating access mechanism	18
11. Chemical structures of cocaine, CFT, and RTI 82	32
12. Small molecule docking analysis	43
13. Molecular dynamics simulations	45
14. Comparison of rDAT-RTI 82 complexes before and after molecular dynamic simulation	47
15. Schematic diagram of endogenous Met residues in DAT	50
16. Characterization of Met-substituted hDATs	51
17. CNBr mapping of [¹²⁵ I]RTI82-labeled TM6 DAT mutants	53
18. SCAM protection analysis of S1 and S2 binding pockets	57

19.	Chemical structures of cocaine, CFT, and [¹²⁵ I]MFZ 2-24	69
20.	MFZ 2-24 and DAT RosettaLigand docking complexes and molecular dynamics simulation	76
21.	MFZ 2-24 and DAT Induced Fit Docking complexes and molecular dynamics simulation	78
22.	CNBr mapping of [¹²⁵ I]MFZ 2-24-labeled DAT mutants	81
23.	SCAM protection analysis of S1 and S2 binding pockets	84
24.	Chemical structures of cocaine, benztropine, [¹²⁵ I]GA II 34, [¹²⁵ I]MFZ 2-24, and [¹²⁵ I]RTI 82	92
25.	Photoaffinity labeling of hDAT with [¹²⁵ I]GA II 34	97
26.	Photoaffinity labeling, in situ proteolysis, and immunoprecipitation of [¹²⁵ I]GA II 34 labeled rDAT	98
27.	Localizing [¹²⁵ I]GA II 34 covalent attachment N-terminal to Met-106	99
28.	CNBr mapping of [¹²⁵ I]GA II 34 labeled DAT to TM1	100
29.	SCAM protection analysis of S1 and S2 binding pockets	103
30.	Depolarization causes CaMK-dependent reduction of membrane YFP-DAT levels in HEK cells	119
31.	Amphetamine causes redistribution in membrane DAT and the GPCR, GPR40, is insensitive to depolarization-induced changes in membrane expression	120
32.	Depolarization-dependent redistribution of YFP-DAT is not PKC-dependent	121
33.	CaMKII inhibitor, KN93, attenuates but does not abolish depolarization induced Ca ²⁺ influx	122
34.	Depolarization-induced reduction in surface-membrane-biotinylated DAT is due to CaMKII-dependent endocytosis	124
35.	Membrane levels of the endogenous transferrin receptor (TfR) are unchanged upon membrane depolarization	125
36.	Membrane depolarization with KCl increases internalization of JHC 1-064/DAT complexes in HEK cells	126

37.	Depolarization-dependent internalized DAT preferentially localizes to early but not recycling endosomes	128
38.	Membrane potential state alters cell membrane YFP-DAT levels	130
39.	Membrane potential state significantly alters DAT-mediated current	132
40.	Fluorescently-tagged protein expression and imaging scheme for TIRF imaging of neurons and example effect of resulting prolonged Arch activation	134
41.	Neuronal membrane potential rapidly alters membrane-surface DAT level	135
42.	Depolarization enhances internalization of JHC 1-064/DAT complexes in midbrain primary cultured neurons	136
43.	Competition 5-HT uptake analysis in forebrain derived synaptosomes	149
44.	Competition 5-HT uptake analysis in isolated platelets	151
45.	Time course analysis of brain and serum levels of citalopram and the metabolite desmethylcitalopram	153
46.	Location of autism-associated SERT variants	158
47.	Cysteine probes used to assess conformational changes through SCAM	162
48.	MTSES reactivity at Cys-109 is altered by the regulatory domain variants	163
49.	Cys-277 is more accessible to MTSEA in ASVs	164
50.	Cys-109 is more accessible to MTSET in sodium-free buffer in ASVs	166
51.	MTSEA reactivity at Cys-109 in sodium-free buffer is unaltered	167
52.	Cocaine does not protect Cys-277 from MTSEA inactivation in ASVs G56A, I425L, L550V, and K605N	169
53.	Transport is blunted in ASVs compared to control in the mimicked hyperphosphorylated T276D background	170
54.	Accessibility of Cys-277 is altered in the ASVs compared to control in the mimicked dephosphorylated T276A background	171
55.	ASVs induce an outward-facing conformation	174

LIST OF TABLES

Table	Page
1. Activity of Phe-319 mutants and inhibitory potency of RTI 82	49
2. Log IC ₅₀ values for inhibition of [³ H]5-HT uptake	150
3. LC-MS/MS quantification of citalopram and the metabolite desmethylocitalopram in brain and serum	154

ACKNOWLEDGMENTS

This dissertation would not have been possible were it not for the people in my life. First and foremost, I'd like to thank my family. To Dakota, the love of my life, thank you for your constant support and dedication to our life together. To my parents, Richard and Joanne, thank you for teaching me the value of hard work and for instilling within me a desire to better myself and care for those around me. To the best sister a girl could ask for, Brigitte, thank you for being my best friend and confidant. I credit these four members of my support system for forming me into the person I am today.

To my mentor, Dr. Keith Henry, I could not have asked for a better influence. Thank you for guiding me through graduate school and for being an unfailing mentor during every success and failure of mine. I am truly grateful for all that you have done for me. To Drs. Carvelli, Foster, Rosenberger, and Vaughan, thank you for always encouraging my professional and scientific development and for teaching me by example. I will forever be indebted to you for your guidance and support.

I would also like to recognize all the collaborators who made this dissertation a reality. To the labs near and far that contributed their time and effort to collaborative projects, thank you for your commitment and dedication to your work. I would especially like to thank the past and present members of the Henry lab for their research expertise as well as for their friendship. The same goes for the graduate students I had the pleasure of getting to know throughout the years. I survived graduate school because of them and the countless hours spent celebrating life or commiserating over shared research failures.

To God and my four best friends who gave me strength when I was weak.

ABSTRACT

The dopamine (DAT) and serotonin (SERT) transporters are monoamine neurotransmitter transporters (MATs) responsible for the reuptake of dopamine (DA) or serotonin (5-HT) from the synapse following vesicular release, effectively regulating synaptic neurotransmission. Blockade of these transporters by antagonists such as psychostimulant drugs or transporter mutations that affect function can compromise DA or 5-HT homeostasis and impact fundamental brain processes including movement, emotion, behavior, motivation, and memory. To address these issues, my dissertation research focused on: (1) identifying and characterizing the cocaine binding site in DAT, (2) determining the influence of membrane depolarization on DAT trafficking, (3) investigating antidepressant metabolite action in an antidepressant-insensitive mouse model, and (4) understanding the link between the structural and functional changes induced by mutations in SERT associated with autism spectrum disorder.

Cocaine binding site in DAT – Through the development and utilization of several high affinity, photoactivatable cocaine ligands we identified a cocaine binding site in the core of DAT, a site that overlaps with the putative DA binding site, supporting a competitive mechanism for cocaine inhibition of DA uptake. (Chapters II-IV)

Influence of membrane depolarization on DAT trafficking – Trafficking of mature DAT to and from the cell membrane is a highly regulated process. Within this process, we demonstrated that membrane depolarization alone could induce a CaMKII α - and dynamin-dependent rapid reversible reduction in membrane DAT. (Chapter V)

Characterization of antidepressant metabolites in the blockade of 5-HT reuptake – As studies of the antidepressant selective serotonin reuptake inhibitors (SSRIs) have revealed discrepancies between acute and chronic dosing treatments, we evaluated the sensitivity of SSRI metabolites in a mouse model of depression and identified a role for metabolites in antidepressant administration that may confound study conclusions. (Chapter VI)

Autism-associated SERT mutations – Previously, several rare SERT coding variants were identified in humans with autism spectrum disorder that augment 5-HT transport function. We studied the structure of these variants and discovered alterations in SERT tertiary structure, which likely impact the catalytic activity or surface expression of SERT. (Chapter VII)

CHAPTER I

INTRODUCTION

Solute Carrier Superfamily of Transporters

Transporters are membrane-bound proteins that mediate the translocation of impermeant solutes across cellular membranes (Kristensen et al. 2011; Lin et al. 2015) either through passive, also known as facilitated, transport, where solutes move down their concentration gradient, or active transport, in which an ion/solute gradient is created with the help of ATP (primary active) or used (secondary-active) to drive transport of solutes against their concentration gradient (Hediger et al. 2003). Of the major transporter superfamilies, the solute carrier (SLC) superfamily consists of approximately 350-400 membrane-spanning transporters organized according to 20-25% sequence identity into 43-55 families (Hediger et al. 2003; He, Vasiliou, and Nebert 2009; Lin et al. 2015). This superfamily is responsible for transporting a diverse range of substrates including inorganic ions, amino acids, sugars, metals, neurotransmitters, vitamins, and fatty acids (He, Vasiliou, and Nebert 2009; Hediger 2013). Despite distinct substrates, SLC transporters have remarkably similar tertiary structures, as all the solved crystal structures reveal a 5 + 5 α -helical arrangement where transmembrane domains (TMs) 1-5 are aligned antiparallel to TMs 6-10 suggesting a conserved structural mechanism within the SLC superfamily (Forrest and Rudnick 2009; Krishnamurthy, Piscitelli, and Gouaux 2009; Abramson and Wright 2009; Boudker and Verdon 2010).

The solute carrier 6 (SLC6) family of secondary active transporters is one of the largest SLC families and is responsible for transport of amino acids and amino acid derivatives into cells

by utilizing the electrochemical potential difference of Na^+ across the cell membrane to couple ‘downhill’ movement of Na^+ to ‘uphill’ movement of substrate (Chen, Reith, and Quick 2004; Kristensen et al. 2011; Pramod et al. 2013). As this coupled transport of Na^+ and substrate occurs in the same direction and, in some cases, is accompanied by co-transport of Cl^- , the SLC6 family is also referred to as symporters or Na^+/Cl^- -dependent transporters, even though some members exhibit counter-transport of K^+ (Rudnick and Clark 1993; Rudnick 1998). This family encodes for a group of 20 highly similar transporter proteins that are divided into four subgroups based on substrate specificity and sequence similarity, namely the monoamine neurotransmitter transporters, the γ -aminobutyric acid (GABA) transporters, and two amino acid transporter branches that, in several instances, have been further subdivided into either orphan, neurotransmitter, or nutrient transporters (Bröer 2006; Kristensen et al. 2011; Bröer and Gether 2012; Pramod et al. 2013). This dissertation is concerned with the subset of the SLC6 family known as the neurotransmitter transporters (NTT) with primary focus on the SLC6A family of monoamine neurotransmitter transporters (MATs), including the serotonin (SERT), norepinephrine (NET), and dopamine (DAT) transporters, which are responsible for reuptake of the biogenic monoamine neurotransmitters serotonin (5-HT), norepinephrine (NE), or dopamine (DA), respectively.

Physiological Functions and Molecular Characteristics of MATs

MATs have an important role in the central nervous system (CNS), as their primary physiological function is regulation of neurotransmitter homeostasis, which is associated with modulation of mood, motor function, aggression, anxiety, depression, addiction, appetite, attention, etc. (Hahn and Blakely 2007; Ramamoorthy, Shippenberg, and Jayanthi 2011). Expressed in both dendrites and axons of their respective monoaminergic neurons, MATs

regulate neurotransmission through the reuptake of neurotransmitters from the synapse following vesicular release (Fig. 1a) (Torres, Gainetdinov, and Caron 2003) as well as contribute to neurotransmitter recycling; return of the neurotransmitter to the presynaptic neuron allows the secondary-active, proton-coupled vesicular monoamine antiporters, VMAT1 and VMAT2, which are integral membrane proteins in vesicles, to sequester neurotransmitter not yet enzymatically degraded by monoamine oxidases (MAOA and MAOB) (Iversen 1971; Shih, Chen, and Ridd 1998; Eiden et al. 2003; Blakely and Edwards 2012; Lawal and Krantz 2013). Importantly, as regulators of synaptic signaling, altered MAT expression and/or catalytic activity impact the plasticity of synaptic signaling due to dynamic changes in the number and function of transporters.

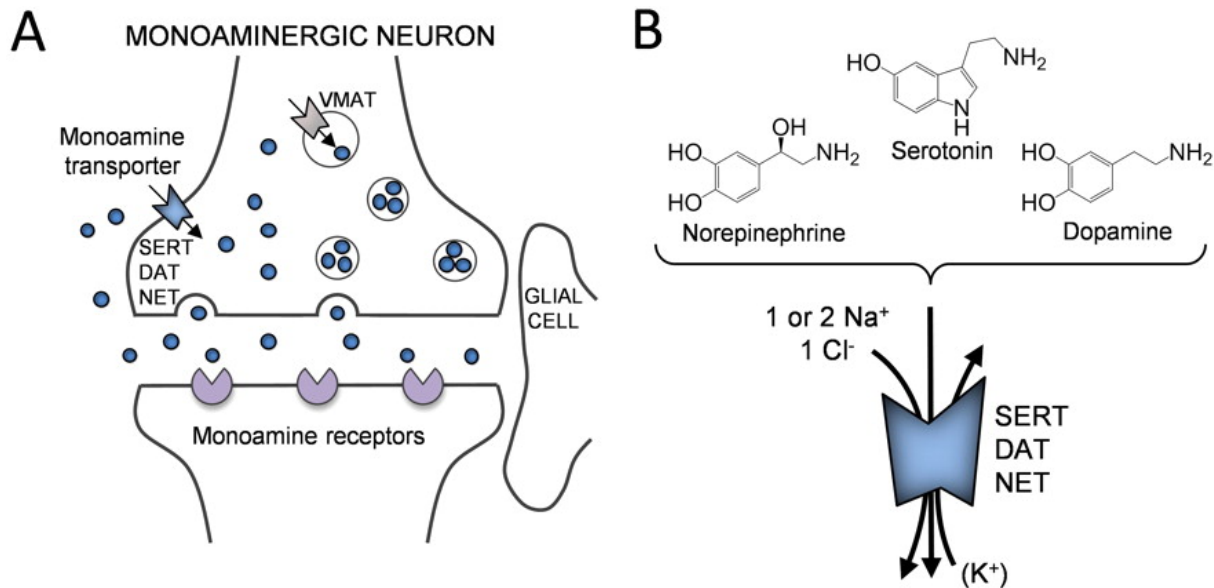


Figure 1. Role of MATs in synaptic transmission. (a) Schematic representation of monoaminergic synaptic terminals. VMATs sequester 5-HT, DA, or NE into synaptic vesicles, which fuse with the membrane upon synaptic transmission releasing neurotransmitters into the synaptic cleft to act on post- and presynaptic receptors. MATs are crucial for termination of neurotransmission through rapid reuptake of neurotransmitters into the presynaptic neuron and are important for maintaining low neurotransmitter concentrations outside synapses. (b) Chemical structures of the endogenous substrates for MATs and ion coupling stoichiometry for neurotransmitter reuptake. (Reprinted by permission from Kristensen, Andersen, Jørgensen, Sørensen, Eriksen, Loland, Strømgaard, and Gether, SLC6 Neurotransmitter Transporters: Structure, Function, and Regulation, *Pharmacol Rev* 63(3): 585-640, 2011.)

NET

SLC6A2 encodes for NET, a MAT with K_M values of 0.4 μM for NE and 0.7 μM for DA, indicating a high affinity not only for the endogenous substrate, but for DA as well (Gether et al. 2006), which transports one substrate molecule in symport with one Na^+ and one Cl^- ion (Gu, Wall, and Rudnick 1996; Bröer and Gether 2012) (Fig. 1b). It is distributed throughout the brain, adrenal gland, intestine, kidney, testis, and placenta with ties to ADHD (Kim et al. 2006), depression (Hahn and Blakely 2007), and blood pressure regulation (Halushka et al. 1999). In NET knockout mice, the synaptic lifetime of NE is prolonged and the mice themselves have lower body weight and a decreased locomotor response to novelty (Xu et al. 2000). Furthermore, these mice display lower body temperature as a result of the thermoregulatory role of NE as well as enhanced morphine analgesia due to increased stimulation of α_2 -adrenoreceptors (Bohn et al. 2000).

DAT

SLC6A3 encodes for DAT, a MAT with K_M values of 2.5 μM for DA and a lower affinity for NE, 20 μM , which transports one molecule of substrate coupled to two Na^+ ions and one Cl^- ion (Gu, Wall, and Rudnick 1994; Sonders et al. 1997; Bröer and Gether 2012) (Fig. 1b). It is distributed throughout the brain and has a role in ADHD (Hahn and Blakely 2007), bipolar disorder (Grunhage et al. 2000), Tourette syndrome (Tarnok et al. 2007), and addiction (Kristensen et al. 2011; Pramod et al. 2013). DAT knockout mice are dwarf (Bossé et al. 1997), hyperactive (Giros et al. 1996; Gainetdinov et al. 1999; Spielwoy et al. 2000), and exhibit cognitive deficits including disrupted sensorimotor gating (Ralph et al. 2001) and sleep dysregulation (Wisor et al. 2001). These physiological changes are a result of the neurochemical changes in which DA persists up to 300-fold longer in the extracellular space, a rate that is

synonymous with diffusion mediated clearance (Giros et al. 1996), thereby increasing the steady-state extracellular DA concentration 5-fold (Giros et al. 1996; Jones et al. 1998; Gainetdinov, Sotnikova, and Caron 2002; Chen, Reith, and Quick 2004). Furthermore, despite normal social interactions in adult animals, female mice without DAT have an impaired capacity to care for their offspring (Giros et al. 1996).

SERT

SLC6A4 encodes for SERT, a MAT with K_M values of 0.45 μM for 5-HT. Furthermore, recent evidence suggests that SERT is also capable of transporting DA, but with lower substrate affinity, higher maximum velocity, and the requirement for higher Na^+ and Cl^- (~10- and 100-fold, respectively) to drive transport (Larsen et al. 2011; Bröer and Gether 2012). One molecule of substrate is transported in symport with one Na^+ and one Cl^- ion followed by antiport of one K^+ ion, which is thought to be important in outwardly rectifying the transporter (Fig. 1b) (Gu, Wall, and Rudnick 1996; Rudnick 1998). It is distributed throughout the brain, intestine, placenta, epithelium, and platelets and is linked to autism (Cook et al. 1997; Sutcliffe et al. 2005), obsessive-compulsive disorder (Ozaki et al. 2003), anxiety (Lesch et al. 1996), and depression (Stahl 1998). In SERT knockout mice, the extracellular concentration of 5-HT is increased 6-fold while the intracellular concentration is reduced by 60-80% (Bengel et al. 1998; Murphy et al. 1999; Fabre et al. 2000), which leads to increased anxiety-related behaviors, reduced locomotor activity, and exaggerated stress responsiveness (Rudnick et al. 2013).

MAT Structure and Mechanism of Transport

After cloning of MATs (Pacholczyk, Blakely, and Amara 1991; Giros et al. 1992; Ramamoorthy et al. 1993), but prior to solved SLC crystal structures, each MAT structure was probed intensively using site-directed mutagenesis, alanine scanning, cysteine accessibility,

hydropathy analysis, and other biochemical approaches. These techniques predicted a transporter topology of 12 membrane spanning domains connected by alternating extracellular and intracellular loops with both N- and C-termini located intracellularly (Fig. 2), but lacked the resolution needed to define tertiary structure. Attempts to crystallize members of the SLC6 family were, up until very recently, stunted due to problems in obtaining pure and stable transporters in the large quantities needed for protein crystallization (Tate et al. 2003; Rasmussen and Gether 2005; Kristensen et al. 2011; Caron and Gether 2016). However, over a decade ago, with the advent of the first reported high-resolution X-ray crystallographic structure of a SLC6 bacterial homolog came a much-anticipated surge in our understanding of MAT structure.

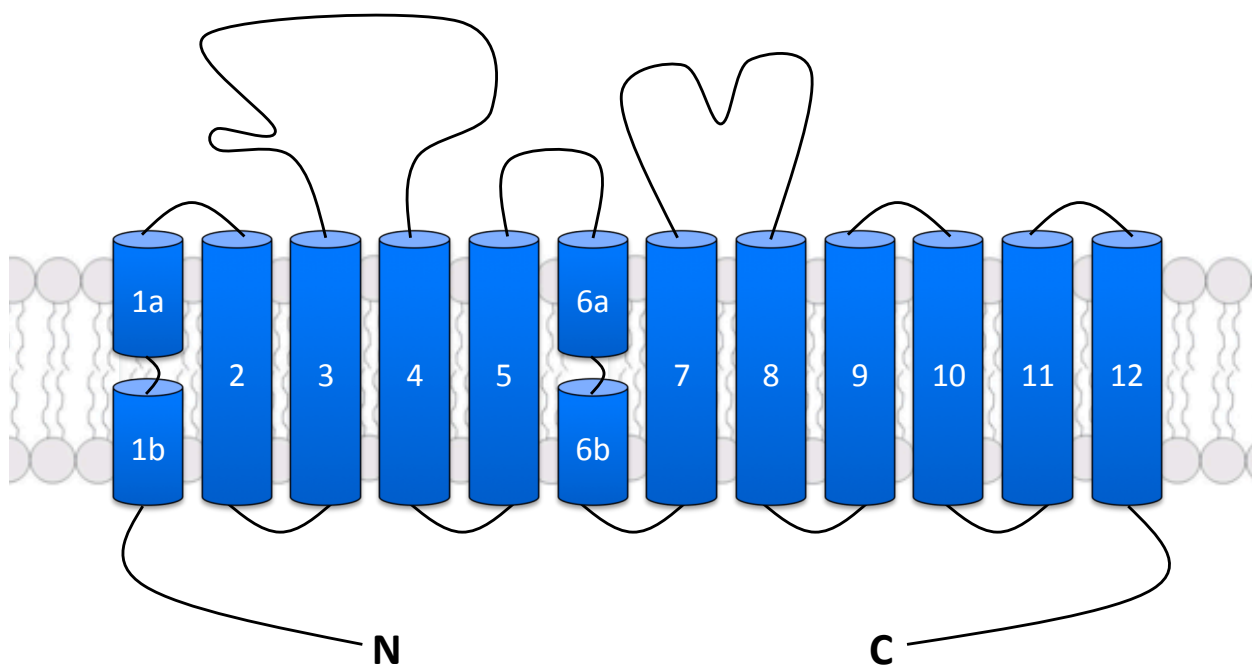


Figure 2. Structure and topology of MATs. MATs are composed of twelve membrane spanning domains that are connected by alternating extracellular and intracellular loops with both amino (N) and carboxyl (C) termini located intracellularly.

The leucine transporter (LeuT), from the thermophile bacterium *Aquifex aeolicus*, is a prokaryotic homolog of SLC6 transporters with an overall sequence identity of roughly 20-25% compared to MATs, a number that increases to 50-67% when considering the core domains

involved in substrate binding (Yamashita et al. 2005; Kristensen et al. 2011). LeuT is an amino acid Na⁺-dependent symporter with specificity for the hydrophobic amino acids alanine, leucine, methionine, and glycine (Singh et al. 2008). Since 2005, LeuT has been crystallized in multiple conformations corresponding to occluded (Yamashita et al. 2005), extracellularly-facing (Singh et al. 2008), intracellularly-facing (Krishnamurthy and Gouaux 2012), and inhibitor-bound forms (Singh, Yamashita, and Gouaux 2007; Zhou et al. 2007; Zhou et al. 2009). These crystals provided a template from which MAT homology models were constructed, a method often put into practice to investigate ligand binding sites through small molecule docking and molecular dynamics (Beuming et al. 2008; Andersen et al. 2009; Dahal et al. 2014). However, another surge in structural understanding of MATs has developed in the last few years with the crystallization of the eukaryotic *Drosophila melanogaster* DAT (dDAT) (Penmatsa, Wang, and Gouaux 2013; Wang, Penmatsa, and Gouaux 2015; Penmatsa, Wang, and Gouaux 2015), with greater than 50% sequence identity to its mammalian counterparts, and, more significantly, the first high-resolution crystallographic MAT structure of hSERT (Coleman, Green, and Gouaux 2016).

Crystal structures and biochemical data support a MAT architecture that is composed of an inverted-topological repeat of the first ten TMs, known as the LeuT fold, in which TMs 1-5 and TMs 6-10 have the same overall arrangement, but are aligned antiparallel to one another (Fig. 3) (Yamashita et al. 2005; Forrest et al. 2008). TMs 11 and 12 however are located on the periphery of the 5 + 5 core, suggestive of a specific role in structure, regulation, or dimerization (Just et al. 2004), as 70% of prokaryotic SLC6 members lack TM12 altogether (Quick et al. 2006). The TMs are connected by 6 extracellular and 5 intracellular loops (ELs 1-6 and ILs 1-5) with N- and C-termini located in the cytosol. Except for short, unwound segments in the middle

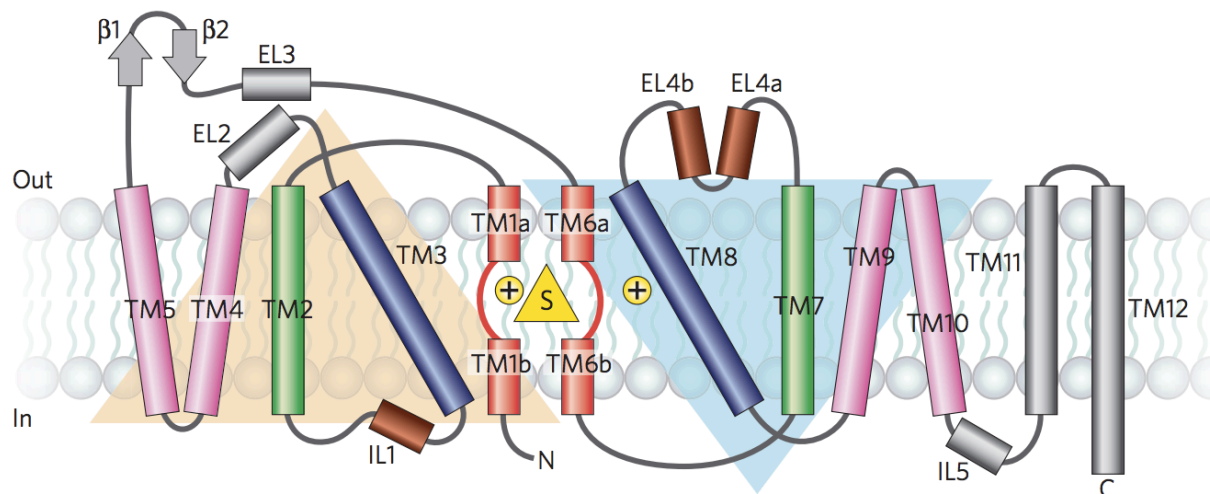


Figure 3. Architecture of the LeuT fold. View of the 5 + 5 α -helical architecture composed of an inverted-topological repeat of TMs 1-5 aligned antiparallel to TMs 6-10. The central, or primary (S1) substrate and ion binding site is formed by TMs 1, 3, 6, and 8. Substrate and ions are depicted as a yellow triangle and yellow circles, respectively. (Reprinted by permission from Macmillan Publishers Ltd: Nature – Krishnamurthy, Piscitelli, and Gouaux 2009.)

of TMs 1 and 6, the TMs are exclusively α -helical and packed into a cylindrical bundle. TMs 1, 3, 6, and 8 form a central, or primary, substrate and ion binding site (S1) that is occluded from the extracellular and intracellular milieu by external and internal gates formed from side chains of TMs 1, 3, 6, 8, and 10 (Yamashita et al. 2005; Krishnamurthy and Gouaux 2012; Wang, Penmatsa, and Gouaux 2015). Two Na^+ ion coordination sites lie proximal to the S1 binding site while Cl^- binds near the Na1 site, which is consistent with coupling of these ions to substrate transport (Forrest et al. 2007; Zomot et al. 2007; Penmatsa, Wang, and Gouaux 2013; Coleman, Green, and Gouaux 2016). SERT also exhibits antiport of K^+ though, to date, the K^+ binding site is not yet elucidated. A secondary substrate, or S2, binding site, whose existence and role are much debated, is located above the external gate in the large extracellular vestibule (Coleman, Green, and Gouaux 2016).

As LeuT has been the focus of crystallization in the past decade, for the purpose of deciphering MAT tertiary structure, multiple crystals have been obtained in conformations

corresponding to various stages of substrate translocation or those adopted upon inhibitor binding. For this reason, the following sections will focus primarily on LeuT crystal structure findings and biochemical evidence while also considering the more recent crystallization of dDAT and hSERT.

S1 Binding Site

LeuT. The substrate, or S1, binding site in LeuT is divided into a polar region that is formed exclusively by the unwound regions of TMs 1 and 6 and a hydrophobic pocket formed by the side chains of TMs 1, 3, 6, and 8 (Yamashita et al. 2005; Singh et al. 2008). The polar region accommodates the α -amino and α -carboxylate groups of the amino acid substrates by forming hydrogen bonds with the exposed main carbonyl oxygen and nitrogen atoms in the unwound sections of TMs 1 and 6. Furthermore, the two Na^+ ions interact with these unwound regions and are proposed to stabilize the leucine binding site as well as the overall structure itself (Gether et al. 2006). The α -carboxyl group of leucine interacts with the sodium at Na1, an interaction that does not occur in MATs as DA, NE, and 5-HT lack a carboxyl group; however, a glycine at position 24 in LeuT, which is replaced by an aspartate at the corresponding position in MATs, is predicted to be in immediate proximity of Na1, thus likely substituting for the missing substrate carboxyl group.

Of the 11 S1 residues in LeuT that coordinate leucine, 7 are conserved across all MATs (Kristensen et al. 2011) indicating a conserved S1 site between LeuT and MATs, consistent with experimental evidence where several S1 residues were identified as major determinants for substrate affinity (Henry et al. 2003; Beuming et al. 2006; Rudnick 2006; Henry, Meiler, and Blakely 2007; Kanner and Zomot 2008).

MATs. As mentioned previously, attempts to crystallize MATs were unsuccessful due to a proposed loss in ligand binding after detergent extraction and a general resistance to crystallization (Penmatsa, Wang, and Gouaux 2013; Coleman, Green, and Gouaux 2016). However, after a thorough process of identifying and engineering thermostabilizing mutations in dDAT and hSERT, the lab of Eric Gouaux has identified several MAT crystal structures with substrate bound (Wang, Penmatsa, and Gouaux 2015) or in complex with antagonists (Penmatsa, Wang, and Gouaux 2013; Wang, Penmatsa, and Gouaux 2015; Penmatsa, Wang, and Gouaux 2015; Coleman, Green, and Gouaux 2016). For the purpose of discussing the S1 binding site in MATs, the following will review the structures of dDAT with DA and antagonists bound in S1 (Wang, Penmatsa, and Gouaux 2015).

As predicted by previous biochemical analyses and consistent with LeuT crystal structures (Huang and Zhan 2007; Beuming et al. 2008; Bisgaard et al. 2011; Koldsø et al. 2013), DA binds to a central substrate binding pocket surrounded by TMs 1, 3, 6, and 8 (Fig. 4a,b and 5a,e). The positively charged amine group of DA interacts with the negatively charged aspartate on TM1 corresponding to G24 in LeuT while the catechol group interacts with residues from TMs 3, 6, and 8. Unlike in simulations where the DA binding site was dehydrated (Huang and Zhan 2007), this dDAT crystal structure elucidated a hydrogen bond network formed by two water molecules that link DA to Na¹ (Fig. 4b), an interaction that is not duplicated in LeuT as the carboxylate of leucine directly coordinates Na⁺ at this site. However, this crystal is a snapshot of the transporter in an extracellularly-facing conformation; upon shifting to an occluded conformation, as identified by the isosteric DA analogue 3,4-dichlorophenethylamine (DCP) (Fig. 5b,e), there is no evidence of water molecules associating with DCP, suggesting that

dehydration of the binding pocket occurs with formation of an occluded state (Wang, Penmatsa, and Gouaux 2015).

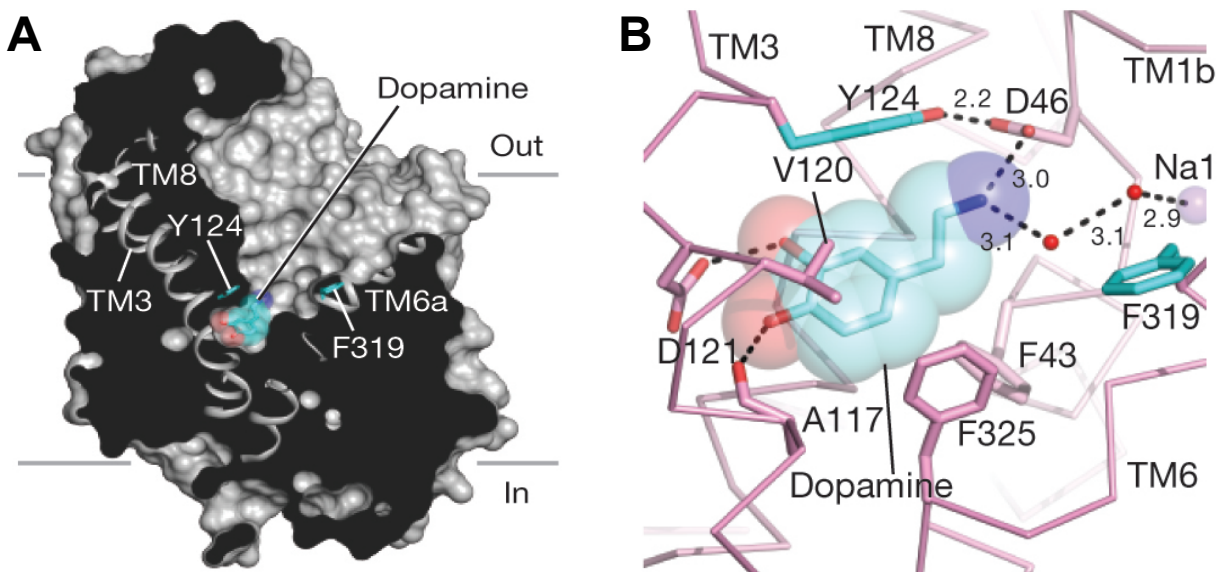


Figure 4. DA occupies the central, S1 binding site. (a) Surface representation of the dDAT/DA crystal complex viewed parallel to the membrane. DA is depicted as cyan spheres and residues Y124 and F319, which form an aromatic extracellular lid during translocation, are shown as cyan sticks on the left and right sides of DA, respectively. (b) Close-up view of the S1 binding pocket with DA bound. Hydrogen bonds are shown as dashed lines while sodium ions and water are shown as purple and red spheres, respectively. (Reprinted by permission from Macmillan Publishers Ltd: Nature – Wang, Penmatsa, and Gouaux 2015.)

dDAT has also been crystallized in complex with antagonists bound to S1, including amphetamines and cocaine (Wang, Penmatsa, and Gouaux 2015) as well as the antidepressants nortriptyline, (Penmatsa, Wang, and Gouaux 2013), nisoxetine, and reboxetine (Penmatsa, Wang, and Gouaux 2015). By comparing these structures, it is clear that S1 can accommodate ligands of various sizes through structural rearrangement in the unwound region of TM6 and positional changes of the side chains of residues F319 and F325 (Fig. 5). In the case of the substrates DA and amphetamine, the functional amine and aromatic groups at opposite ends allow for multiple interactions with residues from TMs 1, 3, 6, and 8, ultimately stabilizing the several conformations that occur with substrate translocation. Conversely, antagonists with

tropane moieties, such as cocaine, and antidepressants, which have bulky aromatic moieties, appear to prevent formation of an occluded structure by hindering the movement of the extracellular gate (Fig. 5c,f) or by blocking the overall transporter flexibility required for conformational changes (Fig. 5d,f).

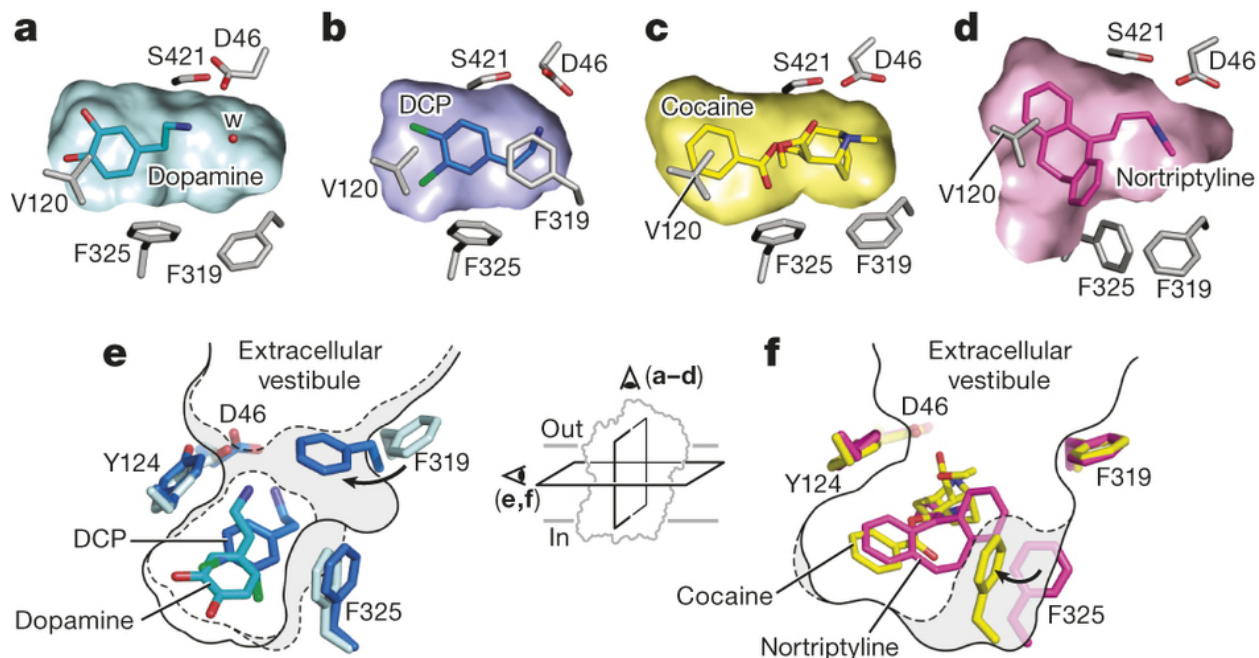


Figure 5. S1 accommodates high- and low-affinity interactions with various ligands. (a-d) Transverse sections of the S1 binding site in dDAT with DA (a), DCP (b), cocaine (c), or nortriptyline (d) bound. **(e-f)** Schematic representing the plasticity of the binding pocket in the presence of DCP (e), which adopts an occluded conformation as seen by the inward rotation of F319, cocaine (f), which binds to S1 in a manner similar to the extracellularly-facing DA bound structure, and nortriptyline (f), where accommodation of multiple aromatic rings is accomplished by orienting F319 and F325 outward. (Reprinted by permission from Macmillan Publishers Ltd: Nature – Wang, Penmatsa, and Gouaux 2015.)

S2 Binding Site

LeuT. The extracellular pathway, or extracellular vestibule, which forms the solvent accessible path from the extracellular space to the S1 site, has been argued to possess a second substrate binding site, designated S2 (Shi et al. 2008). S2 is separated from S1 by a hydrophobic lid, formed by the aromatic residues Y108 on TM3 and F253 on TM6, as well as a salt bridge,

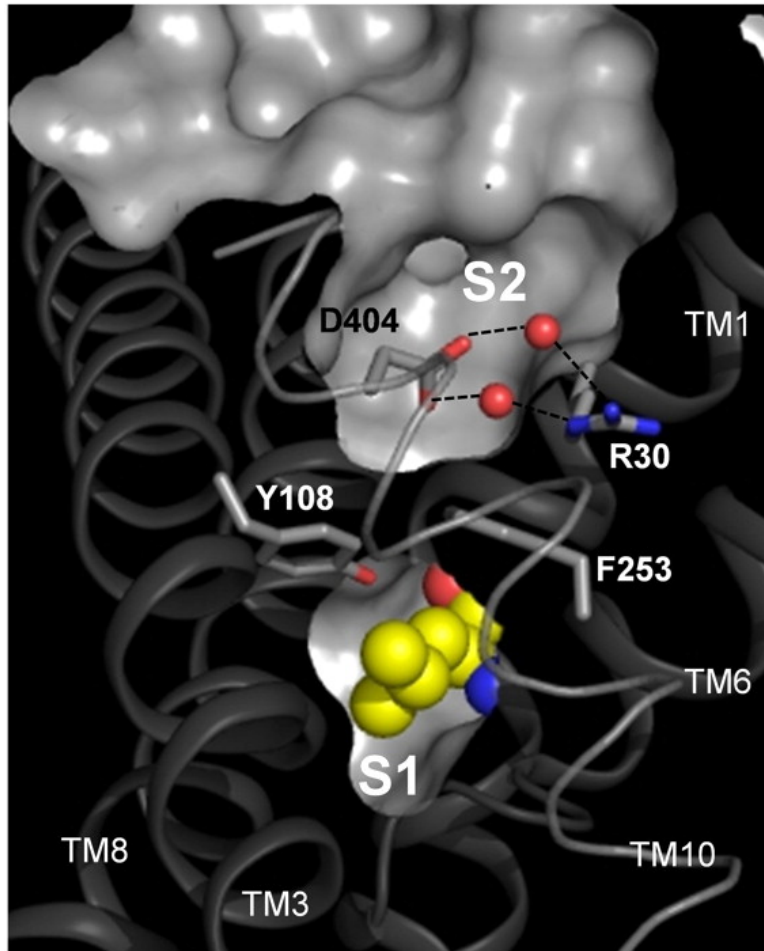


Figure 6. Location of the LeuT S2 binding site in relation to S1. TMs 1, 3, 6, 8, and 10 line the extracellular vestibule S2 binding site which is separated from S1 via an extracellular gate, a water-mediated salt bridge between R30 and D404, and an aromatic lid, Y108 and F253. (Reprinted by permission from Kristensen, Andersen, Jørgensen, Sørensen, Eriksen, Loland, Strømgaard, and Gether, *SLC6 Neurotransmitter Transporters: Structure, Function, and Regulation*, *Pharmacol Rev* 63(3): 585-640, 2011.)

created by the side chains of R30 on TM1 and D404 on TM10 (Fig. 6). Occupancy of the S2 pocket by a second substrate molecule has been proposed to trigger conformational changes necessary for release of substrate from S1 into the cytosol (Shi et al. 2008; Zhao et al. 2011), a result that is refuted by others (Piscitelli, Krishnamurthy, and Gouaux 2010). Though no structures have been crystallized with a substrate molecule bound to S2, several inhibitors and detergents have been crystallized in this extracellular space, which allows for inhibition of

substrate translocation and suggests a mechanism of action for MAT inhibitors (Zhou et al. 2007; Singh et al. 2008; Zhou et al. 2009; Quick et al. 2009; Coleman, Green, and Gouaux 2016).

MATs. Prior to crystallization of the first human MAT structure, biochemical evidence and computational studies based on LeuT co-crystallized with antagonists bound in the outer vestibule identified a binding site in S2 for selective serotonin reuptake inhibitors (SSRIs) (Chen et al. 2005; Plenge, Gether, and Rasmussen 2007) and tricyclic antidepressants (TCAs) (Sarker et al. 2010), both of which primarily act on SERT to block reuptake of 5-HT. Binding of an antagonist to the S2 site results in allosteric modulation by acting as a functional lid and attenuating dissociation of the inhibitor in S1, which enhances its dwell time to antagonize transporter function (Fig. 7) (Chen et al. 2005; Neubauer, Hansen, and Wiborg 2006; Plenge et al. 2012). These results were recently supported by the hSERT crystal structure (Coleman, Green, and Gouaux 2016). However, the S2 site may actually represent many binding sites in the

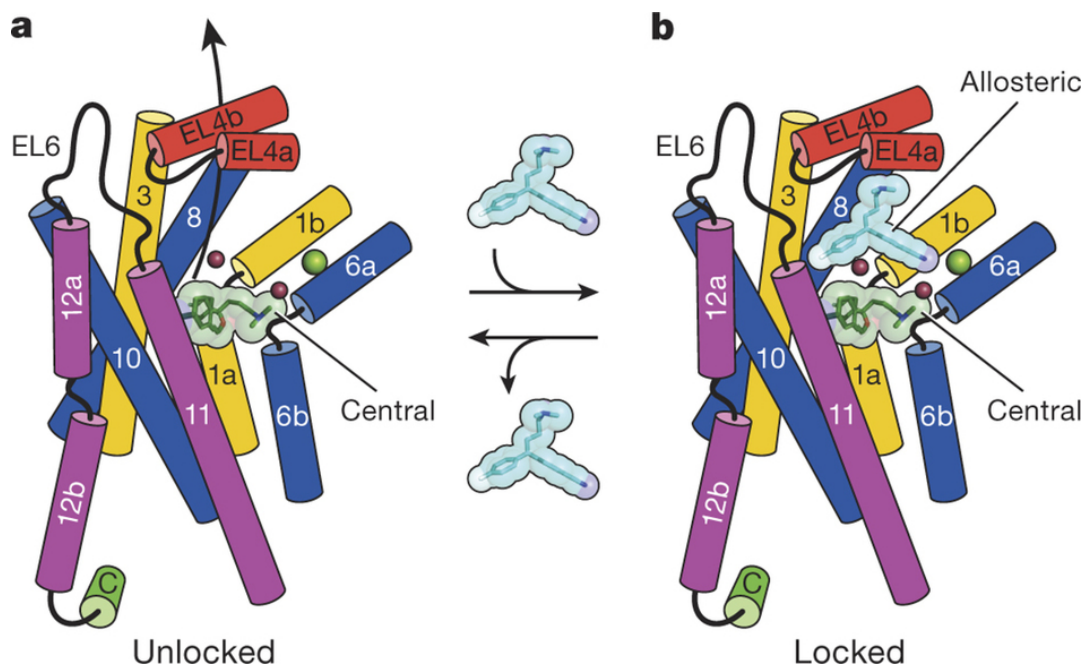


Figure 7. Allosteric modulation of inhibitor binding. (a) Citalopram (dark green) binds to S1 while a second molecule binds to S2 (b) acting as a functional lid, which slows the dissociation of the S1 bound inhibitor. (Reprinted by permission from Macmillan Publishers Ltd: Nature – Coleman, Green, and Gouaux 2016.)

outer vestibule that can accommodate multiple ligands, as several analogs developed recently appear to bind to distinct locations in S2 (Banala et al. 2013; Kumar et al. 2015; Tomlinson et al. in preparation). Further evaluation of these ligands should help to elucidate critical S2 residues involved in antagonist binding

Debate regarding the existence of a S2 site in MATs is likely stunted due to the very recent crystallization of two hSERT structures: a citalopram-bound transporter with citalopram molecules bound in both S1 and S2 and a paroxetine-bound structure in which paroxetine is bound in S1 and maltose, derived from a detergent molecule, is bound in S2 (Fig. 8) (Coleman, Green, and Gouaux 2016). In these structures, the secondary site is defined by residues in TMs 1, 6, 10, and 11 as well as ELs 4 and 6, regions that when mutated alter allosteric potency (Neubauer, Hansen, and Wiborg 2006; Zhong et al. 2009; Plenge et al. 2012) though the

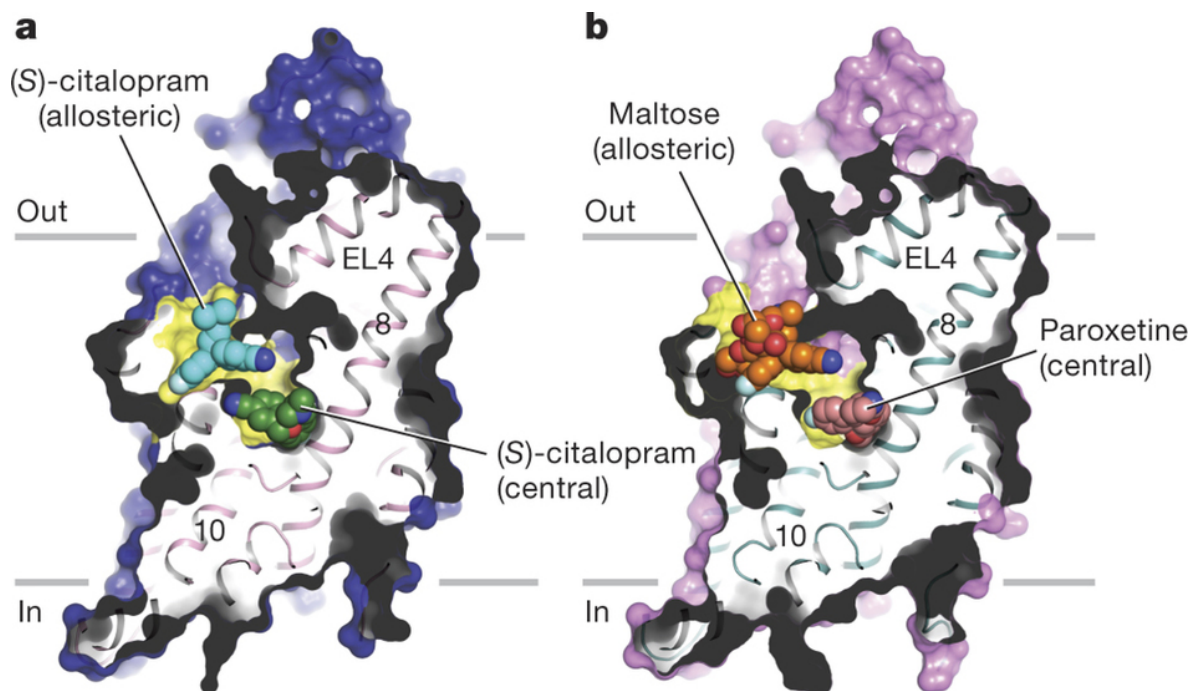


Figure 8. hSERT allosteric binding site. Sagittal slice through hSERT crystal structures in complex with citalopram (a), bound not only in S1, but in the allosteric, S2 site as well, and paroxetine (b), where paroxetine is bound in S1 and maltose, a sugar derivative, is bound in S2. (Reprinted by permission from Macmillan Publishers Ltd: Nature – Coleman, Green, and Gouaux 2016.)

physiological mechanism is not well established (Jacobsen et al. 2014). Comparison of these two structures suggests that S2 is plastic, as it appears to adopt different conformations based on the composition of the bound molecule. This finding suggests that occupancy of S2 may inhibit or support transport activity depending on the size and shape of the allosteric ligand. Furthermore, by superimposing the S2 site identified in hSERT crystals onto the same region in dDAT, it is apparent that these sites are distinct, even though the S1 sites in hSERT and dDAT are structurally similar (Fig. 9). For instance, EL6, which was shown to contribute to the S2 site in

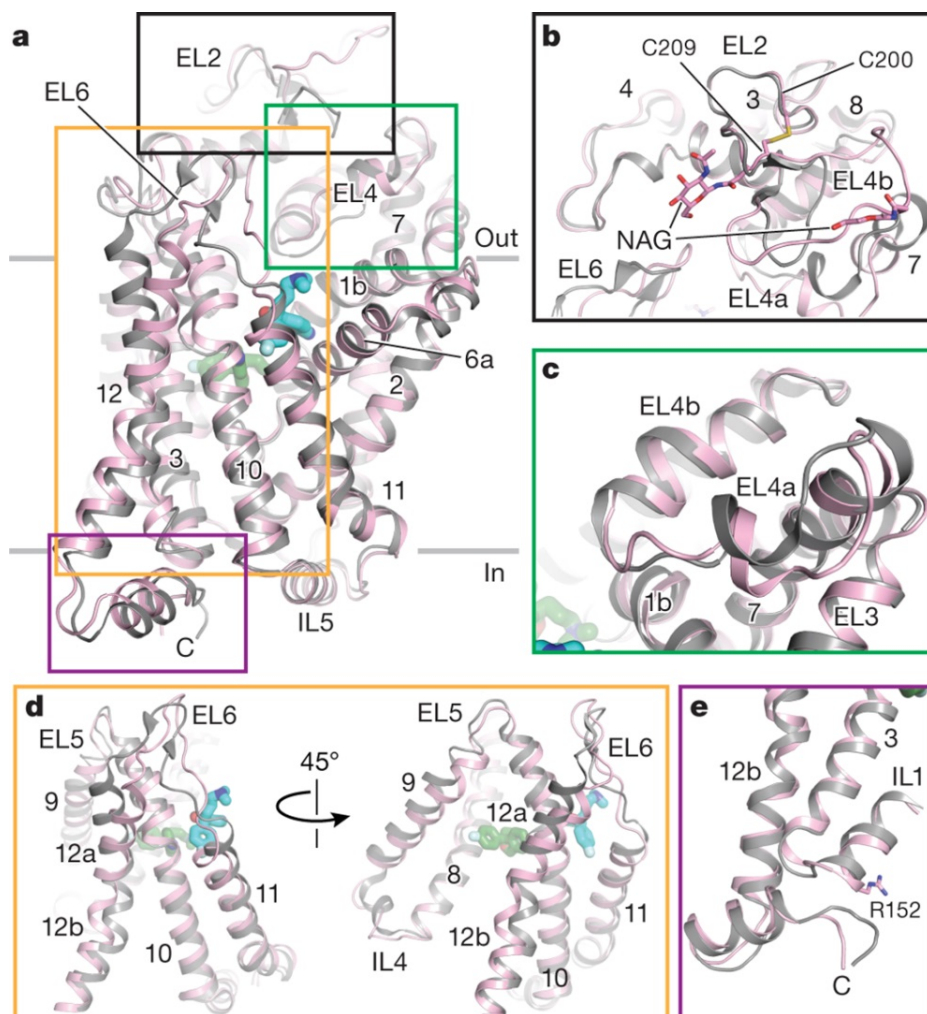


Figure 9. Alignment of SERT and DAT. (a) Overall alignment of SERT (pink) and dDAT (grey) with citalopram bound to the central (green) and allosteric (cyan) sites. Regions that differ structurally include EL2 (b), EL4 (c), the allosteric site (d) and the C-terminus (e). (Reprinted by permission from Macmillan Publishers Ltd: Nature – Coleman, Green, and Gouaux 2016.)

hSERT, is the most diverse when comparing amino acid sequences and adopts a conformation unique to hSERT, consistent with SERT selective allosteric ligands that do not impact DAT or NET (Coleman, Green, and Gouaux 2016).

Alternating Access Mechanism of Transport

A transport mechanism was envisioned in the late 1950s in which substrate translocation was mediated by several conformations that either allowed access to the substrate binding site, through an outward-facing conformation or an inward-facing conformation, or occluded the substrate from the external or internal medium (Mitchell 1957; Wilbrandt and Rosenberg 1961). This model was later refined and is now widely accepted as the alternating access mechanism (Jardetzky 1966; Mitchell 1990) though there are several variations. One of the proposed models is the rocking bundle model (Forrest et al. 2008; Forrest and Rudnick 2009), which suggests that TMs 1, 2, 6, and 7 form a bundle that rocks in relation to the scaffold TMs 3, 4, 5, 8, and 9. Conversely, the hinge model (Krishnamurthy, Piscitelli, and Gouaux 2009) proposes that flexing movements of TMs 1 and 6 is sufficient for substrate translocation and is supported by the conformational rigidity of TMs 2 and 7 preventing both the external and internal gates from being open at the same time. The rocking bundle model, which was proposed prior to the crystallization of an intracellularly-facing conformation, suggested that the core TMs 1, 2, 6, and 7 moved as a unit, but analysis of LeuT crystallized facing inward (Krishnamurthy and Gouaux 2012), however, indicates that only a portion of the core helices move as a unit. Therefore, the actual mechanism may consist of some of the components proposed in each model as opening and closing of the extracellular and intracellular gates depends on hinge-like bending of the unwound regions of TMs 1 and 6 together with multiple adjustments of TMs 1, 2, 6, and 7 and movements of extracellular loops, particularly EL4 (Fig. 10) (Krishnamurthy and Gouaux 2012).

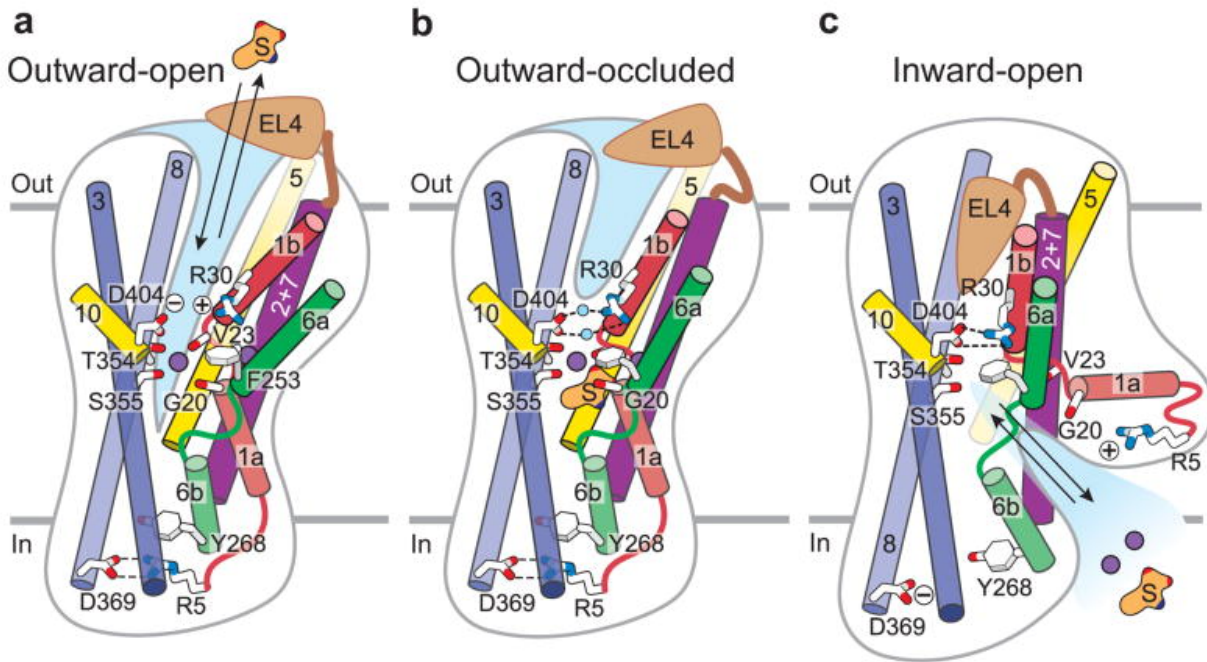


Figure 10. LeuT alternating access mechanism. Depicted are the conformational changes associated with substrate translocation from outward-open (**a**) to outward-occluded (**b**) followed by inward-open (**c**). TMs 1, 2, 6, and 7 as well as EL4 in particular undergo multiple adjustments when transitioning from an extracellularly-facing conformation to an intracellularly-facing conformation. (Reprinted by permission from Macmillan Publishers Ltd: Nature – Krishnamurthy and Gouaux 2012.)

MAT Pathophysiology and Polymorphisms

The crystal structures and biochemical evidence detailed above allow us to understand more about transporter structure and function as well as provide insight into pathophysiology. For example, genetic variation in MATs, either through single nucleotide polymorphisms (SNPs) or variable number of tandem repeats (VNTRs), has been implicated in a wide spectrum of neurological and neuropsychiatric disorders due to the identification of human *SLC6* MAT polymorphisms that lead to altered transporter expression, function, or regulation. Understanding the correlation between genetic perturbation of MATs and phenotypes in physiology and pathophysiology has the potential to elucidate improved pharmacotherapies. Therefore, the

following sections will highlight the predominant genetic changes in MATs identified in disease states.

NET

Depression is thought to involve the noradrenergic, dopaminergic, and serotonergic systems. NET has been implicated because levels of NET are decreased in individuals with major depressive disorder (Klimek et al. 1997). NET is also the target of amphetamines used to treat ADHD and is important in attention, vigilance, learning, memory, and stress (Biederman and Spencer 1999; Heim and Nemeroff 2001; Hahn et al. 2009). SNPs have been identified in non-coding, promoter, and coding regions of the *SLC6A2* gene (Hahn and Blakely 2007; Pramod et al. 2013) and are linked to several disorders and disease states.

Orthostatic intolerance (OI), a disorder characterized by an increase in resting heart rate not accompanied by hypotension (Robertson 1999), was linked to NET dysfunction after a patient with OI demonstrated standing-induced decreased NE clearance and decreased intraneuronal metabolism of NE (Jacob et al. 1999). Genetic analysis revealed an individual heterozygous for a nonsynonymous SNP, in which a highly conserved Ala in TM9 was converted into a Pro (A457P) (Shannon et al. 2000), a mutation that was significantly correlated with increased standing-induced heart rate and plasma NE. Co-expression of NET with the NET A457P mutant resulted in loss of NE transport likely due, in part, to decreased surface expression exerted by the dominant-negative effect of A457P NET in complex with wild-type NET (Shannon et al. 2000; Hahn, Robertson, and Blakely 2003). These findings suggest that heterozygous mutations may have a broader impact than homozygous mutations due to the additional dominant-negative effect (Hahn and Blakely 2007) and that the phenotype of elevated standing heart rate may be linked to NET dysfunction.

In studies of populations with altered cardiovascular phenotypes, including extreme blood pressure or long QT syndrome (Halushka et al. 1999; Iwasa et al. 2001), NET variants A369P in EL4 and N292T in EL3 were identified. The A369P mutant generated a total loss of DA and NE transport associated to its complete loss of surface expression whereas N292T resulted in a 50% loss of transport matched by a similar reduction in expression (Hahn, Mazei-Robison, and Blakely 2005; Hahn and Blakely 2007). As both mutants altered total and surface levels of hNET when coexpressed, these findings support that intracellularly retained or mistargeted mutant transporters exert dominant-negative effects on the expression and activity of wild-type transporters through the formation of oligomers (Hahn, Robertson, and Blakely 2003; Sitte, Farhan, and Javitch 2004).

DAT

As dopaminergic systems mediate motor activity, cognition, reward, attention, motivation, and mood (Giros and Caron 1993; Carlsson 1987; Koob, Sanna, and Bloom 1998; Björklund and Dunnett 2007; Palmiter 2008), DAT polymorphisms within coding, non-coding, and promoter regions of the *SLC6A3* gene have been implicated in ADHD, ASD, bipolar disorder, drug abuse, schizophrenia, Parkinson disease, and Tourette syndrome (Nieoullon 2002; Thapar, O'Donovan, and Owen 2005). Genetic variation in DAT was recently shown to increase connections between frontal, parietal, and striatal nodes in a manner that correlated with elevations in impulsivity and inattention, two prominent traits of both ADHD and ASD (Gordon et al. 2012). Furthermore, identification of mutation A559V, located in TM12 of DAT, in two male siblings with ADHD (Mazei-Robison et al. 2005; Mazei-Robison et al. 2008), in a patient with bipolar disorder (Grunhage et al. 2000), and in two subjects with ASD (Bowton et al. 2014), supports a shared pathophysiology in these disorders.

A559V was found to decrease DAT-mediated, amphetamine-induced DA efflux without impacting normal DAT transport function (Mazei-Robison et al. 2005), though under basal conditions A559V supports anomalous DA efflux (Mazei-Robison et al. 2008). It was later discovered that the efflux properties of this mutant might be regulated through the D₂ autoreceptor (Bowton et al. 2010). Interestingly, though the DAT substrate amphetamine (AMPH) binds hDAT A559V (Mazei-Robison et al. 2008; Bowton et al. 2010), it is not an efficiently transported substrate in relation to the wild-type transporter (Bowton et al. 2014). AMPH also causes reduced DAT surface expression (see chapter five) (Saunders et al. 2000; Kahlig et al. 2006), a mechanism that is not apparent in A559V likely due to the lack of intracellular accumulation of AMPH (Bowton et al. 2014), as this is required to cause DAT redistribution from the membrane (Kahlig et al. 2006). Finally, DAT trafficking is modulated by PKC β -dependent D₂ activation (Chen et al. 2013) and, in A559V, inhibition of PKC β restored AMPH-induced trafficking suggestive of a role for PKC β activity in the A559V trafficking deficits (Bowton et al. 2014). In combination, these insights could shed light on the underlying dysregulations that are shared by ADHD, bipolar disorder, and ASD.

SERT

The role of SERT and 5-HT is broad, contributing to sleep, cognition, mood, aggression, appetite, and sexual and motor activity (Coccaro 1989; Hahn and Blakely 2007). Disturbances in serotonergic signaling by non-coding VNTRs as well as rare coding variants have been implicated in anxiety, depression, ASD, gastrointestinal disorders, ejaculatory disorders, obesity, and OCD (Owens and Nemeroff 1994; Gershon 2005; Wolters and Hellstrom 2006; Kristensen et al. 2011).

Located in the *SLC6A4* promoter, 5-HTTLPR is an insertion/deletion polymorphism of two 22-base pair repeat elements located approximately 1 kb upstream of transcription initiation that gives rise to what has been termed the short (S) allele consisting of 14 repeats or the long (L) allele consisting of 16 repeats (Lesch et al. 1996; Kristensen et al. 2011; Kenna et al. 2012). SERT expression is modulated by variation in the length of this promoter region with the L allele conferring threefold greater basal transcriptional activity (Heils et al. 1996; Heils, Mössner, and Lesch 1997; Nakamura et al. 2000). Due to decreased transcription, the S allele of 5-HTTLPR, also known as the “risk allele”, has been associated with anxiety-related personality traits (Lesch et al. 1996; Holmes, Murphy, and Crawley 2003), major depressive disorder (Clarke et al. 2010; Kiyohara and Yoshimasu 2010), bipolar disorder (Anguelova, Benkelfat, and Turecki 2003; Cho et al. 2005), and a predisposition for poor response to treatment with SSRIs (Serretti et al. 2007). Conversely, the L allele is linked to OCD (Bloch et al. 2008), completed suicide (Du et al. 1999; Du et al. 2001), and ADHD (Seeger, Schloss, and Schmidt 2001; Retz et al. 2008; Thakur et al. 2010). In combination, it is apparent that the 5-HTTLPR polymorphism and its effects on expression predisposes individuals to several disorders, though it is important to consider epigenetic factors as well as how the influence of the S and L alleles may vary based on stimulus intensity and previous experience (Hahn and Blakely 2007; Kenna et al. 2012).

Several studies have identified rare, nonsynonymous genetic variants in the SERT gene that affect transport function. A screen of 450 individuals discovered the SNP I425V (Glatt et al. 2001) that was later linked to OCD by identification in seven subjects from two families, tracking the allele (as well as the 5-HTTLPR L allele) with diagnoses of OCD or OC personality disorder in six out of the seven individuals (Ozaki et al. 2003). Heterologous expression of this mutation showed enhanced 5-HT transport either through constitutive activation normally

supported by PKG stimulation (Kilic, Murphy, and Rudnick 2003) or elevated surface SERT density (Prasad et al. 2005). Relatedly, a genetic study of 341 ASD-associated families in 2005 identified five SNPs located in the coding region of SERT that, similar to I425V, resulted in elevated transport relative to wild-type SERT (Sutcliffe et al. 2005). The two mutations located on the N- and C-termini, G56A and K605N respectively, are insensitive to regulation through the PKG and p38 MAPK pathways suggesting that transport is elevated due to enhanced catalytic activity (Sutcliffe et al. 2005; Prasad et al. 2005). Conversely, the three transmembrane domain variants, I425L, F465L, and L550V, affect 5-HT transport as a result of elevated surface SERT density (Prasad et al. 2009). All mutants, but K605N, had a significant association with rigid compulsive behaviors in 120 autistic families with linkage at 17q11.2, the *SLC6A4* locus, suggesting a link between a gain-of-function SERT phenotype and ASD. The functional and structural impact of these SNPs will be discussed further in chapter seven.

MAT Pharmacology and Therapeutic Intervention

The association of MATs with the disorders and diseases discussed above has made them important pharmacotherapeutic drug targets for decades. In addition, MATs are the primary targets for several psychostimulant drugs of abuse.

Antidepressants

The development of the TCA imipramine in the early 1950s (Azima and Vispo 1958; Kuhn 1958) provided a breakthrough in treatment of depression and an understanding of the underlying mechanism of action of antagonism of SERT and NET function (Pacholczyk, Blakely, and Amara 1991; Ramamoorthy et al. 1993). However, severe side effects resulting from the broad action of TCAs on SERT, NET, and several other classes of receptors, including muscarinic, histaminergic, and α -adrenergic receptors (Owens et al. 1997; Iversen 2000; Gillman

2007), spurred the development of a new generation of antidepressants with improved selectivity (Kaiser and Setler 1981). These include compounds selectively targeting SERT (SSRIs) such as citalopram, fluoxetine, and paroxetine (Wong and Bymaster 1995), compounds selectively targeting NET (selective norepinephrine reuptake inhibitors, NRIs) such as reboxetine (Andersen et al. 2009), and compounds targeting both SERT and NET (serotonin-norepinephrine reuptake inhibitors, SNRIs) such as venlafaxine (Wong and Bymaster 2002). Though originally designed to treat major depressive disorder, antidepressants have also been efficacious for treatment of anxiety, OCD, ASD, and eating disorders (Cook and Leventhal 1996; Hollander et al. 2004; Bröer and Gether 2012).

Several antidepressants require molecular recognition in hSERT by the S1 residues Tyr-95 in TM1 and Ile-172 in TM3 to bind with high affinity (see chapter six) (Barker et al. 1998; Henry et al. 2006; Thompson et al. 2011). For example, by using human and drosophila SERT chimeras (Barker et al. 1998), the combined mutation of Y95F and I172M decreased the potency of racemic citalopram (a mix of both R- and S-isomers of citalopram) by ~10,000 fold (Henry et al. 2006), suggestive of a high affinity antidepressant binding site in S1. However, as affinity of citalopram for SERT is not completely abolished by these mutations, it was proposed that an additional binding site exists. This hypothesis was recently confirmed by the crystallization of hSERT in complex with citalopram bound in S1 as well as in an allosteric S2 site (Coleman, Green, and Gouaux 2016).

Cocaine

The recreational drug cocaine is a rapidly acting, non-selective, and moderate affinity inhibitor of all three MATs (Eshleman et al. 1999). However, the stimulatory and rewarding properties of cocaine result from binding to DAT and inhibiting DA reuptake (Giros et al. 1996;

Chen et al. 2006). This cocaine-mediated inhibition of DA reuptake has been proposed to occur by both competitive (see chapters two, three, and four) (Beuming et al. 2008; Bisgaard et al. 2011; Dahal et al. 2014) and noncompetitive mechanisms (Huang, Gu, and Zhan 2009; Hill et al. 2011; Merchant and Madura 2012; Schmitt, Rothman, and Reith 2013). More specifically, the abuse liability of cocaine and cocaine-like antagonists is related to binding affinity and selectivity (Heikkila, Cabbat, and Duvoisin 1979; Kuhar, Ritz, and Boja 1991; Newman and Kulkarni 2002; Newman and Katz 2009) as well as rate of drug entry into brain (Kimmel et al. 2008) and occupancy of DAT (Lindsey et al. 2004).

Because of the increase in synaptic dopamine levels, it was originally assumed that all DAT antagonists would elicit behavioral effects similar to those of cocaine; that is, besides a difference in potency, each drug would be readily self-administered, produce strong psychomotor stimulation, and be highly addictive (Ritz et al. 1987; Bergman et al. 1989; Cline et al. 1992; Katz, Izenwasser, and Terry 2000). However, several atypical DAT antagonists do not produce the same increase in self-administration or locomotor stimulation as most DAT inhibitors (Carroll et al. 2009; Vosburg et al. 2010). In particular, the piperazine-based compound GBR12909 in comparison to cocaine exhibits increased affinity for and slower dissociation from DAT resulting in prolonged duration of DAT inhibition (Rothman et al. 1991). However, the drug has a slower onset to block DAT and mice pre-treated with GBR12909 displayed decreased self-administration of cocaine (Baumann et al. 1994; Glowa et al. 1995; Tella 1995) likely due to the reduced ability of cocaine to increase extracellular DA (Rothman et al. 1991). Though originally a promising cocaine-abuse pharmacotherapy, it prolonged the QTc interval in Phase II clinical trials of cocaine-experienced subjects (Vocci, Acri, and Elkashef 2005), suggestive of inhibition of a voltage-gated potassium channel (Tang et al. 2001). Analysis

of several benztropine analogs, a related class of atypical DAT antagonists, identified compounds with high affinity and selectivity for DAT though treatment attenuated hyperlocomotor activity and decreased drug discrimination in rats trained to recognize cocaine from saline (Rothman et al. 2008), indicating their potential as cocaine-abuse therapeutics.

CHAPTER II

COMPUTATIONAL AND BIOCHEMICAL DOCKING OF THE IRREVERSIBLE COCAINE ANALOG RTI 82 DIRECTLY DEMONSTRATES LIGAND POSITIONING IN THE DOPAMINE TRANSPORTER CENTRAL SUBSTRATE-BINDING SITE

Introduction

The dopamine transporter (DAT) is a presynaptic plasma membrane protein that is responsible for driving the reuptake of dopamine (DA) from the synapse following its vesicular release. This activity controls the magnitude and duration of dopaminergic neurotransmission by maintaining synaptic DA homeostasis (Nianhang Chen and Reith 2004; Gether et al. 2006; Torres and Amara 2007) and is critical for proper functioning of the nervous system (Giros et al. 1996). Dysfunction of DAT is hypothesized to contribute to dopaminergic disorders such as schizophrenia, bipolar disorder, attention deficit hyperactivity disorder, autism spectrum disorder, Tourette syndrome, Parkinson disease, and hereditary DAT deficiency syndrome (Gether et al. 2006; Torres and Amara 2007; Hahn and Blakely 2007; Pramod et al. 2013; Gainetdinov and Caron 2003; Kurian et al. 2011). Many drugs such as bupropion and methylphenidate that bind to DAT and inhibit transport are used therapeutically to regulate dopaminergic signaling in disease states, whereas others such as cocaine induce psychomotor stimulation and addiction. Many but not all uptake blockers are reinforcing, and some such as the benzotropines can counteract a number of cocaine's behavioral effects (Desai et al. 2005; Velázquez-Sánchez et al. 2010; Loland et al. 2008). This suggests the potential for development of improved pharmacotherapies for drug abuse and other DA disorders, but despite years of

research, the molecular basis by which structurally distinct inhibitors interact with DAT and induce differential neurochemical and behavioral outcomes remains incompletely understood.

DAT and the related cocaine-sensitive norepinephrine and serotonin transporters (NET and SERT) belong to the neurotransmitter sodium symporter (NSS) subfamily of solute carrier 6 transporters (SLC6A) that share a common topology of 12 transmembrane (TM) domains connected by extracellular (EL) and intracellular (IL) loops (Pramod et al. 2013; Kristensen et al. 2011; Brøer and Gether 2012). Solute translocation is driven by a Na⁺- and Cl⁻-dependent alternating access mechanism in which the proteins cycle through outwardly and inwardly facing conformations that bind and release substrates on opposite sides of the membrane (Forrest et al. 2008). Major insights into structural mechanisms of NSS proteins have come from the homologous prokaryotic leucine transporter (LeuT) from *Aquifex aeolicus*, which has been crystallized in conformations corresponding to outwardly facing, occluded, inwardly facing, and inhibitor-bound forms (Yamashita et al. 2005; Zhou et al. 2007; Zhou et al. 2009; Singh, Yamashita, and Gouaux 2007; Singh et al. 2008; Krishnamurthy and Gouaux 2012). These structures reveal that outwardly facing transporters possess an aqueously accessible external vestibule that opens to a compact central/primary substrate-binding site (S1) composed of residues from TM domains 1, 3, 6, and 8 (Yamashita et al. 2005). Binding of substrate, two Na⁺ (Na1 and Na2) ions, and one Cl⁻ ion to their respective sites triggers conformational changes leading to closure of an extracellular gate that occludes S1, followed by opening of the intracellular gate and generation of an inwardly facing form that releases solutes to the cytoplasm (Forrest et al. 2008; Watanabe et al. 2010; Faham et al. 2008; Gabrielsen et al. 2012; Felts et al. 2014; Henry et al. 2011; Zdravkovic et al. 2012; Zhao et al. 2011; C. Zhao et al. 2012; Caplan, Subbotina, and Noskov 2008; Koldsø et al. 2011). The S1 site is highly conserved in mammalian

transporters, and mutagenesis of many DAT residues near this site, including Phe-76, Asp-79, Val-152, Phe-155, Tyr-156, Asn-157, Phe-319, Val-327, and Ser-421, reduces dopamine transport (Kitayama et al. 1992; Lin et al. 1999; Lin, Wang, and Uhl 2000; Chen, Vaughan, and Reith 2001; Zhicheng Lin and Uhl 2002; Beuming et al. 2008; Henry et al. 2006; Lee et al. 2000), supporting the participation of these amino acids in substrate recognition or translocation. In particular, Asp-79 in TM1 of DAT and the homologous Asp residues in NET and SERT coordinate the positive charge on monoamine substrates and play an essential role in transport (Pramod et al. 2013; Kristensen et al. 2011; Bröer and Gether 2012; Yamashita et al. 2005; Barker et al. 1999; Penmatsa, Wang, and Gouaux 2013). However, a second, highly controversial substrate site (S2) proposed to play a role in the initiation of transport has been identified in LeuT in the extracellular vestibule above the outer gate (Zhao et al. 2011; Piscitelli, Krishnamurthy, and Gouaux 2010; Quick et al. 2009; Wang, Elferich, and Gouaux 2012). The S2 site may also be conserved in mammalian NSS transporters, but its existence and role in NSS function remain a topic of debate.

Intensive efforts to understand the basis for cocaine interaction with DAT, NET, and SERT have relied on site-directed mutagenesis (SDM), substituted cysteine accessibility method (SCAM) (Henry et al. 2003; Ferrer and Javitch 1998; Sen et al. 2005; Chen, Sachpatzidis, and Rudnick 1997), and quantitative structure activity relationship (QSAR) of ligand pharmacophores (Carroll et al. 1991; Carroll et al. 1994). Many studies support the formation of a salt bridge between the conserved Asp residue in the unwound region of TM1 and the positively charged tropane nitrogen of cocaine, suggesting that cocaine binds near S1 and competes with substrate for interaction at this crucial site (Kitayama et al. 1992; Beuming et al. 2008; Henry et al. 2006; Henry et al. 2003; Chen, Sachpatzidis, and Rudnick 1997; Carroll et al.

1992). Numerous other residues, including Leu-104, Phe-105, Ala-109, Asn-157, Tyr-251, Tyr-273, Thr-315, Ser-320, Thr-455, and Ser-459 found throughout core TM domains of DAT, have also been implicated in the binding of cocaine and its analogs (Beuming et al. 2008; Wu and Gu 2003; Chen, Han, and Gu 2005; Itokawa et al. 2000; Bisgaard et al. 2011), but it has been difficult to unambiguously assign antagonist binding functionalities based on mutation-based strategies due to potential indirect effects on protein structure. Overlap of high affinity inhibitor binding with the S1 site is supported by biochemical studies (Henry et al. 2006; Henry et al. 2003; Chen, Sachpatzidis, and Rudnick 1997; Andersen et al. 2009) and by recent structures of *Drosophila* (d) DAT and a LeuT/SERT hybrid co-crystallized with antidepressants (Penmatsa, Wang, and Gouaux 2013; Wang et al. 2013). However, some DA transport inhibitors lack the charged nitrogen necessary to form the salt bridge with Asp-79 (Ukairo et al. 2005; Madras et al. 1996; Meltzer et al. 1997), suggesting that inhibitor binding can occur without this interaction and thus may not be limited to the S1 pocket (Plenge et al. 2012). This possibility is supported by crystal structures of LeuT complexed at relatively low affinity with several selective serotonin uptake inhibitors (SSRIs) and tricyclic antidepressants (TCAs) in regions that overlap with S2 (Zhou et al. 2007; Zhou et al. 2009; Singh, Yamashita, and Gouaux 2007; Wang et al. 2013). However, as yet no crystal structures of NSS transporters complexed with cocaine have been obtained to distinguish between these possibilities, and many unknowns remain regarding the mechanistic relationship of S1 and S2 sites to each other and to the actions of cocaine and other categories of transport inhibitors.

In this study, we investigated the site of cocaine binding on DAT by combining the strategies of comparative modeling, small molecule docking, molecular dynamics, peptide mapping, and SCAM protection to identify the attachment site for the irreversible cocaine analog

[¹²⁵I]3β-(*p*-chlorophenyl)tropane-2β-carboxylic acid, 4'-azido-3'-iodophenylethyl ester ([¹²⁵I]RTI 82) (Fig. 11) (Carroll et al. 1992). RTI 82, cocaine, and the commonly used cocaine analog (–)-2β-carbomethoxy-3β-(4-fluorophenyl)tropane (CFT) share a common pharmacophore consisting of the tropane ring and 3β-phenyl group that direct high affinity binding (Carroll et al. 1991; Carroll et al. 1994). All of these compounds bind noncovalently to DAT, but [¹²⁵I]RTI 82 contains a photoactivatable 4'-azido-3'-iodophenylethyl ester (AIP) moiety that forms a highly reactive singlet nitrene that reacts with C–H or N–H groups when the sample is irradiated with ultraviolet light, thus forming a covalent bond with the protein (Geurink et al. 2012; Kotzyba-Hibert, Kapfer, and Goeldner 1995). Using irreversible labeling as a strategy for determining the site of ligand-protein interaction, we previously demonstrated that [¹²⁵I]RTI 82 cross-links to human (h) DAT within a 40-residue region encompassing TM6 (Vaughan et al. 2007). Utilizing this information as a molecular constraint in flexible docking of RTI 82 to rat (r) DAT homology models based on “outward-occluded” and “open-to-out” LeuT crystal structures (Protein Data Bank codes 2A65 and 3F3A), we identify RTI 82 binding in the S1 pocket in an orientation that suggests TM6 residue Phe-319 as the likely site of AIP adduction. This prediction was verified by focused mapping of the [¹²⁵I]RTI 82 attachment site using methionine substitution mutagenesis and cyanogen bromide (CNBr) digestion and by SCAM analyses that indicate protection of S1 but not S2 residues by cocaine and RTI 82. These positive function findings physically localize the tropane pharmacophore to the S1 site in transport-competent mammalian transporters and provide information crucial for refinement and experimental verification of results obtained by homology modeling.

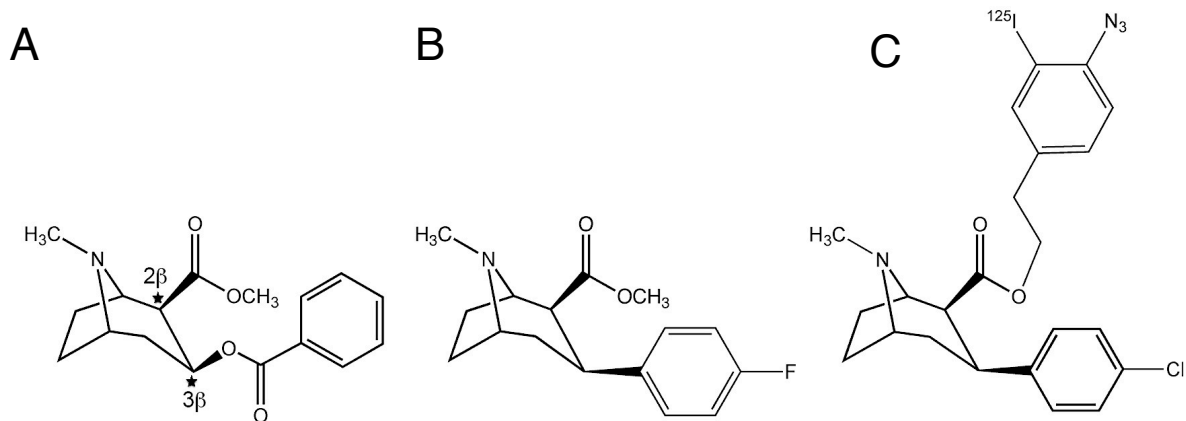


Figure 11. Chemical structures of cocaine, CFT, and RTI 82. *A*, structure of cocaine highlighting the tropane ring 2β-methyl ester and 3β-phenyl ester (*stars*). *B*, structure of CFT showing phenyl fluoride moiety appended directly to the 3β position of the tropane pharmacophore. *C*, structure of [¹²⁵I]RTI 82 showing substitution of 3β-phenyl chloride moiety and 2β-phenyliodoazido moiety on the tropane pharmacophore. The N₃ group undergoes covalent adduction to the protein upon irradiation with UV light.

Methodology

Comparative DAT Homology Model Construction

The three-dimensional coordinates from the outward-occluded and open-to-out crystal structures (Protein Data Bank IDs 2A65 and 3F3A, respectively) of the LeuT from *A. aeolicus* (Uniprot accession number O67854), were mapped onto rDAT sequence based on the comprehensive sequence alignment from Beuming *et al.* (Beuming *et al.* 2006) to construct the occluded and outward facing homology models of rDAT. The missing atomic densities in the loop regions of the transporter were rebuilt using the kinematic closure method (Mandell, Coutsias, and Kortemme 2009) in Rosetta3.1 (Leaver-Fay *et al.* 2011). The N and C termini, which are missing in LeuT, were truncated in the rDAT model to yield a structure consisting of amino acids 65–601, which includes TMs 1–12. Side chains for all residues in the protein were built using Rosetta's Metropolis Monte Carlo rotamer search algorithm (Kuhlman *et al.* 2003). The starting rDAT model was subjected to six iterative rounds of relaxation and minimization

using Rosetta3.1 to produce an ensemble of 100 rDAT models each for 2A65 and 3F3A. The top 10 ranked models based on the Rosetta E_{total} score for each template were verified manually and carried forward for docking.

RosettaLigand Docking

The three-dimensional structure for the RTI 82 ligand was built using “builder” of the Molecular Operating Environment (Chemical Computing Group, Inc. 2012) program and energy-minimized and was output as a mol file. The mol file was used as input for Rosetta3.1 to generate 1000 RTI 82 rotamers. The ligand parameter file, which assigns Rosetta atom types to the molecule for use in RosettaLigand 3.1 (RL), was generated using the Rosetta3.1 script “molfile_to_params.py”. Because of the multiple resonance states of the azide group and lack of an available parameterized force field for this chemical group, we utilized the atom type Nhis which was assigned to the azide nitrogens by Rosetta. Manually changing the atom types to Nhis-Nlys-Nlys, Nhis-NH₂O-NH₂O, Nlys-Nlys-Nlys, or Ntrp-Ntrp-Ntrp to test other bond hybridization and charge states resulted in markedly poorer docking energy scores. For the ensemble of 10 rDAT models built from the LeuT 2A65 structure, the collection of 1000 RTI 82 conformers was randomly docked into the structures using RL (Meiler and Baker 2006). For more information regarding the RL docking protocol, see Combs *et al.* (Combs et al. 2013). Briefly, RTI 82 was placed at a coordinate in the rDAT model equivalent to the substrate-binding site in LeuT and allowed to randomly translate within a 10-Å sphere. Acceptable ligand translations underwent up to 1000 random rotations to energetically optimize the pose and minimize clashes. Residue side chains within 6 Å of RTI 82 were repacked using a Metropolis Monte Carlo simulated annealing algorithm and scored using the knowledge-based Rosetta energy function `interface_delta`, which is the difference between the total binding energy

$E_{(\text{transporter} + \text{ligand})}$ and the sum of the energy of the individual components $E_{(\text{transporter})} + E_{(\text{ligand})}$ separated by 500 Å. A total of 25,000 ligand dockings were conducted for the 10 models from 2A65. The process was repeated for 3F3A-based models.

The resulting rDAT-RTI 82 complexes were ranked based on the interface_delta scores, and the top 10% of each of the 10 rDAT structures was compiled and evaluated by ligand-based r.m.s.d. clustering (Combs et al. 2013). The top scoring 10% rDAT-RTI 82 complexes were evaluated by two methods as follows: 1) complexes found in the largest r.m.s.d.-based clusters were ranked by score, and 2) rDAT-RTI 82 complexes were filtered for RTI 82 poses with the azido moiety within 5 Å of residues of TM6 and the tropane nitrogen within 5 Å of residue Asp-79.

Induced Fit Docking

The top Rosetta rDAT homology models of the 3F3A and 2A65 templates were modified to include two Na⁺ ions and one Cl⁻ ion in their reported positions (Yamashita et al. 2005; Forrest et al. 2007) using Maestro (Schrödinger, LLC, Portland, OR). The protein was relaxed, optimized for hydroxyl and thiol groups, and minimized using default options in the protein preparation module of the Maestro software package (Maestro Schrödinger, LLC, Portland, OR). RTI 82 conformers were generated using the LIGPREP (Version 2.5) protocol. RTI 82 conformers were docked into the rDAT homology models containing Na⁺ and Cl⁻ ions utilizing induced fit docking (IFD) protocol (Sherman et al. 2006). As the Na⁺ and Cl⁻ ions were relaxed during the IFD analysis, we verified that the ions remained coordinated by the same side chains before and after docking. The final ranking of the docked poses comes from the composite score, which is GlideScore + 0.05 × PrimeEnergy.

Molecular Dynamic Simulations

Molecular dynamic simulations (GROMACS) were conducted on RTI 82 docked rDAT homology models with incorporated Na^+ and Cl^- ions. The top ranked RTI 82 docked rDAT poses were embedded in the center of a pre-equilibrated 1-palmitoyl-2-oleoyl-phosphatidylcholine (POPC) lipid bilayer (along the z axis, coinciding with the normal of the POPC bilayer) using Visual Molecular Dynamics package (Humphrey, Dalke, and Schulten 1996). The dimensions of the simulation box were $20 \times 20 \times 14$ Å containing one protein, one ligand, $\sim 50,000$ TIP3P water molecules, and ~ 225 POPC molecules. 186 Na^+ and 188 Cl^- counter-ions were added to obtain electroneutrality for the system reaching a salt concentration of 150 mM. All simulations were carried out with GROMACS version 4.5.4 (Hess et al. 2008) using CHARMM27 force field under periodic boundary conditions. SwissParam (Zoete et al. 2011) was used to generate RTI 82 topology and parameter files, based on the Merck molecular force field, that are compatible with CHARMM and GROMACS. Isothermal-isobaric ensemble with velocity scaling (V-rescale) thermostat and Parrinello-Rahman barostat was used to perform simulations. For the CHARMM force field operating in GROMACS, electrostatics were calculated using particle mesh Ewald (Darden, York, and Pedersen 1993) with appropriate cutoffs as follows: $r_{\text{list}} = 1.3$; $r_{\text{coulomb}} = 1.3$; $r_{\text{vdw}} = 1.2$; $\text{vdwtype} = \text{switch}$; and $\text{rvdw_switch} = 0.8$. Fourier spacing of 0.12 nm and a particle-mesh Ewald electrostatic order of 4 was employed. V-rescale thermostat with a coupling constant of 0.1 ps was used to separately couple protein, lipid, and solvent, including water and ions. The pressure was coupled using the Parrinello-Rahman algorithm at 1 bar with a coupling constant of $\rho = 1$ ps, using a uniform compressibility of $4.5 \times 10^{-5} \text{ bar}^{-1}$. The coordinates were saved every 100 ps with an integration time step of 2 fs. The LINear Constraint SolVer (LINCS) algorithm was used to restrain all bond

lengths (Hess et al. 1997). The minimized, ion-bound rDAT-RTI 82 complexes in the POPC bilayer were further equilibrated for 4 ns in GROMACS at a temperature of 303 K, by fixing the position of the docked complex through application of position restraints of $1000 \text{ kJ}\cdot\text{mol}^{-1}\cdot\text{nm}^{-2}$ on each heavy atom, whereas lipids and water were allowed to move normally. After an initial equilibration for 4 ns, the production runs were performed for 60 ns. The pressure was maintained at 1 atm using semi-isotropic pressure coupling to a Parrinello-Rahman barostat with a coupling constant of 5 ps. Conformations resulting from the production phase of each simulation were stored at intervals of 100 ps and analyzed. PyMOL (Delano 2013) was used to generate the molecular graphic diagrams.

Cell Culture and Site-directed Mutagenesis

For photoaffinity labeling experiments, WT and mutant cDNAs in pcDNA3.1/His vector were stably expressed in Lewis lung carcinoma-porcine kidney (LLC-PK₁) cells. All mutants in the study were generated using the Stratagene QuikChange® kit and verified by sequencing (Northwoods DNA, Solway MN, Eurofins MWG Operon, Huntsville, AL). Mutants for SCAM analysis were generated in the E2C background (C90A and C305A) of pcDNA3-rDAT and expressed transiently in HeLa or HEK-GripTite cells (Invitrogen) using Lipofectamine® 2000 (Invitrogen) or TransIT®-LT1 (Mirus). WT and mutant r/hDAT cells were maintained in a humidified chamber with 5% CO₂ at 37 °C in α -minimum essential medium (AMEM: 5% fetal bovine serum, 2 mM L-glutamine, 200 $\mu\text{g}/\text{ml}$ G418, and 100 $\mu\text{g}/\text{ml}$ penicillin/streptomycin) for LLC-PK₁ cells or Dulbecco's modified Eagle's medium (DMEM: 10% FBS, 100 units/ml penicillin G, 100 $\mu\text{g}/\text{ml}$ streptomycin, and 0.25 $\mu\text{g}/\text{ml}$ amphotericin B) for HeLa and GripTite cells (600 $\mu\text{g}/\text{ml}$ G418). Once plated, the S321M line was grown at 29 °C for better expression of mature DAT.

[³H]Dopamine Uptake and [³H]CFT Binding Assays

WT and mutant His-hDAT LLC-PK₁ cells were grown in 24-well plates to 80–90% confluency. For [³H]DA uptake, cells were rinsed twice with 500 µl of 37 °C Krebs-Ringer/HEPES buffer (KRH: 25 mM HEPES, 125 mM NaCl, 4.8 mM KCl, 1.2 mM KH₂PO₄, 1.3 mM CaCl₂, 1.2 mM MgSO₄, 5.6 mM glucose, pH 7.4). Uptake was performed in a final volume of 500 µl of KRH with nonspecific uptake determined with 100 µM (–)-cocaine. Assays were initiated by addition of 10 nM [³H]DA plus 3 µM DA and allowed to proceed for 8 min at 37 °C. For [³H]CFT binding, cells were rinsed twice with 500 µl of ice-cold KRH and incubated with 10 nM [³H]CFT in KRH for 2 h on ice in a final volume of 500 µl. Binding was performed in triplicate with nonspecific binding determined with 30 µM mazindol. Uptake and binding reactions were quenched by washing cells twice with ice-cold KRH followed by solubilization of cells with radioimmunoprecipitation assay buffer (RIPA: 1% Triton X-100, 0.1% SDS, 150 mM NaCl, 1 mM EDTA, 50 mM Tris-HCl, pH 7.5) containing protease inhibitors. Lysates were assessed for radioactivity by liquid scintillation counting and for protein content by the BCA method. DAT expression was assessed by immunoblotting with hDAT monoclonal antibody 369 (mAb 369, Chemicon International) with band densities quantified using Bio-Rad Quality One software. All assays were performed in triplicate and repeated at least three times. Results were normalized for DAT levels and expressed relative to the WT protein set at 100%. Statistical significance was determined by ANOVA with post hoc Dunnett test with significance set at $p < 0.05$.

RTI 82 Synthesis and Radioiodination

RTI 82 and the amino precursor of [¹²⁵I]RTI 82 were synthesized using modifications (Carroll et al. 1992) of the original procedure. Radioiodination was conducted as described previously (Lever et al. 1993).

Photoaffinity Labeling and CNBr Peptide Mapping

These procedures were performed as described previously (Vaughan et al. 2007; Parnas et al. 2008). WT and mutant cells were washed twice with ice-cold KRH and incubated with 5 nM [¹²⁵I]RTI 82 in KRH buffer for 2 h on ice in the presence or absence of 30 μM (–)-cocaine. Cells were irradiated with ultraviolet light (254 nm) for 5 min to covalently attach the ligand to the protein. The cells were washed twice with cold KRH to remove unbound ligand and were lysed with RIPA containing protease inhibitor for 30 min on ice with shaking. The lysates were centrifuged at 20,000 × *g* for 12 min at 4 °C, and supernatants were subjected to electrophoresis on 8% Tris-glycine polyacrylamide gels for gel purification or were immunoprecipitated with anti-His antibody and electrophoresed on 4–20% Tris-glycine polyacrylamide gels, followed by autoradiography. For CNBr analysis, photolabeled DAT bands were excised from the gel, electroeluted, dialyzed against purified H₂O, lyophilized to dryness, and suspended in vehicle. Aliquots were counted in a scintillation counter, and equal amounts of radioactivity were subjected to peptide mapping. To assess fragment deglycosylation, samples were treated with vehicle or 150 units of neuraminidase (New England Biolabs) for 1 h at 37 °C followed by addition of 3000 units of PNGase F (New England Biolabs) for 15 h at 22 °C prior to treatment with CNBr. For CNBr proteolysis, samples were resuspended in 70 μl of 70% formic acid with or without addition of 1 M CNBr for 24 h at 22 °C in the dark. Reactions were quenched with 1 ml of purified water, and samples were lyophilized to dryness, followed by four additional

rounds of resuspension with water and lyophilization. Samples were resuspended in 4SB buffer (50 mM Tris, 5 mM EDTA, 4% SDS, pH 7.4) and subjected to acetone precipitation followed by centrifugation at $20,000 \times g$ for 15 min. Pellets were solubilized in sample loading buffer (0.625 M Tris-HCl, 2% SDS, 10% glycerol, 5% 2-mercaptoethanol, 0.005% bromphenol blue) and analyzed by SDS-PAGE/autoradiography on 4–20% gels. For each experiment, 2–3 mutants were photoaffinity-labeled and analyzed with WT DAT exactly in parallel, and all results were replicated at least three times. CNBr peptide masses were calculated using PeptideCutter via ExPASy.

RTI 82 Potency in Phe-319 Mutants

HeLa cells were plated at a density of 50,000 cells/cm² in 24-well culture plates, incubated for 24 h, and transfected with rDAT constructs using GeneCellin (Bulldog Bio) (1 μ l per 200 ng of DNA). Following transfection (24 h), cells were washed with 37 °C KRH buffer and then incubated with 50 nM or 5 μ M [³H]DA and increasing concentrations of nonradiolabeled RTI 82 without photoactivation. Transport was terminated after 15 min by washing with cold KRH. Cells were then dissolved in MicroScint 20 (PerkinElmer Life Sciences) scintillation fluid, and radioactivity was quantified by a TopCount scintillation counter. Specific uptake was determined by subtracting uptake observed in nontransfected cells. For binding analyses, transiently transfected cells were washed twice with ice-cold KRH buffer followed by addition of various concentrations of competitor and 10 nM [³H]CFT. Samples were incubated at 4 °C for 2 h, washed twice with KRH, and dissolved in MicroScint 20 scintillation fluid, and radioactivity was quantified as above. Nonspecific binding was determined with 30 μ M mazindol. All experiments were performed in triplicate and repeated in three or more

separate assays. IC₅₀ data were analyzed using a one-way ANOVA and post hoc Dunnett test (Prism 4, GraphPad).

SCAM Protection Analysis of S1- and S2-binding Sites

HeLa or GripTite cells were plated and transfected as described above. For cocaine protection, HeLa cells were treated 24 h post-transfection with 5 μ M (-)-cocaine or vehicle for 10 min at 37 °C followed by addition of 5 mM MTSET for 10 min at room temperature in PBS/CM buffer (137 mM NaCl, 2.7 mM KCl, 10.1 mM Na₂HPO₄, 1.8 mM KH₂PO₄, 0.1 mM CaCl₂, 1.0 mM MgCl₂, pH 7.4). Post-treatment, cells were washed with PBS/CM and incubated in KRH buffer at 37 °C for 30 min to allow for cocaine dissociation. Cells were then washed with KRH and assayed for transport activity by incubation with 50 nM [³H]DA. Uptake was terminated after 15 min by washing with cold KRH. Cells were dissolved in MicroScint Beta (PerkinElmer Life Sciences), and radioactivity was quantified as described above. All experiments were repeated in three or more separate assays. Cocaine inhibition of uptake was verified in samples that did not undergo washout. Data were analyzed using a two-way ANOVA followed by a post hoc Bonferroni test (Prism 4). For RTI 82 protection studies, GripTite cells (Invitrogen) were processed 48 h post-transfection by washing twice with PBS/CM and incubating with 10 or 50 μ M RTI 82 or vehicle for 5 min followed by addition of 0.1 mM MTSEA-biotin (Biotium). Cells were then processed as described previously (Henry et al. 2003) to obtain cell lysates that were incubated with NeutrAvidin-agarose resin (ThermoFisher) to extract surface proteins labeled by MTSEA-biotin. Equal amounts of protein from total samples as determined by BCA assay (ThermoFisher) and equivalent volumes of surface protein pools were processed by SDS-PAGE and immunoblotting using anti-DAT monoclonal antibody (mAb 16). Surface and total DAT levels were quantitated from the density of immunoblot bands using

ImageJ (National Institutes of Health). Surface values were normalized to total DAT levels and are expressed as percent of untreated samples. Data were analyzed using a paired *t* test (Prism 4).

Results

Computational Docking of RTI 82

To facilitate elucidation of RTI 82 attachment to DAT, we generated LeuT-based comparative models of DAT followed by analysis of RTI 82 binding poses obtained from two independent computational docking methodologies, RL and IFD. For both methods, docking of RTI 82 was performed using rDAT homology models based on the LeuT outward-occluded (2A65) and open-to-out (3F3A) crystal structures. For RL, an ensemble of starting structures was used (10 for each conformation) (Kaufmann et al. 2009), and for IFD the lowest energy (top-scoring) structure from Rosetta homology modeling was refined using Protein Preparation Wizard (Schrodinger Software Suite), resulting in one structure each from the 2A65- and 3F3A-based templates. Best fit ligand-docked poses from these methods (see below) were then analyzed by molecular dynamics.

RosettaLigand

The rDAT-RTI 82 complexes obtained from RL docking, termed “decoys,” were ranked according to their interface_delta score that measures the interaction energy between the ligand and the protein (Combs et al. 2013). The top 10% ($n = 2500$ for each model) was evaluated by clustering of the ligand poses using CLUSTER with a 5 Å cutoff (Combs et al. 2013). The analysis resulted in five clusters of which clusters one and four contained the largest number of decoys (517 and 422, respectively) with the ligand occupying the central S1-binding site, and the remaining clusters contained between 11 and 178 decoys. In clusters one and four, the top 50 scoring decoys were initially filtered using molecular distance constraints from biochemical data

to identify complexes where the RTI 82 azido group was within 5 Å of any atoms between residues 272–344 of rDAT, and the tropane nitrogen of RTI 82 was positioned within 5 Å of the Asp-79 side chain (Kitayama et al. 1992; Vaughan et al. 2007).

In the 2A65-based outward-occluded models (Fig. 12A), the top 10 scoring decoys that satisfied the molecular constraints were chosen for further analysis. Notably, the top scoring models resulting from this selection method were identified as the highest scoring models prior to applying the distance filters, indicating that the computational docking methods were capable of identifying poses that were corroborated by biochemical cross-linking. Additionally, before the filtering step, all of the top-scoring decoys positioned the negatively charged carboxyl oxygen of Asp-79 within 3.5 Å of the positively charged tropane N, supporting salt bridge formation as a major contributor to energetically favorable binding. The top scoring 2A65-based decoys also displayed interaction between the RTI 82 3β-phenyl chloride group and TM3 residue Asn-157, an interaction that has previously been suggested as important for CFT and benztropine analog binding (Beuming et al. 2008; Bisgaard et al. 2011). In this “best pose,” which fulfilled multiple major biochemical constraints (Fig. 12A, *green sticks*), the AIP moiety was oriented toward the external vestibule with the arylazide positioned proximal to the phenyl side chain of Phe-319, suggesting this residue as the likely site of RTI 82 adduction.

In the 3F3A-based outward-facing models, analysis of the decoys generated from docking of RTI 82 to rDAT revealed that the AIP moiety fell within 4 Å of TM6 in 310 of the top scoring docked complexes. The azido group was positioned proximal to Phe-319 and Phe-325 in 208 and 224 of the complexes, respectively, with many of the poses placing the azido within 4 Å of both residues simultaneously. However, none of the 310 poses satisfied the second distance constraint between the tropane N and the Asp-79 side chain, and therefore, these decoys

were not further analyzed by MD. It is possible that the inability of Rosetta to account for Na^+ and Cl^- during the minimization of the ensemble of DAT structures may have had more of a negative impact on the more “open” 3F3A-based models than the “occluded” 2A65-based models and resulted in structures that were less able to approximate the native, ligand-bound conformation resulting in the inability to obtain a biochemically supported binding pose. However, given that Phe-325 was the most frequently identified candidate residue from these “outward-facing” models, its potential as a possible site of adduction was investigated in CNBr peptide mapping studies.

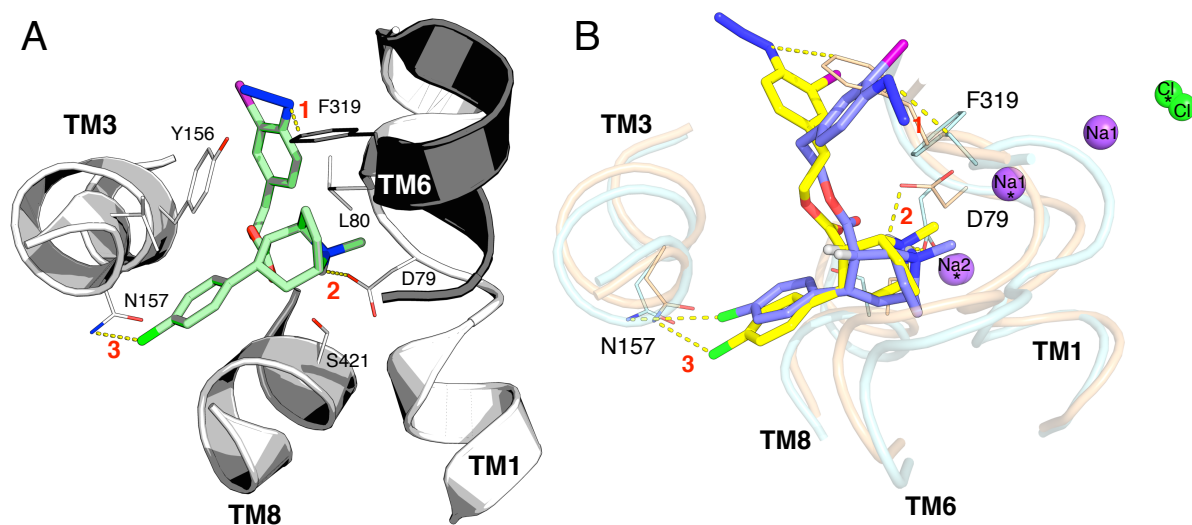


Figure 12. Small molecule docking analysis. *A*, best RL rDAT/RTI 82-docked complex based on energy and constraint fulfillment. Image depicts transmembrane domains 1, 3, 6, and 8 from the LeuT-based rDAT homology model from the crystal structure of the outward-occluded template 2A65. RTI 82 is represented by *green sticks*, and side chains of select residues are represented as *lines*. *Dashed yellow lines* indicate ligand-residue interactions between azido nitrogen of RTI 82 and Phe-319 (1), tropane N of RTI 82 and carboxyl oxygen of Asp-79 (2), and phenyl chloride of RTI 82 and side chain N of Asn-157 (3). *B*, RTI 82 docking to rDAT open-to-out and outward-occluded models using IFD. Transmembrane domains 1, 3, 6, and 8 from LeuT-based rDAT homology models based on outward-occluded and outward-facing templates 3F3A and 2A65 are represented as *cyan* and *brown tubes*, respectively. Na^+ and Cl^- ions are represented as *purple* and *green spheres*. 2A65 ions are designated with an *asterisk*. The best binding modes of RTI 82 identified in the IFD protocol are depicted as *blue sticks* for 3F3A-based model and *yellow sticks* for 2A65-based model. *Dashed yellow lines* indicate ligand-residue interactions between azido nitrogen of RTI 82 and Phe-319 (1), tropane N of RTI 82 and carboxyl oxygen of Asp-79 (2), and phenyl chloride of RTI 82 and side chain of Asn-157 (3).

Induced Fit Docking

Docking analyses using IFD in the Schrödinger software suite (Fig. 12B) were conducted to allow for the integration of energetic contributions of Na⁺ and Cl⁻ ions to ligand binding during the docking step (Yamashita et al. 2005; Barker et al. 1999; Forrest et al. 2007; Zomot et al. 2007; Wall, Innis, and Rudnick 1993). This alternative approach yielded 12 and 34 decoys from 2A65- and 3F3A-based models, respectively. Although the best scoring decoys consisted of RTI 82 poses in which the tropane N could be either protonated or unprotonated, only poses with protonated ligand were carried forward based on current data (Zhan et al. 2005) and analysis using FIXPKA in QUACPAK Version 1.5.0 (QUACPAC 2011), which predicts protonation of the group at pH 7.4. In both the 2A65- and 3F3A-based models, the top scoring poses positioned RTI 82 in the S1 pocket such that the AIP moiety was oriented toward Phe-319, with a π - π stacking interaction between the phenyl rings of the AIP group and the Phe-319 side chain (Fig. 12B). For the 2A65-based model, the two top scoring poses differed in their proximity to Phe-319 by only 0.011 Å, with the best energy scoring pose being selected (Fig. 12B, *yellow sticks*). For the 3F3A-based models, the AIP groups in the top two poses were proximal to the Phe-319 side chain with distances of 3.5 and 3.9 Å and the docking scores of -11.45 and -12.12, respectively. As the docking scores were similar, the best 3F3A pose (Fig. 12B, *blue sticks*) was selected based on proximity of Phe-319 and the azido group of RTI 82.

MD Simulation of RL and IFD Docked RTI 82 Poses

To further refine the RTI 82 pose in the rDAT-RTI 82 complexes, the best-docked structures from RL and IFD analyses were embedded in a POPC lipid bilayer and refined by MD simulation for 60 ns in GROMACS (Hess et al. 2008). The r.m.s.d. analysis of the ligand atoms and C α atoms of DAT during simulation revealed that RTI 82 was stable in the binding pocket

throughout the simulation (Fig. 13). In particular, we monitored the stability and time-dependent changes of two key protein-ligand interactions during simulation as follows: 1) the carboxylate oxygen of Asp-79 and the protonated tropane N, and 2) the amide nitrogen of Asn-157 and the 3 β -phenyl chloride. In all simulations, a stable (occupancies of 58% for RL-2A65, 52% for IFD-2A65, and 98% for IFD-3F3A) salt bridge interaction distance (3.5 Å) was observed between the RTI 82 tropane N and the Asp-79 carboxyl oxygen (*red and black lines* in Fig. 13, *A–C*). In the RL-2A65 and IFD-3F3A simulations, this interaction is maintained through periodic reciprocal reorientation of the O δ 1 and O δ 2 atoms. In contrast, using a 4-Å cutoff, the predicted polar interaction between Asn-157 and the RTI 82 3 β -phenyl chloride was observed to be stable (70% occupancy) only in the RL-docked pose (Fig. 13*A*, *blue line*), whereas negligible interaction (2–4% occupancy) was found in the IFD-docked poses (Fig. 13, *B and C*, *blue lines*).

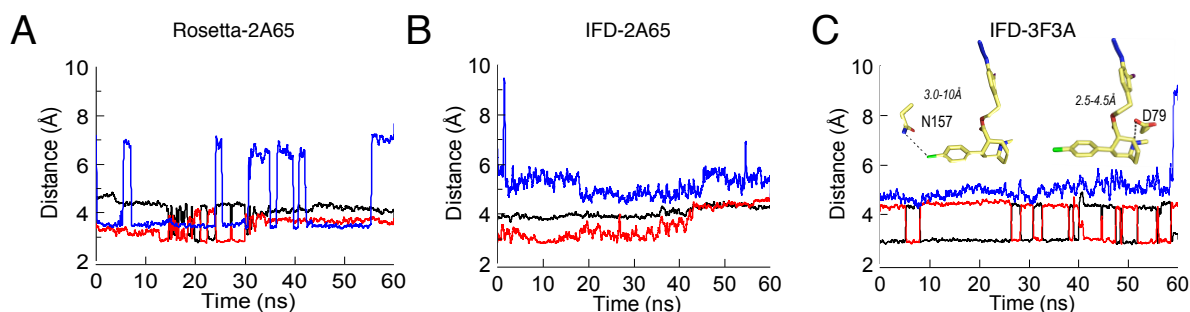


Figure 13. Molecular dynamics simulations. Time-dependent changes in distances between RTI 82 and residues involved in anchoring and orienting the ligand in the binding pocket reveal stable complexes during simulation in RL-docked, 2A65-based model (*A*), IFD-docked, 2A65-based model (*B*) and IFD-docked, 3F3A-based model (*C*). Shown are the distances during simulation between the side chain oxygen atom of Asp-79 and the protonated N of RTI 82 (*red and black traces* for O δ 1 and O δ 2), which ranged from 2.5 to 4.5 Å (*right inset*, *C*) and the amide nitrogen of Asn-157 and phenyl chloride of RTI 82 (*blue traces*), which ranged from 3.0 to 10.0 Å (*left inset*, *C*). Traces were smoothed using 5-point averaging in SciDavis (OpenSource).

The best poses obtained by RL and IFD before and after MD simulation are illustrated in Fig. 14. All of the docking methodologies, irrespective of the input rDAT model, yielded RTI 82

poses with the AIP arm extended out of the S1 pocket and toward the external vestibule (Fig. 14, A–C). In RL (Fig. 14A), RTI 82 docked in the outward-occluded model exhibited a structure with the AIP group in a bent conformation (*green sticks*), and after MD simulation, the AIP moiety displayed an extended and more linear conformation (Fig. 14A, *magenta sticks*). This extended AIP configuration was also found in the IFD-generated pose from the occluded form, both prior to (*yellow sticks*) and after (*black sticks*) MD simulation (Fig. 14B). This extension may be stabilized by an interaction between the AIP azido moiety and outer gate residue Arg-85 (Fig. 14, A and B). In contrast, in the IFD-generated open-to-out complex (Fig. 14C, *blue sticks*), the AIP group was slightly bent prior to simulation such that it formed a π - π stacking interaction with Phe-319 (*blue arrowhead*). During simulation of this docked complex, the AIP functional group (Fig. 14C, *brown sticks*) was repositioned between TM6 and TM10 near Ala-479, yet maintained π - π stacking with Phe-319 (*brown arrow*).

Notably, the position of the RTI 82 tropane pharmacophore was relatively unchanged in all poses following simulation, indicating that this functionality is the major contributor to ligand-protein interaction. In fact, during simulation, we consistently observed a slight translation of the tropane ring deeper into the binding pocket (Fig. 14, A–C). This was accompanied by similar adjustments of interacting residues Phe-76, Asp-79, Phe-325, and Val-327, which maintained their coordination with the ligand (Fig. 14, A–C). The interaction of the RTI 82 3 β -phenyl chloride with Asn-157 was also maintained during MD simulation of the RL pose (Fig. 14A) but was lost in both IFD decoys (Fig. 14, B and C). The validity of our poses is further supported by recent crystal structures of the LeuT/SERT hybrid (Wang et al. 2013) and dDAT (Penmatsa, Wang, and Gouaux 2013) transporters that show binding of SSRI and TCA antidepressants to S1. The binding pose of nortriptyline at the dDAT S1 pocket (Penmatsa,

Wang, and Gouaux 2013) overlaps substantially with our RTI 82 pose as shown in Fig. 14D. These findings indicate that many classes of high affinity neurotransmitter transporter inhibitors may assume similar poses within the S1 pocket.

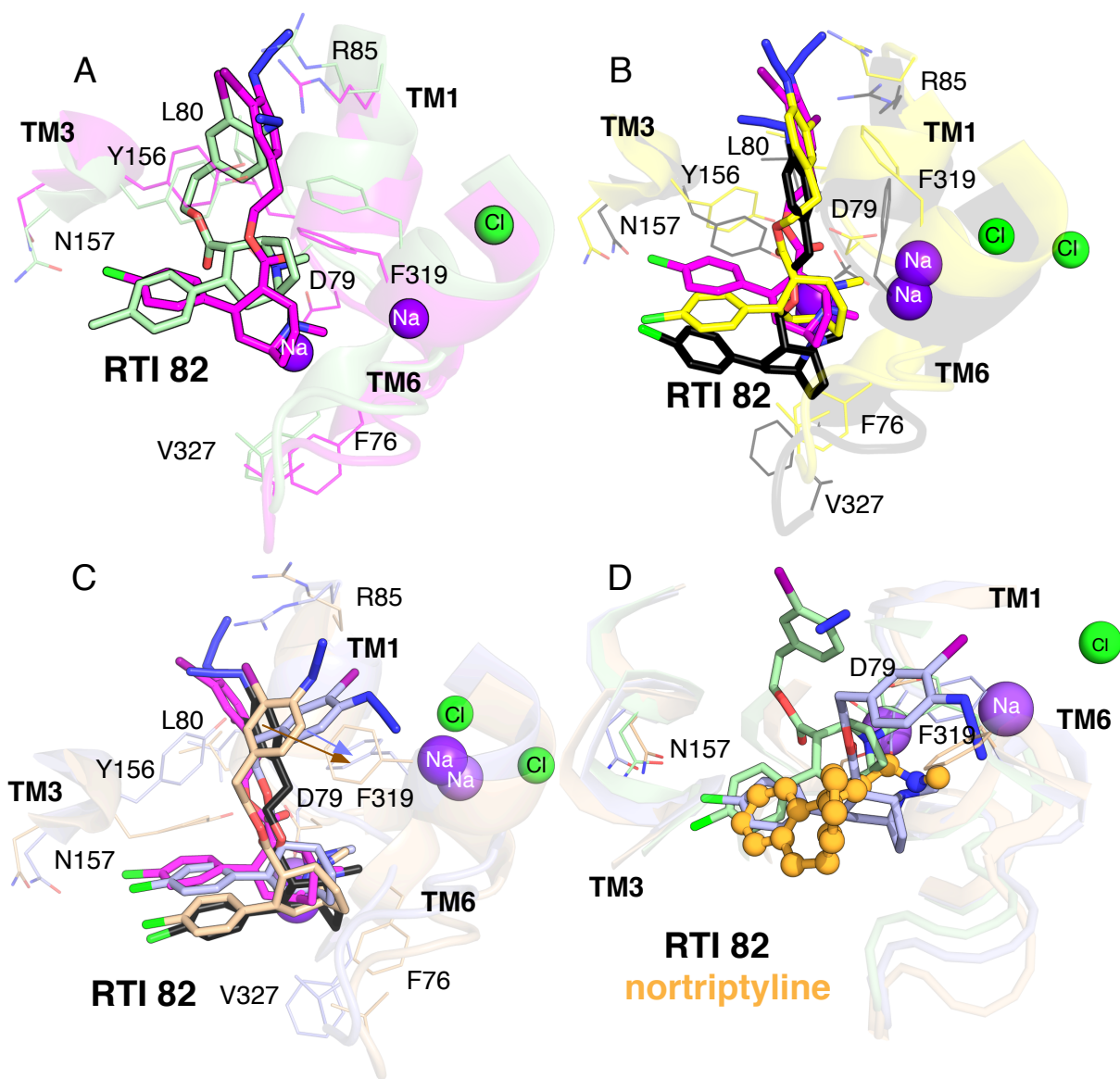


Figure 14. Comparison of rDAT-RTI 82 complexes before and after molecular dynamic simulation. *A*, superimposition of RL-docked, 2A65-based rDAT-RTI 82 complex before (*green*) and after (*magenta*) simulation. *B*, IFD-docked, 2A65-based rDAT-RTI 82 complex before (*yellow*) and after (*black*) simulation are shown in comparison with the MD-simulated, RL-docked RTI 82 pose (*magenta*). *C*, IFD-docked, 3F3A-based RTI 82-rDAT complex before (*blue*) and after (*brown*) MD simulation. *Arrows* indicate potential π - π stacking interactions. The RL (*magenta*) and 2A65-based (*black*) post-MD poses are also shown. *D*, overlay of the RL-

docked and 2A65-based (*green*) and IFD-docked and 3F3A-based (*blue*) rDAT-RTI 82 complexes in comparison with nortriptyline binding from the dDAT crystal structure (*orange spheres*). In each panel, relevant residues are illustrated as lines, and Na⁺ and Cl⁻ ions are represented by *purple* and *green spheres*, respectively.

Analysis of 4'-Azido-3'-iodophenyl Moiety Interactions with Phe-319

Our poses showing the proximity of the RTI 82 AIP group to the Phe-319 side chain suggested aromatic stacking as the basis for their interaction. To investigate this possibility, we generated a panel of conservative and nonconservative Phe-319 mutants (F319Y, F319W, F319M, F319C, and F319D) to analyze the potency of non-crosslinked RTI 82 to inhibit [³H]DA transport and [³H]CFT binding (Table 1). Using 50 nM DA to assess transport, the F319Y, F319W, and F319M mutants showed 8–43% of the WT DAT activity level, whereas uptake was undetectable in the F319C and F319D mutants (Table 1). The significant reduction in high affinity transport in F319M, F319C, and F319D DATs is consistent with the loss of aromatic interaction needed for Phe-319 to interact with its gating partner Tyr-156 (Kristensen et al. 2011; Yamashita et al. 2005; Singh, Yamashita, and Gouaux 2007). RTI 82 transport inhibition potencies did not differ between the WT protein or the Phe-319 mutants substituted with aromatic (Trp or Tyr) or nonaromatic hydrophobic (Met) residues, indicating that π - π interactions between the RTI 82 AIP group and the side chain of Phe-319 do not provide major contributions to RTI 82 binding. However, the potency of RTI 82 to inhibit [³H]CFT binding in F319C and F319D DATs was reduced by 4.3- and 7.1-fold (Table 1), indicating that inhibitor effects require hydrophobicity at Phe-319. We also found that when higher concentrations of DA (5 μ M) were used for uptake, the F319C and F319D mutants remained nonfunctional, suggesting that the charge substitution at this position may impact substrate affinity. However, transport activity could be restored in the F319C mutant to 79% upon application of 3.5 mM DA, whereas the F319D mutant remained nonfunctional.

Table 1. Activity of Phe-319 mutants and inhibitory potency of RTI 82. Data are presented as mean \pm S.E.; $n \geq 3$. Data were analyzed by one-way ANOVA with Dunnett's post hoc test.

	% Activity of rDAT	Competitive Uptake ^a RTI 82 IC ₅₀ (nM)	Competitive Binding ^c RTI 82 IC ₅₀ (nM)
rDAT	100 ^{a,b}	21 \pm 6	20 \pm 5
F319Y	27 \pm 5 ^a	21 \pm 7	ND
F319W	43 \pm 6 ^a	27 \pm 5	ND
F319M	8 \pm 6 ^a	19 \pm 6	ND
F319C	0 ^a , 79 \pm 3 ^d	ND	85 \pm 13**
F319D	0 ^a , 0 ^b , 0 ^d	ND	142 \pm 13***

^a [³H]DA (50 nM)

^b [³H]DA (5 μ M)

^c [³H]CFT (10 nM)

^d [³H]DA (3.5 mM)

ND - Not Determined

Data are presented as mean \pm S.E.; $n \geq 3$

Data were analyzed by one-way ANOVA with Dunnett's post-hoc test.

** $p < 0.01$, *** $p < 0.001$

CNBr Peptide Mapping of [¹²⁵I]RTI 82-Labeled TM6 Mutants

We then sought to validate the prediction from computational modeling that Phe-319 was the likely site of RTI 82 adduction. For this, we generated methionine (Met) substitutions of residues flanking Phe-320 in hDAT, which corresponds to Phe-319 in rDAT, for use in CNBr peptide mapping. hDAT is identical to rDAT in amino acid sequence across the region mutated for these studies (hDAT residues 318–330), and it was used because the two additional Met residues present in EL2 and EL3 of rDAT (Fig. 15) would significantly complicate the CNBr digestion analyses. In addition, to further strengthen the interpretation of the proteolysis patterns, we introduced all TM6 Met substitutions in an M272L background to eliminate Met-272 as a CNBr proteolysis site (Vaughan et al. 2007). In hDAT, Met-272 is the only Met between TM2 and TM7. Thus, in the M272L background, the introduction of Met into TM6 would result in generation of CNBr fragments of \sim 50 kDa that would extend from TM2 (Met-106, Met-111, or Met-116) to the inserted Met or CNBr fragments of \sim 6 kDa that would extend from the inserted

Met to Met-371 in TM7 (Fig. 15). The masses of the labeled CNBr fragments produced thus indicate the relative positions of the inserted Mets and the site of [¹²⁵I]RTI 82 adduction. For ease of discussion, we refer to the double mutants with TM6 Met substitutions in the M272L background solely by the TM6 mutation (*e.g.* V318M hDAT indicates M272L/V318M hDAT) and to the CNBr fragments by the flanking Mets, although the N terminus of each fragment is the residue following a proteolyzed Met.

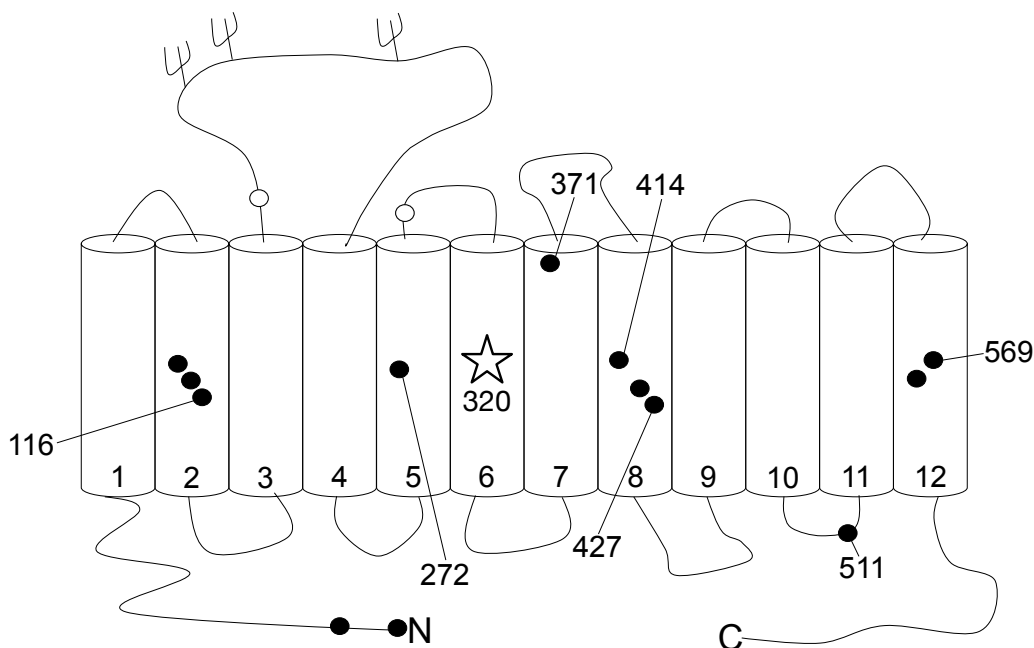


Figure 15. Schematic diagram of endogenous Met residues in DAT. The membrane topology of hDAT is shown with *cylinders* representing TM domains 1–12 and branched structures in EL2 indicating glycosylation sites. *Filled circles* show positions of endogenous Mets present in both hDAT and rDAT (numbering specific for hDAT), and *open circles* represent Mets present only in rDAT. The *star* represents the predicted adduction site of RTI 82 at Phe-320.

The mutants used for this study (V318M, C319M, F320M, S321M, L322M, V324M, and I330M) were stably expressed in LLC-PK₁ cells and assessed for expression, [³H]DA uptake, and [³H]CFT binding (Fig. 16). The expression levels determined by immunoblotting ranged from ~50 to 100% of WT DAT (Fig. 16A), with all showing expression of full-length, mature protein. When normalized for transporter expression levels, the mutants showed [³H]DA uptake

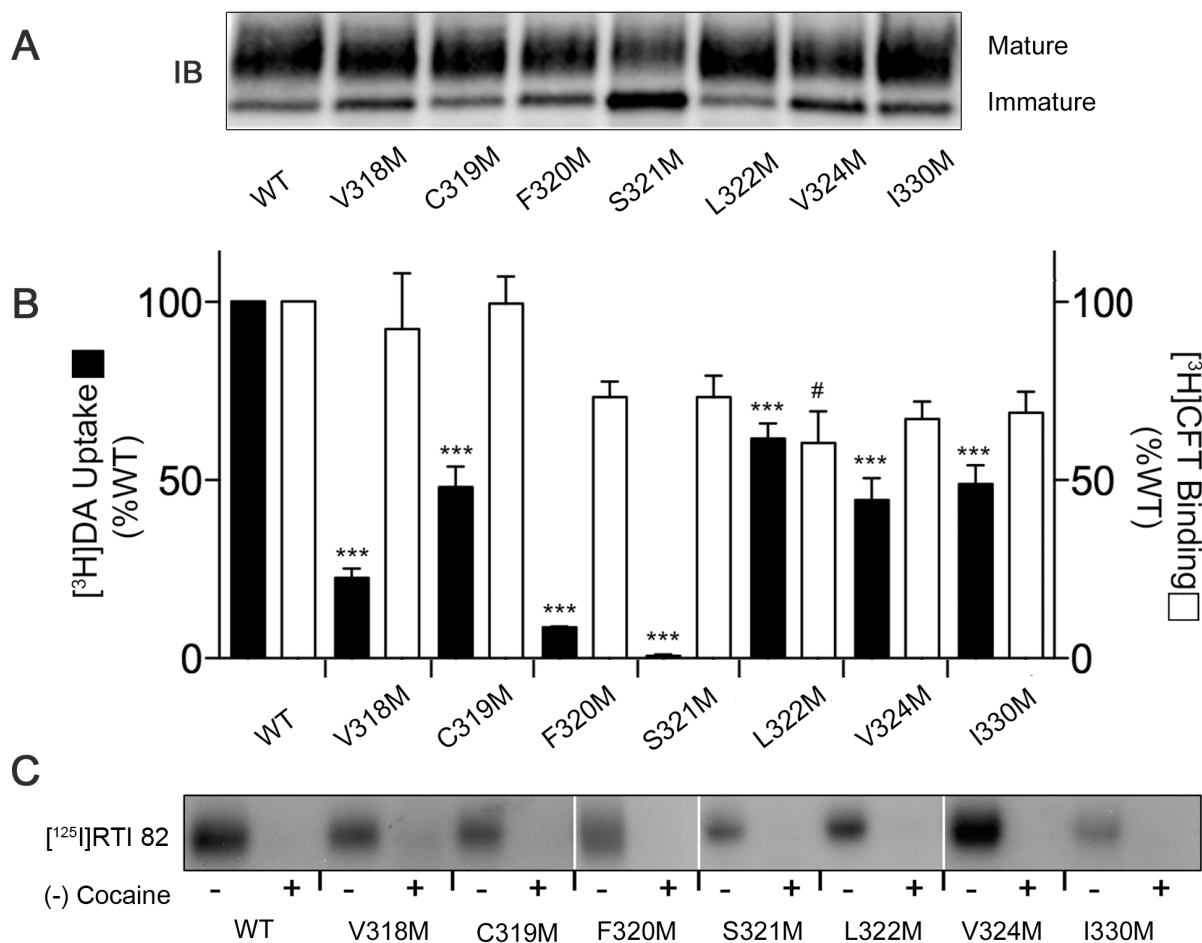


Figure 16. Characterization of Met-substituted hDATs. *A*, LLC-PK₁ cells expressing the indicated DAT forms were lysed, and equal amounts of protein were immunoblotted (IB) for DAT. *B*, LLC-PK₁ cells stably expressing the indicated DAT forms were assayed for [³H]DA uptake (filled bars) or [³H]CFT binding (open bars). Values shown (means of ± S.E.) are normalized for total DAT protein and expressed relative to the WT level (100%). #, *p* < 0.05 versus WT binding; ***, *p* < 0.001 versus WT uptake, by ANOVA with Dunnett's multiple comparison test. *C*, autoradiograph of the indicated hDAT forms photolabeled with [¹²⁵I]RTI 82 in the presence or absence of 30 μM (-)-cocaine.

values that ranged from ~20 to 60% of the WT protein, except for F320M and S321M, which exhibited <10% of the WT activity (Fig. 16B). Loss of transport in these mutants is consistent with their functional roles, as Phe-320 is proposed to act as a substrate pocket gating residue, and Ser-321 coordinates Na⁺ at the Na1 site (Yamashita et al. 2005; Penmatsa, Wang, and Gouaux 2013). [³H]CFT binding for the mutants was impacted less than transport, ranging from ~60 to

90% of WT levels when normalized for expression (Fig. 16B), and all forms showed [¹²⁵I]RTI 82 photoaffinity labeling that was fully blocked by cocaine (Fig. 16C), indicating that the mutations did not substantially disrupt the cocaine binding pocket.

For peptide mapping studies, the photolabeled proteins were gel-purified and subjected to treatment with vehicle (formic acid) or CNBr, followed by SDS-PAGE/autoradiography. Within each experiment, equal amounts of radioactivity for WT and mutant forms were analyzed to allow for direct comparison of peptide fragment production. Fig. 17A shows a compilation of representative peptide maps produced from three or more independent replicates for each mutant, with schematic diagrams indicating the origin of the labeled fragments in the primary sequence and site of [¹²⁵I]RTI 82 adduction (*star symbol*). Full-length, unproteolyzed DAT migrates at ~90 kDa (Fig. 17A, *odd-numbered lanes*) with no low molecular weight fragments observed. Aggregates seen at ≥180 kDa are most likely induced by the formic acid treatment, as they were not seen in samples subjected directly to electrophoresis. CNBr treatment of WT hDAT produced a labeled fragment of ~11 kDa (Fig. 17A, *lane 2, arrow a*), as we demonstrated previously (Vaughan et al. 2007), that corresponds to the region between Met-272 and Met-371 (calculated mass 10.6 kDa, *shaded region in schematic diagram a*), as well as larger fragments that likely arise from missed cleavage of Met-272. CNBr treatment of [¹²⁵I]RTI 82-labeled V318M and C319M hDATs produced fragments of ~6 kDa (Fig. 17A, *lanes 4 and 6, arrow b*) that are consistent with peptides extending from the inserted Mets to Met-371 (calculated masses ~5.6 kDa; *shaded region in schematic diagram b*), with higher molecular weight fragments in these samples also indicating missed cleavage of the inserted Mets. In contrast, mutants F320M, S321M, L322M, V324M, and I330M produced only the ~50-kDa fragments (Fig. 17A, *arrow c*)

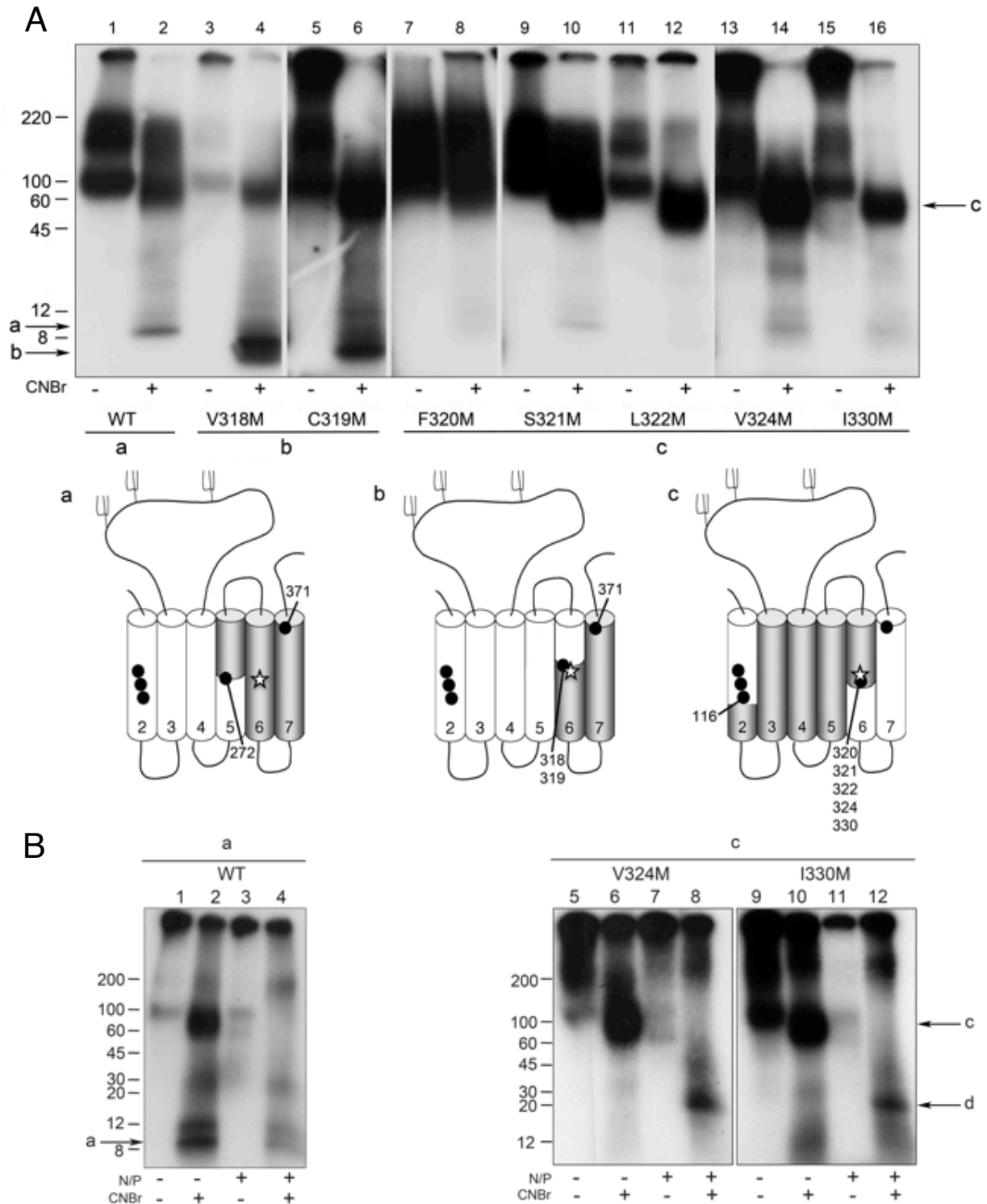


Figure 17. CNBr mapping of $[^{125}\text{I}]\text{RTI82}$ -labeled TM6 DAT mutants. The indicated DAT forms were photolabeled with $[^{125}\text{I}]\text{RTI 82}$ and gel-purified. *A*, equal amounts of radioactivity were treated with vehicle (formic acid, *odd-numbered lanes*) or CNBr (*even-numbered lanes*) and analyzed by SDS-PAGE/autoradiography. Unproteolyzed DAT is present in *odd-numbered*

lanes at ~90 kDa. CNBr proteolysis of the WT protein produces a fragment of ~11 kDa (*lane 2, arrow a*) that corresponds to the *shaded region* in *schematic diagram a*. CNBr treatment of V318M and C319M hDATs produces fragments of ~6 kDa (*lanes 4 and 6, arrow b*) that correspond to the *shaded region* in *schematic diagram b*. CNBr treatment of the remaining constructs produced fragments of ~50 kDa (*lanes 8, 10, 12, 14, and 16, arrow c*) that correspond to the *shaded region* in *schematic diagram c* but no fragments of <8 kDa. *Filled circles* in schematic diagrams represent Mets present in the constructs and the *star* represents the site of ligand adduction at Phe-320. *B*, equal amounts of radioactivity were subjected to the indicated combinations of neuraminidase plus PNGase F treatment (*N/P*) and CNBr digestion. *Arrow a*, CNBr fragment obtained from untreated and deglycosylated WT DAT; *arrow c*, CNBr fragments obtained from V324M and I330M DATs prior to deglycosylation; *arrow d*, CNBr fragments obtained from V324M and I330M DAT after deglycosylation.

that correspond to the *shaded region* in *schematic diagram c* (calculated peptide masses ~22.4–23.3 kDa, with additional ~25 kDa of mass contributed from EL2 *N*-linked carbohydrate), with no production of fragments with masses of <8 kDa. Note that full-length DAT and the larger peptide fragments run with anomalously low electrophoretic mobility on these high percent gels and that more accurate mass estimates of the ~50-kDa CNBr fragment were obtained using lower concentration gels (Vaughan et al. 2007).

To verify that the 50-kDa fragments in these mutants originated from the indicated region, we performed deglycosylation analysis of selected mutants with neuraminidase and PNGase F, which cleave terminal sialic acids and *N*-linked carbohydrates from canonical *N*-glycosylation sites in EL2 (Vaughan and Kuhar 1996; Li et al. 2004). For full-length WT, V324M, and I330M DATs (Fig. 17B, *lanes 1, 5, and 9*) treatment with neuraminidase plus PNGase F led to reductions in molecular mass due to deglycosylation (*lanes 3, 7, and 11*, and data not shown). As expected, deglycosylation did not alter the mass of the ~11-kDa WT CNBr fragment (Fig. 17B, *lanes 2 and 4, arrow a*), but it did reduce the masses of the ~50-kDa fragments from V324M and I330M DATs (*lanes 6 and 10; arrow c*) by ~25 kDa (*lanes 8 and 12, arrow d*). These results are consistent with the presence of EL2 in the ~50-kDa peptide

fragments and further validate the indicated origins of the photolabeled fragments in the schematic diagrams.

The cleavage patterns shown in Fig. 17, *A* and *B*, indicate that ligand adduction occurs C-terminal to V318M and C319M and N-terminal to F320M, S321M, L322M, V324M, and I330M, and because CNBr proteolyzes peptide bonds on the C-terminal side of Mets, they demonstrate that the adduction of [¹²⁵I]RTI 82 occurs at Phe-320. These results also rule out a significant level of [¹²⁵I]RTI 82 adduction to other residues within this stretch of TM6, including Phe-326, an interaction that was suggested in a large portion of the decoys from RL docking to the outward-facing rDAT model.

Although CNBr proteolysis of [¹²⁵I]RTI 82-labeled F320M, S321M, L322M, V324M, and I330M did not produce the ~6-kDa fragments seen in V318M and C319M hDATs, some lightly labeled fragments of ~8–10 kDa were seen in some digests. These fragments likely originate from adduction of [¹²⁵I]RTI 82 to a different region of the DAT primary sequence, as we have obtained preliminary evidence from antibody-based mapping that a small fraction of [¹²⁵I]RTI 82 adduction occurs C-terminal to TM6. Multisite incorporation of DAT photoaffinity labels has been previously demonstrated (Vaughan et al. 2001) and likely occurs due to the proximity of the TM domains in the protein core in conjunction with small fluctuations in AIP moiety orientation during the photoactivation process. However, the significantly lower labeling intensity of this secondary site relative to that occurring in TM6 indicates that Phe-320 is the predominant site of adduction.

Analysis of RTI 82 Protection of S2 Residues from Inactivation by Methanethiosulfonate (MTS) Reagents

The convergence of our computational docking and peptide mapping results strongly indicated that binding of the RTI 82 tropane pharmacophore occurs within the S1-binding site

and positions the AIP group for adduction to Phe-319/320. However, Phe-319 is present at the interface between S1 and S2 (Fig. 18A), and thus RTI 82 tropane positioning in S2 could potentially also result in cross-linking of this site. To assess this possibility, we analyzed several residues present in S1 (*yellow sticks*), S2 (*magenta sticks*), or intermediate positions (*green sticks*) of the DAT permeation pathway (Fig. 18A) for cocaine- and RTI 82-induced protection from SCAM reagents. All mutants were made in an MTSET-insensitive rDAT E2C (C90A and C305A) background (Gaffaney et al. 2014).

For transport protection experiments, we generated Cys mutations of residues Trp-84, Ile-159, Asp-475, and Ala-479, which are part of S2 or line the S1-S2 transition region (Fig. 18A, *magenta* and *green sticks*). All mutants were active, possessing DA transport activities ranging from 15 to 78% of the E2C DAT level. As expected, MTSET treatment of E2C DAT did not reduce uptake, consistent with the remaining Cys residues in the protein being inaccessible to the reagent. For protection analysis, cells were co-incubated with cocaine prior to addition of MTSET. All DAT forms preincubated with cocaine showed recovery of transport activity after washing (wash control), demonstrating the reversibility of cocaine binding. MTSET treatment of W84C, I159C, D475C, and A479C DATs resulted in a 60–90% loss in transport activity (Fig. 18B), indicating full or partial accessibility of these residues to modification. Co-incubation of the cells with (–)-cocaine during MTSET treatment did not protect the mutants from inactivation indicating a lack of cocaine pharmacophore binding in S2. In addition, the sensitivity of I159C DAT to MTSET was enhanced compared with the non-cocaine-treated condition, suggesting that binding induced a conformational change that makes the I159C side chain more accessible to the reagent. We were unable, however, to assess RTI 82 protection of these residues by this method as RTI 82-pretreated cells recovered only a small amount of transport activity, even with

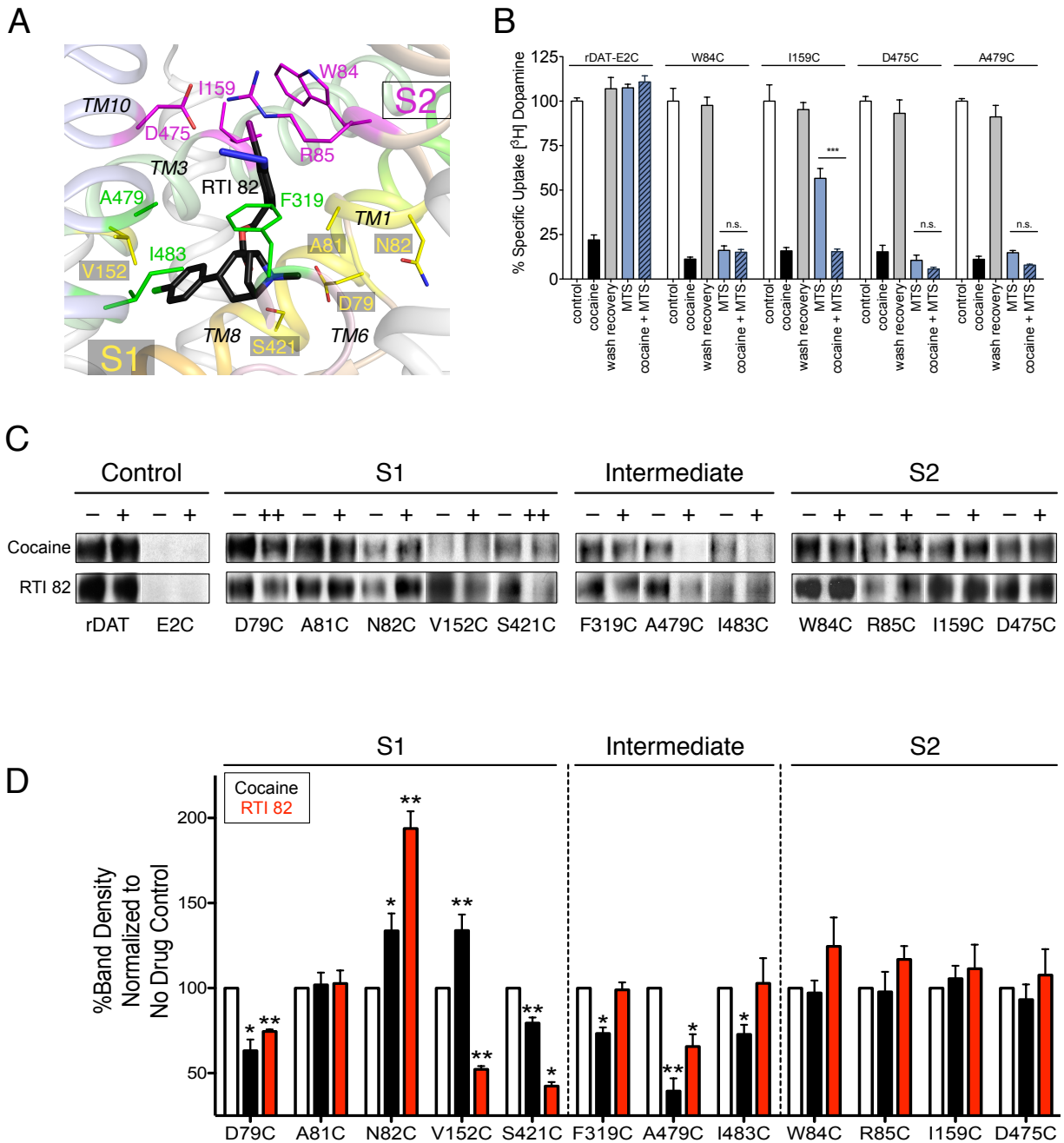


Figure 18. SCAM protection analysis of S1 and S2 binding pockets. *A*, representation of Cys-engineered mutants in the S1 (yellow sticks) and S2 (magenta sticks) binding pockets as well as residues that reside in the interface between S1 and S2 (green sticks). The RosettaLigand pose for RTI 82 is shown (black sticks). *B*, HeLa cells transiently expressing the indicated DAT mutants were preincubated with vehicle or 5 μ M (–)–cocaine for 10 min followed by addition of 5 mM MTSET for 10 min. Cells were washed and incubated for 30 min at 37 $^{\circ}$ C to release bound cocaine and analyzed for recovered activity by [3 H]DA transport assays. The samples labeled *Control* and *Cocaine* (white and black bars, respectively) were assayed following an initial wash and served as a control to verify cocaine inhibition of uptake. Results are normalized

to percent activity of control, and the values represent the mean \pm S.E. from three independent experiments. MTS-treated samples with or without cocaine pretreatment were analyzed using two-way ANOVA with a post hoc Bonferroni test. ***, $p < 0.001$; *n.s.*, not significant. *C*, immunoblots of the surface pool of DAT Cys mutants in the DAT E2C background purified with MTSEA-biotin in the absence (–) or presence of cocaine (+, 100 μ M; ++, 1 mM (*top panel*)) or RTI 82 (+, 10 μ M; ++, 50 μ M) (*bottom panel*). *D*, quantification of DAT bands in *C* and total DAT expression (data not shown) were determined using ImageJ (National Institutes of Health). Surface samples were normalized to total DAT and the surface cocaine- (*black bars*) or RTI 82 (*red bars*)-treated samples were expressed as percent of the respective untreated samples (*white bars*). The data represent three or more independent experiments. Paired *t* test analysis was used to determine significant differences between RTI 82-treated and -untreated samples. *, $p < 0.05$; **, $p < 0.01$.

extensive washing. This lower level of RTI 82 reversibility may be due to a slower release caused by hydrophobicity of the AIP or to other structural differences from (–)-cocaine related to its higher affinity. Furthermore, the impact of Cys substitution at S1 residues prevented accessibility testing by this method.

For these reasons, we assessed the ability of RTI 82 and cocaine to protect S1 and S2 residues by Cys-directed biotinylation. For these analyses, we generated additional S1 and S2 Cys mutations at Asp-79, Ala-81, Asn-82, Arg-85, Val-152, Phe-319, Ser-421, and Ile-483. All mutants were expressed as full-length proteins and were active for [³H]CFT binding. MTSEA-biotin protection assays were done using 10 μ M RTI-82 or 100 μ M cocaine, except for D79C and S421C DATs, which exhibited a marked loss in potency to inhibit binding and required higher inhibitor concentrations (50 μ M RTI-82 or 1 mM cocaine) for protection analyses.

Surface rDAT was readily labeled with MTSEA-biotin, and this labeling was unaffected by addition of RTI 82 or cocaine (Fig. 18C, *Control*). Biotinylation of rDAT E2C was undetectable (Fig. 18C, *Control*), confirming its use as a suitable background for analysis of inserted Cys residues. Recovery of biotinylated rDAT surface protein from the S1 mutants D79C and S421C was significantly reduced in the presence of either RTI-82 or cocaine, indicating the protection of these residues from the MTS reagent (Fig. 18, *C* and *D*). V152C and N82C showed

different patterns of reactivity, with V152C reactivity increased by cocaine but reduced by RTI-82, and N82C reactivity being increased by both cocaine and RTI 82 (Fig. 18, *C* and *D*). Val-152 is critical for high affinity antagonist binding and is thought to form important hydrophobic interactions with both substrates and inhibitors (Yamashita et al. 2005; Beuming et al. 2008; Henry et al. 2006), and thus the slight differences in cocaine and RTI 82 structure apparently induce different alterations of the Cys side chain that results in the differential accessibility. Asn-82 is homologous to Asn-101 in human SERT, which is a structurally dynamic residue important in coupling to Na⁺ ions at the Na1 site (Felts et al. 2014; Henry et al. 2011), with our data supporting an increased accessibility of this site upon cocaine or RTI 82 binding. In contrast, neither RTI 82 nor cocaine altered the MTS accessibility of S2 residues W84C, R85C, I159C, and D475C (Fig. 18, *C* and *D*). Together, these findings strongly indicate that RTI-82 and cocaine bind to DAT in the S1 but not the S2 site.

Residues Phe-319, Ile-483, and Ala-479 lie at the interface between S1 and S2 (Fig. 18*A*, *green sticks*). Co-incubation with cocaine protected all of these sites from MTS modification, whereas RTI 82 protected only A479C (Fig. 18, *C* and *D*). This outcome is not unexpected given that the AIP group of RTI 82 is oriented toward the outer vestibule and may prevent complete transition to the occluded structure, leaving the residues accessible to modification. Cocaine lacks the AIP group and may thus induce fuller transition to the occluded structure that provides more complete protection of these residues, which could account in part for the differential effects of RTI 82 and cocaine on increased or decreased MTS accessibility in S1 residues N82C and V152C. In addition, we found that cocaine protected A479C from MTS attack in the MTSEA-biotin pulldown study (Fig. 18*C*) but not in the washout studies (Fig. 18*B*). This discrepancy may be due to bulk size difference between MTSEA-biotin and MTSET. These

results suggest that the MTS accessibility of the intermediate residues may provide a readout for the S1 site on the transporter indicating whether a bound antagonist induces an occluded or more open conformation.

Discussion

The kinetic interactions of DAT with cocaine and its analogs are complex, resulting in high and low affinity binding states (Madras et al. 1989; Boja et al. 1998) and competitive and noncompetitive uptake inhibition (Missale et al. 1985; McElvain and Schenk 1992). We currently lack a complete mechanistic understanding of these properties, as some mutagenesis and comparative modeling studies support the interaction of cocaine at S1, where it could suppress transport by competing with substrate for key interactions (Beuming et al. 2008; Bisgaard et al. 2011), although other studies support binding near S2, where it could allosterically stabilize an inactive state of the transporter (Huang, Gu, and Zhan 2009; Hill et al. 2011; Merchant and Madura 2012; Schmitt, Rothman, and Reith 2013). It has been proposed that these binding modes are not mutually exclusive and that cocaine may initially bind near the S2 site before transitioning to S1 following conformational changes (Huang, Gu, and Zhan 2009; Hill et al. 2011). The current collection of LeuT and dDAT crystal structures supports multiple binding sites for substrates and inhibitors (Yamashita et al. 2005; Zhou et al. 2007; Zhou et al. 2009; Singh, Yamashita, and Gouaux 2007; Singh et al. 2008; Penmatsa, Wang, and Gouaux 2013; Quick et al. 2009; Wang et al. 2013; Plenge et al. 2012; Schmitt, Rothman, and Reith 2013; Indarte, Madura, and Surratt 2008) and both allosteric and competitive inhibition mechanisms (Pramod et al. 2013; Kristensen et al. 2011; Zhou et al. 2009; Singh, Yamashita, and Gouaux 2007; Singh et al. 2008; Krishnamurthy and Gouaux 2012; Henry et al. 2006; Piscitelli, Krishnamurthy, and Gouaux 2010; Quick et al. 2009; Wang, Elferich, and Gouaux 2012;

Andersen et al. 2009; Plenge et al. 2012; Schmitt, Rothman, and Reith 2013; Plenge, Gether, and Rasmussen 2007; Singh 2008; Piscitelli and Gouaux 2012). To date, however, no high resolution crystal structures of cocaine-bound SLC6 transporters have been obtained (Pramod et al. 2013; Kristensen et al. 2011; Henry, Meiler, and Blakely 2007), and the exact cocaine binding site(s) on DAT and their relationships to the various kinetic states remain unresolved.

As a positive function approach to these issues, our groups have developed irreversible binding tropane and benztropine analogs as probes for physical identification of ligand interaction sites (Vaughan et al. 2007; Parnas et al. 2008; Vaughan et al. 1999). Here, we provide the first identification of a specific photoaffinity analog contact point on DAT, and we used this information in conjunction with modeling and SCAM analysis to directly demonstrate binding of the tropane pharmacophore in the S1 substrate site. [¹²⁵I]RTI 82 labeling of DAT occurs with appropriate pharmacology (Vaughan et al. 2007), and because our photolabeling analyses utilized 5 nM ligand, the [¹²⁵I]RTI 82 adduction site identified in this study represents the high affinity, pharmacologically relevant antagonist-bound state of the transporter. It is likely that this site closely correlates with the (–)-cocaine-binding site, as the compounds share the *N*-methyl tropane pharmacophore that drives high affinity cocaine recognition (Runyon and Carroll 2008) and differ only in the substitution of the 3β-benzoyl ester with a phenyl chloride and addition of the 2β-ethyl aryliodoazido moiety.

Several other lines of pharmacological and structural evidence support the validity of our findings and extend our understanding of the binding pocket. First, our top scoring models predict salt-bridge interaction between Asp-79 and the tropane nitrogen of RTI 82, consistent with the demonstrated requirement of this interaction in cocaine and CFT binding (Kitayama et al. 1992; Beuming et al. 2008; Carroll et al. 1994). During MD simulations of rDAT-RTI 82

complexes, we observed a slight downward translation of RTI 82 deeper into the S1 pocket, but importantly, the ligand maintained interaction with Asp-79, corroborating its importance in RTI 82 binding. This is likely to represent an important molecular motif in all NSS proteins, as interaction of *N*-based antagonists with the TM1 Asp residue has also been demonstrated in the dDAT and the SERT/LeuT hybrid transporter co-crystallized with bound SSRI and TCA inhibitors (Penmatsa, Wang, and Gouaux 2013; Wang et al. 2013). A second important interaction was identified between the phenyl chloride of RTI 82 and Asn-157, which parallels the interaction of this residue with the phenyl fluoride of CFT (Beuming et al. 2008). It is unclear whether Asn-157 would interact with cocaine, which possesses a nonhalogenated benzoyl ester at the 3 β position and suggests this interaction as likely to contribute to the higher binding affinity of CFT and RTI 82 (Runyon and Carroll 2008). In addition, residues homologous to Val-152 and Ser-421, which we found as contact points for RTI 82 binding, have been implicated in high affinity antagonist binding in SERT (Henry et al. 2006; Andersen et al. 2009). Finally, in both RL and IFD, the RTI 82 poses we identified are virtually superimposable with respect to tropane pharmacophore orientation in the S1 pocket and extension of the arylazido arm out of the pocket toward the external vestibule. These findings are consistent with QSAR studies demonstrating that the tropane pharmacophore drives the major component of cocaine analog binding, and it provides a structural rationale for findings that bulky substituents can be accommodated at the 2 β position of the tropane ring without significant impact on affinity (Runyon and Carroll 2008).

The adduction site of RTI 82, Phe-319/320, functions as a gating residue on the outer margin of the S1 binding pocket and performs a crucial role in the transition between the “outward” and outward-occluded states by aromatic interaction with Tyr-156 (Penmatsa, Wang,

and Gouaux 2013). We obtained reasonable docked structures in both the open-to-out and outward-occluded models that identified Phe-319 as the RTI 82 adduction site; thus, it is possible that cocaine-like molecules suppress transport by inhibiting the transition from the outward state to the outward-occluded form or by stabilizing the outward-occluded state and preventing progression to the “inward-facing” structure. Here, our findings from RL docking could indicate that the outward-occluded structure better represents the native binding mode of RTI 82. However, other DAT inhibitors may stabilize distinct transporter conformations that could potentially confer different functional and behavioral outcomes (*e.g.* benzotropines). Computational analysis by Beuming *et al.* (Beuming *et al.* 2008) predicted Phe-320 interaction with the tropane ring of CFT, and the homologous residue in the LeuT/SERT hybrid (Phe-253) has been shown to participate in binding of SSRIs and TCAs (Wang *et al.* 2013). Our findings, however, did not indicate interaction of the RTI 82 tropane with Phe-319. This is likely due to the AIP moiety restricting reorientation of this residue and preventing its movement toward the S1 pocket and closer to the tropane pharmacophore (Penmatsa, Wang, and Gouaux 2013). It is possible that by preventing closure of the aromatic lid, extensions to this arm of RTI 82 could stabilize outward-facing DAT conformations, which might result in different functional outcomes than the inhibitor-stabilized occluded form.

The direct identification of photoaffinity ligand adduction sites confers major advantages for computational analyses of ligand poses by dramatically reducing the conformational space that must be sampled during docking analysis and by providing experimentally determined ligand-protein contact points that can be used as absolute requirements by which recovered binding poses can be filtered. This significantly enhances the confidence with which poses can be interpreted and further analyzed by computational and mutational strategies to clarify overall

transport and transport inhibition mechanisms. In addition, these procedures can be performed in functional mammalian transporters in which the WT form is directly compared with transport- and binding-competent mutant forms, which strongly increases the likelihood that physiologically relevant structures are being assessed. These multiple strengths support the utilization of this approach in further predictive docking analyses of these and other categories of DAT ligands. This is important because to date no SLC6 transporters have been co-crystallized with cocaine-like compounds or atypical DAT inhibitors and because the uncertain structural and functional relationships between mammalian transporters and the mutation-stabilized dDAT and LeuT/SERT hybrid homologs may obscure significant differences in the transport and inhibitor binding properties of the proteins (Penmatsa, Wang, and Gouaux 2013; Wang et al. 2013).

The tremendous sociological and economical impacts of cocaine addiction make basic understanding of the mechanisms of cocaine binding and transport inhibition an important effort, especially with the promise afforded by the identification of the benztropine class of DAT antagonists, which bind to DAT and block DA uptake but do not produce the cocaine-like behavioral profiles and reduce cocaine self-administration in animal models (Tanda, Newman, and Katz 2009; Tanda et al. 2013). It has been suggested that the benztropines may bind distinct conformations of DAT and/or possess a slow rate of occupancy following administration, which may modulate the psychotropic effects of increased synaptic DA (Loland et al. 2008; Beuming et al. 2008; Tanda, Newman, and Katz 2009; Tanda et al. 2013). Recently, modafinil and its *R*-enantiomer (armodafinil) have also been described as having distinctive interactions at DAT that might contribute to their nonaddictive and therapeutic profiles (Merchant and Madura 2012; Schmitt and Reith 2011; Loland et al. 2012). Thus, understanding cocaine binding in relation to

compounds like these atypical DAT inhibitors could provide critical insights for developing medication strategies toward treating cocaine addiction.

CHAPTER III

IDENTIFYING THE ADDUCTION SITE OF THE PHOTOACTIVE AZIDE OF THE IRREVERSIBLE COCAINE ANALOG [¹²⁵I]MFZ 2-24 FOR ELUCIDATING THE COCAINE BINDING SITE IN THE DOPAMINE TRANSPORTER

Introduction

The dopamine transporter (DAT) is a member of the Na⁺/Cl⁻-dependent SLC6A family of solute carriers and functions to maintain dopamine homeostasis through reuptake of dopamine (DA) from the neuronal synapse. Altered DAT function through dysregulation or mutations can impact extracellular DA levels and has been linked to several neurological diseases and disorders including attention deficit hyperactivity disorder, addiction, depression, autism spectrum disorder, bipolar disorder, Parkinson disease, schizophrenia, Tourette syndrome, and hereditary DAT deficiency syndrome (Gainetdinov and Caron 2003; Gether et al. 2006; Torres and Amara 2007; Hahn and Blakely 2007; Pramod et al. 2013; Kurian et al. 2011). DAT activity can be modulated endogenously by various post-translational modifications, including phosphorylation and palmitoylation (Vaughan and Foster 2013), and exogenously by drugs of abuse like cocaine and amphetamines, which block or reverse the transport of DA by DAT and lead to large increases in extracellular DA levels (Ritz et al. 1987; Bergman et al. 1989). Paradoxically, some DAT inhibitors including bupropion, methylphenidate, and benzotropines bind and block DA reuptake but fail to induce the euphoric and addictive behavioral effects seen with cocaine (Volkow et al. 1996; Rothman et al. 2008; Stoops et al. 2012). Understanding the underlying molecular and physiological mechanisms that dictate whether or not a DAT blocker will induce psychotropic and addictive behaviors would greatly advance the development of

pharmacotherapeutics that could be used to treat drug abuse and addiction as well as attention and mood disorders.

Major structural insights into DAT and the other monoamine transporters for serotonin and norepinephrine (SERT and NET) have resulted from the crystal structures of substrate and inhibitor bound complexes of both prokaryotic and eukaryotic SLC6 transporters (Yamashita et al. 2005; Singh, Yamashita, and Gouaux 2007; Singh et al. 2008; Krishnamurthy and Gouaux 2012; Piscitelli and Gouaux 2012; Penmatsa, Wang, and Gouaux 2013; Wang, Penmatsa, and Gouaux 2015; Penmatsa, Wang, and Gouaux 2015; Coleman, Green, and Gouaux 2016). These proteins share a common structure of 12 transmembrane (TM) domains connected by intracellular and extracellular loops, with cytoplasmic N- and C-termini. The topology indicates an architecture of two 5 helix containing bundles arranged antiparallel to one another in the membrane (Shimada et al. 1991; Giros et al. 1992; Itokawa et al. 2000). Comparative modeling utilizing LeuT and dDAT templates assisted in understanding the mammalian monoamine transporters three-dimensional structural architecture as well (Huang and Zhan 2007; Koldsø et al. 2013).

Examination of the substrate and inhibitor binding pockets in crystal structures of LeuT, dDAT, and hSERT demonstrated that antagonists and substrates could occupy a high affinity central substrate binding pocket (S1), generated by TM domains 1, 3, 6, and 8 (Yamashita et al. 2005; Wang, Penmatsa, and Gouaux 2015), and, in the case of many SERT blocking antidepressants, a secondary, low affinity binding site (S2) located in the external vestibule (Singh, Yamashita, and Gouaux 2007; Coleman, Green, and Gouaux 2016). Antagonist occupancy of the S1 site would competitively inhibit transport whereas occupancy of the S2 site is thought to slow the dissociation of the S1 bound compound resulting in an allosteric

prolonging of the inhibitor effect through a noncompetitive mechanism (Chen et al. 2005; Neubauer, Hansen, and Wiborg 2006; Plenge et al. 2012).

Findings from biochemical experiments and QSAR studies on cocaine binding as well as a dDAT/cocaine crystal complex suggest that cocaine could occupy the central, S1 substrate binding pocket in DAT (Carroll et al. 1992; Kitayama et al. 1992; Chen, Sachpatzidis, and Rudnick 1997; Henry et al. 2003; Henry et al. 2006; Beuming et al. 2008; Wang, Penmatsa, and Gouaux 2015). The data generated from site directed mutagenesis studies, where cocaine and cocaine analog binding sites were investigated, identified multiple residues in core TMs, including Leu-104, Phe-105, Ala-109, Asn-157, Tyr-251, Tyr-273, Thr-351 Ser-320, Thr-455, and Ser-459, that are involved in cocaine or cocaine analog binding, arguing against the S2 site as the cocaine binding site in DAT (Itokawa et al. 2000; Wu and Gu 2003; Chen, Han, and Gu 2005; Beuming et al. 2008; Bisgaard et al. 2011). However, indirect effects resulting from these mutations cannot be ruled out (Uhl and Lin 2003).

Here, we utilized the irreversible cocaine analog [^{125}I]N-[4-(4'-azido-3'-iodophenyl)-butyl]-2- β -carbomethoxy-3 β -(4-chlorophenyl) ([^{125}I]MFZ 2-24) (Fig. 19) (Zou et al. 2001; Lever et al. 2005) in combination with comparative modeling, small molecule docking, molecular dynamics, peptide mapping, and SCAM protection analyses to identify the adduction site corresponding to high affinity binding of the photoactivatable ligand to DAT. MFZ 2-24, cocaine, and the cocaine analog (-)-2 β -carbomethoxy-3 β -(4-fluorophenyl)tropane (CFT) share a common pharmacophore consisting of the tropane ring and 3 β -phenyl group that direct high affinity binding (Carroll et al. 1991; Carroll et al. 1994). All of these compounds bind noncovalently to DAT, but [^{125}I]MFZ 2-24 contains a photoactivatable phenyl azido moiety that upon ultraviolet activation forms a highly reactive singlet nitrene that reacts with

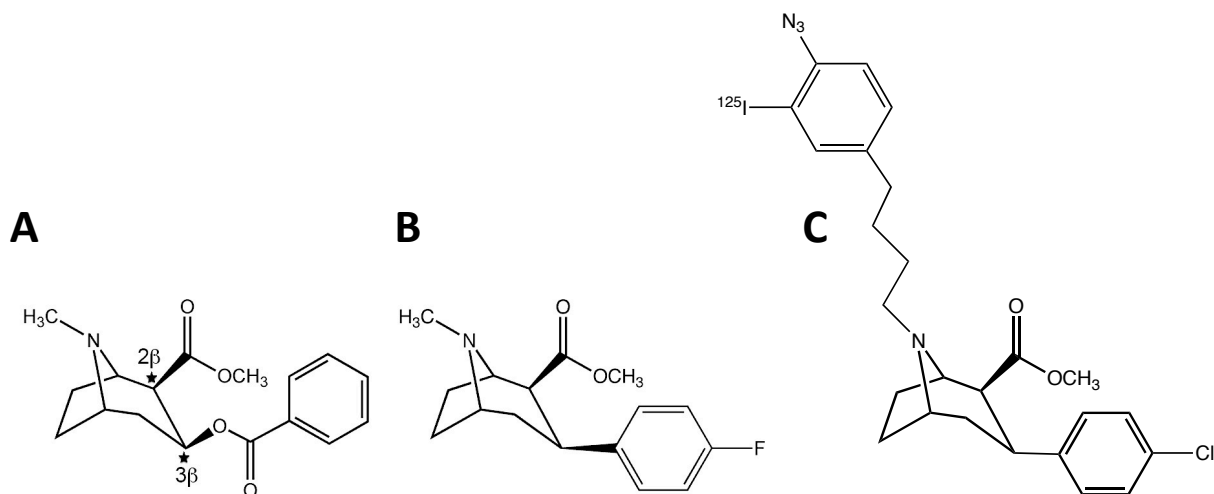


Figure 19. Chemical structures of cocaine, CFT, and [¹²⁵I]MFZ 2-24. (a) Structure of cocaine with tropane N and 3b-phenyl ester moieties indicated by stars. (b) Structure of CFT with phenyl fluoride moiety directly appended to the 3b position on the tropane pharmacophore (star). (c) Structure of [¹²⁵I]MFZ 2-24 with AIP moiety appended directly to the tropane N.

proximal C–H or N–H groups forming a covalent bond with the protein (Kotzyba-Hibert, Kapfer, and Goeldner 1995; Geurink et al. 2012). Using irreversible labeling as a strategy for determining the site of ligand-protein interaction, we previously demonstrated that [¹²⁵I]MFZ 2-24 cross-links to human (h) DAT between Asp-68 and Leu-80, a domain corresponding to the central and extracellularly directed regions of TM1 in DAT (Parnas et al. 2008). In this report, our computational approaches predicted MFZ 2-24 adduction at Leu-80 on TM1 in DAT and this finding was validated by mutagenesis and peptide mapping of the adduction site. Furthermore, our docking models predicted a S1 placement of the tropane core of MFZ 2-24, verified by SCAM analysis, a placement that overlaps with that of the tropane core of another cocaine analog, RTI 82 (Dahal et al. 2014). These findings show direct interaction of the core tropane pharmacophore of MFZ 2-24 with the central, S1 binding site, providing support for a competitive mechanism of action of cocaine for blocking DA transport.

Methodology

Comparative DAT Homology Model Construction

The outward-occluded and open-to-out rDAT homology models used in this study were generated previously (Dahal et al. 2014) using Rosetta3.1 (Leaver-Fay et al. 2011). An open-to-out model of hDAT was constructed with Rosetta3.1 using the *Drosophila* dopamine transporter-nortriptyline co-crystal (PDB ID 4M48) (Penmatsa, Wang, and Gouaux 2013). The top 10 scoring models (Rosetta E_{total} score) for each template were compared visually to the starting structure to verify overall structural integrity before moving forward with docking studies.

Molecular Dynamics Analysis of DAT in Complex with MFZ 2-24

The top scoring MFZ 2-24 poses, in complex with DAT, from RosettaLigand and Induced Fit Docking (IFD) were then subjected to molecular dynamic analysis for 150 ns using GROMACS (Dahal et al. 2014).

Synthesis and Radiolabeling of MFZ 2-24

Synthesis and radiolabeling of MFZ 2-24 was carried out as previously described (Zou et al. 2001; Lever et al. 2005).

Chemicals and Materials

[³H]CFT (76 Ci/mmol) was obtained from Perkin-Elmer (Waltham, MA, USA). [³H]DA (45 Ci/mmol), Protein A Sepharose, and Hyperfilm MP were from GE Healthcare Life Sciences (Piscataway, NJ). Site directed mutagenesis QuikChange® kit was from Stratagene (La Jolla, CA). All other chemicals were purchased from Sigma-Aldrich (St. Louis, MO) or Fisher Scientific (Pittsburgh, PA).

Cell Culture and Site-directed Mutagenesis

Mutant constructs used for peptide mapping were stably expressed in Lewis Lung Carcinoma-Porcine Kidney (LLC-PK₁) cells and were characterized previously (M111L/M116L, L80M/M111L/M116L) (Parnas et al. 2008) or were generated in the M111L/M116L rDAT cDNA background using the Stratagene QuikChange® kit and verified by sequencing (Northwoods DNA, MN). For ease of discussion, mutants V73M, A77M, D79, and L80M generated in the M111L/M116L background are referred by the TM1 mutation only. For stable expression of new constructs, LLC-PK₁ cells were transfected using FuGENE transfection reagent and selected with 800 µg/mL of G418. Cells were maintained in a humidified chamber with 5% CO₂ at 37°C in α -minimum essential medium (AMEM with 5% fetal bovine serum, 2 mM L-glutamine, 200 µg/mL G418, and 100 µg/mL penicillin/streptomycin). Mutants for SCAM analysis were generated in the E2C background (C90A and C305A) of pcDNA3-rDAT using the Stratagene QuikChange® kit and verified by sequencing (Eurofins MWG Operon, Huntsville, AL). WT and mutant cDNAs were expressed transiently in HEK-GripTite cells (Invitrogen) using TransIT®-LT1 (Mirus) (1 µl per 200 ng of DNA). Cells were maintained in a humidified chamber with 5% CO₂ at 37 °C in Dulbecco's modified Eagle's medium (DMEM: 10% FBS, 600 µg/ml G418).

Photoaffinity Labeling and CNBr Peptide Mapping

These procedures were performed as described previously (Dahal et al. 2014). Briefly, cells expressing WT or mutant DATs were washed twice with ice-cold Krebs-Ringers-Hepes (KRH) buffer (25 mM HEPES, 125 mM NaCl, 4.8 mM KCl, 1.2 mM KH₂PO₄, 1.3 mM CaCl₂, 1.2 mM MgSO₄, 5.6 mM glucose, pH 7.4) and incubated with 5 nM [¹²⁵I]MFZ 2-24 in KRH for 2 hr on ice in the presence or absence of 30 µM (-)-cocaine. Cells were irradiated with ultraviolet

light (254 nm) for 5 min to covalently attach the ligand to DAT, washed twice with cold KRH and lysed with radioimmunoprecipitation assay buffer (RIPA: 150 mM NaCl, 125 mM NaH₂PO₄, 2 mM EDTA, 1% Triton X-100, 0.1% SDS, pH 7.4) containing protease inhibitor for 30 min on ice with shaking. The lysates were centrifuged at 20,000 x g for 12 min at 4°C and supernatants were subjected to SDS-PAGE and autoradiography on 8% Tris-glycine polyacrylamide gels. Photolabeled DAT bands were excised from the gel, and protein was electroeluted and dialyzed against MilliQ H₂O. Aliquots were counted in a scintillation counter and equal amounts of radioactivity from each sample were subjected to peptide mapping. For CNBr proteolysis, samples were lyophilized to dryness, and resuspended in 70 µL of 70% formic acid with or without addition of 1 M CNBr and incubated for 24 hr at 22°C in the dark. Reactions were quenched with 1 mL of MilliQ water and samples were lyophilized to dryness, followed by removal of CNBr with four additional rounds of resuspension with water and lyophilization. The final samples were suspended in immunoprecipitation buffer and divided into aliquots. Part of the sample (25-50%) was subjected directly to SDS-PAGE/autoradiography to visualize the total CNBr digestion pattern and the remainder was immunoprecipitated with monoclonal Ab 16 (mAb 16) prior to SDS-PAGE/autoradiography. For each experiment, 2-3 mutants were photoaffinity labeled and analyzed with WT and L80M DAT exactly in parallel and all results were replicated at least 3 times. CNBr peptide masses were calculated using PeptideCutter via ExpASy.

[³H]CFT Binding

LLC-PK₁ cells stably expressing WT and mutant rDATs were grown to ~80% confluency and washed with Hank's balanced salt solution (HBSS). Cells were incubated with 10 nM [³H]CFT in KRH buffer for 2 hr at 4°C. Binding was performed in triplicate with nonspecific

binding determined in the presence of 10 μM mazindol. At the end of the incubation, cells were washed twice with KRH buffer, lysed with 1% TX-100, and samples assessed for radioactivity by liquid scintillation counting.

[³H]DA Uptake

WT or mutant rDAT-LLCPK₁ cells were grown in 24-well plates to ~80% confluency in AMEM at 37°C. Cells were rinsed twice with 0.5 ml KRH buffer followed by addition of 0.5 ml warmed KRH (37°C). Uptake was performed in triplicate and initiated by addition of 10 nM [³H]DA plus 30 μM unlabeled DA, with nonspecific uptake determined in the presence of 100 μM (-)-cocaine. Uptake was allowed to proceed for 8 min at 37°C and cells were rapidly washed three times with ice-cold KRH and solubilized in 1% Triton X-100. Radioactivity contained in lysates was assessed by liquid scintillation counting and protein content was assessed using BCA colorimetric reagent.

SCAM Protection Analysis of S1- and S2-binding Sites

GripTite cells were plated at a density of 150,000 cells/cm² in 24-well culture plates, incubated for 24 hr, and transfected with rDAT constructs using TransIT®-LT1 (Mirus). Following transfection (48 hr), cells were processed as described previously (Henry et al. 2003; Dahal et al. 2014). Briefly, cells were incubated with 10 or 50 μM MFZ 2-24 or vehicle for 5 min in PBS/CM (137 mM NaCl, 2.7 mM KCl, 10.1 mM Na₂HPO₄, 1.8 mM KH₂PO₄, 0.1 mM CaCl₂, 1.0 mM MgCl₂, pH 7.4) followed by addition of 0.1 mM MTSEA-biotin for 10 min (Biotium). Cell lysates were obtained with RIPA solubilization buffer (10 mM Tris, pH 7.4, 150 mM NaCl, 0.1% SDS, 1% Triton X-100, 1% sodium deoxycholate) containing Halt™ Protease Inhibitor Single-Use Cocktail (ThermoFisher) and incubated with NeutrAvidin-agarose resin (ThermoFisher) to extract surface proteins labeled by MTSEA-Biotin. Following a BCA assay

(ThermoFisher) to determine protein concentration, equal amounts of protein from total samples and equivalent volumes of surface protein pools were processed by SDS-PAGE and immunoblotting using anti-DAT monoclonal antibody, mAb 16 (Foster, Pananusorn, and Vaughan 2002; Gaffaney and Vaughan 2004). DAT levels were quantitated from the density of immunoblot bands from at least three separate assays using ImageJ (National Institutes of Health). Surface values were normalized to total DAT levels and are expressed as a percent of untreated samples. Data were analyzed using a paired t test (Prism 4).

Results

Computational Docking of MFZ 2-24 to rDAT Homology Models

To identify the site of MFZ 2-24 adduction to DAT and inform the biochemical crosslinking studies, *in silico* docking was performed on the open-to-out and outward-occluded rDAT comparative models (based on the LeuT crystal structures 2A65 and 3F3A) (Yamashita et al. 2005; Singh et al. 2008) using two independent methods, RosettaLigand (RL) and Induced Fit Docking (IFD).

RosettaLigand Docking

RL docking was performed and the top-scoring 5% (based on the *interface_delta score*, see methods) of the 25,000 RL-docked complexes (termed decoys) were filtered using three biochemically-defined molecular distance constraints. These constraints were defined as 5 Å distance cutoffs between: (1) the MFZ 2-24 azido moiety and any atom in the residues Asp-79 and Leu-80, (2) the tropane N of MFZ 2-24 and the side chain of Asp-79 (Dahal et al. 2014), and (3) the phenyl chloride of MFZ 2-24 and the side chain of Asn-157 (Beuming et al. 2008; Dahal et al. 2014). Using both filters (1) and (2) resulted in 89 and 5 decoys from the open-to-out and outward-occluded models, respectively. The addition of filter (3) reduced the number of decoys

fulfilling the constraints to 9 and 0 for the open-to-out and outward-occluded models, respectively. The top two scoring decoys had poses for MFZ 2-24 that only differed by 1.288 Å RMSD, however, evaluation of the distance between the N atom on the azido group that forms the reactive nitrene on MFZ 2-24 and the nearest C atom on the Leu-80 side chain indicated that the second best-scoring decoy (*interface_delta* score, -12.8) with intramolecular distance of 3.8Å (Fig. 20A) was more consistent with the molecular constraints than the top scoring decoy (*interface_delta* score, -15.4) which had an intramolecular distance of 5.8Å. Therefore, the second-best scoring pose was chosen and carried forward for molecular dynamic simulations.

IFD Docking

MFZ 2-24 was also docked into the open-to-out and outward-occluded models using IFD, which allows for the incorporation of the Na⁺ and Cl⁻ ions along with their energetic and density contributions during the docking analysis (Wall, Innis, and Rudnick 1993; Barker et al. 1999; Yamashita et al. 2005; Forrest et al. 2007; Zomot et al. 2007; Dahal et al. 2014). IFD docking to the open-to-out and outward-occluded models yielded 12 and 2 structures, respectively. Of the 12 open-to-out docked structures, only 1 complex fulfilled the nitrene/Leu-80 distance constraint (Fig. 21A). The nitrene/Leu-80 distance of the remaining 11 structures was >7.4Å, which eliminated them from further consideration. Analysis of the two outward-occluded IFD docked complexes revealed the distance between the nitrene group and the Leu-80 side chain was 5.3 and 5.4Å, which is just outside of the molecular cutoff. However, to determine if refinement would result in a ligand pose that met the filter requirements, the best scoring complex was carried forward for MD analysis.

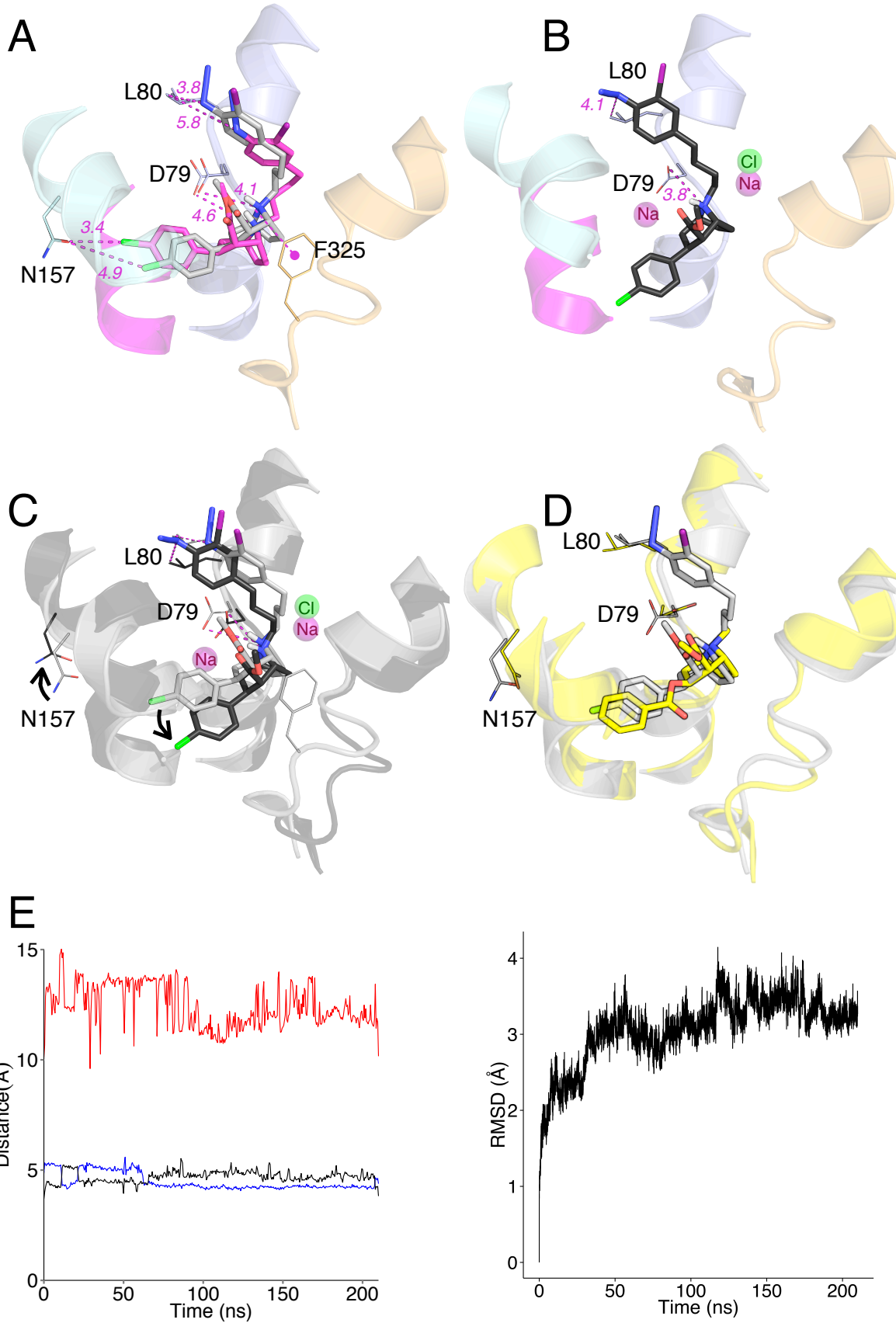


Figure 20. MFZ 2-24 and DAT RosettaLigand docking complexes and molecular dynamics simulation. (a) Best RL rDAT/MFZ 2-24-docked complex based on energy and constraint fulfillment. Image depicts the LeuT-based rDAT homology model from the crystal structure of the open-to-out template 2A65. (b) Molecular dynamics simulation of the RL rDAT/MFZ 2-24-docked complex. (c) Superimposition of RL-docked MFZ 2-24 before (grey) and after (black) simulation. (d) Superimposition of RL-docked MFZ 2-24 pre-simulation (grey) and cocaine (yellow) from *Drosophila* DAT co-crystal. (e) Time-dependent changes in distances following molecular dynamics simulation between the protonated nitrogen of MFZ 2-24 and the side chain oxygen atom of Asp-79 (blue and black traces for $\delta O1$ and $\delta O2$) and the phenyl chloride of MFZ 2-24 and the amide nitrogen of Asn-157 (red traces).

MD Simulation of RL and IFD Docked MFZ 2-24 Poses

To refine the selected RL and IFD poses the ligand-transporter complexes were placed in a POPC lipid bilayer and subjected to 120 ns of MD simulation using GROMACS (Hess et al. 2008). Simulation of the RL f_1217 docked structure resulted in a pivoting movement of MFZ 2-24 around the tropane N such that the phenyl Cl group moved down and away from Asn-157 to a distance of 8.5Å and the phenyl iodo azido arm moved slightly away from TM1 to a distance of 4.1Å (Fig. 20B and 20C). The δO atoms of the Asp-79 side chain appear to alternate in coordinating the tropane N over the duration of the simulation (Fig. 20E), which was also observed in our previous analysis with the cocaine analog RTI 82 (Dahal et al. 2014). Similar to RL, MD analysis of the IFD pose resulted in moderate translation of MFZ 2-24 in the binding pocket. The Leu-80 and Asp-79 side chains also shifted such that they maintained a <5Å distance to the nitrene and tropane N, respectively (Fig. 21B and 21C). However, the intermolecular distance between Asn-157 and the phenyl Cl increases substantially; this constraint was used based on previous comparative modeling and mutagenesis work supporting interaction between the phenyl FI of the cocaine analog CFT and Asn-157 (Beuming et al. 2008). Alignment of the pre- and post-MD RL and IFD-docked structures with the recent co-crystal of cocaine in the *Drosophila* DAT (Wang, Penmatsa, and Gouaux 2015) revealed that the MFZ 2-24 poses from

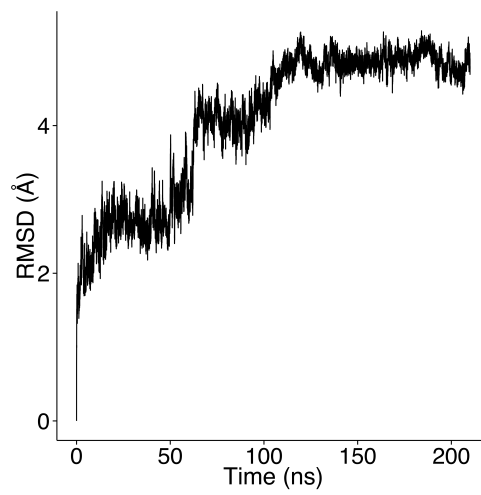
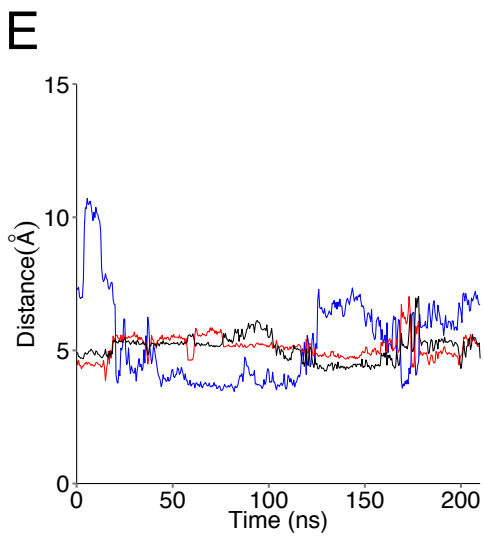
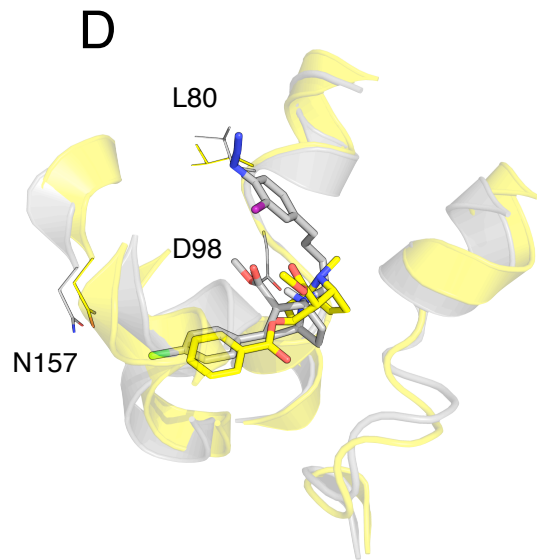
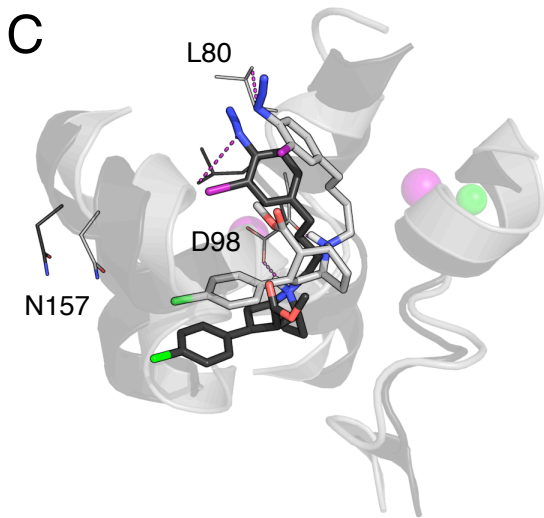
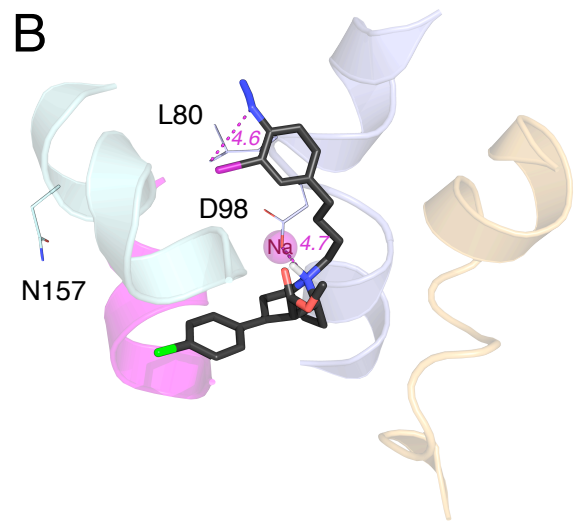
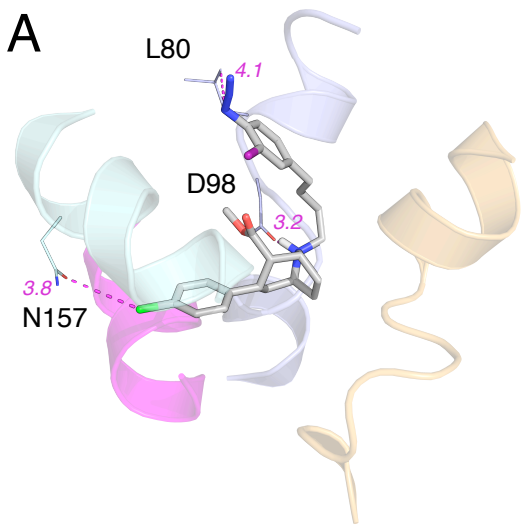


Figure 21. MFZ 2-24 and DAT Induced Fit Docking complexes and molecular dynamics simulation. (a) Best IFD rDAT/MFZ 2-24-docked complex based on energy and constraint fulfillment. Image depicts the LeuT-based rDAT homology model from the crystal structure of the open-to-out template 2A65. (b) Molecular dynamics simulation of the IFD rDAT/MFZ 2-24-docked complex. (c) Superimposition of IFD-docked MFZ 2-24 before (grey) and after (black) simulation. (d) Superimposition of IFD-docked MFZ 2-24 pre-simulation (grey) and cocaine (yellow) from *Drosophila* DAT co-crystal. (e) Time-dependent changes in distances following molecular dynamics simulation between the protonated nitrogen of MFZ 2-24 and the side chain oxygen atom of Asp-79 (blue and black traces for $\delta O1$ and $\delta O2$) and the phenyl chloride of MFZ 2-24 and the amide nitrogen of Asn-157 (red traces).

the pre-MD structures are closer to cocaine in the co-crystal structure than structures following refinement by MD simulations (Fig. 20D and 21D).

Peptide Mapping of Photoaffinity Labeled Site

We previously demonstrated that [125 I]MFZ 2-24 cross-links to DAT in TM1 between Ile-67 and Leu-80 (Parnas et al. 2008). Here we use Met substitution mutagenesis, CNBr proteolysis, and epitope specific immunoprecipitation to further narrow the adduction site. In this approach, Mets are substituted one at a time for endogenous residues between positions 67 and 80 to generate novel CNBr cleavage sites for peptide mapping. The photolabeled proteins are digested and the fragments subjected to immunoprecipitation with mAb 16 directed against N-terminal residues 42-59. There are no endogenous Mets in DAT between positions 11 and 106, thus if [125 I]MFZ 2-24 adducts to a residue N-terminal to the inserted Met, the labeled fragment will contain the epitope for mAb 16 and will immunoprecipitate, whereas if adduction occurs C-terminal to the inserted Met, CNBr digestion will separate the ligand from the antibody epitope and the photolabeled fragment will not immunoprecipitate.

Because molecular modeling suggested adduction of [125 I]MFZ 2-24 at Asp-79 or Leu-80, we focused our efforts on residues close to these sites, inserting Met in place of Val-73, Ala-77, and Asp-79. Mutants were stably expressed in LLC-PK₁ cells and analyzed for expression, [3 H]DA uptake, [3 H]CFT binding, and [125 I]MFZ 2-24 labeling. V73M and A77M DATs were

expressed as full-length protein and showed robust cocaine-sensitive transport and CFT binding activity. D79M DAT expressed poorly and, as expected, showed negligible transport, but the full-length protein displayed a small amount of [¹²⁵I]MFZ 2-24 labeling and was analyzed due to molecular modeling findings that indicated Asp-79 as a possible adduction site.

For peptide mapping studies, the photolabeled proteins were gel purified and subjected to treatment with vehicle (formic acid) or CNBr. For all experiments, WT and L80M DATs were labeled, digested, immunoprecipitated, and electrophoresed in parallel with the new constructs to provide positive controls for generation and immunoprecipitation of labeled fragments. Digested samples were divided into aliquots that were directly subjected to SDS-PAGE/autoradiography to visualize the total spectrum of CNBr fragments or were immunoprecipitated with mAb 16 prior to SDS-PAGE/autoradiography. Within each experiment, samples from WT and mutant forms were adjusted to contain equal amounts of radioactivity to allow for direct comparison of fragment production and immunoprecipitation signals.

Figure 22 shows the results of these analyses from [¹²⁵I]MFZ 2-24-labeled WT and mutant DATs with the accompanying schematic diagrams indicating the origin of the labeled fragments in the primary sequence. Panel A shows the spectrum of total CNBr fragments generated from [¹²⁵I]MFZ 2-24 labeled WT and mutant DATs with left and right panels showing independent analyses of the indicated mutants. In non CNBr-treated samples, full length DAT migrates at ~90 kDa (odd numbered lanes) with no low molecular weight fragments observed. Aggregates seen at ≥ 180 kDa are most likely induced by the formic acid treatment, as they were not seen in samples subjected directly to electrophoresis. CNBr treatment of WT rDAT produced a labeled fragment of ~12 kDa (lane 2; arrow a) that corresponds to the region between Met-1/11

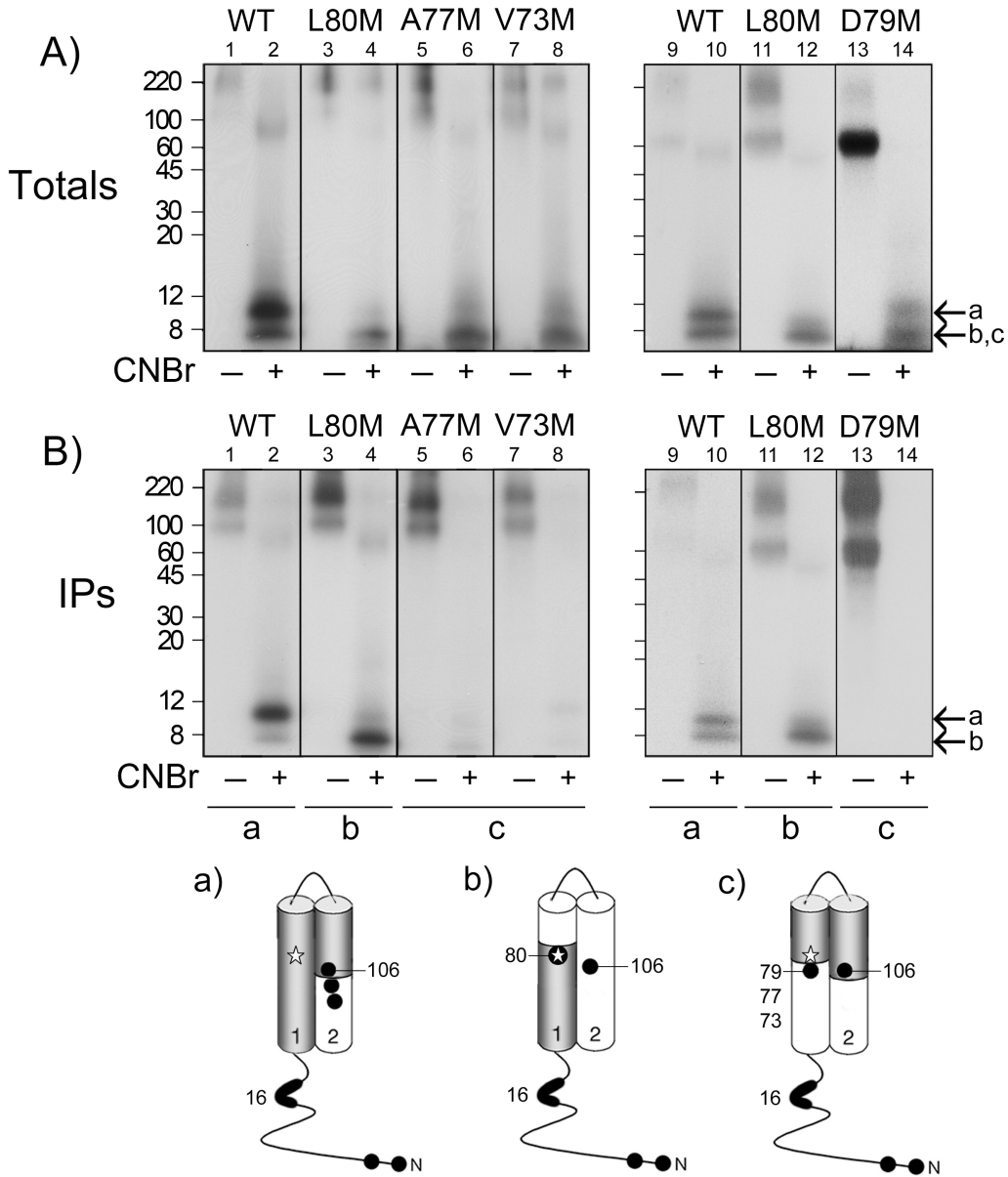


Figure 22. CNBr mapping of [¹²⁵I]MFZ 2-24-labeled DAT mutants. The indicated DAT forms were photolabeled with [¹²⁵I]MFZ 2-24, gel purified, and equal amounts of radioactivity were treated with vehicle (odd numbered lanes) or CNBr (even numbered lanes). Aliquots of each sample were analyzed directly by SDS/PAGE-autoradiography to visualize the total pattern of CNBr fragments (**a**), or were immunoprecipitated with mAb 16 prior to SDS/PAGE-autoradiography (**b**). Left and right panels show independent experiments, and molecular mass markers shown on left gels are indicated by tic marks on right gels. Arrow a indicates migration of ~12 kDa CNBr fragment that extends from the Met-1/11 to Met-106/111/116 and arrows b and c indicate ~3-8 kDa fragments produced by cleavage of exogenous TM1 Mets. Schematic diagrams show the cytosolic N-terminus, TMs 1 and 2, positions of endogenous and exogenous Met residues (filled circles), epitope for mAb 16 (bold line), adduction site of [¹²⁵I]MFZ 2-24 (star), and origin of photolabeled CNBr fragments in primary sequence (grey shading).

and Met-106/111/116 (shaded region in diagram a). The presence of doublets in some experiments is likely due to different proteolysis combinations, as the calculated mass of fragments extending from Met-1 to Met-116 is 12.7 kDa and the calculated mass of fragments extending from Met-11 to Met-106 is 10.5 kDa. CNBr treatment of [¹²⁵I]MFZ 2-24 labeled L80M DAT produced a fragment of ~8 kDa, which is consistent with peptides extending from Met-1 or Met-11 to L80M (shaded region in schematic diagram b) with calculated masses of 7.5 and 8.7 kDa, as demonstrated previously (Parnas et al. 2008). All of the new mutants showed similar levels of CNBr fragments in this low molecular mass region indicating that the ligand became adducted to the protein in a similar manner and arguing against the possibility that the mutation induced adduction of [¹²⁵I]MFZ 2-24 in a different region of the primary sequence that would generate a different fragment pattern. For V73M, A77M, and D79M DATs, a labeled fragment similar to that generated from L80M DAT would be produced if the ligand becomes adducted N-terminal to the new CNBr site whereas a labeled fragment ~3 kDa extending from the new Met to Met106 (shown in diagram c) would be produced if the ligand adducts C-terminal to the new CNBr site. These possible fragments would not be distinguishable by SDS-PAGE and both forms are indicated in Panel A with arrows b and c. Importantly, the intensity of fragment production for mutant DATs was comparable to that of the WT and L80M proteins allowing for direct comparison of immunoprecipitation signals.

Panel B shows the mAb 16 immunoprecipitation profiles of the total digests shown in the upper panels. As we previously demonstrated (Parnas et al. 2008), mAb 16 immunoprecipitated the 12 kDa fragment from the WT DAT (lanes 2 and 10, arrow a) and the 8 kDa fragment from L80M DAT (lanes 4 and 12, arrow b) indicating that ligand incorporation occurs at or N-terminal to Leu-80 (diagrams a and b). In striking contrast, even though labeled fragments were present at

equal intensities in the total digests from V73M, A77M, or D79M DATs, these samples showed negligible immunoprecipitation by mAb 16 (lanes 6, 8, and 14). This strongly indicates that cleavage of TM1 at Mets 73, 77, and 79 separated epitope 16 from the [¹²⁵I]MFZ 2-24 adduction site and thus that adduction occurred C-terminal to those Mets (diagram c). Therefore, because CNBr cleaves the peptide bond on the C-terminal side of Met residues, these data provide strong experimental evidence that [¹²⁵I]MFZ 2-24 adduction occurs at Leu-80.

Analysis of MFZ 2-24 Protection of S1- and S2-binding Pockets from Cys-directed Biotinylation

Our computational docking and peptide mapping results strongly indicate that binding of the MFZ 2-24 tropane pharmacophore occurs within the S1-binding site and positions the azido group for adduction to Leu-80. In order to confirm binding of MFZ 2-24 to S1, we analyzed several residues present in the S1- or S2-binding sites in addition to several that line the transition between S1 and S2 (intermediate residues) in the DAT permeation pathway. Mutants were constructed in a methanethiosulfonate (MTS)-insensitive rDAT E2C (C90A and C305A) background and assessed for MFZ 2-24-induced protection from the SCAM reagent MTSEA-biotin.

Previously (Dahal et al. 2014), we identified that surface rDAT was readily labeled with MTSEA-biotin whereas labeling of rDAT E2C is undetectable (Fig. 23, Control), confirming it as a cysteine-reduced, MTS-inactive background suitable for analysis of inserted Cys residues. Utilizing rDAT E2C as a template, we generated Cys mutations of the S1 residues Asp-79, Ala-81, Asn-82, Val-152, and Ser-421, the S2 residues Trp-84, Arg-85, Ile-159, and Asp-475, and the intermediate residues Phe-319, Ala-479, and Ile-483. MTSEA-biotin protection assays were done using 10 μM MFZ 2-24, except for the mutants D79C and S421C where marked losses in

potency to inhibit binding were observed, which required a higher concentration (50 μ M) for protection analyses.

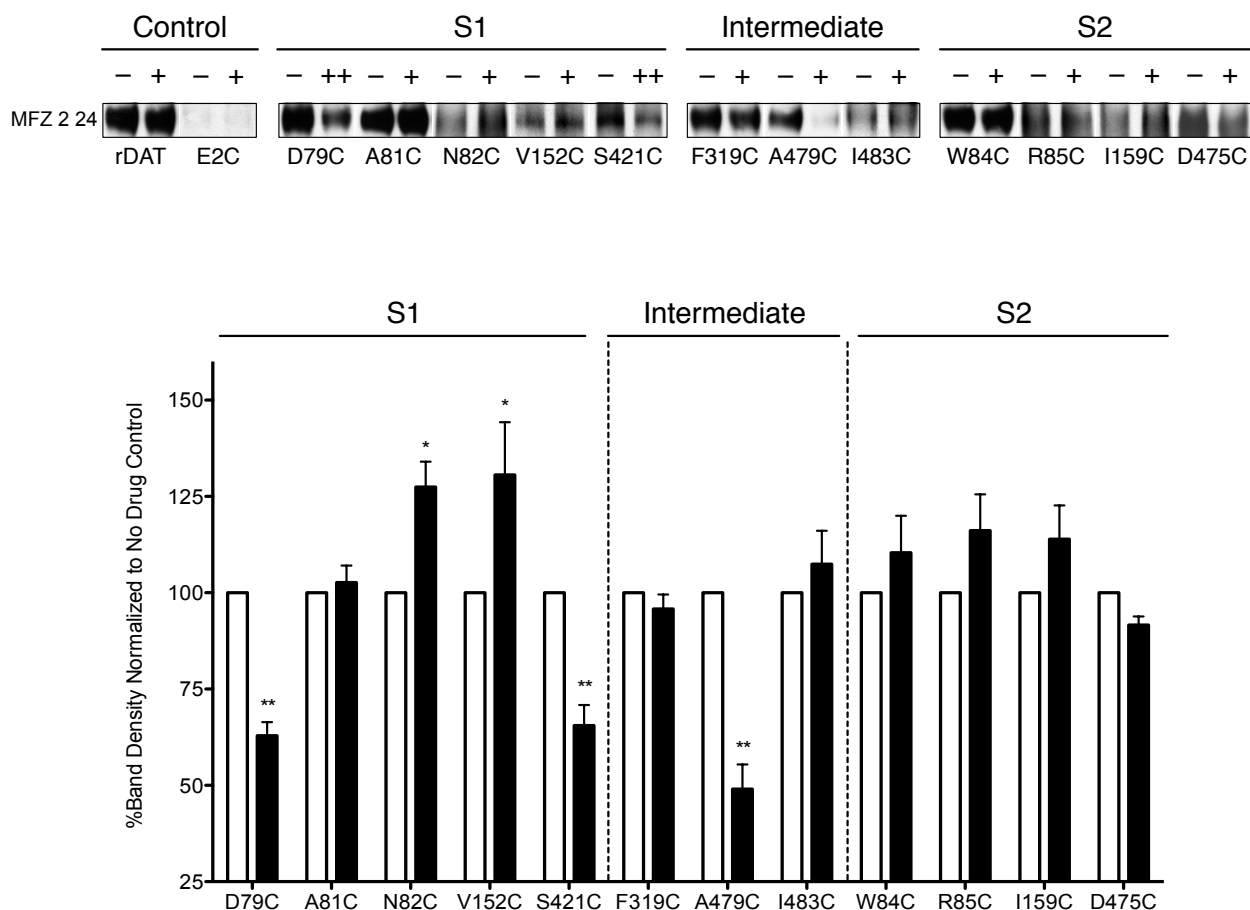


Figure 23. SCAM protection analysis of S1 and S2 binding pockets. (a) Immunoblots of the surface pool of DAT Cys mutants in the rDAT E2C background purified with MTSEA-biotin in the absence (-) or presence of MFZ 2-24 (+, 10 μ M; ++, 50 μ M). (b) Quantification of DAT bands in A and total DAT expression (data not shown) were determined using ImageJ (National Institutes of Health). Surface samples were normalized to total DAT then expressed as a percent of MFZ 2-24-treated samples (black bars) to the respective untreated samples (white bars). These data represent three or more independent experiments. Significant differences between treated and untreated samples were determined with a paired *t* test *, $p < 0.05$; **, $p < 0.01$.

Treatment with MFZ 2-24 did not affect recovery of biotinylated rDAT surface protein (Fig. 23, Control) indicating a lack of protection of residues Cys-90 and/or Cys-305, both of which are located on the extracellular ends of TMs 1 and 6, respectively. Recovery from the S1 mutants D79C and S421C was significantly reduced in the presence of MFZ 2-24 (Fig. 23, S1),

demonstrating protection of these residues from the MTS reagent. Mutant A81C showed no change in recovery whereas MFZ 2-24 increased N82C and V152C recovery in a manner similar to cocaine, unlike RTI 82 (Dahal et al. 2014). This difference in cocaine analog protection likely arises from the position of the phenyl azido moiety, as the RTI 82 extension is oriented toward the external vestibule whereas MFZ 2-24 is bent inwards. In the S2 mutants, MFZ 2-24 did not alter recovery from W84C, R85C, I159C, and D475C (Fig. 23, S2) indicating a lack of protection of these residues from MTS attack. In combination, these data reveal binding of MFZ 2-24 to DAT in the S1, but not S2, site.

The intermediate residues Phe-319, Ala-479, and Ile-483 that lie at the interface between the S1- and S2-binding sites may provide insight into the conformation of DAT that is adopted upon antagonist binding. MFZ 2-24, like RTI 82 (Dahal et al. 2014), only protected mutant A479C from MTS modification (Fig. 23, Intermediate) whereas cocaine protected all intermediate sites. Though the azido groups of RTI 82 and MFZ 2-24 adduct to distinct sites in DAT, each analog has the addition of a phenyl azido moiety that, through its added bulk, may prevent DAT from transitioning to an occluded conformation. Cocaine, however, lacks the phenyl azido group and may induce a more complete transition to the occluded structure therefore providing protection of these residues.

Discussion

Cocaine interactions with DAT are complex and have been proposed to result in high and low affinity binding states (Madras et al. 1989; Boja et al. 1998) that alter uptake through competitive and noncompetitive mechanisms (Missale et al. 1985; McElvain and Schenk 1992). Cocaine may interact at the primary substrate binding site, S1, thereby competing for DA binding (Beuming et al. 2008; Bisgaard et al. 2011; Dahal et al. 2014), or at the S2 site located in

the vestibule on the extracellular side of the outer gate (Huang, Gu, and Zhan 2009; Merchant and Madura 2012; Schmitt, Rothman, and Reith 2013). Binding of cocaine to either of these sites would likely lock the transporter into an inactive conformation, which would block substrate uptake. To address this discrepancy, our groups have developed a series of irreversible binding cocaine analogs to directly identify the site of incorporation. Here, we demonstrate covalent attachment of the cocaine photoaffinity analog MFZ 2-24 to the TM1 residue Leu-80 and, in conjunction with modeling and SCAM analysis, determined that the binding of the tropane pharmacophore occurs in the S1 substrate binding site.

Similar to our previous findings regarding the cocaine photoaffinity analog RTI 82 (Dahal et al. 2014), our top scoring RL and IFD models maintain a salt-bridge interaction between the positively charged tropane nitrogen of MFZ 2-24 and the negatively charged side-chain of residue Asp-79. These models also support an interaction between the phenyl chloride of MFZ 2-24 and Asn-157, an interaction that parallels previous findings with the phenyl chloride of RTI 82 (Dahal et al. 2014) and the phenyl fluoride of CFT (Beuming et al. 2008). Cocaine possesses a nonhalogenated benzoyl ester that does not interact with Asn-157 (Wang, Penmatsa, and Gouaux 2015), suggesting that interaction of a compound with Asn-157 may be dependent on the presence of a halogen. Though this interaction was originally thought to contribute to the higher affinity binding of CFT, RTI 82, and MFZ 2-24 (Runyon and Carroll 2008), recent crystal structures of the cocaine analogs β -CFT and RTI-55 in complex with DAT suggest that Asn-157 does not directly participate in binding and that the halogen substituted phenyl groups do not markedly affect the architecture of the binding pocket (Wang, Penmatsa, and Gouaux 2015). This recent finding may explain why, after MD simulation, the phenyl Cl

group of MFZ 2-24 in our RL and IFD docked structures moves away from Asn-157 to distances greater than 5Å.

The adduction site of MFZ 2-24, Leu-80, coordinates substrate binding by forming a hydrophobic-aromatic interaction with Tyr-156, as mutation of Leu-80 destabilizes Tyr-156 resulting in unmeasurable DA uptake though cocaine and CFT binding are unaffected (Beuming et al. 2008; Parnas et al. 2008). Mutation of the homologous site in SERT also resulted in decreased substrate transport, suggestive of a conserved role for this position in substrate transport (Henry et al. 2003). The S1 location of this residue, one helical turn above the TM1 residue proposed to interact with the tropane nitrogen of MFZ 2-24 (Asp-79), indicates that MFZ 2-24 inhibits DA uptake through a competitive mechanism either by binding to S1 in an occluded or outward-facing conformation. Our models reveal that an outward-facing conformation is more likely as our docking methods were unable to identify an MFZ 2-24/DAT complex based on an occluded homology model. Furthermore, our SCAM data supports binding of MFZ 2-24 in a manner similar to RTI 82 unlike cocaine. Whereas cocaine was able to protect intermediate residues from MTS inactivation, MFZ 2-24 and RTI 82 were unable to. This is likely a result of cocaine binding to an occluded conformation while the added bulk of the phenyl azido moieties of MFZ 2-24 and RTI 82 prevents closure of the extracellular gate and, therefore, formation of an outward-facing conformation.

The physiological effects and economical burden imparted by cocaine abuse are several factors that highlight the importance of understanding the mechanism of cocaine binding and transport inhibition. The advent of the benztropine class of DAT antagonists, compounds that do not produce cocaine-like behavioral profiles (Agoston et al. 1997; Katz et al. 2004), suggests that a cocaine-abuse pharmacotherapeutic is possible. GBR12909 for example was a promising

pharmacotherapeutic as it decreased self-administration of cocaine following pretreatment (Baumann et al. 1994; Glowa et al. 1995; Tella 1995), but due to prolonged QTc intervals in patients participating in Phase II clinical trials (Vocci, Acri, and Elkashef 2005) and the ability to block multiple ion channels (Lacerda et al. 2010), it will likely benefit treatment of abnormal heart rhythms instead (Obejero-Paz et al. 2015; Piccini et al. 2016). Thus, understanding cocaine binding in relation to typical and atypical DAT inhibitors will provide needed insights for developing cocaine-abuse pharmacotherapeutics.

CHAPTER IV

ANTAGONISM OF THE DOPAMINE TRANSPORTER BY THE IRREVERSIBLE BENZTROPINE ANALOG [¹²⁵I]GA II 34 OCCURS AT THE CENTRAL SUBSTRATE-BINDING SITE

Introduction

The dopamine transporter (DAT), a member of the SLC6 family of neurotransmitter transporters, or neurotransmitter sodium symporters (NSS), is responsible for the reuptake of dopamine (DA) from the synapse following vesicular release, effectively regulating dopaminergic neurotransmission. Disruptions in this mechanism of homeostatic regulation have been implicated in a variety of fundamental brain processes, including movement, emotion, behavior, and memory (Pramod et al. 2013; Kristensen et al. 2011). Furthermore, when targeted by the psychostimulant drugs cocaine, amphetamine, and methylphenidate, the function of DAT is inhibited through blockade of transport (Cheng et al. 2015; Gether et al. 2006; Sulzer et al. 2005; Rothman and Baumann 2003), which results in elevated levels of extracellular DA and amplification of dopaminergic signaling. Although drugs of abuse are reinforcing, several classes of DAT uptake blockers have been developed that are both potent and selective yet lack the behavioral effects seen, for example, with cocaine (Rothman et al. 2007; Reith et al. 2015; Schmitt et al. 2008; Schmitt and Reith 2011). This suggests that development of improved pharmacotherapies for drug abuse and DA disorders is possible, though the molecular basis by which structurally distinct classes of inhibitors interact with the transporter and induce differential physiological outcomes is yet unclear.

The SLC6 family of transporters share a common topology of 12 transmembrane (TM) spanning domains connected by intracellular (IL) and extracellular (EL) loops with cytoplasmic N- and C-termini (Pramod et al. 2013; Kristensen et al. 2011; Bröer and Gether 2012). Similar to the biogenic amine, cocaine-sensitive serotonin (SERT) and norepinephrine (NET) transporters, with sequence identities of ~49- and ~67% respectively (Giros et al. 1992; Ramamoorthy et al. 1993; Pacholczyk, Blakely, and Amara 1991; Reith 2002), DAT functions through the use of a Na⁺- and Cl⁻-dependent electrochemical gradient, which drives translocation of substrate against its concentration gradient (Rudnick et al. 2013). Considerable insight into the structural mechanisms underlying substrate translocation emerged from crystal structures of the leucine transporter (LeuT) from *Aquifex aeolicus*, a prokaryotic homolog of the SLC6 transporters, as well as from more recent structures of *Drosophila melanogaster* (d) DAT and human SERT (hSERT) (Yamashita et al. 2005; Wang, Penmatsa, and Gouaux 2015; Coleman, Green, and Gouaux 2016). Based on a predicted alternating access mechanism (Jardetzky 1966), crystal structures have provided snapshots of the transporter in conformations corresponding to the three principal states of the transport cycle: outward-facing, occluded, and inward-facing (Krishnamurthy and Gouaux 2012; Yamashita et al. 2005). An outward-facing conformation opens to an aqueously accessible primary/central binding site (S1) composed of residues from TMs 1, 3, 6, and 8 that, after binding of substrate, two Na⁺ ions (Na1 and Na2), and one Cl⁻ ion, initiates a conformational cascade beginning with the closure of an extracellular gate, which occludes S1, followed by opening of an intracellular gate and release of solutes into the cytoplasm (Zhao et al. 2011; Cheng and Bahar 2015; Tavoulari et al. 2015; Felts et al. 2014; Henry et al. 2011; Forrest et al. 2008). Alternatively, structures of LeuT, dDAT, and hSERT crystallized in complex with inhibitors have identified how the transport mechanism is halted in

the outward-facing or occluded conformation where antagonists are either bound to the S1 site (Penmatsa, Wang, and Gouaux 2015; Wang, Penmatsa, and Gouaux 2015; Penmatsa, Wang, and Gouaux 2013; Singh et al. 2008; Coleman, Green, and Gouaux 2016) or a highly controversial S2 site (Zhou et al. 2009; Quick et al. 2009; Singh, Yamashita, and Gouaux 2007; Zhou et al. 2007; Coleman, Green, and Gouaux 2016), an extracellularly accessible site in the outer vestibule located above the outer gate, of which the existence and functional role still remain a topic of debate (Piscitelli, Krishnamurthy, and Gouaux 2010; Shi et al. 2008).

As DAT is the primary target of cocaine, efforts to understand how the drug interacts with the transporter have identified the formation of a salt bridge between the negatively charged TM1 residue Asp79, a S1 residue responsible for coordinating the positive DA charge (Pramod et al. 2013; Kristensen et al. 2011; Bröer and Gether 2012), and the positively charged tropane nitrogen of cocaine, suggestive of a cocaine binding site in S1 and, consequently, a competitive mechanism of inhibition (Carroll et al. 1992; Kitayama et al. 1992; Beuming et al. 2008). To date, multiple DA uptake inhibitors have been developed in an attempt to identify a cocaine-abuse therapeutic (Rothman 1990; Newman and Kulkarni 2002; Desai et al. 2005). One such compound is benztropine, a DAT antagonist equipotent to cocaine, and its analogs that do not demonstrate cocaine-like behavioral profiles (Newman, Allen, and Izenwasser 1994; Newman et al. 1995; Agoston, Wu, et al. 1997; Katz, Newman, and Izenwasser 1997; Katz et al. 2004; Hiranita et al. 2009), a result originally suggestive of a binding site separate from cocaine (Vaughan et al. 1999; Reith et al. 2001; Chen, Zhen, and Reith 2004; Ukairo et al. 2005; Rothman et al. 2007). However, subsequent computational docking studies and mutational analyses observed that cocaine and benztropines bind to the primary, S1 binding site (Beuming

et al. 2008; Bisgaard et al. 2011), though the interaction with DAT that accounts for the distinct behavioral effects is yet unknown.

To determine the molecular interactions of benztropine with DAT, we developed the irreversible benztropine analog [^{125}I]N-[*n*-butyl-4-(4'-azido-3'-iodophenylethyl-ester)]-4',4''-difluoro-3 α -(diphenylmethoxy)tropane ([^{125}I]GA II 34) (Fig. 24) (Agoston, Vaughan, et al. 1997). GA II 34, benztropine, cocaine, and the cocaine analogs RTI 82 and MFZ 2-24 share the

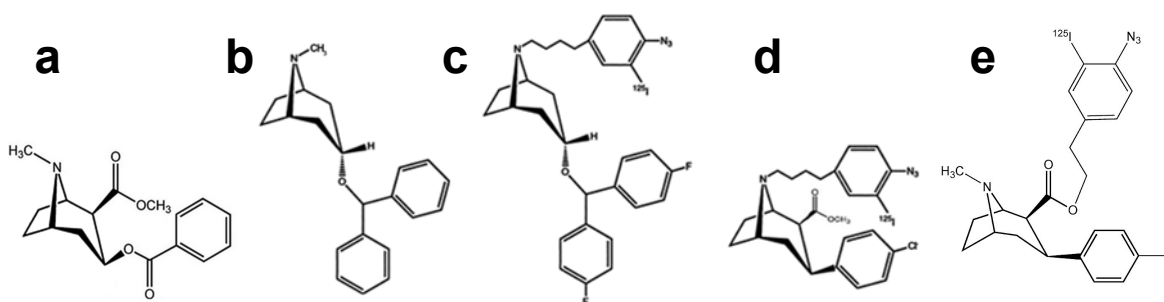


Figure 24. Chemical structures of cocaine, benztropine, [^{125}I]GA II 34, [^{125}I]MFZ 2-24, and [^{125}I]RTI 82. Structures of cocaine (a), benztropine (b), [^{125}I]GA II 34 (c), [^{125}I]MFZ 2-24 (d), and [^{125}I]RTI 82 (e) with the shared tropane nitrogen pharmacophore.

common tropane nitrogen pharmacophore, but [^{125}I]GA II 34 contains a photoactivatable 4'-azido-3'-iodophenylethyl ester (AIP) moiety that forms a highly reactive singlet nitrene upon irradiation with ultraviolet light, thus forming a covalent bond with either a C-H or N-H group in the protein (Kotzyba-Hibert, Kapfer, and Goeldner 1995; Geurink et al. 2012). Using irreversible labeling as a strategy for determining the site of ligand-protein interaction, we previously demonstrated [^{125}I]GA II 34 cross-links to rat DAT (rDAT) within TMs 1-2 (Vaughan et al. 1999). Here, we utilized methionine substitution mutagenesis and cyanogen bromide (CNBr) digestion to narrow the site of [^{125}I]GA II 34 attachment to either residue Asp-79 or Leu-80 as well as substituted cysteine accessibility method (SCAM) analyses that indicated that GA II 34, like cocaine and several cocaine analogs (Dahal et al. 2014; Pramod et al. in preparation), protected residues in S1, but not S2, indicative of a competitive mechanism of inhibition. These

findings localize [¹²⁵I]GA II 34 to a binding site overlapping that of cocaine, but whereas cocaine bound DAT forms a more occluded structure (Dahal et al. 2014), protection of one S2 residue as well as several S1 residues by [¹²⁵I]GA II 34 suggests that the extracellular gate is unable to close and a more outward-open conformation is adopted, a finding that will need to be investigated further to explain the altered behavioral profiles.

Methodology

Cell Culture and Site-directed Mutagenesis

For photoaffinity labeling experiments, wild-type (WT) and mutant cDNAs in pcDNA3-rDAT vector were generated as previously described (Parnas et al. 2008; Dahal et al. 2014) using the Stratagene QuikChange® kit and verified by sequencing (Northwoods DNA, Solway, MN; Eurofins MWG Operon, Huntsville, AL). For stable expression of WT and mutants V78M, L80M, and M111L/M116L/M272L, Lewis Lung Carcinoma-Porcine Kidney (LLC-PK₁) cells were transfected with 2 µg cDNA using FuGENE transfection reagent and selected with 800 µg/mL of G418. Mutants for SCAM analysis, D79C, W84C, R85C, V152C, I159C, F319C, S421C, D475C, and A479C, were generated in the E2C background (C90A and C305A) of pcDNA3-rDAT and expressed transiently in HEK-GripTite cells (Invitrogen) using TransIT®-LT1 (Mirus) (1 µl per 200 ng of DNA). Cells were maintained in a humidified chamber with 5% CO₂ at 37°C in α -minimum essential medium (AMEM with 5% fetal bovine serum, 2 mM L-glutamine, 200 µg/mL G418, and 100 µg/mL penicillin/streptomycin) for LLC-PK₁ cells, or Dulbecco's modified Eagle's medium (DMEM: 10% FBS, 600 µg/ml G418) for HEK-GripTite cells.

GA II 34 Synthesis and Radioiodination

GA II 34 and the amino precursor of [^{123}I]GA II 34 were synthesized using modifications of the original procedure (Agoston, Wu, et al. 1997; Vaughan et al. 1999). Radioiodination was conducted as previously described (Agoston, Vaughan, et al. 1997).

Photoaffinity Labeling and In Situ Proteolysis of Native DAT

These procedures were performed as described previously (Parnas et al. 2008; Vaughan et al. 2007). Rat striatal membranes were homogenized in ice-cold sucrose phosphate (SP) buffer (0.32 M sucrose and 0.1 M Na_2HPO_4 , pH 7.4). The homogenate was centrifuged at 3,000 x g for 3 min. Supernatant was transferred to a fresh tube and centrifuged at 12,000 x g for 12 min. The final membrane pellet was resuspended at a concentration of 20 mg/ml (original wet weight) in Krebs Ringers HEPES (KRH) buffer (25mM HEPES, 125 mM NaCl, 4.8 mM KCL, 1.2 mM KH_2PO_4 , 1.3 mM CaCl_2 , 1.2 mM MgSO_4 , 5.6 mM glucose, pH 7.4) followed by addition of 10 nM [^{125}I]GA II 34. Samples were incubated on ice for 1.5-2 hr, irradiated with UV light (254 nm) for 5 min to covalently attach the ligand to DAT, and washed 3x with 50 mM Tris-HCl to remove unbound ligand. After resuspension to a final concentration of 40 mg/mL original wet weight, 45 μl of photolabeled lysates were treated with 5 μl of trypsin prepared in 50 mM Tris-HCl (10 $\mu\text{g}/\text{ml}$), pH 8.0, and incubated at 30°C for twenty minutes. Digestion was halted with soybean trypsin inhibitor and centrifugation at 20,000 x g for 20 min. Membranes were solubilized with radioimmunoprecipitation assay (RIPA) buffer (150 mM NaCl, 1 mM EDTA, 1% Triton X-100, 0.1% SDS, pH 7.5) containing protease inhibitors (Complete Mini). Lysates were centrifuged at 20,000 x g for 12 min at 4°C, immunoprecipitated with polyclonal antibody 16 (Ab16) or polyclonal antibody 19 (Ab19), and electrophoresed on 4-20% polyacrylamide gels followed by autoradiography.

Photoaffinity Labeling of Expressed DAT

As previously described (Dahal et al. 2014), WT and mutant cells were plated on 6 well plates and, when 90-95% confluent, washed with KRH and incubated with 15 nM ligand on ice for 1.5-2 hr. Irreversible ligand incorporation was achieved with 254 nm UV light for 5 min and unbound ligand removed by washing twice with cold KRH. Samples were lysed with RIPA, the lysates centrifuged, and the supernatant subjected to SDS-PAGE and autoradiography on 8% Tris-glycine polyacrylamide gels. Photolabeled DAT bands were excised and the protein extracted by electroelution (Vaughan 1995). Electroeluted samples were dialyzed against deionized water in 10 kDa cut-off Slide-A-Lyzer dialysis cassettes (Pierce) and lyophilized. Aliquots were counted in a scintillation counter and equal amounts of radioactivity were subjected to peptide mapping.

CNBr Peptide Mapping

Gel purified samples were divided equally based on their radioactivity, lyophilized to dryness, and subjected to CNBr digestion. Samples were resuspended in 70 μ L of 70% formic acid with or without addition of 1 M CNBr for 24 hr at 22°C in the dark. Reactions were quenched with MilliQ water and the samples lyophilized to dryness. To remove excess CNBr, samples were washed and lyophilized 3x followed by resuspension in immunoprecipitation buffer (50 mM Tris-HCl, 0.1% Triton X-100, pH 8.0). Sample was either directly subjected to SDS-PAGE/autoradiography to visualize the total CNBr digestion pattern or first immunoprecipitated with Ab16. For each experiment, mutants were photoaffinity labeled and analyzed with WT or L80M DAT exactly in parallel and all results were replicated twice. CNBr peptide masses were calculated using PeptideCutter via ExPASy.

SCAM Protection Analysis of S1- and S2-binding Sites

GripTite cells were plated at a density of 150,000 cells/cm² in 24-well culture plates, incubated for 24 hr, and transfected with rDAT constructs using TransIT®-LT1 (Mirus). Following transfection (48 hr), cells were processed as described previously (Dahal et al. 2014; Henry et al. 2003). Briefly, cells were incubated with 10 or 50 μ M GA II 34 or vehicle for 5 min in PBS/CM (137 mM NaCl, 2.7 mM KCl, 10.1 mM Na₂HPO₄, 1.8 mM KH₂PO₄, 0.1 mM CaCl₂, 1.0 mM MgCl₂, pH 7.4) followed by addition of 0.1 mM MTSEA-biotin for 10 min (Biotium). Cell lysates were obtained with RIPA solubilization buffer (10 mM Tris, pH 7.4, 150 mM NaCl, 1 mM EDTA, 0.1% SDS, 1% Triton X-100, 1% sodium deoxycholate) containing Halt™ Protease Inhibitor Single-Use Cocktail (ThermoFisher) and incubated with NeutrAvidin-agarose resin (ThermoFisher) to extract surface proteins labeled by MTSEA-Biotin. Following a BCA assay (ThermoFisher) to determine protein concentration, equal amounts of protein from total samples and equivalent volumes of surface protein pools were processed by SDS-PAGE and immunoblotting using anti-DAT monoclonal antibody, mAb 16 (Foster, Pananusorn, and Vaughan 2002; Gaffaney and Vaughan 2004). DAT levels were quantitated from the density of immunoblot bands from three separate assays using Image Studio (LI-COR). Surface values were normalized to total DAT levels and are expressed as a percent of untreated samples. Data were analyzed using a paired *t* test (Prism 5).

Results

Proteolytic Peptide Mapping of [¹²⁵I]GA II 34

Labeling and characterization of DAT with the benzotropine photoaffinity analog [¹²⁵I]GA II 34 was originally demonstrated in rat striatal membranes (Vaughan et al. 1999). To further characterize and reestablish interaction of [¹²⁵I]GA II 34 with the dopamine transporter, LLC-

PK₁ cells expressing human DAT (hDAT) were incubated with 15 nM [¹²⁵I]GA II 34 in the presence or absence of mazindol (Fig. 25). Immunoprecipitation of a ~100 kDa fragment by N-terminal antibody 16 (Ab16), absent with the addition of mazindol, demonstrates specificity of [¹²⁵I]GA II 34 for hDAT.

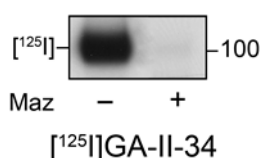


Figure 25. Photoaffinity labeling of hDAT with [¹²⁵I]GA II 34. hDAT LLC-PK₁ cells photolabeled with 15 nM [¹²⁵I]GA II 34 in the absence or presence of 10 μM mazindol followed by immunoprecipitation with Ab16.

To reexamine the incorporation of [¹²⁵I]GA II 34 with rDAT, 20 mg/ml of a rat striatal membrane suspension was incubated with a 10 nM final concentration of [¹²⁵I]GA II 34. The subsequent lysate was treated with 10 μg/ml of trypsin, a protease known to digest peptides at arginine (Arg) and lysine (Lys) residues. The digested samples were immunoprecipitated with Ab16 or C-terminal antibody 19 (Ab19) to generate proteolytic peptide maps. Examination of the peptide maps indicates immunoprecipitation of the ~100 kDa fragment by both Ab16 and Ab19 revealing [¹²⁵I]GA II 34 labeling of rDAT as previously demonstrated (Fig. 26) (Vaughan et al. 1999). Immunoprecipitation of the proteolyzed sample with Ab16 produced a fragment of ~45 kDa previously determined to correspond to digestion at Arg-218 with incorporation of the AIP moiety somewhere within the N-terminus, TMs 1-3, or the glycosylated region of EL2 (Vaughan and Kuhar 1996; Parnas et al. 2008). Incubation of the irreversible cocaine analog [¹²⁵I]RTI 82 labeled DAT with antibody 5, directed against the C-terminal region of EL 2 (Vaughan, Uhl, and Kuhar 1993), has been shown to immunoprecipitate fragments of ~32 and ~10 kDa (Vaughan et al. 2007). Positive peptide maps with Ab19 have yet to be published, but immunoprecipitation of ~32 and ~10 kDa fragments by Ab19 here does not indicate incorporation of the ligand to TMs

4-12 as these fragments are present in the undigested lane as well as the Ab16 lane indicating nonspecific immunoprecipitation.

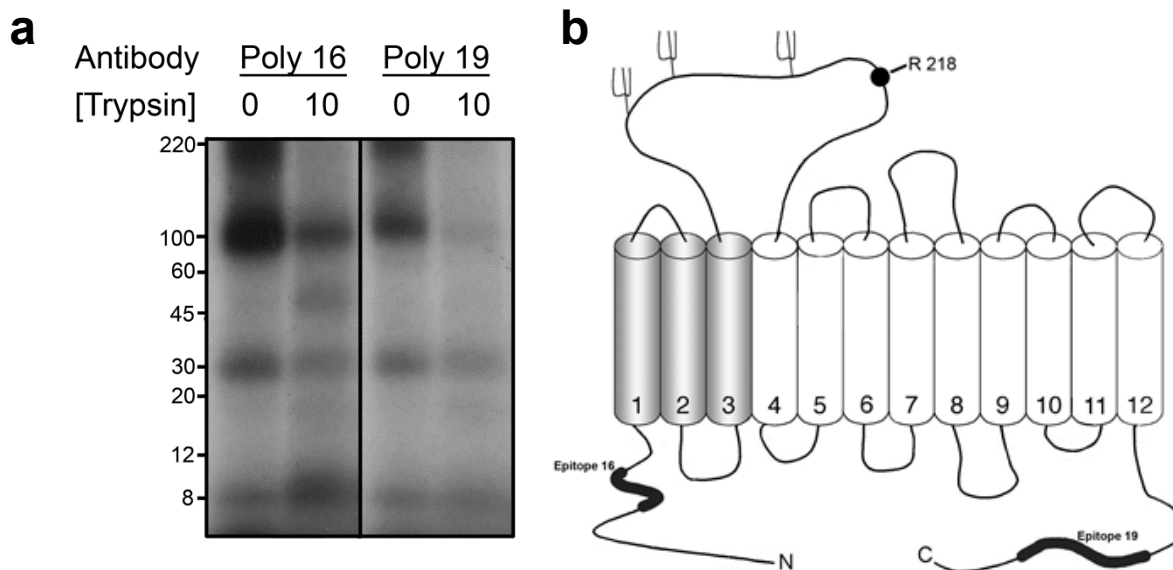


Figure 26. Photoaffinity labeling, in situ proteolysis, and immunoprecipitation of [¹²⁵I]GA II 34 labeled rDAT. (a) Rat striatal membranes photolabeled with 10 nM [¹²⁵I]GA II 34 were digested with 10 μg/ml trypsin followed by immunoprecipitation with Ab16 or Ab19 and SDS PAGE/autoradiography. (b) Schematic diagram of rDAT. TM domains are depicted as cylinders with the black circle representing Arg-218, the potential site of trypsin digestion. The presence of a 45 kDa fragment after immunoprecipitation with Ab16 indicates adduction of [¹²⁵I]GA II 34 within the shaded TMs.

CNBr Mapping of [¹²⁵I]GA II 34 Attachment

Although trypsin digestion is extremely useful as a foundation from which to narrow the site of AIP attachment, the abundance of Lys and Arg residues available for digestion makes it difficult to identify the single residue at which adduction occurs. In contrast, the number of methionine (Met) residues in hDAT is limited to 13 (15 Mets in rDAT) allowing chemical digestion by cyanogen bromide (CNBr) to produce larger fragments while possibly retaining epitopes for immunoprecipitation. To implement CNBr digestion, we photolabeled WT hDAT expressed in HEK cells with [¹²⁵I]GA II 34 as well as a mutant transporter M111L/M116L/M272L, hereby referred to as M272L, which was previously used to localize

incorporation of RTI 82 (Dahal et al. 2014). The M111L/M116L background is used in all mutant DAT constructs to rule out incorporation between residues Met-106, Met-111, and Met-116. CNBr digestion of both [¹²⁵I]GA II 34 labeled WT and M272L produced a ~10 kDa fragment (Figure 27) indicative of AIP adduction to a residue in DAT N-terminal to Met-106. Formation of a ~65 to 75 kDa fragment in M272L suggests a possible second incorporation site of [¹²⁵I]GA II 34 elsewhere in DAT, however it is more likely that this fragment is a result of incomplete digestion of [¹²⁵I]GA II 34 labeled M272L (Gaffaney and Vaughan 2004). Subsequently, as the majority of the radioactive signal is apparent at ~10 kDa, we focused on residues N-terminal to Met-106 to localize the site of AIP covalent attachment.

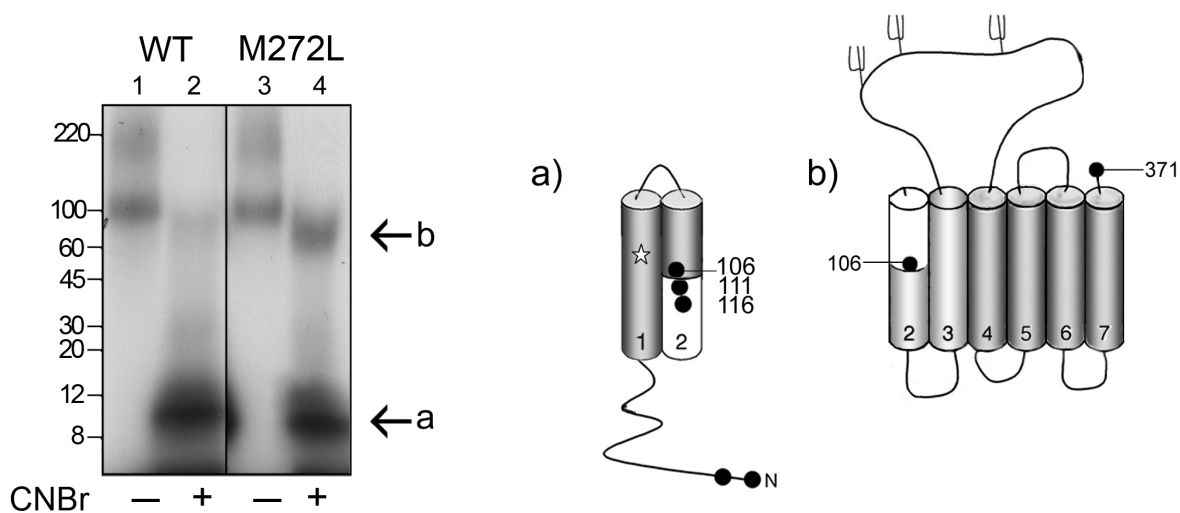


Figure 27. Localizing [¹²⁵I]GA II 34 covalent attachment N-terminal to Met-106. HEK cells expressing WT hDAT or M111L/M116L/M272L hDAT were photolabeled with [¹²⁵I]GA II 34 and gel purified. Samples were treated with formic acid only (vehicle) or CNBr followed by analysis with SDS-PAGE/autoradiography. TM domains are depicted as cylinders. Black circles represent Met residues. CNBr digestion of WT hDAT produced a ~10 kDa (a) fragment indicating adduction N-terminal to Met-106. This fragment occurred after CNBr digestion of M272L as well, along with a ~65-75 kDa (b) fragment likely resulting from incomplete digestion of [¹²⁵I]GA II 34 labeled M272L.

Localizing [125 I]GA II 34 Adduction to TM1 in DAT

Based on the structural similarity of [125 I]GA II 34 to the irreversible cocaine analog [125 I]MFZ 2-24 (Fig. 24), which was recently shown to adduct to Leu-80 (Pramod et al. in preparation), we predicted that incorporation of the AIP moiety of [125 I]GA II 34 to DAT would occur near or at Leu-80 as well. Therefore, mutants M111L/M116L, L80M, and V78M were labeled with [125 I]GA II 34 and subjected to CNBr digestion (Fig. 28). Digestion of the

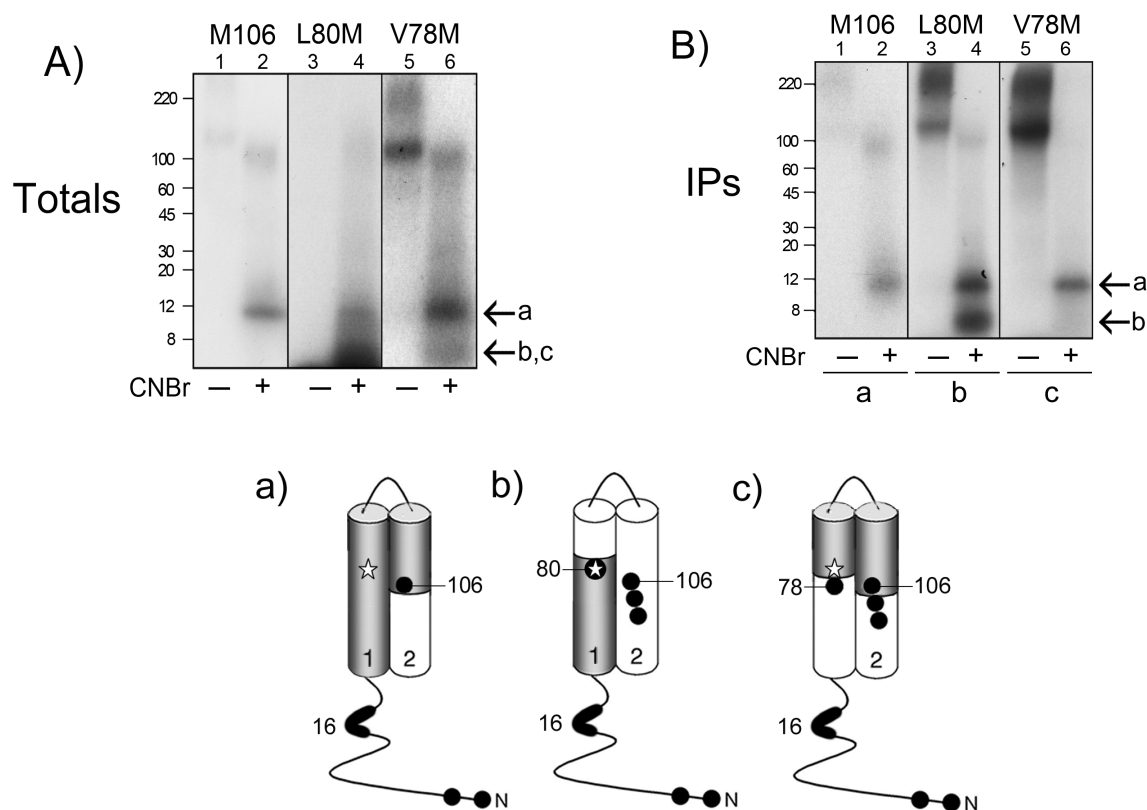


Figure 28. CNBr mapping of [125 I]GA II 34 labeled DAT to TM1. CNBr digestion of [125 I]GA II 34 labeled M111L/M116L (M106), L80M, and V78M (A) immunoprecipitated with Ab16 (B). Digestion of M111L/M116L produced a ~10 kDa (a) fragment corresponding to incorporation of [125 I]GA II 34 to a residue N-terminal to Met-106 while digestion of mutant L80M resulted in ~8 and ~10 kDa fragments, of which the ~8 kDa (b) fragment is consistent with digestion N-terminal to Leu-80. Loss of the ~8 kDa fragment with V78M digestion indicates incorporation of [125 I]GA II 34 C-terminal to Val-78, but at or N-terminal to Leu-80 (c).

M111L/M116L control resulted in a ~10 kDa fragment that immunoprecipitated with Ab16, demonstrating incorporation of [¹²⁵I]GA II 34 to a residue N-terminal to Met-106 as the calculated mass of a fragment extending from Met-11 to Met-106 is 10.5 kDa. [¹²⁵I]GA II 34 labeled L80M produced two fragments of ~8 and ~10 kDa after digestion, both of which immunoprecipitated with Ab16 suggesting incomplete digestion at Met-106. The ~8 kDa fragment is consistent with peptides extending from Met-1 or Met-11 to L80M, with calculated masses of 7.5 and 8.7 kDa, respectively, as we previously described (Parnas et al. 2008). With digestion of V78M however, the ~8 kDa fragment is absent strongly indicating that cleavage of TM1 at Met-78 separated epitope 16 from the [¹²⁵I]GA II 34 adduction site. Thus, binding of the AIP moiety of [¹²⁵I]GA II 34 occurs at or N-terminal to Leu-80, but C-terminal to Val-78, narrowing the site of AIP covalent attachment to either Asp-79 or Leu-80.

Analysis of GA II 34 Protection of S1- and S2-binding Pockets from Cys-directed Biotinylation

Our peptide mapping results suggest that binding of the GA II 34 tropane pharmacophore occurs within the S1-binding site and positions the AIP group for adduction to Asp-79 or Leu-80. To confirm binding of GA II 34 to S1, we analyzed several residues present in the S1- or S2-binding sites in addition to several that line the transition between S1 and S2 (intermediate residues) in the DAT permeation pathway (Fig. 29). Mutants were constructed in a methanethiosulfonate (MTS)-insensitive rDAT E2C (C90A and C305A) background and assessed for GA II 34-induced protection from the SCAM reagent MTSEA-biotin.

Previously (Dahal et al. 2014), we identified that surface rDAT was readily labeled with MTSEA-biotin whereas labeling of rDAT E2C is undetectable (Fig. 29, Control), confirming it as a cysteine-reduced, MTS-inactive background suitable for analysis of inserted Cys residues. Utilizing rDAT E2C as a template, we generated Cys mutations of the S1 residues Asp-79, Ala-

81, Asn-82, Val-152, and Ser-421, the S2 residues Trp-84, Arg-85, Ile-159, and Asp-475, and the intermediate residues Phe-319, Ala-479, and Ile-483. MTSEA-biotin protection assays were done using 10 μ M GA II 34, except for the mutants D79C and S421C where marked losses in potency to inhibit binding were observed, which required a higher concentration (50 μ M) for protection analyses.

Treatment with GA II 34 did not affect recovery of biotinylated rDAT surface protein (Fig. 29, Control) indicating a lack of protection of residues Cys-90 and/or Cys-305, both of which are located on the extracellular ends of TMs. Recovery from the S1 mutants D79C and S421C was significantly reduced in the presence of GA II 34, demonstrating protection of these residues from the MTS reagent (Fig. 29, S1). Mutants A81C and N82C however showed no change in recovery whereas V152C recovery was increased by GA II 34. Notably, Asn-82 accessibility was increased upon cocaine analog binding (Dahal et al. 2014), unlike the benztrapine analog in which the added bulk of a diphenyl results in the differential accessibility.

The intermediate residues Phe-319, Ala-479, and Ile-483 that lie at the interface between the S1 and S2 binding sites may provide insight into the conformation of DAT that is adopted upon antagonist binding. GA II 34, like the cocaine analogs RTI 82 and MFZ 2-24 (Dahal et al. 2014; Pramod et al. in preparation), only protected mutant A479C from MTS modification whereas cocaine protected all intermediate sites (Fig. 29, Intermediate). Though the cocaine and benztrapine analogs differ structurally and each azido group adducts to distinct sites in DAT, each analog has the addition of an AIP moiety that, through its added bulk, may prevent DAT from transitioning to an occluded conformation. Cocaine, however, lacks the AIP group and may induce a more complete transition to the occluded structure therefore providing protection of these residues.

In the S2 mutants, GA II 34 did not alter recovery from R85C, I159C, and D475C indicating a lack of protection of these residues from MTS attack (Fig. 29, S2). Conversely, recovery of surface protein was significantly less in the mutant W84C after GA II 34 treatment, which, based on our computational data (not shown), is not unexpected as the AIP moiety is in close proximity to Trp-84. In combination, these data reveal binding of GA II 34 to DAT in the S1, but not S2, site.

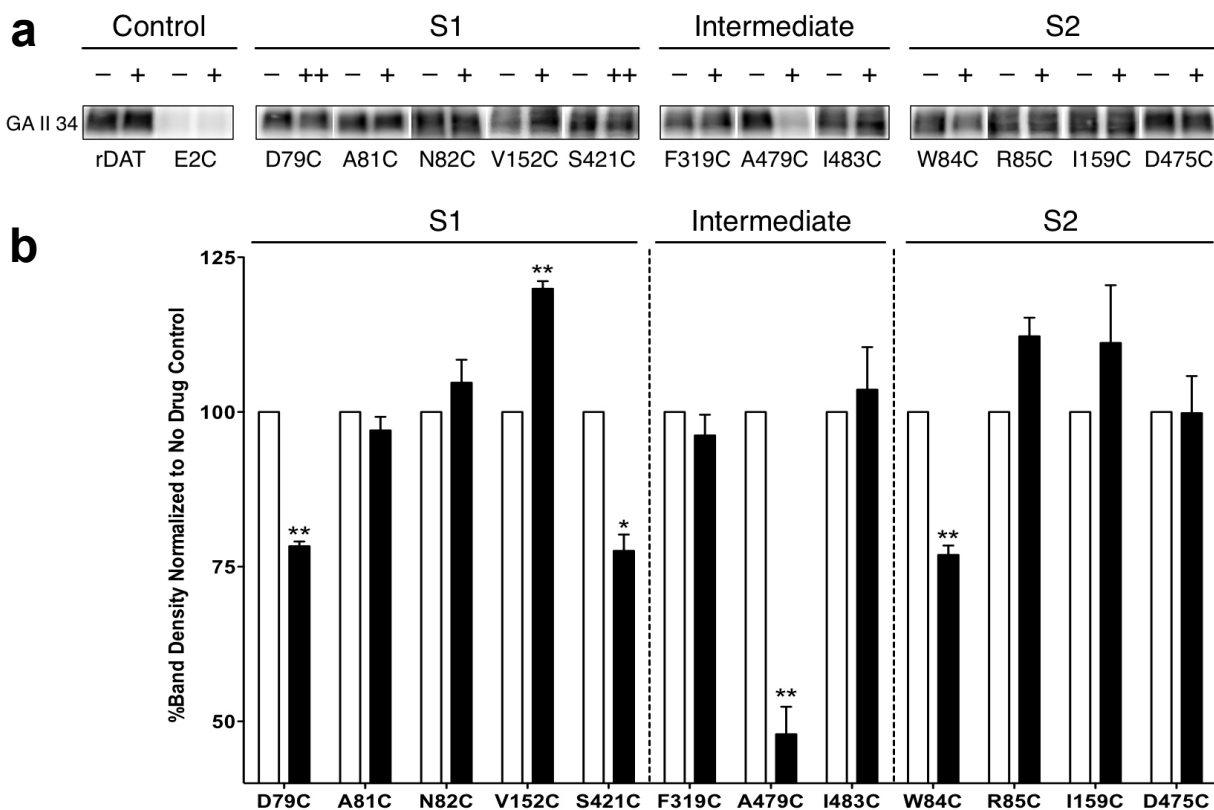


Figure 29. SCAM protection analysis of S1 and S2 binding pockets. (a) Immunoblots of the surface pool of DAT Cys mutants in the rDAT E2C background purified with MTSEA-biotin in the absence (-) or presence of GA II 34 (+, 10 μ M; ++, 50 μ M). (b) Quantification of DAT bands in A and total DAT expression (data not shown) were determined using Image Studio (LI-COR). Surface samples were normalized to total DAT then expressed as a percent of GA II 34-treated samples (black bars) to the respective untreated samples (white bars). These data represent three independent experiments. Significant differences between treated and untreated samples were determined with a paired *t* test *, $p < 0.05$; **, $p < 0.01$.

Discussion

As DAT is the biological target responsible for the abuse liability of cocaine (Kuhar, Ritz, and Boja 1991), several high affinity DAT selective ligands have been developed and tested for the purpose of treating cocaine addiction. Despite substantial effort, there are currently no FDA-approved cocaine-abuse pharmacotherapies (Kim and Lawrence 2014) as the major obstacle with developing DAT antagonists is that they often have pharmacologies similar to cocaine. However, with the advent of the benztropine class of DAT antagonists came the development of compounds that do not demonstrate cocaine-like behavioral profiles (Agoston, Wu, et al. 1997; Katz et al. 2004). These findings suggest that the altered chemical structure of benztropine compared to cocaine results in distinct interactions with DAT that may account for the different pharmacological and behavioral profiles.

To address whether benztropine binds to DAT in a manner that is different from that of cocaine, our groups have developed irreversible binding tropane and benztropine analogs to probe specific sites of ligand interaction (Vaughan et al. 1999; Vaughan et al. 2007; Parnas et al. 2008; Dahal et al. 2014; Pramod et al. in preparation). Previously, we provided evidence that adduction of [¹²⁵I]GA II 34 occurred at a site located within TMs 1-2 (Vaughan et al. 1999) and in the present study we narrowed the site of AIP incorporation to residues Asp-79 or Leu-80 as well as directly demonstrated binding of the benztropine pharmacophore in the central, S1 binding site. As [¹²⁵I]GA II 34 binds near or at Asp-79, a residue vital for the transport of DA (Penmatsa, Wang, and Gouaux 2015) and one that retains 85% homology in the cocaine-sensitive monoamine transporters (Amara and Kuhar 1993), it is likely that a salt-bridge forms between Asp-79 and the tropane nitrogen of GA II 34, an interaction that is duplicated by cocaine and its analogs (Beuming et al. 2008; Dahal et al. 2014; Pramod et al. in preparation).

Furthermore, the near overlap of computationally docked [¹²⁵I]GA II 34 and [¹²⁵I]MFZ 2-24 in a homology model of hDAT (Pramod et al. in preparation, data not shown) supports binding of GA II 34 to a site overlapping that of cocaine.

Prior to the development of the photoaffinity ligand [¹²⁵I]GA II 34, its precursor GA 103, which is not iodinated nor does it have an azido group, was evaluated extensively. This compound demonstrated high affinity and selectivity for DAT, but did not significantly increase locomotor activity in mice (Agoston, Wu, et al. 1997). Furthermore, in rats trained to discriminate cocaine from saline, there was no GA 103 dose-related increase on the cocaine-appropriate response key. Based on these data as well as the ability of [¹²⁵I]GA II 34 to bind to DAT with an affinity equipotent to cocaine (160 nM (Vaughan et al. 1999) compared to 187 nM (Katz et al. 2001)), it was originally suggested that [¹²⁵I]GA II 34 exerts its non cocaine-like effects by binding to a site in DAT distinct from cocaine (Vaughan et al. 1999). As our data suggests otherwise, by supporting a shared binding site, the next step in explaining the varied behavioral profiles of benzotropines and cocaine, which are likely not a result of the antihistaminic and antimuscarinic properties of benzotropines (Newman and Katz 2008), is to identify distinct S1 residues (or S2 residues, as [¹²⁵I]GA II 34 protected Trp-84 from MTS modification) in DAT that preferentially interact with [¹²⁵I]GA II 34. In contrast to previous SCAM analysis (Loland et al. 2008), our findings suggest that cocaine stabilizes an occluded DAT structure (Dahal et al. 2014) while cocaine analogs and [¹²⁵I]GA II 34 prevent closure of the extracellular gate thereby causing DAT to adopt a more extracellularly-facing conformation, results that may explain the altered behavioral profiles. Thus, though the binding sites overlap, understanding the distinct interactions of [¹²⁵I]GA II 34 with DAT in comparison to cocaine will help direct development of cocaine-abuse pharmacotherapies.

CHAPTER V

MEMBRANE POTENTIAL SHAPES REGULATION OF DOPAMINE TRANSPORTER TRAFFICKING AT THE PLASMA MEMBRANE

Introduction

Central nervous system dopaminergic (DAergic) neurotransmission is essential in multiple neurological functions, including cognition, extrapyramidal motor control, the reward pathway and attention (Schultz 2007; Nieoullon 2002; Koob and Volkow 2010; Jaber et al. 1996). In addition to the timing of vesicular release of dopamine (DA) and the expression profiles of G-protein-coupled DA receptors (Mundorf et al. 2000; Beaulieu and Gainetdinov 2011), one major regulator of DA signaling magnitude and timing is the DA transporter (DAT), which rapidly transports extracellular DA into the intracellular space for vesicular re-packaging or effluxes DA through reversal of DAT-mediated transport (Jaber et al. 1997; Sitte et al. 1998). Commonly abused psychotropic drugs, amphetamine (AMPH), methamphetamine and cocaine achieve their effects either by inducing DA efflux through DAT and/or blocking DA uptake (Kahlig et al. 2005; Khoshbouei et al. 2003; Amara and Sonders 1998).

The physiological function of DAT to remove DA is coupled to the translocation of one Cl^- and two Na^+ ions (Sitte et al. 1998; DeFelice and Galli 1998; Sonders et al. 1997), and can even function in the absence of substrate, conducting an uncoupled, cocaine-sensitive, depolarizing current under physiological conditions (Sonders et al. 1997; Ingram, Prasad, and Amara 2002), which is increased in hyperpolarized states (Khoshbouei et al. 2003). In addition to direct modulation of transport function, DAT density at the cell membrane, and

therefore its functional capacity, is also dynamic. Regulated trafficking mechanisms control surface-membrane DAT levels under physiological conditions (Schmitt and Reith 2010; Mortensen and Amara 2003) and in response to DAT substrates (Schmitt and Reith 2010; Mortensen and Amara 2003), thus having an impact on DA homeostasis. Cell signaling molecules involved in the regulation of DAT trafficking range from protein kinase C (PKC) (Pristupa et al. 1998; Sorkina et al. 2005), mitogen-activated protein kinase (Morón et al. 2003) to Akt (Wei et al. 2007) among others (Schmitt and Reith 2010; Mortensen and Amara 2003) and determine the presence of DAT in regulated or constitutive pools segregated to specific membrane microdomains (Cremona et al. 2011; Adkins et al. 2007; Sakrikar et al. 2012). Many DAT substrates also influence DAT trafficking (Schmitt and Reith 2010; Kahlig and Galli 2003; Zahniser and Sorkin 2004), including DA and AMPH, which decrease DAT surface density (Chi and Reith 2003; Zahniser and Sorkin 2009; Saunders et al. 2000), and cocaine, which increases DAT surface expression (Daws et al. 2002).

Interestingly, AMPH's effects are twofold, as it causes DAT internalization (Chi and Reith 2003; Zahniser and Sorkin 2009; Saunders et al. 2000) and a DAT-dependent membrane depolarization (Sonders et al. 1997; Ingram, Prasad, and Amara 2002), which suggests an influence on DAT trafficking via a voltage-dependent mechanism in addition to DAT phosphorylation. Indeed, previous studies using striatal synaptosomes have revealed a reduction in DA uptake in depolarized (elevated KCl) conditions (Woodward et al. 1986; Holz and Coyle 1974), while in vitro preparations have suggested elevated DAT function at hyperpolarized states (Sonders et al. 1997). However, it is not known whether these changes in functional capacity arise from changes in ionic driving forces, essential for DA transport, changes in DAT protein presence at the membrane or both. While changes in the cell membrane voltage state are only

typically considered in terms of neurotransmitter release, action potential generation and timing or in the activity of voltage-sensitive transmembrane proteins, it is possible that changes in membrane potential (MP) alone may rapidly and reversibly affect DAT trafficking to and from the cell surface. Here we use confocal and total internal reflection fluorescence microscopy (TIRFM), biochemistry, electrophysiology and optogenetics to demonstrate the degree to which surface-membrane DAT levels are shaped by and sensitive to MP changes.

Methodology

Cell Culture

Cell lines. HEK cells overexpressing FLAG-tagged or YFP-tagged human DAT (hDAT), HEK FLAG-DAT (Hastrup, Karlin, and Javitch 2001; Hastrup, Sen, and Javitch 2003) or YFP-DAT HEK (Kahlig, Javitch, and Galli 2004), respectively, were a generous gift from Dr. Jonathan Javitch (Columbia University) prepared from HEK293 EM4 as previously described (Goodwin et al. 2009; Eshleman et al. 1994). The addition of the YFP tag and FLAG epitope to hDAT is a widely used construct and has not been shown to alter basic functional properties of the transporter or other transporter-mediated activity (Kahlig and Galli 2003; Hastrup, Karlin, and Javitch 2001; Hastrup, Sen, and Javitch 2003; Goodwin et al. 2009; Saha et al. 2014). HEK cells were maintained in DMEM supplemented with 10% fetal bovine serum (FBS), 5% L-glutamine, penicillin ($50 \mu\text{l ml}^{-1}$) and streptomycin ($50 \mu\text{l ml}^{-1}$) at 37°C and 5% CO_2 . Cells were typically passaged and/or used for electrophysiology or imaging experiments after reaching 60–80% of full confluency (every 2–3 days). To induce expression of constructs not stably expressed in HEK cell lines, HEK293 EM4 cells were transfected using a standard calcium phosphate protocol. Transfected cells were used in experiments 12–36 h after transfection.

Midbrain primary neuron culture. All animals used were housed in the University of Florida's McKnight Brain Institute animal care facility, an Association for Assessment and Accreditation of Laboratory Animal Care International-accredited facility. The University of Florida's Institutional Animal Care and Use Committee approved of all procedures undertaken. Primary cultures of the ventral midbrain containing DAergic neurons were prepared as previously described (Kahlig et al. 2005; Saha et al. 2014; Fog et al. 2006) and are described here in brief. The ventral midbrain, including DA neuron-rich regions, was acutely dissociated and isolated under sterile conditions from 0- to 2-day-old C57Bl/6J mice of both sexes and incubated at 34–36 °C under continuous oxygenation for 30 min in a dissociation medium, containing (in mM): 116 NaCl, 5.4 KCl, 26 NaHCO₃, 25 glucose, 2 NaH₂PO₄, 1 MgSO₄, 1.3 cysteine, 0.5 EDTA, 0.5 kynurenic acid and containing 20 units ml⁻¹ papain. Subsequently, tissue was triturated with fire-polished Pasteur pipettes in glial medium, containing (in %): 50 MEM, 38.5 FBS, 7.7 penicillin/streptomycin, 2.9 D-glucose (45%) and 0.9 glutamine (200 mM). Dissociated cells were pelleted at 450g for 10 min and were re-suspended in glial medium. Cells were plated on 12-mm round coverslips placed in 35 × 10 mm style tissue culture Petri dishes or glass-bottom 35 × 10 mm (MatTek, Ashland, MA) coated with 100 µg ml⁻¹ poly-D-lysine and 5 µg ml⁻¹ laminin. One hour after plating, the medium was changed to neuronal medium, containing (in %): 2 MEM, 75 Ham's-F12 medium, 19 heat-inactivated horse serum, 2 FBS, 1.56 D-glucose (45%), 0.04 insulin (0.025 g ml⁻¹) and 0.4 apotransferrin (50 mg ml⁻¹). Neuronal cultures were transfected with TAGFP-T-DAT, CFP-DAT and/or Arch-YFP constructs via nucleofection (Mouse Nucleofector Kit, programme O-005, Lonza Group Ltd, Basel, Switzerland) immediately before plating or via calcium phosphate 3–5 days after plating using standard protocols. All cultures were used at 7–9 days in vitro (DIV) and 4–9 days post

transfection. No difference between transfection methodologies was observed regarding protein expression level and/or function.

Plasmid Constructs

The plasmid coding for the cyan fluorescent protein-tagged DAT was described previously (Sorkina et al. 2003; Miranda et al. 2005) and was provided as a generous gift from Dr. Alexander Sorkin (University of Pittsburgh). The RFP-tagged hDAT (TagRFP-T-DAT) (Gabriel et al. 2013), generated as previously described, was a gift from Dr. Haley Melikian (University of Massachusetts), and the construct for fatty-acid receptor GPR40-eYFP driven by the cytomegalovirus promoter was a gift from Dr. Sergei Zolotukhin and Seth Currin (University of Florida). DsRed-Rab11 WT (Choudhury et al. 2002), a recycling endosome marker, was a gift from Richard Pagano (Mayo Clinic and Foundation, Addgene plasmid #12679). TagRFP-T-EEA1 (Navaroli et al. 2012), an early endosome marker, was provided by Silvia Corvera (University of Massachusetts Medical School, Addgene plasmid #42635). The GFP-C1-CAMKII α -K42R (Shen and Meyer 1999) was a gift from Tobias Meyer (Stanford University, Addgene plasmid #21221), and the pTfR-PAmCherry1 (Subach et al. 2009) plasmid was a gift from Vladislav Verkhusha (Albert Einstein College of Medicine, Addgene plasmid #31948). To confer optical control of MP hyperpolarization, neuronal cultures were transfected with AAV-CaMK α -eArch 3.0-EYFP plasmid, a generous gift from Dr. Karl Deisseroth (Stanford University). Arch was chosen for its ability to induce large magnitude H⁺-current-hyperpolarizing shifts (10–50 mV) in the neuronal MP, which were relatively stable over seconds to minutes with minimal decay when continuously activated (Mattis et al. 2012; Zhang et al. 2011).

Electrophysiology

HEK cells and cultured neurons were visualized with a $\times 60$ objective on an inverted Nikon Ti Eclipse microscope (Nikon, Melville, NY). All currents and MPs were recorded via an Axoclamp 200A amplifier using the whole-cell configuration after forming a high-resistance seal in the cell-attached configuration ($>1\text{ M}\Omega$). All signals were digitized with a Digidata 1440A at 10 kHz, and a 5-kHz low-pass Bessel filter was applied during acquisition. An additional 2-kHz Gaussian filter was applied to all traces for presentation only. The standard external solution for electrophysiology experiments using HEK cells was the same used in all microscopy and biochemistry experiments and contained (in mM) the following: 130 NaCl, 10 HEPES, 34 Dextrose, 1.5 CaCl₂, 0.5 MgSO₄ and 1.3 KH₂PO₄, with a pH of 7.35 and osmolarity of 275–290 mOsm. Pipettes for whole-cell recordings were pulled from borosilicate glass on a P-2000 laser-based puller (Sutter Instruments, Novato, CA). Pipettes used for recording the MP (3–6 M Ω) were filled with an internal solution containing (in mM) the following: 130 K-gluconate, 10 KCl, 10 HEPES, 1 EGTA, 2 MgCl₂ adjusted to pH 7.35 and osmolarity of 262 mOsm. For recording of DAT-mediated whole-cell currents, pipettes were filled with (in mM) the following: 120 CsCl, 30 dextrose, 10 HEPES, 1.1 EGTA, 2 MgCl₂ and 0.1 CaCl₂ adjusted to pH 7.35 and osmolarity of 264 mOsm. Recordings were performed at 37 °C. For determining DAT-mediated current and IV changes at different holding potentials, a stable IV (–100 to +40 in 20 mV steps) was generated after 5 min of continuously holding the cell at the given potential (–60, –40 or +20 mV), and then the DAT blocker GBR12935 (20 μM) was added to the bath and subsequent IVs were measured every 30–60 s. To determine the DAT-mediated current amplitude, the IV in the presence of GBR12935 (Fig. 39c; protocol #2; grey traces) was subtracted from the preGBR12935 IV following the prolonged clamp of the MP (Fig. 39c; protocol #1; red=+20 mV,

black= -40 mV, blue= -60 mV) to yield the DAT-mediated (GBR12935-sensitive) current at each voltage step of the IV (the curve displayed in Fig. 39d) corresponding with manipulation of the MP state in previous TIRFM experiments (Fig. 38). For statistical comparisons between groups (Fig. 39e,f), the DAT-mediated current (pre-GBR12935–post-GBR12935 amplitude) at the -100 mV step, where DAT-mediated current is largest, was used.

For recording and imaging of DAergic neurons in primary culture, the external solution contained (in mM) the following: 146 NaCl, 5 HEPES, 5 KCl, 30 Dextrose, 2.5 CaCl₂ and 1.2 MgCl₂, with pH 7.35 and had an osmolarity of 290–300 mOsm. Patch pipettes (4–6 M Ω) were filled with an internal solution containing the following (in mM): 135 K-gluconate, 5 KCl, 2 MgCl₂, 10 HEPES, 0.1 EGTA, 2 Mg-ATP and 0.2 Na-GTP, pH adjusted to 7.35 and osmolarity of 270 mOsm. Recordings of the neuronal MP were corrected offline for a calculated liquid junction potential of 16.1 mV. All recordings occurred at 37 °C.

Microscopy

All microscopy analyses were performed at 37 °C, and cells were washed twice with external solution as described above before all experiments. For all imaging experiments, cells/neurons were set on 35-mm glass-bottom dishes (MatTek, Ashland, MA) with glass thickness of 0.13–0.16 mm (TIRFM) or 0.085–0.13 mm (confocal). Wide-field fluorescence images were acquired identically to TIRFM images; however, a Lambda LS Xenon Arc Lamp provided the light source that bypassed the additional TIRFM mirror set and was passed through appropriate excitation (Ex)/emission (Em) filters and dichroic mirror. Microscopy data were analyzed in the Nikon's NIS Elements software.

TIRFM. TIRFM imaging of HEK cells and neurons plated on poly-d-lysine-coated dishes was performed at 37 °C using Nikon Eclipse TE-2000-U inverted microscope, with a $\times 60$

1.49 numerical aperture (NA) objective and equipped with a multiline solid-state laser system (470, 514 and 561 nm) and appropriate filter combination for YFP (Ex: 514 nm/Em: 535 nm), TagRFP (Ex: 561 nm/Em: 584 nm) and CFP (Ex: 445 nm/Em: 475 nm), similar to as previously described (Saha et al. 2014). TIRFM was achieved via the 'through-the-objective' laser guidance method with the laser incident angle set to 76° , which is greater than the critical angle of 62° and generated an evanescent field depth between 66 and 72 nm depending on the wavelength of light used. Temperature control was maintained with a stage and an objective heater (20/20 Technology Inc.). Image exposure time was coupled with laser excitation duration at 200–300 ms, and laser intensity was maintained at 40–60% of maximum intensity, but neither changed throughout the course of a given experiment. Images were detected digitally using an attached CoolSNAP HQ2 CCD camera and stored on a computer hard drive at 5–10-s intervals. For imaging of HEK cells, baseline images were acquired during perfusion of standard external solution before changing the solution to 100-mM KCl-based external solution (osmotically balanced) or 10 μ M AMPH, prepared as described above, or throughout the entirety of being held in the whole-cell configuration. For simultaneous patch-clamp and TIRFM, membrane-holding potentials of +20, –40 and –60 mV were determined in preliminary experiments to approximate endogenous resting potential of these cells (–40 mV), to mimic the effects of 100-mM KCl depolarization (+20 mV) and to oppose depolarizing effects of +20 mV with a similar magnitude of change (–60 mV).

For quantification of cell-surface fluorescence intensity of isolated HEK cells and primary culture neurons, regions of interest were created, including the TIRFM footprint of each HEK cell in its entirety or the neuron's soma. For all image sequences, a background ROI similar to the size of a cell was placed in a region devoid of cells/fluorescence and was subtracted from

the entire image and recalculated for each frame. The mean intensity (in arbitrary fluorescent units) over time was monitored and plotted/analyzed as a fraction of the baseline intensity (the mean raw intensity of all frames within 30–60s before initiation of indicated manipulation) and used for analysis. Bleaching was controlled for in two ways. The first was the inclusion of a vehicle group and/or non-patched adjacent cells for each assay appropriately. However, because of relatively large observed cell-to-cell variability in the change in baseline fluorescence over time ranging from -3.0 to $+2.1\%$ per min (average $0.4 \pm 0.3\%$ per min), a correction factor or rate was determined for each cell and was used to account for this change in each cell. Since the bleaching rate with the current TIRFM imaging parameters was linear, a linear fit was generated for 120 s before a solution change and was used to determine that the rate of bleaching was extrapolated over the entire 12–15 min experiment. This projected rate of change in fluorescence intensity due to bleaching was then accounted for during each experiment.

Confocal microscopy and JHC 1-064 labeling of DAT. Imaging of YFP-DAT (Ex: 514 nm, Em: 540/30 nm), mCherry, dsRed and JHC 1-064 (all Ex: 561 nm, Em: 585/65 nm) was performed using the Nikon A1R confocal system mounted on a Nikon Eclipse Ti-E inverted microscope (Nikon) using a $\times 60$ 1.49 NA Plan-Apo objective (Nikon). For YFP-DAT and endosome co-localization experiments, YFP-DAT HEK cells grown on glass-bottom dishes and transfected with TagRFP-T-EEA1 or DsRed-Rab11 were treated with either 100 mM KCl for 5 min, 10 μ M AMPH for 1 h or with standard external solution vehicle throughout all the experiments at 37 °C. After the treatment, the dishes were placed on ice and washed with the ice-cold standard external solution, then washed two more times with ice-cold PBS solution and then fixed in 3.7% paraformaldehyde. Cells were then washed and imaged using identical imaging parameters (for example, laser power, gain, and so on) immediately in PBS. For co-localization

analysis, a region of interest (ROI) was drawn over the intracellular space of each cell in the raw image and the Pearson correlation coefficient for the two channels was calculated on a cell-by-cell basis in NIS Elements (Nikon). For clarity and image display only, a single-count 3×3 pixel matrix smooth was applied, and intensity of all pixels was enhanced by 40%.

The fluorescent cocaine analogue, JHC 1-064, which has a high affinity for DAT, was used as previously described to selectively label membrane-resident DAT (Cha et al. 2005; Eriksen et al. 2009; Eriksen et al. 2010; Rickhag et al. 2013). When YFP-DAT HEK cells had reached 60–80% confluency after 2–3 days or midbrain primary culture neurons had reached DIV 5, they were washed twice with the appropriate standard external solution and incubated with 10–20 nM JHC 1-064 for a minimum of 30 min at 4 °C. After at least 30 min, the JHC 1-064-containing solution was removed and replaced with fresh 4 °C external solution. Immediately, the dish was placed on the stage, and cells were selected and a baseline image was acquired. Following acquisition, the cold solution was removed and replaced with either vehicle or KCl-based external solution at 37 °C, and images were acquired every 5 min. Imaging parameters (for example, laser power, gain, pinhole, and so on) were identical for images of HEK cells and were within the imaging series of each neuron. For analysis of JHC 1-064/DAT complexes in HEK cells, an area devoid of cells was selected and used as a background ROI, and the mean pixel intensity of this region was subtracted from intensity of all pixels. For determination of the mean intracellular intensity, an ROI was drawn within the boundaries of each cell and the mean intensity (normalizing for changes in cell size) was again normalized to the intensity of the entire image to account for bleaching and was plotted as a fraction of the initial internal fluorescence in the original control 4 °C image (Kahlig et al. 2006). For manual

counts of intracellular JHC 1-064 puncta and clarity for display (Fig. 36 and 42), all images were processed identically.

Depolarization-induced Ca^{2+} influx. Neuronal intracellular free calcium [Ca^{2+}], was measured using cell-permeant, ratiometric calcium dye Fura-2 AM (Life Technologies). Primary culture of midbrain neurons were washed twice with 37 °C external solution supplemented with 1% bovine serum albumin (fatty acid free). Neurons were then incubated in external solution containing 5 μM Fura-2 AM in dark at 37 °C for 40 min. Cultures were then washed twice with supplemented external solution and incubated at 37 °C for another 20 min in either external solution (control) or external solution containing KN93 (10 μM) or KN92 (10 μM). KN93 or KN92 were also present in the bathing solution throughout subsequent imaging. The neurons were then incubated for another 10 min under continuous perfusion of standard external before switching the bath perfusion to 100 mM KCl-based external, all at 37 °C on an inverted Nikon TE2000-E microscope, before starting the imaging using a CoolSNAPHQ2 camera and 40x, 1.3 oil immersion Plan Fluor objective lens. The Fura-2 dye was excited using excitation wavelengths of 340 nm (for Ca bound Fura-2) and 380 nm (for free Fura-2) and emission detected at single wavelength of 510 nm with images collected at 1Hz. Both image acquisition and analysis were done using Nikon Elements Advanced Research imaging software (Nikon Instruments) and data were quantified in a ratiometric manner and normalized to basal values.

Biotinylation Assay

For biotinylation assays, YFP-DAT HEK cells or parental HEK293 cells were plated on 24-well poly-D-lysine-coated plates at a density of 2×10^5 cells per well and transfected with either GFP-C1-CaMKII α -K42R or pTfR-PAmCherry1, as previously described (Dahal et al. 2014). Forty-eight to ninety-six hours after plating, cells were pre-treated (30 min) with external

solution (vehicle) or 80 μ M Dynasore, followed by 30 min treatment with vehicle, vehicle+10 μ M KN92 or vehicle+10 μ M KN93. Cells were then washed and treated for 5 min with either vehicle, 10 μ M AMPH, 2.5 μ M PMA, iso-osmotic 50 mM KCl, iso-osmotic 100 mM KCl, 100 mM KCl+KN92 or 100 mM KCl+KN93. Cell-surface proteins were then biotinylated and analyzed via western blot analysis as described previously (Felts et al. 2014). Total protein concentrations for each sample were determined using the Pierce BCA protein assay kit (Thermo Scientific), and the resulting values were used to load equal amounts of protein for each sample when conducting SDS-PAGE. Blots of total and surface protein were probed with an N-terminal-targeted anti-DAT monoclonal antibody (1:1,000; mAb 16 (Foster et al. 2003); a gift from Dr. Roxanne Vaughan of the University of North Dakota) or an anti-transferrin receptor antibody (1:1,000; C2F2, BD Biosciences), and the density of the immunoblot bands was quantitated using ImageJ (NIH) or Image Studio (LI-COR). Prism5 (GraphPad) was used for statistical analysis following normalization of surface values to vehicle and determination of the vehicle variance by normalizing to AMPH.

Drug/Solution Application and Optical Stimulation

In electrophysiology, microscopy and biochemistry experiments, increased KCl concentrations (100 mM) were achieved by replacing NaCl in the standard external solution or ACSF with KCl in an equa-molar manner, conserving osmolarity. For TIRFM imaging of HEK cells, vehicle (standard external solution), the KCl-based external solution or 10 μ M AMPH was applied via bath perfusion using a laminar flow insert for 35-mm Petri dishes at a rate of 2 ml min⁻¹. For neuronal recordings and TIRF microscopy, vehicle or KCl-based external solution was applied via pressure (2 psi) injection from a pipette identical to recording pipettes positioned 20 μ m from the cell body. HEK293 or YFP-DAT HEK cells were exposed to either

80 μ M Dynasore (Gabriel et al. 2013) (Thermo Fisher Scientific), 10 μ M KN92, 10 μ M KN93 or 10 μ M BIM (all from EMD Millipore) for 25–30 min before and throughout treatment with vehicle or 100 mM KCl to maintain the respective inhibition of dynamin, CaMK and PKC throughout each imaging or biotinylation experiment as indicated.

For steady-state photo-activation of eArch3.0 in cultured neurons, 590-nm light was generated from a light-emitting diode (LED) source (Thorlabs) and coupled to an optical fibre and placed at a 45° angle, with the tip 150–200 μ m from the cell body. The output at the fibre tip (200 μ m diameter) was regulated via a potentiometer on the externally-triggered LED driver and was calibrated so that the light power density at the tip was 15 mW mm⁻². Changes in MP in response to eArch 3.0 activation were determined by taking the average MP over 50 ms before light onset and the last 50 ms of a 1-s light pulse.

Data Analysis

All data were analyzed with Microsoft Excel, IBM SPSS, Prism5 or Igor Pro. Statistical analyses used for comparison are identified in the legend, and all values are the mean \pm s.e.m., unless otherwise stated.

Results

MP Depolarization Reduces Membrane DAT Levels

AMPH-mediated activation of DAT induces a depolarizing DAT-mediated Na⁺ current and simultaneously causes internalization of cell-surface-membrane DAT (Ingram, Prasad, and Amara 2002; Saunders et al. 2000). To determine whether AMPH-induced DAT internalization was the result of a psychostimulant-specific action or may be, in part, due to activation of voltage-sensitive mechanisms, we performed live cell TIRFM of yellow fluorescent protein-tagged DAT (YPF-DAT) in Human Embryonic Kidney (HEK) cells when perfused with only

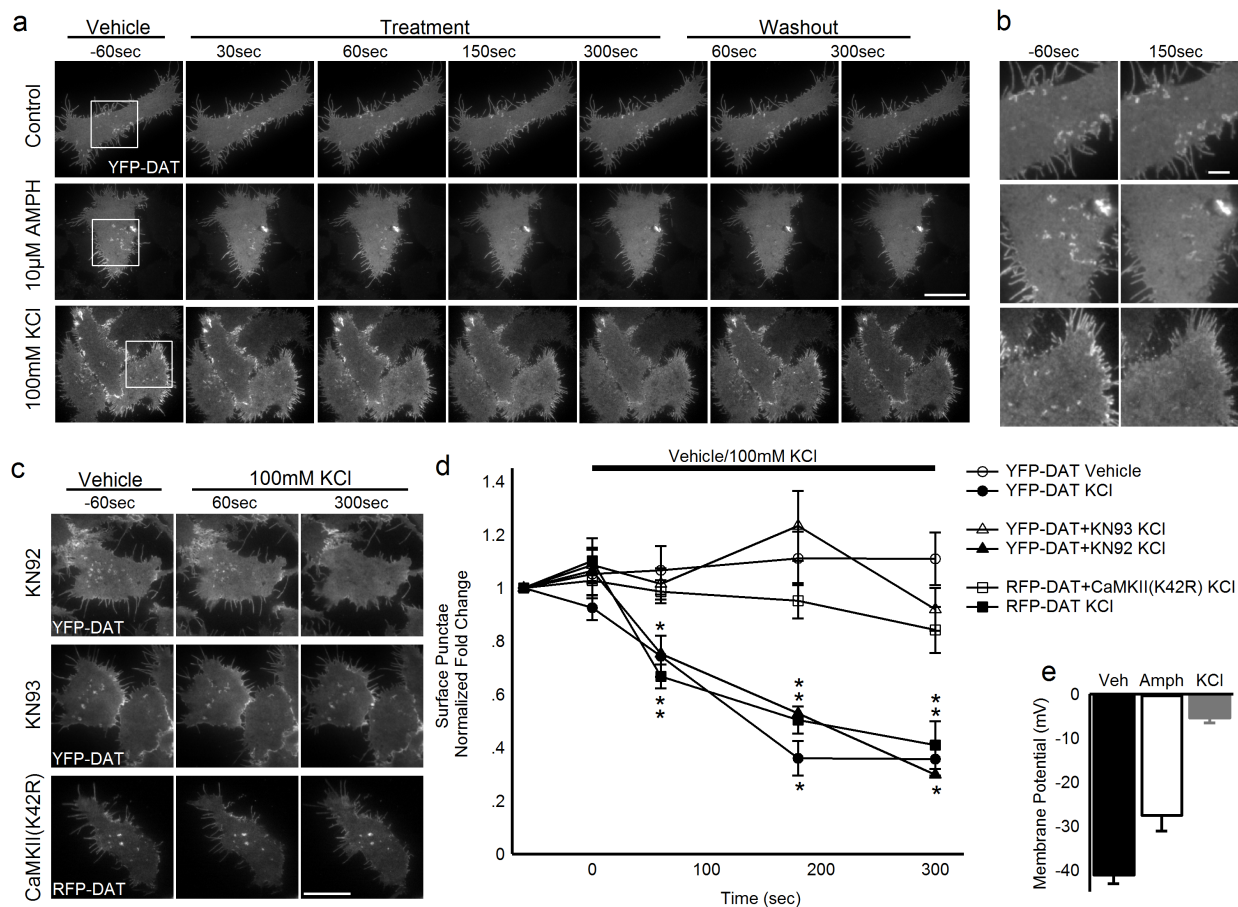


Figure 30. Depolarization causes CaMK-dependent reduction of membrane YFP-DAT levels in HEK cells. (a) Representative live cell sequential TIRF microscopy images of YFP-DAT HEK cells 60 s before and throughout 5 min perfusion with vehicle (standard external solution, top row), 10 μ M amphetamine (middle row; $N=5$, $n=14$) or depolarizing 100 mM KCl-based external solution (bottom row) followed by a 5 min washout period. Scale bar, 20 μ m. (b) Enlarged insets corresponding to boxes in left-most column before and 150 s after vehicle (top pair), 100 mM KCl (middle pair) and 10 μ M amphetamine (bottom pair). Scale bar, 5 μ m. (c) TIRF microscopy images of YFP-DAT HEK cells 60 s before and throughout 5 min perfusion, with 100 mM KCl pre-incubated with 10 μ M KN92 (top), 10 μ M KN93 (middle) or expressing a kinase-inactive CaMKII-K42R. Scale bar, 20 μ m. (d) Mean \pm s.e.m. normalized fold change in number of YFP-DAT puncta per cell when perfused with vehicle (open circles; $N=5$, $n=17$), 100 mM KCl only (closed circles; $N=6$, $n=14$), 100 mM KCl when pre-incubated and perfused with 10 μ M KN92 (closed triangles; $N=5$, $n=12$) or 10 μ M KN93 (open triangles; $N=6$, $n=23$) and RFP-DAT puncta expressed alone (closed squares; $N=9$, $n=9$) or co-expressing a kinase-inactive GFP-CaMKII-K42R (open squares; $N=10$, $n=12$) during 100 mM KCl perfusion. (e) Mean \pm s.e.m. steady-state membrane potential of YFP-DAT HEK cells perfused with vehicle, 10 μ M amphetamine or 100 mM KCl ($n=5-7$ cells per group). Using independent samples t -test $*P<0.05$ for comparison of 100 mM KCl effects with respective controls.

extracellular solution (vehicle), 10 μ M AMPH or 100 mM KCl (Fig. 30), which depolarized cells by 13.5 and 35.7 mV, respectively (Fig. 30e). The distribution of YFP (yellow fluorescent protein)-DAT at the cell membrane (TIRFM footprint) was unchanged throughout perfusion of vehicle, whereas 10 μ M AMPH noticeably altered the YFP signal in the TIRFM footprint within the first 60 s, causing a reduction in surface-membrane high-intensity regions and puncta that did not recover in washout (Fig. 30a,b and 31a), in line with previous reports at longer

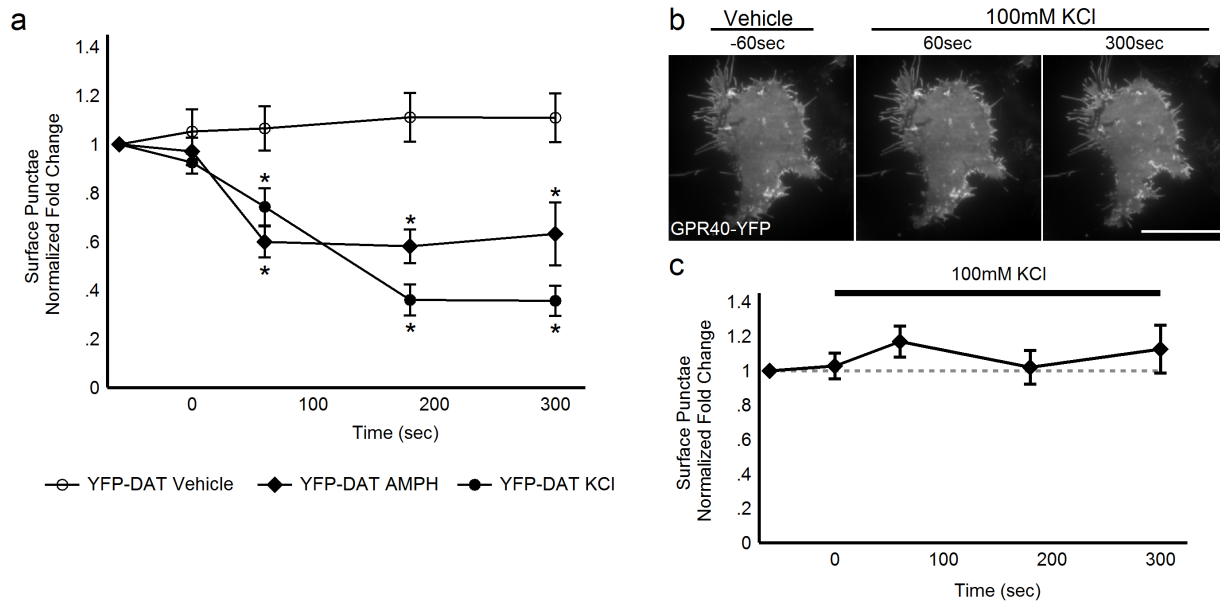


Figure 31. Amphetamine causes redistribution in membrane DAT and the GPCR, GPR40, is insensitive to depolarization-induced changes in membrane expression. (a) Timecourse plot of mean \pm s.e.m. normalized (to pre-KCl time point) number of membrane surface-resident YFP-DAT punctae before and during vehicle (open circles; $N=5$, $n=17$), 10 μ M amphetamine (diamonds; $N=5$, $n=14$) or 100 mM KCl (closed circles; $N=6$, $n=14$) bath application showing the amphetamine-induced loss of membrane DAT stabilizes after 2 min and is not as dramatic and depolarization-induced membrane DAT loss. $*P<0.05$ compared to control with independent samples t -test. **(b)** Distribution of the membrane G-protein coupled receptor, GPR40-eYFP, is unaffected by membrane depolarization. Live cell sequential TIRF microscopy images of GPR40-eYFP-transfected HEK cells 60 sec before and throughout 5 min perfusion with depolarizing 100 mM KCl-based external solution ($N=7$, $n=7$). Scale bar is 20 μ m. **(c)** Timecourse plot of mean \pm s.e.m. normalized (to pre-KCl time point) number of membrane surface-resident GPR40-eYFP punctae before and during 100 mM KCl bath application indicates the relative insensitivity of the trafficking of this naturally-occurring membrane protein to depolarization ($N=7$, $n=7$).

AMPH treatment durations (Sorkina et al. 2009). Similarly, depolarizing 100-mM KCl-based external solution significantly altered the YFP-DAT distribution in TIRFM footprint; however, the effects occurred rapidly, obvious within 30 s, and typically all YFP puncta and high-intensity regions were absent from the surface membrane after 3 min (Fig. 30a,b,d). In contrast to AMPH, treatment with KCl resulted in the return of YFP signal profile and the reappearance of YFP puncta immediately on washout (Fig. 30a). To determine the relative specificity of this effect of depolarization for DAT, we identically depolarized HEK cells transfected with an eYFP-tagged version of an unrelated naturally occurring membrane protein, GPR40 (La Sala et al. 2013), which had a membrane distribution similar to DAT, but its trafficking appeared insensitive to depolarization (Fig. 31b,c).

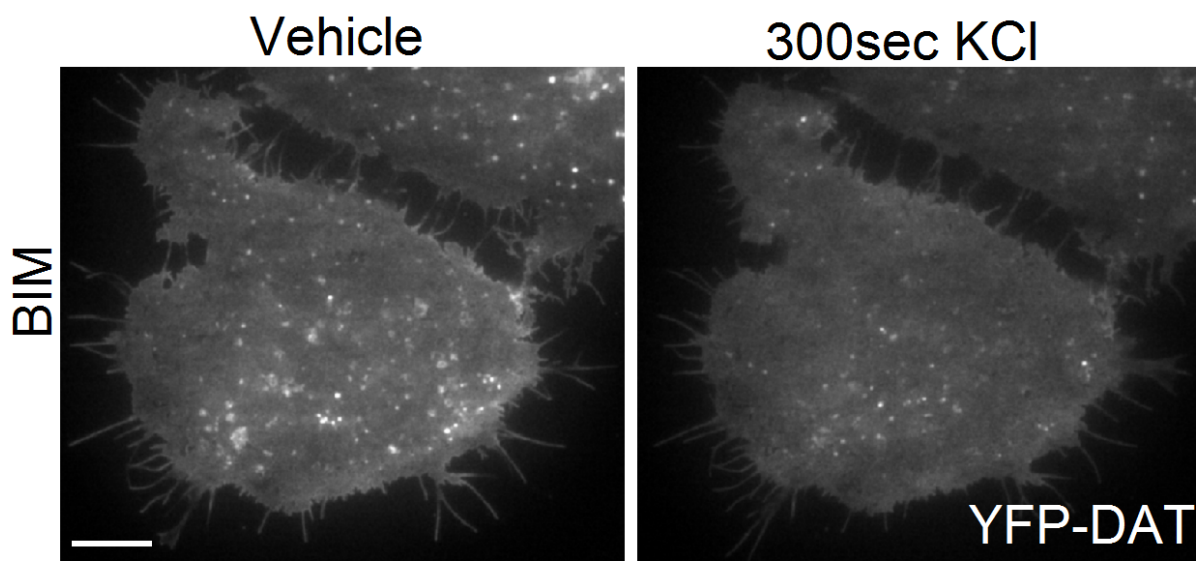


Figure 32. Depolarization-dependent redistribution of YFP-DAT is not PKC-dependent. Representative TIRF microscopy images of HEK YFP-DAT cells 60 sec before and throughout 5 min perfusion with 100 mM KCl pre-incubated with 10 μ M bisindolylmaleimide I (BIM; $N=4$, $n=8$). Scale bar is 10 μ m.

Since the depolarization induced by KCl will likely increase free $[Ca^{2+}]$ and trigger the activation of Ca^{2+} -dependent signaling molecules, we chose to determine the role of CaMKII and

PKC in initiating this depolarization-induced redistribution. The depolarization-induced loss of YFP-DAT signal did not appear affected by the PKC inhibitor, bisindolylmaleimide I (10 μ M; Fig. 32). However, the KCl depolarization-induced loss of YFP-DAT surface puncta was significantly reduced in the presence of the CaMK inhibitor KN93 (10 μ M) relative to the same treatment in the presence of the inactive homologue, KN92 (10 μ M; Fig. 30c,d), which produced results similar to KCl treatment alone (Fig. 30a–d). However, because of the KN93-induced attenuation of the depolarization-triggered Ca^{2+} influx (Fig. 33), we chose to biochemically

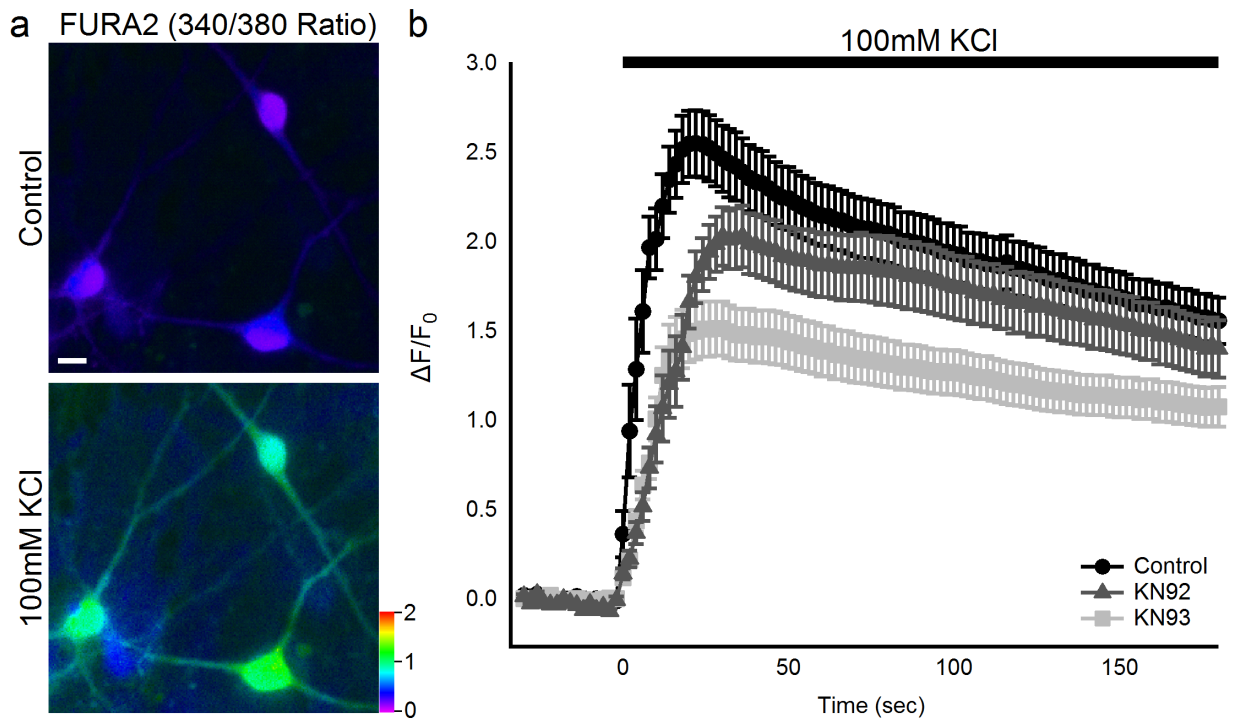


Figure 33. CaMKII inhibitor, KN93, attenuates but does not abolish depolarization induced Ca^{2+} influx. (a) Representative Fura-2 ratiometric (340 nm/380 nm) image of midbrain primary culture neurons before (top) and during the peak Ca^{2+} signal (bottom) evoked with bath application of 100 mM KCl in control conditions. Image color scale of raw ratio values for emission intensity excited by 340 nm/380 nm light. (b) Mean \pm s.e.m. normalized change in FURA2 fluorescence ($\Delta F/F_0$) ratiometric signal in response to 100 mM KCl-based external solution (black; control) and when the CaMKII inhibitor, KN93 (10 μ M; light gray), or its inactive homolog, KN92 (10 μ M; dark gray), are pre-incubated with the neuronal cultures and included in the bathing solution. The black bar indicates the administration of 100 mM KCl-based external solution. Values are mean \pm s.e.m. ($N=4-5$, $n=23-26$).

inhibit CaMKII α specifically and assess membrane DAT using TIRFM by co-expressing a kinase-inactive version of CaMKII α , a green fluorescent protein (GFP)-tagged K42R mutant and RFP (red fluorescent protein)-DAT. In response to KCl-induced depolarization, RFP-DAT alone behaved similarly to YFP-DAT; however, when GFP-CaMKII α -K42R was co-expressed, KCl treatment was unable to alter the membrane distribution of RFP-DAT (Fig. 30c,d). These changes in membrane DAT in response to depolarization (100 mM KCl application) and repolarization (washout) suggest that the MP state is capable of bidirectionally shaping the cell-surface distribution of DAT through activation of CaMKII α .

Membrane DAT Reduction is CaMKII α and Dynamin Dependent

To determine the degree to which real-time changes in the YFP-DAT TIRFM footprint were indicative of changes in DAT protein density at the cell membrane, a cell-surface biotinylation assay was used to quantify differences in membrane DAT protein levels. In YFP-DAT HEK cells, compared with vehicle treatment (100%, n=17), surface DAT (Fig. 34) was significantly reduced following a similar 5 min treatment as above with both 50 mM (62 \pm 6%, n=14) and 100 mM (70 \pm 5%, n=17) KCl-based external solution as well as the positive control treatments with AMPH (10 μ M; 59 \pm 7%, n=13) and the PKC agonist phorbol myristate acetate (PMA, 2.5 μ M; 53 \pm 5%, n=13). The CaMKII α dependency of this effect observed in TIRFM studies was also supported by biotinylation experiments (Fig. 34), wherein 100 mM KCl had little effect on membrane DAT protein when YFP-DAT HEK cells were transfected with the kinase-inactive, dominant-negative GFP-CaMKII α -K42R (105 \pm 11%, n=6) or in the presence of the CaMK inhibitor KN93 (10 μ M; 98 \pm 9%, n=9), whereas the inactive homologue KN92 did not significantly block the KCl-dependent reduction in surface DAT (10 μ M; 63 \pm 6%, n=12). To determine whether the reduction in membrane DAT distribution observed using TIRFM and

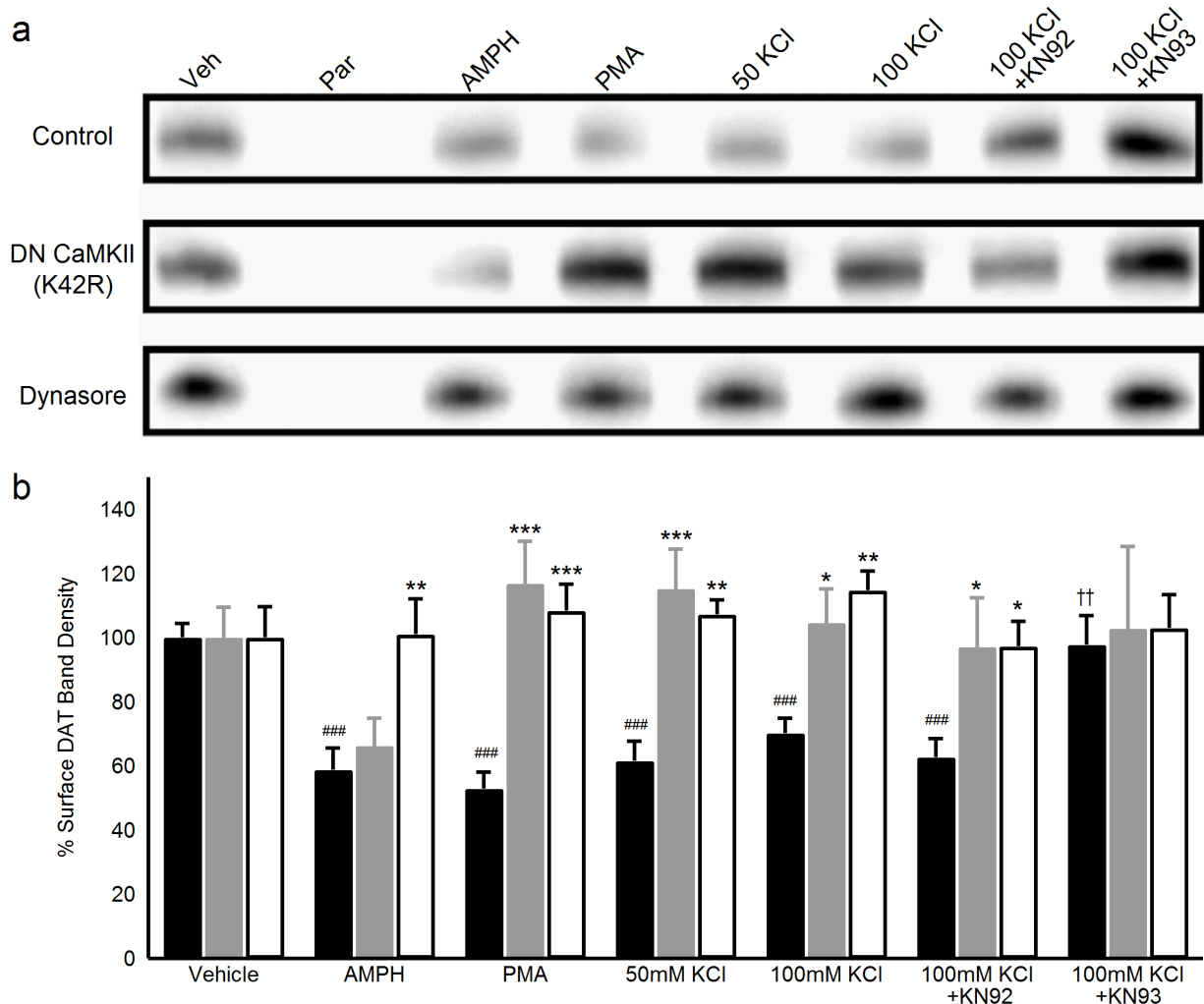


Figure 34. Depolarization-induced reduction in surface-membrane-biotinylated DAT is due to CaMKII-dependent endocytosis. (a) Representative western blots show the surface DAT present under each indicated condition. (b) Mean±s.e.m. DAT band density from YFP-DAT HEK cells (control, black bars) or YFP-DAT HEK cells transfected with GFP-C1-CAMKIIα-K42R (grey bars) or YFP-DAT HEK pre-treated (30 min) with external solution (vehicle) or 80 μM Dynasore (white bars), followed by 30 min treatment with vehicle, vehicle+10 μM KN92 or vehicle+10 μM KN93. Cells normalized to vehicle treatment from at least five independent experiments indicate that AMPH, PMA and depolarization-induced reduction in surface DAT are endocytosis-dependent (Dynasore-sensitive), and both PMA- and depolarization-induced internalization are CaMKIIα-dependent. Depolarization-induced internalization is sensitive to both pharmacological and molecular inhibition of CaMKII activity. A two-way analysis of variance (ANOVA) with Bonferroni *post hoc* test was performed to identify significant differences from control ($*P\leq 0.05$; $**P\leq 0.01$; $***P\leq 0.001$), a one-way ANOVA with a Dunnett's *post hoc* test to determine changes from vehicle treatment ($###P\leq 0.001$) and an unpaired *t*-test to compare KN92 and KN93 treatments ($††P\leq 0.01$). See text for number of experiments.

confirmed using biotinylation was a trafficking event, we evaluated the capacity for depolarization to induce a loss in surface DAT in the presence of Dynasore, a dynamin inhibitor (Gabriel et al. 2013). Indeed, inhibition of dynamin by Dynasore blocked depolarization- (115±6%, n=6), AMPH- (101±11%, n=6) and PMA-dependent (108±8%, n=6) internalization of DAT in HEK cells, whereas expression of CaMKIIα-K42R only blocked depolarization- and PMA-dependent (117±13%, n=6) but not AMPH-dependent (66±9%, n=6) internalization (Fig. 34). Importantly, treatment with 100 mM KCl did not alter surface levels of the native or overexpressed, membrane-resident transferrin receptor in comparison with vehicle control, providing further support for the specificity of depolarization-induced downregulation of membrane DAT (Fig. 35). Taken together, these data suggest that CaMKIIα- and dynamin-dependent pathways are involved in depolarization-dependent DAT trafficking at the cell membrane.

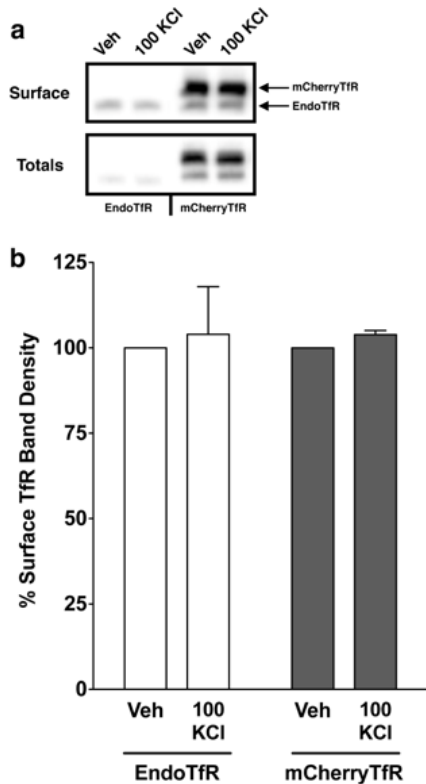


Figure 35. Membrane levels of the endogenous transferrin receptor (TfR) are unchanged upon membrane depolarization. (a) Representative Western blots show the surface and total TfR present when HEK-293 cells (left, EndoTfR) or HEK-293 cells transfected with a positive control pTfR-PAmCherry1 plasmid (right, mCherryTfR) were treated for 5 min with either standard external solution (veh) or 100 mM KCl-based external solution. (b) Mean±s.e.m. surface TfR band density from HEK-293 cells when normalized to vehicle treatment ($n=3$) indicate that surface levels of endogenous TfR or mCherry-tagged TfR are unchanged upon membrane depolarization ($n=3$). Arrows indicate endogenous and mCherry TfR as labeled.

MP Depolarization Internalizes JHC 1-064/DAT Complexes

Next, we used JHC 1-064 (Cha et al. 2005), a fluorescent cocaine analogue, to label cell membrane-resident DAT in HEK FLAG-DAT cells in conjunction with live cell confocal microscopy to investigate whether KCl-induced membrane depolarization would drive the internalization of cell-surface JHC 1-064/DAT complexes, an approach used previously to study DAT trafficking to defined endosome compartments in vitro (Fig. 36a) (Eriksen et al. 2009). In

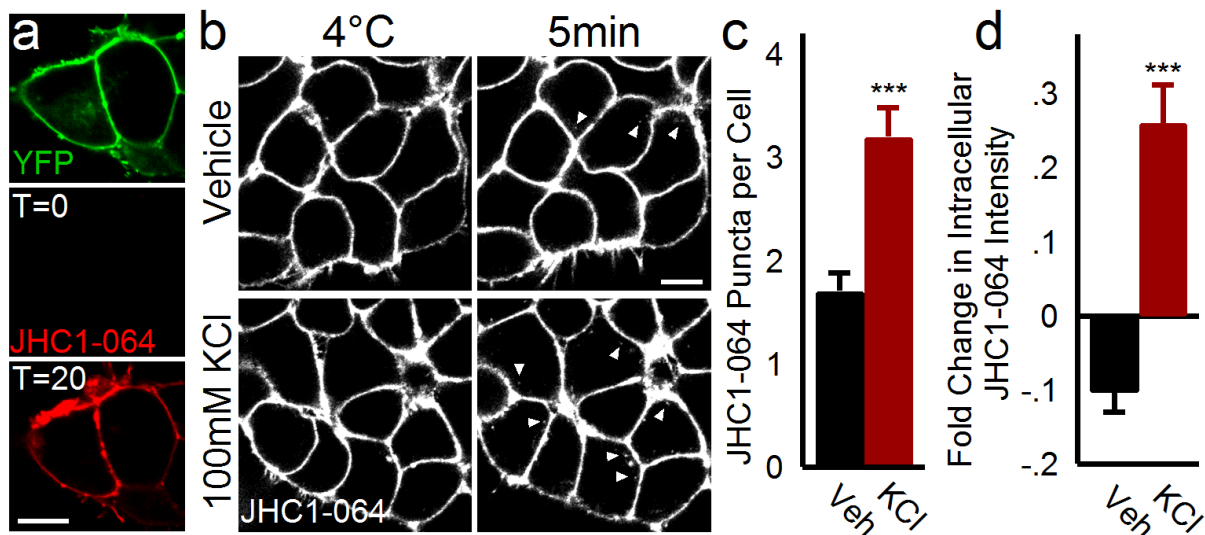


Figure 36. Membrane depolarization with KCl increases internalization of JHC 1-064/DAT complexes in HEK cells. (a) JHC 1-064 binds to surface DAT in HEK cells. Confocal image of YFP signal in YFP-DAT HEK cells (top), with no initial detectable fluorescence emitted between 553 and 617 nm when excited with 561 nm (bottom left, T=0 min) until after 20 min exposure to 10 nM JHC 1-064 (bottom right) corresponding with YFP fluorescence. (b) Representative confocal images of JHC 1-064/DAT labeling (white) at $\sim 4^\circ\text{C}$ and 5 min following solution change at 37°C . Note the increase at 5 min in the number of white intracellular puncta in the KCl condition. (c,d) Mean \pm s.e.m. number of individual JHC 1-064/DAT puncta per cell (c) and normalized (to 4°C) fluorescence intensity (d) in the intracellular space corresponding to vehicle ($N=3$, $n=69$, black bars) or 100 mM KCl-containing solution treatment ($N=3$, $n=85$, red bars). Independent samples *t*-tests were used to compare vehicle with KCl effects. Scale bars, 10 μm . *** $P<0.0001$ using independent samples *t*-test.

all cases, the presence of JHC 1-064/DAT complex puncta in the intracellular space was limited or nonexistent at 4°C (Fig. 36b). However, when changing bath temperature from 4 to 37°C with either vehicle or depolarizing (iso-osmotic) 100-mM KCl-based external solution (Fig. 36b–

d), the number of fluorescent punctate JHC 1-064/DAT complexes (Fig. 36c) and average intracellular fluorescence intensity (Fig. 36d) were significantly greater in depolarizing KCl-based external solution (3.2 ± 0.3 puncta per cell; normalized fold change in intracellular JHC 1-064 intensity: 0.26 ± 0.05) compared with vehicle (1.7 ± 0.2 puncta per cell; normalized fold change in intracellular JHC 1-064 intensity: -0.10 ± 0.05).

MP Depolarization Redistributes DAT into Early Endosomes

To determine the identity of the intracellular destination of depolarization-dependent internalized DAT, fluorescent versions of the endosome markers (which were not apparent at the cell membrane in TIRFM), EEA1 (TagRFP-T-EEA1) that marks early endosomes or the recycling endosome marker Rab11 (DsRed-Rab11), were expressed in HEK YFP-DAT cells and then treated with standard external solution (vehicle), iso-osmotic 100 mM KCl-based external solution for 5 min or 10 μ M AMPH for 5 min as a temporal comparison. Another time point of 60 min AMPH (10 μ M) treatment was used as a positive control as it has been shown previously to cause DAT internalization to specific endosomes (Sorkina et al. 2005; Hong and Amara 2013; Eriksen et al. 2010; Rao, Simmons, and Sorkin 2011), and would thus allow for comparability to previous work. Average Pearson correlation coefficients per cell for intracellular YFP-DAT and TagRFP-T-EEA1 or DsRed-Rab11 in vehicle (EEA1: 0.17 ± 0.01 ; Rab11: 0.19 ± 0.01) were significantly less than in cells treated with AMPH at 5 min for EEA1 (0.32 ± 0.03 ; Fig. 37a,b) and Rab11 (0.47 ± 0.06 ; Fig. 37c,d), while 60 min AMPH treatment increased YFP-DAT association with EEA1 (0.24 ± 0.01 ; Fig. 37a,b), but not Rab11 (0.22 ± 0.15 ; Fig. 37c,d). Similarly, depolarizing conditions significantly enhanced the co-localization of intracellular YFP-DAT with EEA1 (0.30 ± 0.02 ; Fig. 37a,b) over vehicle and 60 min AMPH treatments, although comparable to the 5 min AMPH treatment. The treatment had no effect on the degree of

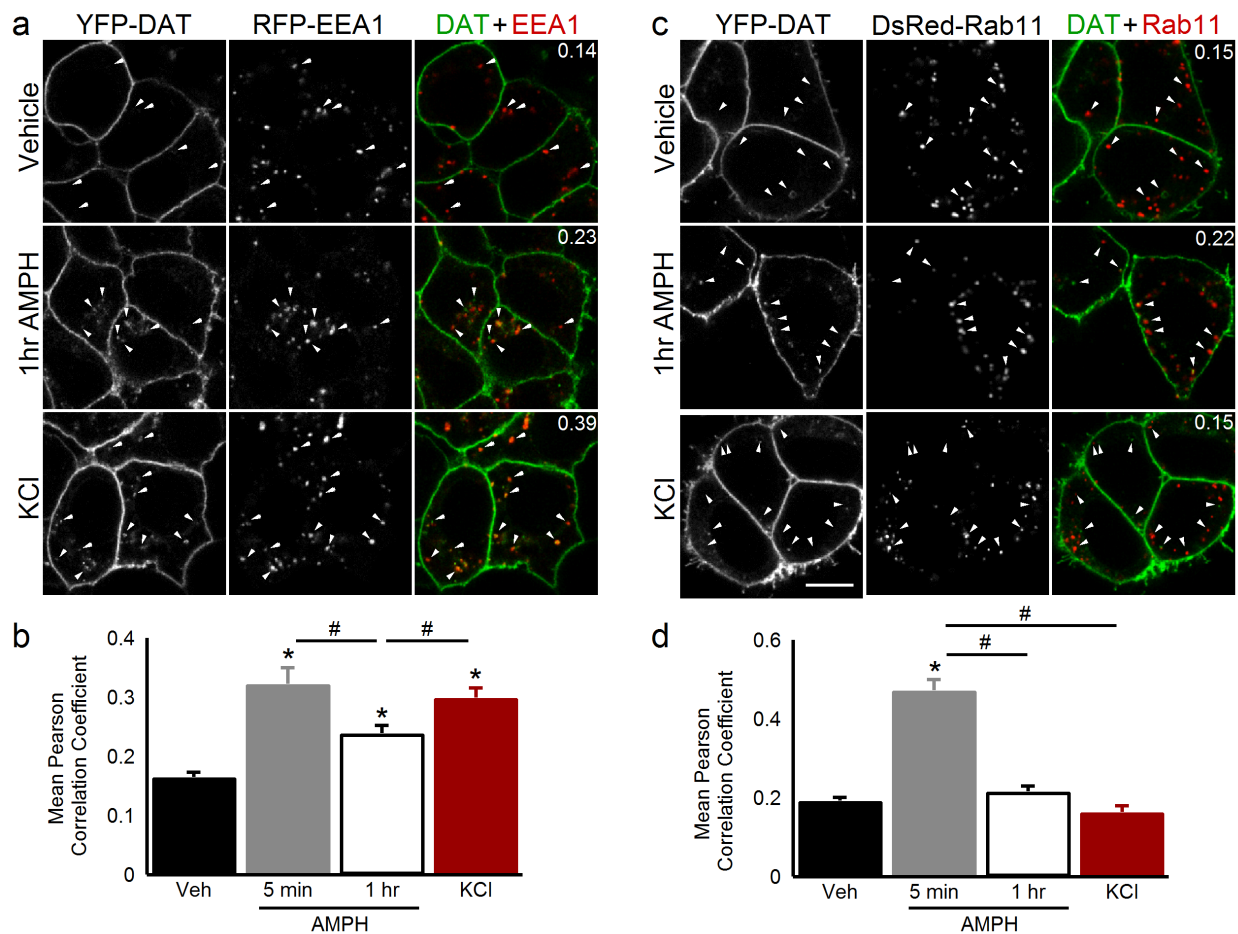


Figure 37. Depolarization-dependent internalized DAT preferentially localizes to early but not recycling endosomes. (a,c) Representative single-plane confocal images of (left) YFP-DAT, (middle) TagRFP-T-EEA1 (a) or DsRed-Rab11 (c) and merge of the two (right) expressed in HEK cells treated with vehicle (top; EEA1: $N=5$, $n=106$; Rab11: $N=6$, $n=77$), 10 μ M amphetamine for 1 h (middle; EEA1: $N=3$, $n=50$; Rab11: $N=3$, $n=61$) or 5 min (EEA1: $N=2$, $n=27$; Rab11: $N=2$, $n=13$) or 100 mM KCl for 5 min (bottom; EEA1: $N=3$, $n=84$; Rab11: $N=3$, $n=4$). (b,d) Mean \pm s.e.m. Pearson correlation coefficient per cell of intracellular YFP-DAT signal with EEA1 (b) or Rab11 (d) for vehicle, 5 min and 1 h amphetamine and 100 mM KCl-treated cells. Value inset in merged images is the mean Pearson correlation coefficient for cells in given image. Scale bar, 10 μ m and applies to all images. * $P < 0.05$ compared with vehicle, # $P < 0.05$ for indicated comparison using ANOVA with Bonferroni *post hoc* test.

association of intracellular YFP-DAT with Rab11 (0.16 ± 0.07 ; Fig. 37c,d) compared with vehicle. While biotinylation and confocal imaging inherently lack the temporal resolution of TIRFM, the collective results indicate that MP depolarization rapidly reduces cell-surface-membrane DAT and internalizes the transporter to intracellular early endosome compartments,

suggesting that membrane DAT levels and DAT trafficking may be partially dependent on the MP state and therefore could change rapidly with MP fluctuation on local changes in the activity of receptors, ion transporters and channels.

Change in MP State Alters Cell Surface Membrane DAT Levels

To further examine whether the membrane distribution of DAT is altered in response to MP changes (depolarization and hyperpolarization), we employed simultaneous single-cell TIRFM and whole-cell patch clamp electrophysiology (Fig. 38a). This technique allowed for time-resolved, bidirectional and precise control of the MP and provided internal controls in adjacent non-clamped cells. Acquisition of TIRFM image sequences (5-s intervals) throughout the course of 5 min duration voltage steps indicated that the surface YFP-DAT signal is stable during whole-cell voltage clamp at -40 mV (typical MP for YFP-DAT HEK cells; Fig. 38b–e), but MP changes from baseline to hyperpolarized (-60 mV; Fig. 38b,f–h) or depolarized ($+20$ mV; Fig. 38b,i–k) potentials could rapidly (between frames, 5 s duration) increase or reduce, respectively, YFP-DAT puncta in the TIRFM footprint (Fig. 38b). In some cases, the 5-s interframe interval during depolarization was sufficient to eliminate all DAT puncta from the cell surface, and hyperpolarization to -60 mV caused complete recovery of the fluorescent signal profile within 5–10 s (Fig. 38b). The effect of the hyperpolarizing voltage step on the TIRFM footprint intensity of patch-clamped cells rapidly increased, typically plateauing within 5 min, and began to reverse (decrease in intensity) following return of the membrane voltage to -40 mV (Fig. 38f). Continuous clamping of the MP at -40 mV did not significantly alter the YFP-DAT TIRFM footprint intensity at 3 min relative to adjacent cells ($n=4$ clamped, four adjacent cells; $P>0.05$; Fig. 38c–e). However, when comparing intensity changes between clamped and adjacent cells 3 min into the voltage step, stepping the MP to -60 mV significantly increased the YFP-

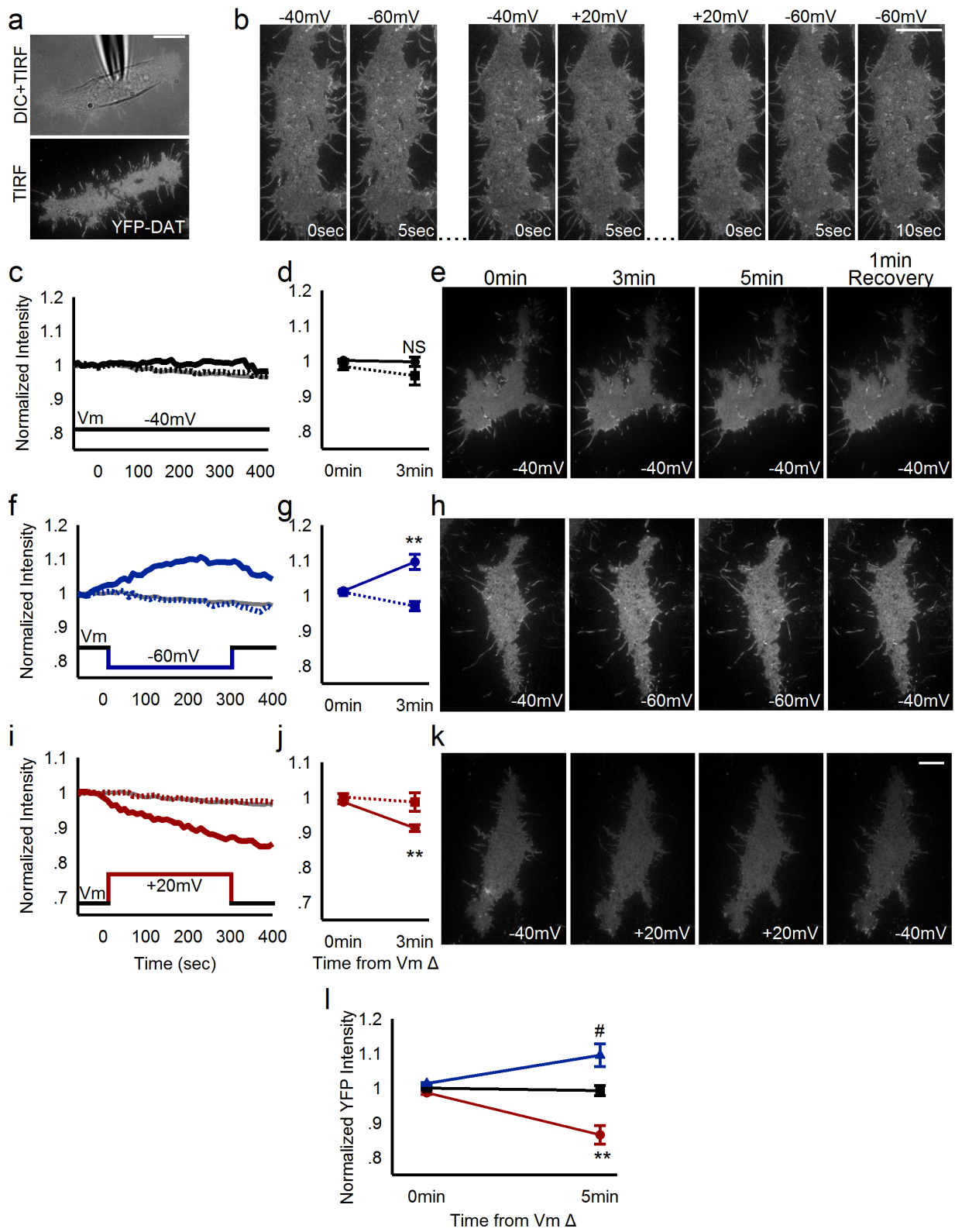


Figure 38. Membrane potential state alters cell membrane YFP-DAT levels. (a) Simultaneous whole-cell patch-clamp recording with the patch pipette visible in dissolved inorganic carbon (top) of YFP-DAT HEK cell and TIRF imaging of YFP-DAT (white) of the same cell (bottom). (b) TIRF image sequence with 5 s interframe interval of YFP-DAT HEK cell footprint with the membrane potential clamped at indicated holding potentials. Hyperpolarized potentials (−40 to −60 mV transition) increase cell-surface YFP-DAT signal, while depolarized potentials (−40 to +20 mV transition) reduces cell-surface YFP-DAT within 5 s and recovers within 5–10 s on hyperpolarization (+20 to −60 mV transition). (c,f,i) The mean normalized intensity of the surface-membrane YFP-DAT over time for all clamped cells (solid line) held at −40 mV (c), −60 mV (f) and +20 mV (i) for 5 min. Error bars are omitted for clarity, and the mean intensity for matched corresponding adjacent non-patched cells (color-matched dashed line) and the mean of all non-patched adjacent cells (grey line) are included for comparison. (d,g,j) Normalized fluorescence intensity values for patched-clamped (solid line) and paired adjacent cells (dotted line) before (0 min) and 3 min after membrane potential change ($n=4-5$ cells per group). (e,h,k) Representative images of YFP-DAT HEK TIRFM footprints of patched cells before (0 min), 3 and 5 min after the membrane potential change and 1 min after returning the membrane potential to −40 mV. (l) Average normalized YFP intensities at 5 min after the potential change to hyperpolarized (−60 mV, blue) or depolarized (+20 mV, red) membrane potentials are significantly different relative to continuous clamping near the endogenous (−40 mV, black) membrane potential. # $P<0.05$, ** $P<0.001$ using independent samples t -test. All values are mean±s.e.m. Scale bars, 10 μm .

DAT TIRFM footprint intensity ($n=5$ clamped, five adjacent cells; $P<0.01$; Fig. 38f–h), while stepping to +20 mV produced the opposite effect ($n=5$ clamped, five adjacent cells; $P<0.01$; Fig. 38i–k). Further comparison of voltage effects between only cells clamped at −40, −60 or +20 mV also indicates a significant difference in normalized YFP-DAT TIRFM footprint intensity for the −60 mV ($n=5$ cells; $P<0.05$) and +20 mV ($n=5$ cells; $P<0.001$) condition when compared with the −40 mV ($n=4$ cells) condition 5 min following the voltage change (Fig. 38l).

Change in MP State Alters DAT-Mediated Current

Since the mere presence of DAT at the cell surface (YFP fluorescence signal) is not necessarily indicative of relative DAT function, we sought to determine whether MP change-induced variations in the surface DAT density (Fig. 38) correlated with the uncoupled DAT-mediated current. To investigate this, as in previous TIRFM experiments, the MP was clamped for 5 min at +20, −40 or −60 mV but was followed by acquisition of a baseline IV curve (Fig. 39a). The subsequent GBR12935-sensitive current was then taken as the DAT-mediated current

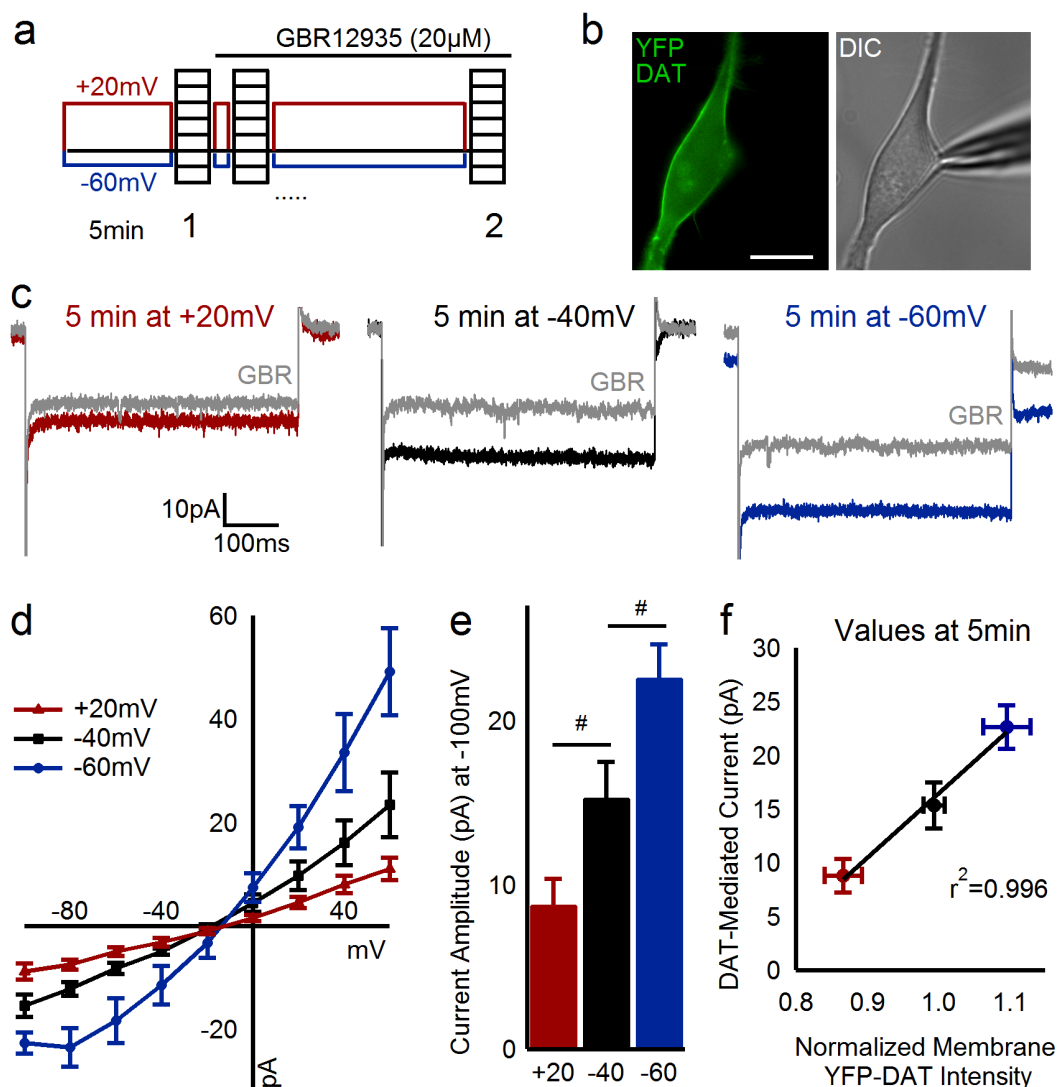


Figure 39. Membrane potential state significantly alters DAT-mediated current. (a) Schematic of the whole-cell voltage protocol for examining membrane potential state-dependent changes in DAT-mediated current recorded from HEK cells expressing YFP-DAT (see Methods). (b) Representative image of an YFP-DAT HEK cell following the complete recording paradigm for the +20 mV condition. Scale bar, 10 μm. (c) Representative current responses of the -100 mV voltage step before (colored trace) and after 20 μM GBR12935 (grey trace) for the given prolonged holding potential condition. (d) Group average IV plots for each voltage-state condition. (e) Bar graphs depict the mean current amplitude at -100 mV step from full IV plot for each condition and were used for statistical comparison between groups ($n=5-8$ cells per group). (f) Average DAT-mediated current amplitude plotted against the relative mean fraction of original intensity of the YFP-DAT TIRFM footprint (from Fig. 5) for cells patched at control, hyperpolarized and depolarized potentials indicates a positive correlation between increasing DAT-mediated current density and peri-membrane YFP intensity with TIRF microscopy. # $P < 0.05$ using independent samples t -test. All values are mean \pm s.e.m.

for each cell for a given condition. Cells clamped at -40 mV (near their endogenous resting MP) had a DAT-mediated current amplitude of -15.3 ± 2.16 pA ($n=8$; Fig. 39c–f, black). However, when cells were depolarized to $+20$ mV for 5 min (Fig. 39c–f, red), the DAT-mediated current (-8.8 ± 1.6 pA, $n=7$) was significantly reduced by 42.3% ($P < 0.05$), and cells hyperpolarized to -60 mV for 5 min (Fig. 39c–f, blue) displayed a 47.7% larger ($P < 0.05$) DAT-mediated current (-22.6 ± 2.0 pA, $n=5$) compared with cells held at -40 mV. For comparison of MP state-dependent changes in YFP-DAT membrane density (Fig. 38) and DAT functional capacity, the average fold change in YFP-DAT TIRFM footprint intensity and DAT-mediated current amplitude for each MP-holding potential state are plotted against each other (Fig. 39f), indicating a positive correlation between the two measures. While the cell-surface-membrane DAT levels (TIRFM) are influenced by the MP state, these data imply that functional DAT may be particularly influenced by MP state changes as they are more profoundly affected.

Neuronal MP Changes Alter Surface-Membrane DAT Levels

To determine whether MP influences surface-membrane DAT density in functional neurons, real-time imaging of membrane DAT (TIRFM fluorescence footprint) was coupled with two characterized non-invasive methods (Fig. 40) of transient reliable membrane depolarization and hyperpolarization: 100-mM KCl focal application (Fig. 41a) and archaerhodopsin (Arch) activation (Fig. 41b), respectively. Cultured primary neurons were transfected with TagRFP-T-DAT (RFP-DAT) or CFP-DAT with or without co-transfection with Arch-YFP (Arch-YFP; Fig. 40) and were subjected to whole-cell recordings (K-gluconate-based internal solution) or imaging in the presence of tetrodotoxin (TTX) and receptor blocker cocktail (see Methods), unless otherwise indicated. Pressure application of KCl-based external solution induced a

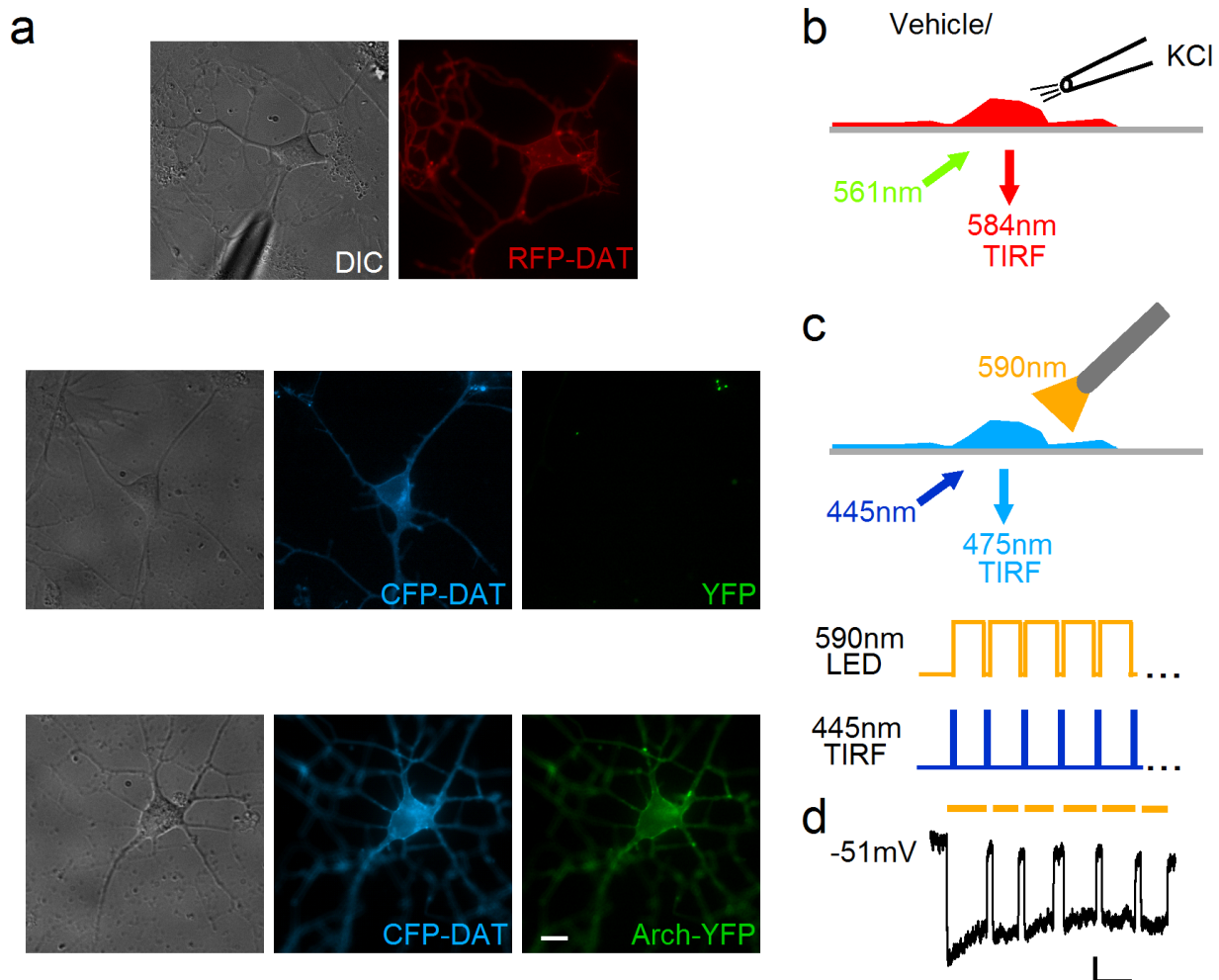


Figure 40. Fluorescently-tagged protein expression and imaging scheme for TIRF imaging of neurons and example effect of resulting prolonged Arch activation. (a) DIC and fluorescent images of midbrain primary culture neurons expressing TagRFP-T-DAT with picospritzer pipette positioned 20 μm from soma (top), CFP-DAT (middle) or CFP-DAT and Arch-YFP (bottom) imaged in wide-field fluorescence. (b-c) Schematic of simultaneous TIRF imaging of TagRFP-T-DAT and transient KCl-induced (applied via picospritzer pipette) membrane depolarization (b) or TIRF imaging of CFP-DAT and transient Arch-activation-induced membrane hyperpolarization via stimulation with adjacent optical fiber placed near the soma (c, upper). (c) Lower: For imaging, the timing of Arch photostimulation was continuous except during the 200-300 ms TIRF illumination and exposure period during which time the 590 nm LED light source was inactive. (d) Representative recording of membrane potential from primary culture neuron expressing Arch-YFP in response to pulses of 590 nm light stimulation via adjacent optical fiber corresponding to temporal parameters of stimulation/pauses during simultaneous TIRF imaging. Scale bar is 5 sec and 5 mV.

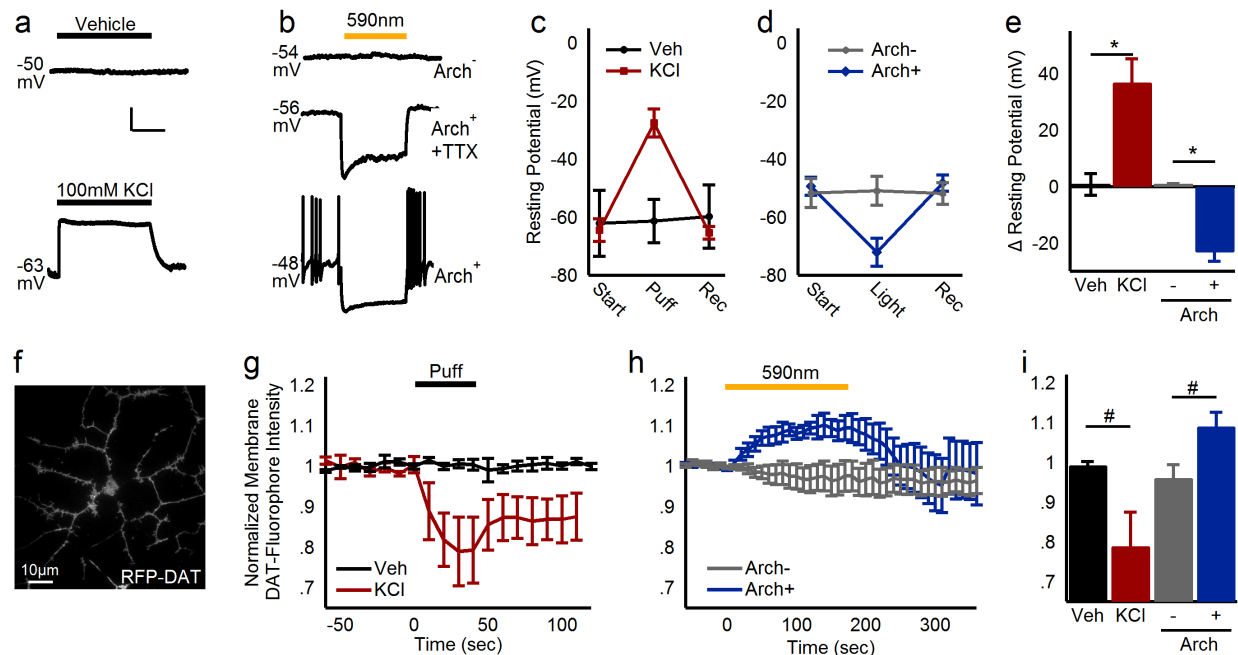


Figure 41. Neuronal membrane potential rapidly alters membrane-surface DAT level. (a,b) Cultured neuron membrane potential response to (a) vehicle or 100 mM KCl and (b) 590 nm stimulation in neurons with/without YFP-Arch 0.5 mM TTX omitted in bottom trace. Scale bar, 10 s (a) and 500 ms (b) and 10 mV for (a,b). (c) Membrane potential before, during and after vehicle (black; $n=3$) or 100 mM KCl (red; $n=4$) and (d) 590 nm light stimulation of neurons with (blue; $n=13$)/without (grey; $n=3$) Arch-YFP expression. (e) Resting potential change. (f) TIRFM image of primary culture neuron expressing RFP-DAT. (g) The mean normalized intensity of the surface RFP-DAT during vehicle (black; $n=4$) or 100 mM KCl (red; $n=3$) application. (h) The mean normalized intensity of the surface CFP-DAT when a 590 nm light pulse was delivered to cells with (blue; $n=5$)/without (grey; $n=4$) Arch-YFP expression. (i) Normalized somatic membrane RFP- or CFP-DAT fluorescence change for each condition. $^{\#}P<0.05$, $*P<0.01$ with independent samples t -test.

reversible 36.9 ± 8.3 -mV membrane depolarization in RFP-DAT-expressing neurons (Fig. 41a,c–e), and photo-activation (590 nm) of Arch caused a reversible -23.3 ± 3.2 -mV membrane hyperpolarization (Fig. 41a,c–e). In the absence of TTX, Arch activation suppressed action potential firing and induced a rebound burst when the light was turned off (Fig. 41b) and was relatively stable over long pulse durations (Fig. 40) used for subsequent imaging experiments (Mattis et al. 2012). The MP of neurons lacking Arch-YFP expression was unaffected by 590 nm light stimulation.

On characterizing the reliability of these tools, we performed simultaneous TIRFM of primary culture neurons (Fig. 41f) during each manipulation (Fig. 40b and Fig. 41g,h). TIRFM of neurons expressing RFP-DAT while focally applying 100 mM KCl-based external solution (Fig. 40b) for a short duration (45 s) caused a rapid and dramatic reduction ($-21.1\pm 8.5\%$) in the RFP-DAT TIRFM footprint intensity, while vehicle application had no effect (Fig. 41g). Similarly, bath application of 100 mM KCl-based external solution also enhanced the internalization of endogenous DAT in primary neurons labeled with JHC 1-064, causing a dramatic increase in JHC 1-064 complexes in the intracellular space (Fig. 42). In contrast,

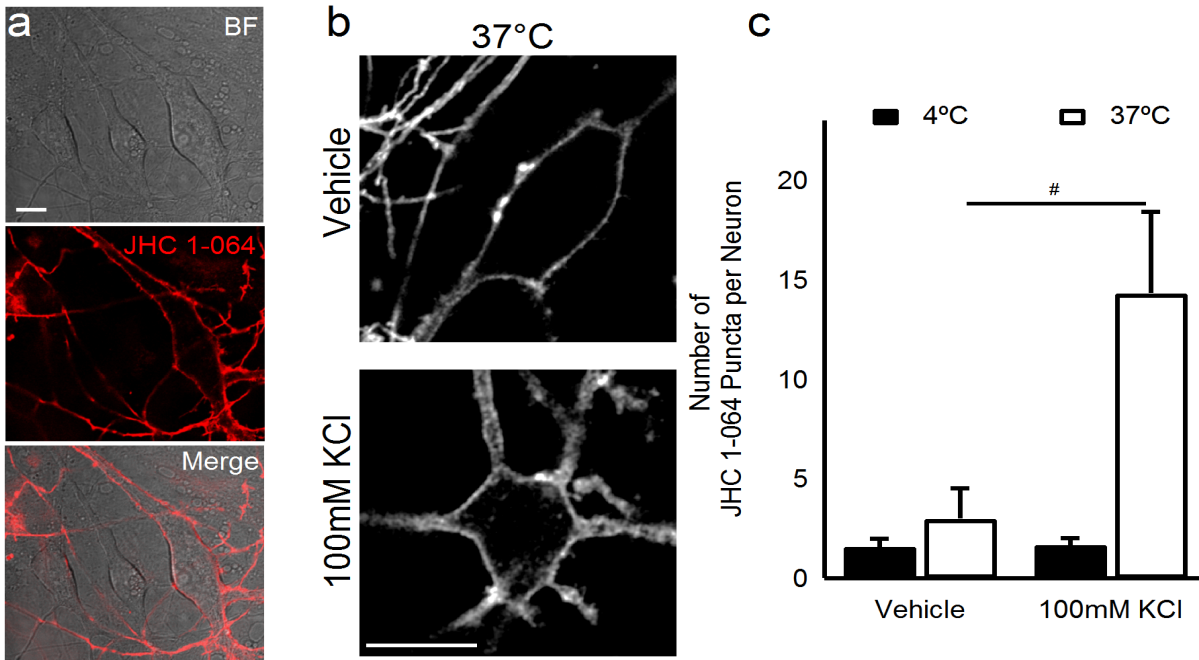


Figure 42. Depolarization enhances internalization of JHC 1-064/DAT complexes in midbrain primary cultured neurons. a) JHC 1-064 (10 nM for 30 min) labels membrane DAT in a subset of mouse midbrain primary culture neurons. Scale bar is 10 μ M. b) Single plane confocal image of primary neuron cell bodies labeled with JHC 1-064 imaged 5 min after replacing bath solution with 37°C standard (vehicle; top) or KCl-based external solution (bottom). Note JHC 1-064 punctae present only in the intracellular space of the neuron exposed to depolarizing KCl-based external solution. Scale bar is 20 μ M. c) Average number of JHC 1-064 punctae in the intracellular space of neurons at 4°C and after being at 37°C in standard ($n=5$) and KCl-based ($n=3$) external solution. Within a given condition, the same cells are represented in the 4°C and 37°C states. # $P<0.05$ using independent samples *t*-test. Values are mean \pm s.e.m.

simultaneous MP hyperpolarization via activation of Arch by 590 nm light staggered with TIRFM imaging of CFP-DAT (Fig. 41h) indicated that hyperpolarization caused a reversible increase ($+9.0\pm 3.5\%$) in CFP-DAT intensity in the TIRFM footprint overtime, which stabilized after 120 s (Fig. 41h). No significant change ($-3.8\pm 3.3\%$) in CFP-DAT TIRFM footprint intensity was observed in neurons lacking Arch-YFP expression (Fig. 41h). These KCl-induced decreases and Arch activation-induced increases in neuronal cell-surface DAT TIRFM signal, which parallel MP state-dependent changes in the surface density of DAT protein (Figs 30, 34, 36-38) and DAT function (Fig. 39) in YFP-DAT HEK cells, were significantly different from their respective controls (depolarization: $P<0.05$, hyperpolarization: $P<0.05$; Fig. 41i).

Discussion

The presence of DAT at the cell membrane is crucial in the regulation of DAergic signaling, timing and magnitude throughout the brain, and thus any alteration in the functional capacity of the transporter may significantly have an impact on neurological functions in which DA is involved. Previous studies have demonstrated that KCl-induced depolarization reduces DA uptake (Woodward et al. 1986; Holz and Coyle 1974), and that membrane hyperpolarization increases DAT-mediated inward current and DA uptake (Sonders et al. 1997), albeit with an unknown mechanism. Here we asked whether changes in MP alone may rapidly and reversibly regulate DAT trafficking. One aspect regulating transporter function is that the trafficking of mature DAT to and from the cell membrane is a highly regulated process, which is affected in various disease states and by the activity of DAT-targeting psychostimulants. Using live cell TIRFM and biotinylation on identically treated HEK cells expressing YFP-DAT, we determined that membrane depolarization alone could induce a CaMKII α - and dynamin-dependent (Figs 30 and 34) rapid reversible (increase in hyperpolarization recovery) reduction in membrane DAT

(Fig. 30). This depolarization-induced effect on DAT distribution in the TIRFM footprint was distinctly different when compared with the effects of AMPH, which did not recover as quickly. Another difference between AMPH- and depolarization-induced DAT internalization is the insensitivity of AMPH-induced internalization to the loss of CaMKII α activity through the coexpression of a dominant-negative, kinase-inactive CaMKII α (Fig. 34), which, along with the sensitivity of both versions to KN93, may suggest that different isoforms of the kinase may have distinctly different roles in regard to regulating DAT function. Notably, similar fast changes in membrane DAT levels have been reported using this approach with acute AMPH exposure (Furman, Chen, and Guptaroy 2009). However, the direction of the AMPH effect on human DAT using the multifaceted approach reported here contrasts with this previous finding and could be due to intrinsic differences between rat and human DAT, AMPH concentrations and/or cell types.

To determine the degree of DAT internalization, with the DAT-specific fluorescent cocaine analogue, JHC 1-064 (Eriksen et al. 2009), we followed the distribution of JHC 1-064 fluorescence (JHC 1-064/DAT complexes; Fig. 36) when cells were left at rest or depolarized. These data suggested that indeed membrane-resident DAT was being more rapidly brought into the intracellular space when depolarized as compared with constitutive internalization (Fig. 36c,d). While biotinylation and confocal imaging inherently lack the temporal resolution of TIRFM, together, results indicate that in contrast to the effects of AMPH on DAT, depolarization resulted in DAT being segregated specifically into early endosome compartments (EEA1), but not recycling endosomes (Rab11; Fig. 37). This divergence in the destination of internalized DAT in cells treated with AMPH versus those simply depolarized again suggests the involvement of differing mechanisms, which may leave initially internalized DAT residing in

early endosomes free to transition into rapid recycling endosomes, distinct from recycling endosomes (Grant and Donaldson 2009), putatively underlying the faster recovery to the membrane surface during hyperpolarization.

Although few studies have examined DAT activity immediately after depolarization or following the return to the resting hyperpolarized state, our data provide a potential mechanism for the decreased DA uptake in striatal synaptosomes during the fast phase of depolarization-induced DA release (Holz and Coyle 1974). Therefore, to determine any bidirectionality of the KCl effect on DAT trafficking, we used whole-cell voltage-clamp techniques to clamp the MP of YFP-DAT HEK cells while performing TIRFM simultaneously (Fig. 38). Once cells were clamped near their endogenous resting potential (-40 mV), the YFP-DAT TIRFM footprint was relatively similar over time (Fig. 38c–e). However, when stepping the membrane-holding potential from -40 mV to a hyperpolarized potential, an increase in YFP-DAT intensity and puncta number in the TIRFM footprint began immediately (Fig. 38b) and plateaued after 3 min (Fig. 38f–h). In contrast, when cells were depolarized the opposite effect occurred with a loss of YFP-DAT signal, which paralleled the effects seen in the presence of depolarizing KCl (Fig. 38i–k). In fact, the $\sim 10\%$ change in YFP-DAT intensity directly corresponded to reductions in DAT-mediated (GBR12935-sensitive) current when cells were clamped at depolarized or hyperpolarized potentials (Fig. 39). On the basis of these data and the known electrogenic nature of DAT-mediated DA uptake and efflux, we hypothesize that at depolarized conditions, where efflux is more likely to occur (Khoshbouei et al. 2003), the cell may actively attenuate this efflux by downregulating DAT at the membrane. In contrast, membrane hyperpolarization, known to facilitate DA uptake (Sonders et al. 1997), may be doing so through interactions with ionic driving forces and increases in membrane DAT.

With two tools that induced reversible and reliable depolarization (focal KCl application) or hyperpolarization (Arch activation) of magnitudes, similar to those used in previous experiments (Fig. 41a–e), we used TIRFM to monitor fluorescent-tagged DAT expressed in midbrain primary cultures during MP manipulation. The effect of these manipulations on membrane DAT levels were larger than in HEK cells using methods that induced similar voltage differences, implying that these effects are indeed applicable to neuronal populations and results obtained using HEK cells are relevant to shaping conclusions about MP-dependent trafficking of DAT in the nervous system. Together, these data indicate that, while the magnitude of change in membrane DAT levels due to MP changes varies depending on the assay, all changes observed are in a physiologically relevant range and the direction of the effect (increase or decrease) is in agreement across all examinations.

This effect of the MP on DAT trafficking sheds light on an additional mechanism by which the activation of hyperpolarizing D₂Rs may be altering DA transport. The activation of D₂Rs has long been understood to enhance DAT function (Meiergerd, Patterson, and Schenk 1993), and previous studies have suggested that a D₂R activation initiates a signaling cascade to upregulate cell-surface DAT (Morón et al. 2003). Although others have examined how changes in the neuronal MP similarly to those initiated by D₂R activation may alter DAT function and found no impact on [³H]-DA uptake (Prasad and Amara 2001), those experiments were performed at room temperature, which likely attenuates trafficking rates as opposed to the studies here conducted at near-physiological temperatures (37 °C). Thus, this methodological difference may explain the discrepancies between that [³H]-DA uptake study (Prasad and Amara 2001) relative to the data presented here. Nevertheless, collectively this study and previous studies support the involvement of multifaceted regulatory mechanisms for DAT trafficking that

are substrate-, kinase- and activity-dependent. The existence of multiple regulatory mechanisms supports the notion that the DAT proteins at the membrane are responsive to diverse regulatory mechanisms. The overriding mechanism for activation of a given trafficking pathway will be determined by the nature of the stimulation and the availability of specific regulatory constituents.

DA signaling is crucial in many neurological functions, as aberrations in DA neurotransmission contribute to multiple neuropsychiatric disorders, including addiction (Koob and Volkow 2010; Kalivas 2007), Parkinson's disease and movement disorders (Vernier et al. 2004; Kurian et al. 2011; Hansen et al. 2014), schizophrenia (Lodge and Grace 2011; Cordeiro et al. 2010) and attention-deficit hyperactivity disorder (ADHD) (Nieoullon 2002), all of which have been linked to how extracellular DA may be mishandled by altered DAT expression and function (Sakrikar et al. 2012; Cordeiro et al. 2010; Madras, Miller, and Fischman 2002). As a result, disease-related deviations from physiological states and variations in neuronal MPs may be altering the functional capacity of DAT by affecting its trafficking to and from the membrane. This dynamic balance of electrophysiological and biochemical processes to regulate subtle but essential aspects of neurotransmission opens a range of possibilities for exploring related aberrations in disease states and in pharmacotherapy targeting this interaction. Broadly, the regulation of protein (DAT) trafficking by the MP may provide additional means by which plasticity (for example, activity-dependent changes) in DAergic and possibly non-DAergic systems is maintained and controlled.

CHAPTER VI

INHIBITION OF SEROTONIN TRANSPORT IS ALTERED BY METABOLITES OF SELECTIVE SEROTONIN AND NOREPINEPHRINE REUPTAKE INHIBITORS AND REPRESENTS A CAUTION TO ACUTE OR CHRONIC TREATMENT PARADIGMS

Introduction

The serotonin transporter (SERT) is a member of the solute carrier 6 (*SLC6*) family of neurotransmitter transporters. SERT is expressed in the brain and periphery (Baganz and Blakely 2013; Berger, Gray, and Roth 2009), where it is the primary mechanism for termination of serotonergic signaling following vesicular release of serotonin (5-hydroxytryptamine, 5-HT). Altered activity of SERT has been implicated in multiple neurobehavioral disorders, including major depression, autism spectrum disorder, anxiety, post-traumatic stress disorder and obsessive-compulsive disorder (Daws and Gould 2011; Lucki 1998). Antidepressants (ADs) such as tricyclic antidepressants (TCA), selective serotonin reuptake inhibitors (SSRI), and serotonin-norepinephrine reuptake inhibitors (SNRI) effectively block 5-HT and/or norepinephrine (NE) reuptake thereby increasing synaptic levels of those neurotransmitters. Of these drugs, SSRIs and SNRIs are prescribed most often due to their superior safety profile. Although treatment with SSRIs and SNRIs effectively block 5-HT and/or NE reuptake almost immediately upon administration, chronic blockade is required for clinical efficacy (Schloss and Henn 2004; Andersen, Kristensen, et al. 2009). The mechanisms underlying the delay in clinical efficacy of AD treatment and the distinct roles of both NET and SERT as primary targets in depression are areas that remain poorly understood (Wong and Licinio 2001; Nemeroff and Owens 2002).

Structurally, SERT and the related norepinephrine and dopamine transporters contain 12 transmembrane domains (TMs), of which TMs 1, 3, 6, and 8 form the majority of the substrate permeation pathway as well as key interactions with ions, substrates, and antagonists (Yamashita et al. 2005; Penmatsa, Wang, and Gouaux 2013; Field, Henry, and Blakely 2010; Henry et al. 2003). Species scanning mutagenesis studies of SERT TM domains have identified several well conserved residues that are important molecular determinants responsible for high-affinity antidepressant binding (Barker et al. 1998; Henry et al. 2006; Andersen, Taboureau, et al. 2009; Kumar et al. 2015). For example, the isoleucine at position 172 (I172) in human and mouse SERT (hSERT and mSERT, respectively) was shown to mediate high-affinity binding for numerous antidepressants as substitution to methionine (the identity of the amino acid at the homologous position (M167) in *Drosophila* SERT) resulted in a dramatic loss in inhibitory potencies for the SERT antagonists citalopram, fluoxetine, sertraline, and cocaine. Importantly, the I172M substitution does not alter normal 5-HT transport or SERT surface expression (Thompson et al. 2011; Henry et al. 2006). The unique properties of this mutation allow for the generation of a transporter that has normal 5-HT transport capability but is virtually pharmacologically invisible to many antidepressants. In fact, SERT M172 transgenic mice show a loss in sensitivity to multiple SSRIs without altering 5-HT transport or synaptic levels of 5-HT (Thompson et al. 2011). Notably, the actions of SSRIs in wild-type mice are often compared to the SERT null mouse (Bengel et al. 1998), which could be inappropriate due to the developmental role of 5-HT in serotonergic and non-serotonergic systems. Chronic loss of appropriate serotonergic tone caused by the SERT null genotype results in multiple physiological and behavioral phenotypes that make any comparisons to the wild-type mouse during SSRI treatment confounding and problematic at best (Holmes, Murphy, and Crawley 2003). The SERT

M172 AD-insensitive mouse represents a significant step forward and a powerful new tool to define the role of SERT and 5-HT signaling following AD administration.

In humans and rodents, most SSRIs and SNRIs are metabolized to demethylated forms by cytochrome P450 enzymes, found primarily in the liver (Velasquez et al. 2016). Many of these demethylated metabolites are active antagonists of SERT mediated 5-HT transport (Sánchez and Hyttel 1999). However, the selectivity and potency of these metabolites for mSERT versus mSERT M172 has not been evaluated. In this study, we investigate the sensitivity of mSERT M172 in midbrain synaptosomes and platelets for antagonism by multiple SSRIs, SNRIs, and their metabolites. Furthermore, we look at the generation of the citalopram metabolite desmethylcitalopram in serum and brain tissue at 45 min and 2 hr following intraperitoneal injections to determine if SSRI chronic treatment regimens could be impacted by bioactive metabolites that have equivalent or biologically relevant potencies at SERT and SERT M172. This information is critical to ensuring that the physiological and behavioral effects observed with AD administration are due to the action of the parent compound and not to metabolites.

Methods

Animals

Serotonin transporter (SERT) M172 knock-in mice were previously generated on a 129S6 background (Thompson et al. 2011). The M172 knock-in and I172 wild-type littermates (8-12 weeks old) from heterozygous breeding litters were used for the *ex vivo* serotonin transport inhibition assays. Age-matched I172 wild-type C57BL/6J (Jackson Laboratory) mice from homozygous breeding litters were used for mass spectrometry (MS) analysis. Food and water was provided *ad libitum* and mice were maintained on a 12 hr light/dark schedule. All animal

procedures follow approved protocols of the UTHSCSA or IACUC/UNDACC animal use and care committees.

Synaptosome and Platelet-rich Plasma (PRP) Preparations

Samples were prepared as previously described (Thompson et al. 2011), but adapted to obtain both synaptosomes and PRP from the same animal to minimize the number of animals used. Briefly, mice were deeply anesthetized using Euthasol (500 μ l/animal) (Virbac AH, TX) and effectiveness assessed using foot pinch. Following ophthalmectomy for PRP preparation, blood was collected and the brain (forebrain and midbrain) dissected on ice for synaptosome preparation.

Brain blocks were homogenized in a buffer solution (containing 0.32 M sucrose and 4.2 mM HEPES, pH 7.4). Synaptosomal pellets were obtained through two-stage centrifugation: the homogenate was spun at 1,500 rpm for 15 min at 4°C and then the supernatant at $1.5 \times 10,000$ g for 15 min at 4°C. Synaptosomal pellets were resuspended with Krebs-Ringer HEPES buffer (KRH; 130 mM NaCl, 1.3 mM KCl, 2.2 mM CaCl₂, 1.2 mM MgSO₄, 1.2 mM KH₂PO₄, 1.8 g/L D-glucose, 10 mM HEPES, pH 7.4, 100 mM pargyline, and 100 mM ascorbic acid). Synaptosomal suspensions were assessed for protein content using a spectrophotometer (Thermo Scientific, USA) and then diluted to 1,500 μ g/ μ l with KRH buffer. The prepared synaptosomes were maintained on ice until dispensed for serotonin transport assays.

Collected blood was anticoagulated with Acid Citrate Dextrose Solution A (BD Franklin Lakes, NJ) at a ratio of 100 μ l per 500 μ l then centrifuged at $150 \times g$ for 20 min at 22°C to obtain PRP (the upper, clear supernatant). The PRP was assessed for platelet counts/ μ l by using a hemocytometer then stored at room temperature, to prevent platelet activation, until use in competition 5-HT uptake assays.

5-HT Competition Uptake Assays

Transport of 5-HT was assayed as described previously (Zhu, Blakely, and Hewlett 2006). Briefly, [³H]5-HT (100 nM) and serial dilutions of SERT inhibitors were prepared separately in KRH for synaptosomes or a buffered solution (150 mM NaCl, 50 mM Tris HCl, 25 mM EDTA, pH 7.4, 100 mM pargyline, and 100 mM ascorbic acid) for platelets. In a final volume of 250 µl (150 µl synaptosome or PRP, 50 µl [³H]5-HT, and 50 µl antagonist), the assay was initiated by incubation in a water bath for 10 min at 37°C followed by immediate filtration over 0.3% polyethylenimine-coated glass fiber filters using a cell harvester. Filter-bound radioactivity was quantified by a Beckman LS 6000 liquid scintillation counter. All transport assays were performed in duplicate. Radioactivity was normalized as a percentage of inhibition and plotted to determine the IC₅₀ of the tested antagonist.

Animal Injections and Measurement of Brain and Serum Drug Concentrations

VK05-19.Oxalate S-Citalopram, a gift from Amy Newman (NIH-NIDA), and the metabolite (S)-N-Desmethylcitalopram (Toronto Research Chemicals Inc, Cat #D291571) were administered via intraperitoneal injection in 0.9% NaCl at 10 mg/kg, 5 ml/kg respectively. For mass spectrometry analysis, imipramine was used as an internal standard while citalopram and desmethylcitalopram were used as positive controls and were reconstituted in 100% methanol with a final concentration of 5 ng.

Brain Tissue and Serum Preparations

At 45 minutes and 2 hours post-injection, mice were decapitated. Whole brains were frozen and stored in liquid nitrogen (N₂). Trunk blood was collected, centrifuged for 10 min at 4°C, 10,000 rpm and the supernatant transferred to cryovials for storage in N₂. Brain tissue was pulverized to a fine powder under N₂ to allow for a homogeneous mixing of different brain

compartments and extracted using a one-step protocol (Brose, Baker, and Golovko 2013). For extraction, 10 mg of brain tissue or 10 μ L of plasma was mixed with 90 μ L of 100% methanol. Treated samples were spiked with the internal standard imipramine while positive vehicle controls were spiked with imipramine and citalopram, desmethylcitalopram, or both citalopram and desmethylcitalopram. The vehicle negative control contained only 100% methanol. Samples were briefly sonicated on ice, vortexed and centrifuged for 10 min at 4°C, 10,000 rpm. Collected supernatant was diluted 100 fold with 90% methanol in water.

UPLC-MS/MS Analysis for Citalopram and Desmethylcitalopram

Compounds were resolved on a Waters ACUITY UPLC HSS T3 column (1.8 μ M, 100 Å pore diameter, 2.1 \times 150mm, Waters, Milford, MA) with an ACUITY UPLC HSS T3 pre-column (1.8 μ M, 100 Å pore diameter, 2.1 \times 5mm, Waters) at a temperature of 55°C. Analytes were eluted using a Waters ACUITY UPLC pump with a well plate autosampler at 8°C. 10 μ L of sample was injected on column.

The separation was based on the previously described method (Brose and Golovko 2013; Brose, Golovko, and Golovko 2016). Solvent A was water containing 0.1% formic acid and solvent B was acetonitrile with 0.1% formic acid. The flow rate was maintained at 0.45 mL/min. The initial conditions of 39% B were held for 0.5 min. Solvent B was increased to 40.5% over 6.88 min, followed by an increase to 70% over 1.62 min, then increased to 75% over 3 min, and further increased to 98 over 1.5 min where it was held for 5.3 min to elute hydrophobic molecules from the column. At 20 min, solvent B was returned to initial conditions over 0.2 minutes to re-equilibrate the column for 2min.

Compounds were analyzed using a triple quadrupole mass spectrometer (Xevo TQ-S, Waters) with electrospray ionization optimized in a positive mode. The capillary voltage was

3.29 kV and cone voltage was 14 V. The desolvation temperature was 500°C and the source temperature 150°C. The desolvation gas flow was 1000 L/hr, the cone gas flow was 150 L/hr, and the nebulizer gas was at 5.0 Bar. The collision gas was set at 0.18 mL/min. MassLynx V4.1 software (Waters) was used for instrument control, acquisition, and sample analysis.

Citalopram and desmethylcitalopram were quantified using imipramine as an internal standard. Compound's MS/MS parameters were optimized for multiple reactions monitoring (MRM) mode by direct infusion of a standard solution of each analyte. Citalopram was quantified using 325.18/109.04 mass transition (collision energy (CE) 14 V) with 325.18/234.14 conformational ion (CE 24V); desmethylcitalopram was quantified using 311.16/109.04 mass transition (CE 14 V) with 311.16/262.15 conformational ion (CE 16V); and imipramine was quantified using 281.20/86.09 mass transition (CE 14 V) with 281.20/208.11 conformational ion (CE 36V). The mass transitions for analytes and the selection of internal standard were consistent with previous reports (Jiang et al. 2010).

Results and Discussion

A previous study revealed that in comparison to wild-type mice, the SSRIs citalopram and fluoxetine display significantly reduced potencies for inhibition of SERT mediated 5-HT uptake in forebrain derived synaptosomes from M172 SERT mice (Thompson et al. 2011). Similarly, in this study, the SSRIs citalopram, fluoxetine, and sertraline as well as the SNRI venlafaxine showed significant losses in potency for antagonism of M172 synaptosomes, reductions ranging from 16-fold (fluoxetine) to 631-fold (citalopram) (Fig. 43, Table 2). As multiple SSRIs and SNRIs have active metabolites with half-lives long enough to make them biologically relevant (Sánchez and Hyttel 1999), we also characterized the correlate metabolites desmethylcitalopram, norfluoxetine, desmethylsertraline, and desvenlafaxine. Comparison of

Synaptosomes

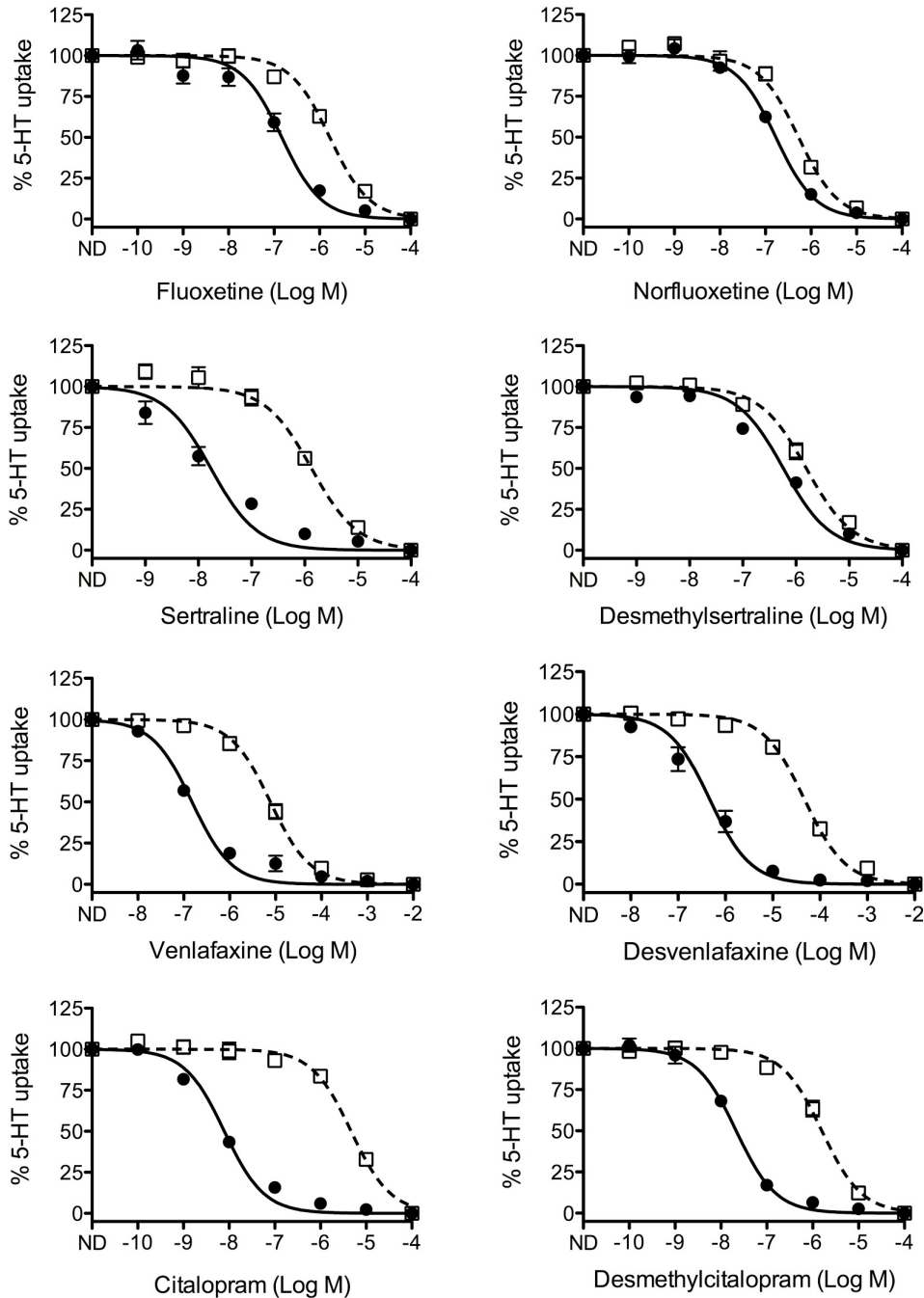


Figure 43. Competition 5-HT uptake analysis in forebrain derived synaptosomes. Forebrain derived synaptosomes were prepared from wild-type and M172 mice and utilized to assess the ability of multiple SSRI class drugs and their metabolites to compete for [³H]5-HT uptake. All SSRIs showed decreased potency in the M172 synaptosomes, while some metabolites showed similar potency in both wild-type and M172 synaptosomes. (n = 4-8 per drug; p < 0.05, two-tailed Student t test).

Table 2. Log IC₅₀ values for inhibition of [³H]5-HT uptake. Competition uptake analysis of PRP and forebrain derived synaptosomes, derived from wild-type and M172 mice, was performed to calculate IC₅₀s for multiple SSRIs and their active metabolites. Fold shift compares the rightward shift in potency for inhibiting SERT activity in wild-type and M172.

	Platelets			Synaptosomes		
	Log IC ₅₀		Fold Shift	Log IC ₅₀		Fold Shift
	WT	M172		WT	M172	
Fluoxetine	-7.4 ± 0.12	-6.2 ± 0.20	16	-7.0 ± 0.16	-5.8 ± 0.06	16
Norfluoxetine	-7.0 ± 0.06	-6.7 ± 0.13	2	-6.8 ± 0.04	-6.3 ± 0.02	3.2
Sertraline	-8.0 ± 0.05	-6.1 ± 0.18	79	-7.8 ± 0.21	-5.9 ± 0.05	79
Desmethylsertraline	-7.3 ± 0.04	-6.4 ± 0.11	7.9	-6.2 ± 0.13	-5.8 ± 0.08	2.5
Venlafaxine	-6.4 ± 0.12	-3.9 ± 0.12	316	-6.8 ± 0.07	-5.1 ± 0.09	50
Desvenlafaxine	-6.3 ± 0.18	-4.3 ± 0.06	100	-6.8 ± 0.07	-5.1 ± 0.06	50
Citalopram	-7.8 ± 0.07	-5.0 ± 0.06	631	-8.1 ± 0.09	-5.3 ± 0.04	631
Desmethylcitalopram	-7.6 ± 0.25	-5.0 ± 0.06	398	-7.7 ± 0.04	-5.8 ± 0.11	79

potencies of norfluoxetine and desmethylsertraline to inhibit 5-HT uptake of SERT and M172 SERT containing synaptosomes revealed that the compounds no longer exhibited strong selectivity for inhibition of SERT over M172 SERT and showed a fold change in IC₅₀ values of 3.2- and 2.5-fold, respectively. However, desvenlafaxine and desmethylcitalopram retained selectivity for wild-type SERT over M172 SERT (50- and 79-fold, respectively) (Fig. 43, Table 2). It is important to note that the potency of the metabolite desmethylsertraline to inhibit 5-HT uptake in wild-type SERT is decreased 40-fold in reference to its parent compound sertraline, a reduction which may be due, in part, to a shift in binding of the metabolite to a lower affinity site. Conversely, metabolites norfluoxetine, desvenlafaxine, and desmethylcitalopram inhibit 5-HT uptake in wild-type SERT at potencies similar to their parent compounds (\leq 2.5-fold change). For this reason, it is plausible that these metabolites in particular contribute to physiological blockade of transport and have a role in the effects observed following AD administration.

Platelets

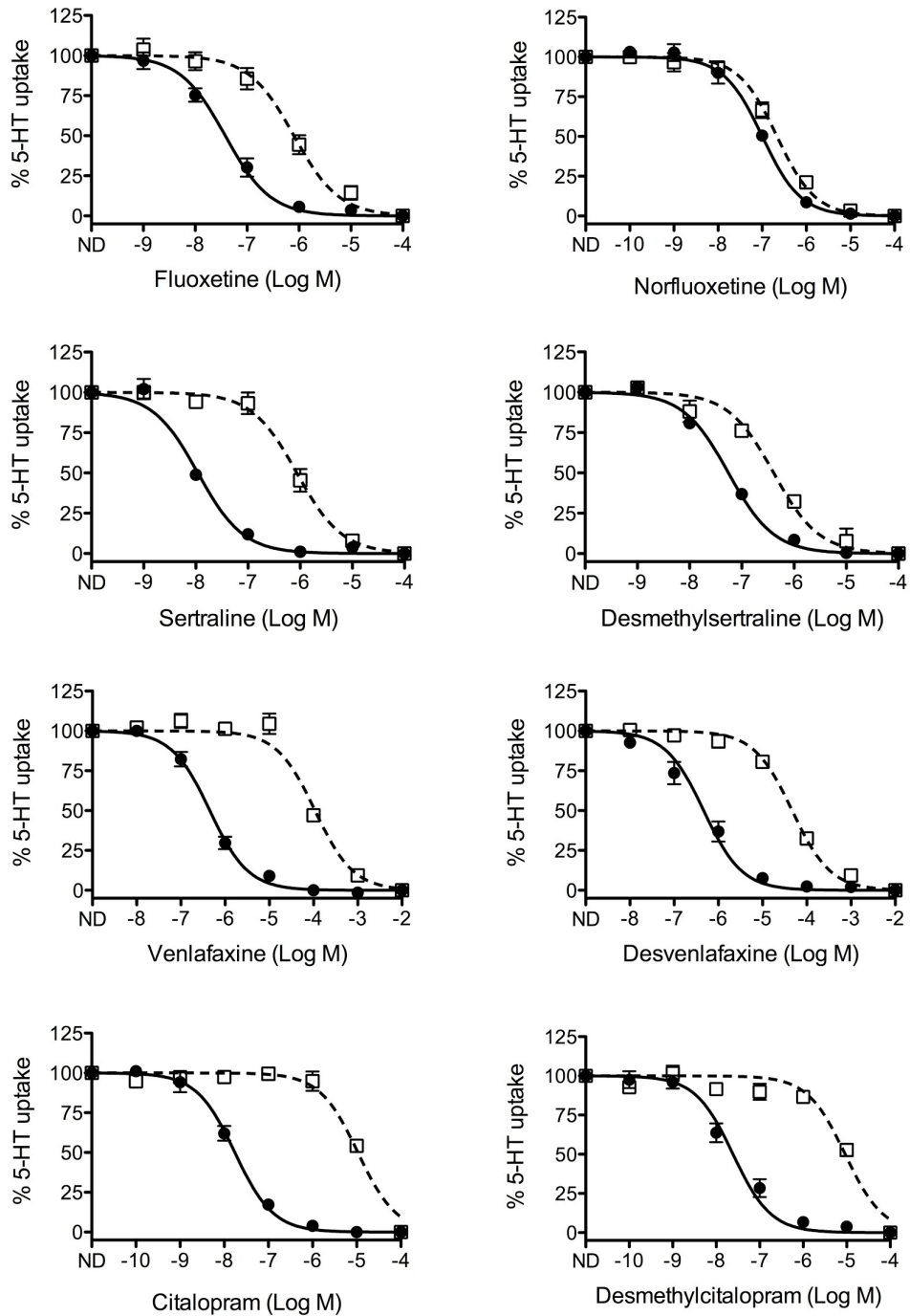


Figure 44. Competition 5-HT uptake analysis in isolated platelets. Isolated platelet rich plasma (PRP), from wild-type and M172 mice, was utilized to assess the ability of multiple SSRI class drugs and their metabolites to compete for [3 H]5-HT uptake. All SSRIs showed decreased potency in the M172 platelets, while some metabolites showed similar potency in both wild-type and M172, comparable to what was seen in synaptosomes. (n = 5-7 per drug; p < 0.05, two-tailed Student t test).

Similar to SERT, NET is a significant target of SNRIs and, though our 5-HT uptake assays should not be affected by the presence of NET, we also tested platelets to eliminate any contribution of NET. Platelets isolated from whole blood are often used as peripheral markers (Oreland and Hallman 1989) in human studies of SERT as they are easily obtained from subjects (Yubero-Lahoz et al. 2013). In addition, platelets cannot synthesize 5-HT and are therefore entirely dependent on SERT mediated uptake to accumulate 5-HT (Ni and Watts 2006; Berger, Gray, and Roth 2009). Our inhibitory data from platelets are consistent with the synaptosomal results with respect to the direction of potency changes (Fig. 44, Table 2). However, there were some differences in the magnitude of the fold-change of drug potencies between platelets and synaptosomes. Platelets likely lack some of the SERT interacting proteins present in neurons, which could account for the magnitude differences in potency changes. Nevertheless, the identical trends support our conclusions. As we are primarily focused on metabolite action in the brain, the following analyses are from synaptosome results.

Analysis of SERT activity from midbrain synaptosomes derived from the M172 mouse reveals that the fluoxetine metabolite norfluoxetine shows a slight decrease in antagonist potency for wild-type SERT but gains potency for inhibiting M172 SERT resulting in a significant reduction in selectivity (16-fold to 3.2-fold) (Fig. 43, Table 2). Norfluoxetine has been reported to return to the brain where it can build up significantly due to its longer half-life compared to fluoxetine and is thus likely the major antagonist of 5-HT uptake by SERT in both wild-type and M172 SERT mice. Desmethylsertraline, the break-down product of sertraline, also displays reduced selectivity for SERT over M172 SERT (79-fold to 2.5 fold) in synaptosomes, but importantly is 40-fold less potent than sertraline for inhibiting wild-type SERT and is therefore unlikely to significantly contribute to inhibition of 5-HT uptake. Venlafaxine and its metabolite

desvenlafaxine have virtually identical potencies for inhibition of SERT and M172 SERT in synaptosomes, as each compound exhibits 50-fold selectivity for SERT over M172 SERT. Therefore, even if desvenlafaxine can return to the brain, it would inhibit the same as venlafaxine. Desmethylcitalopram, the primary metabolite of citalopram, exhibits reduced but still robust selectivity for inhibition of SERT over M172 SERT (631-fold to 79-fold).

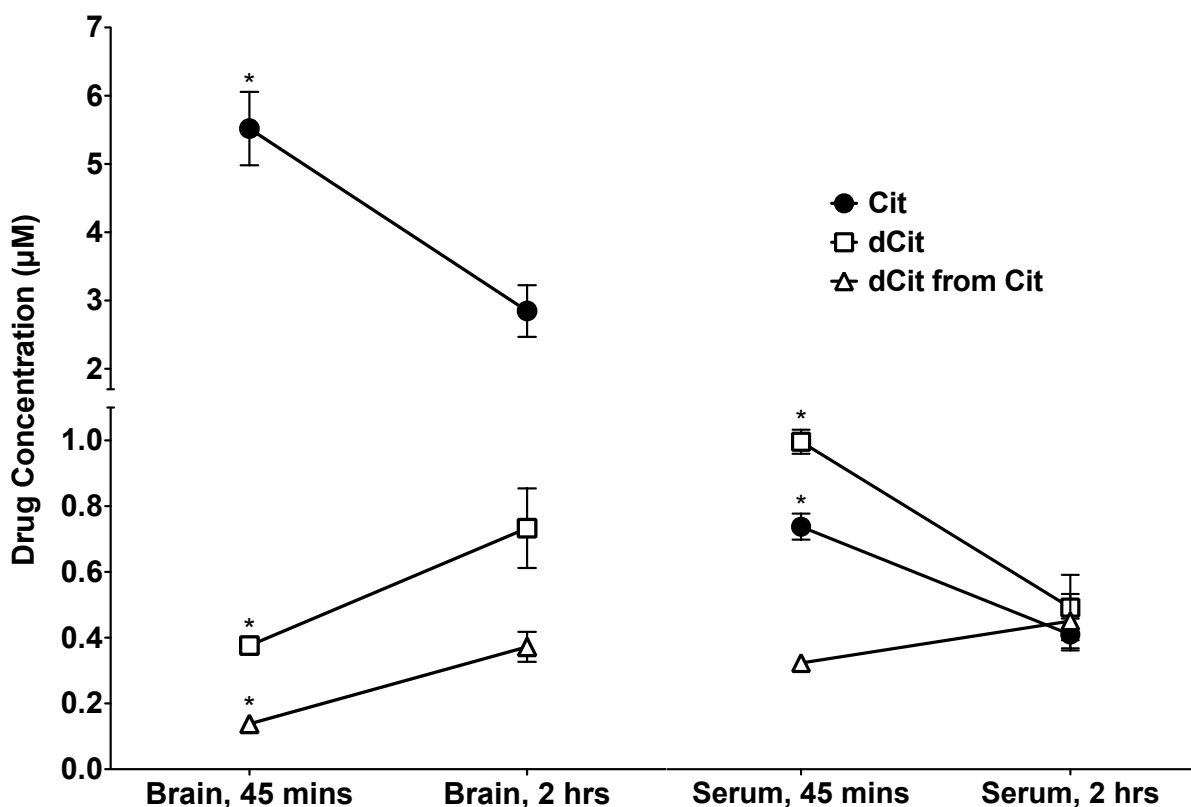


Figure 45. Time course analysis of brain and serum levels of citalopram and the metabolite desmethylcitalopram. Age-matched C57BL/6J mice were injected with either citalopram or desmethylcitalopram and sacrificed at 45 min or 2 hr post-injection. The analytes were isolated from whole brain or serum and detected by LC-MS/MS. In the brain and serum, citalopram levels (● Cit) decrease from 45 min to 2 hr, whereas the metabolite desmethylcitalopram (Δ dCit from Cit) levels increase only in the brain over time. As a control, mice injected with the metabolite desmethylcitalopram (△ dCit) show an accumulation of the metabolite in the brain, when comparing 45 min and 2 hr, but a decreased concentration in the serum, as seen with the citalopram derived metabolite. $n \geq 2$ mice, unpaired *t*-test was used to compare 45 min to 2 hr (*, $p < 0.05$).

Having established that AD metabolites are capable of antagonizing SERT mediated 5-HT transport in *ex vivo* assays, we next determined whether the metabolite desmethylcitalopram is capable of crossing the blood brain barrier, as re-entry into the brain following first-pass metabolism could contribute to the behavioral effects observed with chronic SSRI treatment. Desmethylcitalopram was selected due to its importance in our ongoing studies. Wild-type mice injected intraperitoneally with citalopram or its metabolite desmethylcitalopram were sacrificed after 45 mins or 2 hr and blood serum or brain tissue extracts analyzed by liquid chromatography and mass spectrometry to quantify the parent compounds and metabolites. Comparison of the 45 min and 2 hr time points revealed that brain and serum citalopram levels decrease over time (Fig. 45, Table 3). During this period, desmethylcitalopram levels metabolized from citalopram increased in the brain, but not in the serum. Likewise, mice directly injected with the metabolite itself show an accumulation in the brain over time and a loss over time in the serum. Importantly, desmethylcitalopram, unlike norfluoxetine, maintains selectivity for wild-type SERT and is therefore not expected to interfere with citalopram treatment studies in the M172 mouse.

Table 3. LC-MS/MS quantification of citalopram and the metabolite desmethylcitalopram in brain and serum. Age-matched C57BL/6J mice were injected with either citalopram or desmethylcitalopram and sacrificed at 45 min or 2 hr post-injection. The analytes were isolated from whole brain or serum and detected by LC-MS/MS. $n \geq 2$ mice, unpaired *t*-test was used to compare 45 min to 2 hr (*, $p < 0.05$).

	Brain (μM)			Serum (μM)		
	Time		<i>t</i> test	Time		<i>t</i> test
	45 min	2 hr		45 min	2 hr	
Citalopram	5.52 \pm 0.54	2.85 \pm 0.38	*	0.76 \pm 0.04	0.42 \pm 0.05	*
Desmethylcitalopram	0.38 \pm 0.03	0.73 \pm 0.12	*	1.03 \pm 0.04	0.51 \pm 0.10	*
Desmethylcitalopram from Citalopram	0.14 \pm 0.01	0.37 \pm 0.05	*	0.33 \pm 0.01	0.46 \pm 0.09	n.s.

In conclusion, synaptosomes and platelets derived from M172 SERT mice show a reduced sensitivity to multiple SERT antagonists, as was previously demonstrated (Thompson et al. 2011). However, the ability of bioactive metabolites to antagonize 5-HT uptake by the M172 SERT substitution has not previously been studied. Here we explored the potency of these drugs for antagonism of wild-type versus M172 SERT and found that studies using the M172 mouse that require selective inhibition of wild-type SERT over M172 SERT need to account for active metabolites and determine if there are changes in selectivity, inhibitory potency, and blood brain barrier passage and retention. Compounds that lose selectivity but retain similar potencies as the parent compound are problematic and should not be used.

CHAPTER VII

AUTISM-LINKED MUTATIONS IN THE HUMAN SEROTONIN TRANSPORTER INDUCE DISTINCT STRUCTURAL CHANGES THAT MAY ACCOUNT FOR THE ALTERED FUNCTION OF THE TRANSPORTER

Introduction

Autism spectrum disorder (ASD) is diagnosed in one out of every 68 children in the United States (CDC, 2014) and whereas individuals present with a range of behavioral manifestations, most share common symptoms including communication and social deficits as well as restrictive and repetitive behaviors (American Psychiatric Association, 2013). The varied presentations of ASD suggests it is a complex disorder with numerable causes, however, a genetic link has been identified in up to 25% of cases (Huguet, Ey, and Bourgeron 2013). Furthermore, twin studies have identified concordance rates of up to 92% in identical twins supporting that ASD can be heritable and under genetic control (Bailey et al. 1995).

Early physiological studies revealed that 25-30% of autistic individuals exhibit elevated whole blood serotonin (5-HT) levels (Schain and Freedman 1961; Hanley, Stahl, and Freedman 1977), termed hyperserotonemia, a biomarker that predated the broad acceptance of 5-HT as a neurotransmitter (Folk and Long 1988). This biomarker continues to be useful in today's population of ASD individuals (Gabriele, Sacco, and Persico 2014; Muller, Anacker, and Veenstra-VanderWeele 2016) and is one of the primary traits most consistently associated with the disorder (Cook and Leventhal 1996; Veenstra-VanderWeele and Blakely 2012) suggesting that dysregulation of the serotonergic system contributes to biological mechanism and behaviors

associated with ASD. Furthermore, this associative link is strengthened by the efficacy of selective serotonin-reuptake inhibitors (SSRIs) are used to treat some symptoms of ASD (Hollander et al. 2004). SSRIs bind and inhibit the normal activity of the serotonin transporter (SERT), an integral membrane protein belonging to the SLC6 family of transporters expressed on presynaptic serotonergic neurons (Moore, Halaris, and Jones 1978; Baganz and Blakely 2013) and at numerous sites in the periphery including platelets (Qian et al. 1995), which acts in the brain to terminate serotonergic signaling by coupling the reuptake of 5-HT from the synapse into the presynaptic neuron to the electrochemical gradients of Na^+ , Cl^- , and K^+ (Kristensen et al. 2011; Pramod et al. 2013). Alterations in SERT functional levels have been shown to modulate serotonergic tone and are implicated in mood and behavioral disorders (Ramamoorthy et al. 1993; Barker and Blakely 1995) whereas regulation of SERT activity and trafficking at the membrane of platelets modulate blood 5-HT levels, as 5-HT is produced by enterochromaffin cells lining the lumen of the gastrointestinal tract (Gershon 2004) and is sequestered inside platelets by SERT when they pass through enteric circulation (Anderson, Feibel, and Cohen 1987).

Structurally, SERT is composed of twelve transmembrane domains (TMs) related by a pseudo-twofold axis in which TMs 1-5 and TMs 6-10 have the same overall internal arrangement, but are aligned antiparallel to one another (Coleman, Green, and Gouaux 2016). The amino (N) and carboxyl (C) termini, which are located intracellularly, contain multiple sites for regulation by phosphorylation (Ramamoorthy et al. 1998; Ramamoorthy et al. 2007) as well as mediate protein-protein interactions (Haase et al. 2001; Quick 2003; Carneiro and Blakely 2006; Carneiro et al. 2008). To date, multiple ASD-linked SERT coding variants (ASVs) have been identified including, but not limited to, G56A located on the N terminus, I425L on TM8,

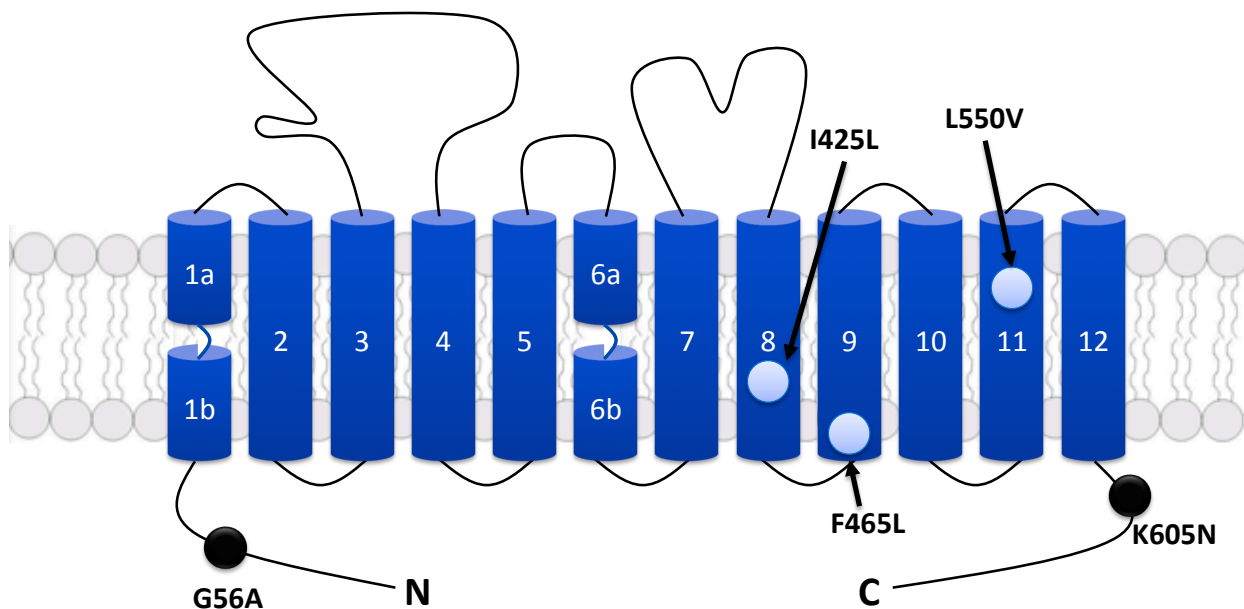


Figure 46. Location of autism-associated SERT variants. Variants are overlaid on a 2-D representation of SERT. Regulatory domain variants are shaded black whereas the transmembrane domain variants are shaded blue.

F465L on TM9, L550V on TM11, and K605N on the C terminus (Fig. 46). Each ASV, with the exception of K605N, is significantly associated with phenotypic increases in stereotypic utterances, unusual preoccupations, compulsions/rituals, resistance to trivial changes, and unusual attachment to objects (Tadevosyan-leyfer et al. 2003; Sutcliffe et al. 2005). Functional analyses of these variants indicate an increase in 5-HT transport relative to wild type human SERT (hSERT) for all mutants whereas surface expression was elevated only in I425L, F465L, and L550V (Prasad et al. 2005; Prasad et al. 2009). The hyperactivity of the cytoplasmic variants G56A and K605N has been suggested to result from loss of regulation by phosphorylation due to the observation that activators and inhibitors of the cyclic GMP-dependent protein kinase (PKG) and the p38 mitogen-activated protein kinase (p38 MAPK) pathways are ineffective in modulating the enhanced phosphorylation levels in G56A (Prasad et al. 2005; Veenstra-VanderWeele et al. 2012). These results reinforce that the gain-of-function of the G56A and

K605N variants results from catalytic activation or possible disruptions in phosphatase interactions whereas an increase in surface expression impacts 5-HT homeostasis in ASVs I425L, F465L, and L550V.

As the exact mechanism(s) underlying SERT hyperactivity in these ASVs remains unclear, it is imperative to understand how mutations in the structural core of the transporter can result in the same functional and physiological outcome as mutations in distant regulatory termini domains. Here we present structural analyses of the ASVs for the purpose of identifying either common or distinct conformational changes, representative of altered tertiary structure, that could mediate the observed changes in catalytic activity and surface expression.

Methodology

Cell Culture and Site-directed Mutagenesis

ASVs were introduced into native or cysteine-reduced SERT backgrounds of pcDNA3-hSERT using the Stratagene QuikChange® kit and verified by sequencing (Eurofins MWG Operon, Huntsville, AL). Analysis of the intracellular Cys-277 probe required introduction of the ASVs into the X5C background (C15A, C21A, C109A, C357I, and C622A) (Sato et al. 2004) prior to transient expression in HEK-GripTite cells (Invitrogen) using TransIT®-LT1 (Mirus) (1 µl per 200 ng of DNA). Cells were maintained in a humidified chamber with 5% CO₂ at 37°C in Dulbecco's modified Eagle's medium (DMEM: 10% FBS, 600 µg/ml G418).

Cysteine Accessibility Analysis

Conformational changes assessed by rate of inactivation. GripTite cells were plated at a density of 10,000 or 50,000 cells/well in 24-well culture plates, incubated for 24 h, and transfected with hSERT constructs. Following transfection (24 h), cells were washed with 37°C PBS/CM buffer (137 mM NaCl, 2.7 mM KCl, 10.1 mM Na₂HPO₄, 1.8 mM KH₂PO₄, 0.1 mM

CaCl₂, 1.0 mM MgCl₂, pH 7.4) or NMDG-Cl buffer (120 mM NMDG-Cl, 5.4 mM KCl, 1.2 mM CaCl₂, 10 mM glucose, 7.5 mM HEPES, pH 7.4) and then incubated with 1 mM MTSET, 10 mM MTSES, or 2 mM MTSEA for 1-10 min at room temperature. Post-treatment, cells were washed with PBS/CM or NMDG-Cl buffer and assayed for transport activity by incubation with 50 nM [³H]5-HT for 5 min at 37°C in MKRHG buffer (5 mM Tris, 7.5 mM HEPES, 120 mM NaCl, 5.4 mM KCl, 1.2 mM CaCl₂, 1.2 mM MgSO₄, 10 mM glucose, pH 7.4). Cells were dissolved in MicroScint™-20 (PerkinElmer Life Sciences) scintillation fluid and counts/min of radioactivity were determined using a TopCount NXT scintillation counter. Specific uptake was determined by subtracting uptake observed in nontransfected cells. All experiments were repeated in three or more separate assays and data fit to a one phase decay. Half-life values estimated from inactivation were analyzed using a one-way ANOVA followed by a post hoc Dunnett's test (GraphPad Software Prism 5).

Antagonist- or substrate-induced protection of Cys-277. For protection studies, 50,000 GripTite cells were plated and transfected as described above. 24 h post-transfection, cells were pretreated with vehicle, 50 μM 5-HT, or 50 μM cocaine for 10 min at 37°C before addition of 1 mM MTSEA in PBS/CM buffer for 10 min at room temperature. After washing to remove unreacted MTSEA, remaining activity was assayed by [³H]5-HT (50 nM for 5 min at 37°C) in MKRHG buffer, radioactivity quantified as above, and data analyzed using a two-way ANOVA followed by a post hoc Bonferroni test.

Cys-277 accessibility in mimicked hyper- or de-phosphorylated SERT. 50,000 GripTite cells transfected to express ASVs in PKG phosphorylation-dependent (S277C) or mimicked hyper- (T276D) and de- (T276A) phosphorylated backgrounds were treated with vehicle or 1 mM MTSEA in PBS/CM buffer for 10 min at room temperature. Following

treatment, cells were assayed for transport activity by 50 nM [³H]5-HT for 5 min at 37°C in MKRHG buffer. Radioactivity was quantified as above, normalized for surface and total SERT expression, and data analyzed using a one- or two-way ANOVA followed by a post hoc Dunnett's or Bonferroni test, respectively.

Protein Expression Analysis

Surface proteins were biotinylated as previously described (Henry et al. 2003). Briefly, surface proteins were biotinylated using 1.5 mg/mL EZ-Link™ Sulfo-NHS-SS-Biotin (Thermo Scientific™) in PBS/CM buffer and analyzed via Western blotting. Total protein concentrations were determined using the Pierce BCA protein assay kit (Thermo Scientific™) and the resulting values used to load equal amounts of protein when conducting SDS-PAGE on 10% gels. Blots of total and surface protein were probed with either an N-terminal monoclonal antibody at a concentration of 1:1500 (ST51-2, MAb Technologies) or a C-terminal directed polyclonal antibody at a concentration of 1:5000 (#48, a gift from Dr. Randy Blakely) followed by quantitation of the immunoblot bands using Image Studio (LI-COR).

Results

Sensitivity of Cys Probes to MTS Reagents

Residue Cys-109 (Fig. 47), an endogenous cysteine residue located on the extracellular end of transmembrane domain 1 (TM1 or TM1b), and the engineered mutant Cys-277, positioned on TM5 proximal to the cytoplasm (Fig. 47), have been shown to exhibit altered sensitivity to thiol modifying reagents, including methanethiosulfonates (MTS). This method, known as the substituted cysteine accessibility method (SCAM), utilizes the reaction between charged, hydrophilic, sulfhydryl reagents and endogenous or engineered cysteine residues to elucidate SERT conformational changes induced by mutations and/or antagonist, substrate, or

ion binding (Androutsellis-Theotokis, Ghassemi, and Rudnick 2001; Henry et al. 2003; Zhang and Rudnick 2006; Forrest et al. 2008; Field, Henry, and Blakely 2010; Henry et al. 2011; Felts et al. 2014; Dahal et al. 2014). Recent crystal structures of the homologous bacterial leucine transporter (LeuT) and the homologous *Drosophila* dopamine transporter (dDAT) confirm that TM1b and TM5, the respective locations of Cys-109 and Cys-277, undergo significant conformational changes during substrate transport (Singh et al. 2008; Krishnamurthy and Gouaux 2012; Penmatsa, Wang, and Gouaux 2013). Thus, the sensitivity of Cys probes 109 and 277 will be assessed in the ASV backgrounds in order to identify conformational changes at the extracellular (Cys-109) or cytoplasmic (Cys-277) face of SERT.

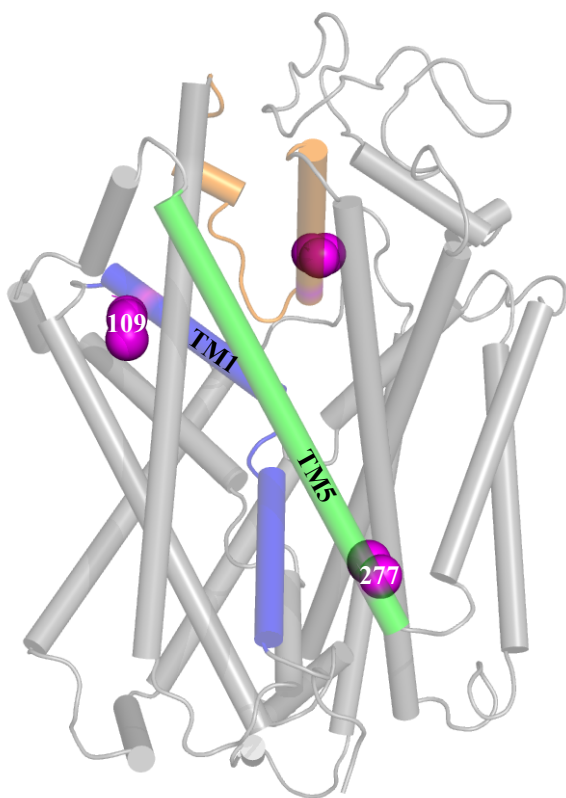


Figure 47. Cysteine probes used to assess conformational changes through SCAM. The extracellular Cys-109 probe (purple shaded circle) is located at the extracellular end of TM1 (blue cylinder) whereas the intracellular Cys-277 probe (purple shaded circle) is located at the base of TM5 (green cylinder) proximal to the cytoplasm.

The endogenous cysteine residue Cys-109 is responsible for the majority of the sensitivity to externally applied MTS reagents (Fig. 48, + *Control* is Cys-109 and - *Control* is Ala-109) (Chen, Liu-Chen, and Rudnick 1997). Therefore, reactivity of a negatively charged,

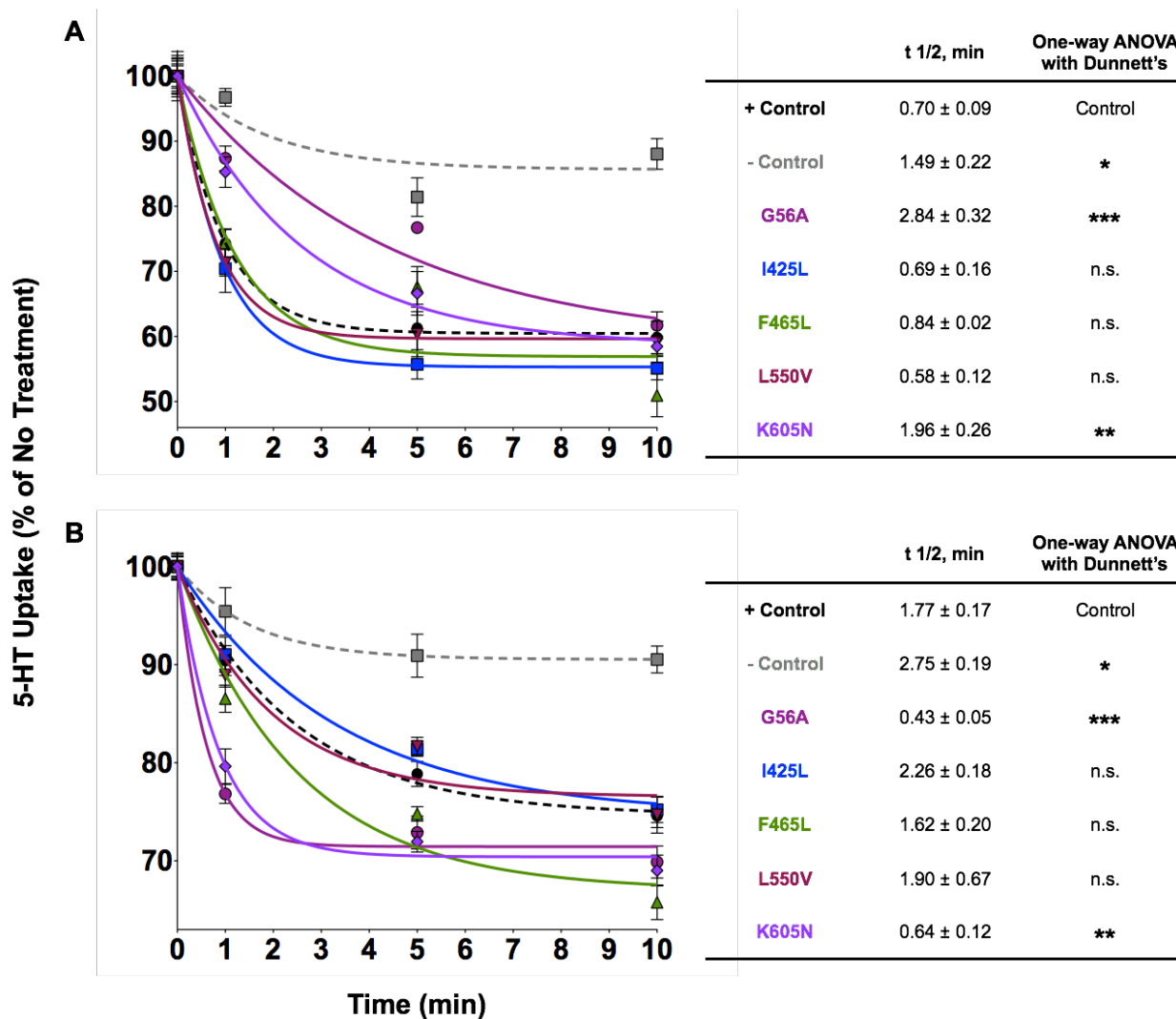


Figure 48. MTSES reactivity at Cys-109 is altered by the regulatory domain variants. HEK-GripTite cells plated at low- (a) or high-density (b) and transfected to express ASVs were treated with 10 mM MTSES in PBS/CM buffer for the indicated time. Following treatment, the cells were assayed for [³H]5-HT transport (50 nM for 5 min). Transport activity is plotted as a percent of untreated cells and the values represent the mean ± S.E. from three or more independent experiments. The t ½ values are estimated from inactivation and analyzed with a one-way ANOVA followed by a post hoc Dunnett's test.

membrane impermeant MTS reagent, MTSES, was evaluated at this location in the ASV backgrounds. Furthermore, based on the initial phases of this study that suggested cell density impacts the accessibility of a Cys-probe, we tested for Cys reactivity in both low- and high-density systems, in which cells were plated at a density of 10,000 or 50,000 cells/well. In a low-

density system, MTSES reactivity at Cys-109 was decreased in the cytoplasmic, regulatory domain ASVs G56A and K605N (Fig. 48a). However, in a high-density system, the results were inverted as reactivity was increased in G56A and K605N (Fig. 48b), likely resulting from a change in cell-cell or protein-protein interactions.

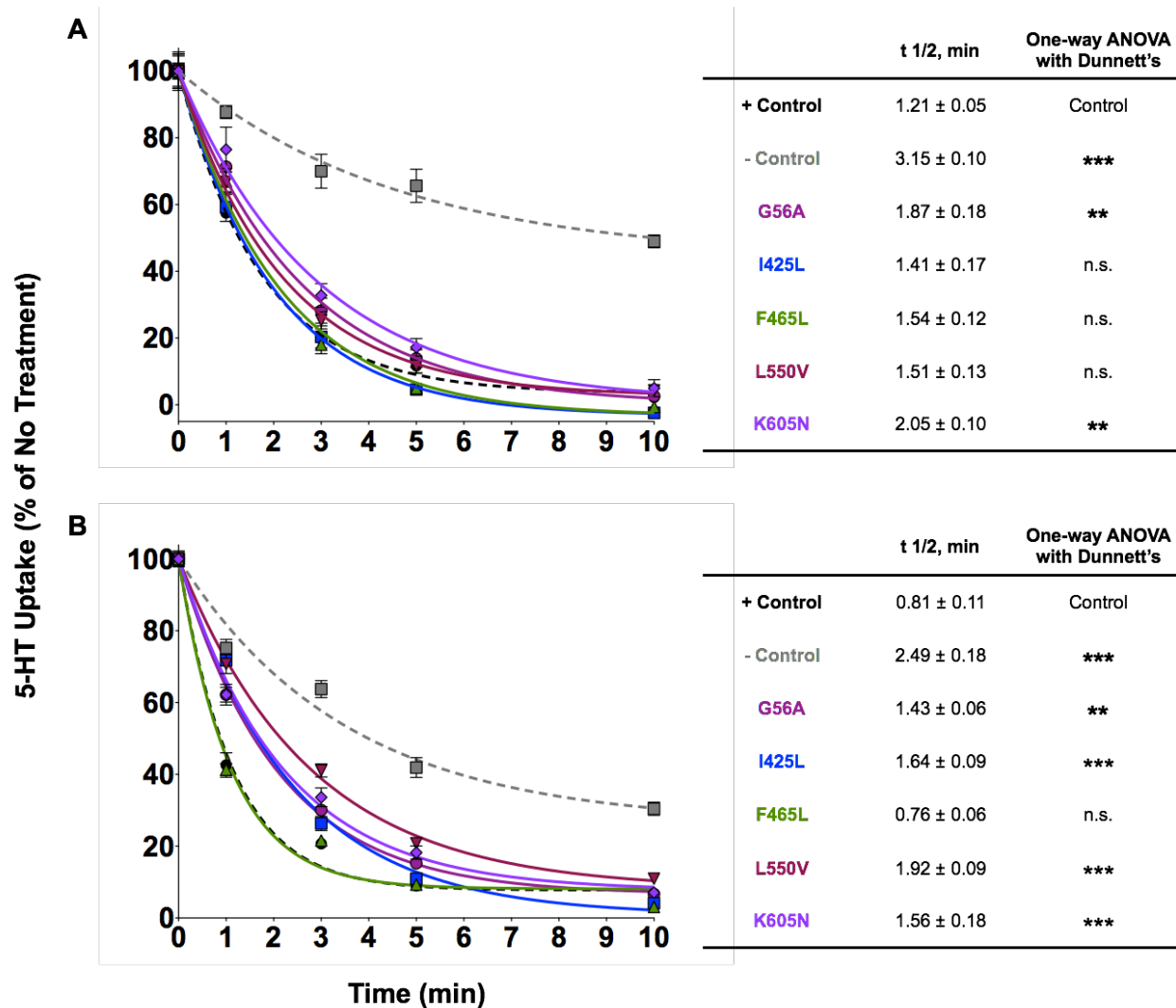


Figure 49. Cys-277 is more accessible to MTSEA in ASVs. HEK-GripTite cells plated at low- (a) or high-density (b) and transfected to express ASVs in the S277C/X5C background were treated with 2 mM MTSEA in PBS/CM buffer for the indicated time. Following treatment, the cells were assayed for [³H]5-HT transport (50 nM for 5 min). Transport activity is plotted as a percent of untreated cells and the values represent the mean ± S.E. from three or more independent experiments. The t ½ values are estimated from inactivation and analyzed with a one-way ANOVA followed by a post hoc Dunnett's test.

The intracellular location of the engineered Cys-277 probe requires the use of a membrane-permeant MTS reagent, MTSEA, which is (+) charged. Though Cys-109 is the most reactive extracellular cysteine to MTS reagents, membrane-permeant reagents can react with the several Cys residues on the cytoplasmic face that are accessible to MTS. For this reason, a Cys-reduced background was engineered such that the primary reactivity of MTSEA occurs at Cys-277 (Fig. 49, + *Control* is Cys-277/X5C and - *Control* is Ser-277/X5C) (Sato et al. 2004). Subsequently, each ASV was introduced into the S277C/X5C background and tested in low- and high-density cell systems for conformational changes based on changes in reactivity of MTSEA at Cys-277. In a low-density system, reactivity of MTSEA was decreased in the cytoplasmic, regulatory domain ASVs G56A and K605N (Fig. 49a). Similarly, in a high-density system, reactivity was decreased in the ASVs G56A and K605N as well as in the transmembrane domain ASVs I425L and L550V, but was unchanged from the positive control in the ASV background of F465L (Fig. 49b).

MTS Reactivity is Cation Dependent

Studies have revealed that Cys-109 accessibility is altered in a cation-dependent manner (Chen, Liu-Chen, and Rudnick 1997; Felts et al. 2014). Therefore, we chose to replace Na^+ in the buffer with the large monovalent cation *N*-methyl-D-glucamine (NMDG^+) in order to uncover ASV-induced conformational changes in an NMDG^+ -bound SERT conformation, as NMDG^+ cannot functionally replace or presumably bind to the highly selective Na^+ binding sites in SERT (Felts et al. 2014). Reactivity of the large, positively charged, and membrane-impermeant MTSET was increased at Cys-109 in the cytoplasmic, regulatory domain ASVs G56A and K605N in both low- and high-density systems buffered with NMDG^+ (Fig. 50a and 50b, respectively, + *Control* is Cys-109 and - *Control* is Ala-109). Furthermore, in a high-density

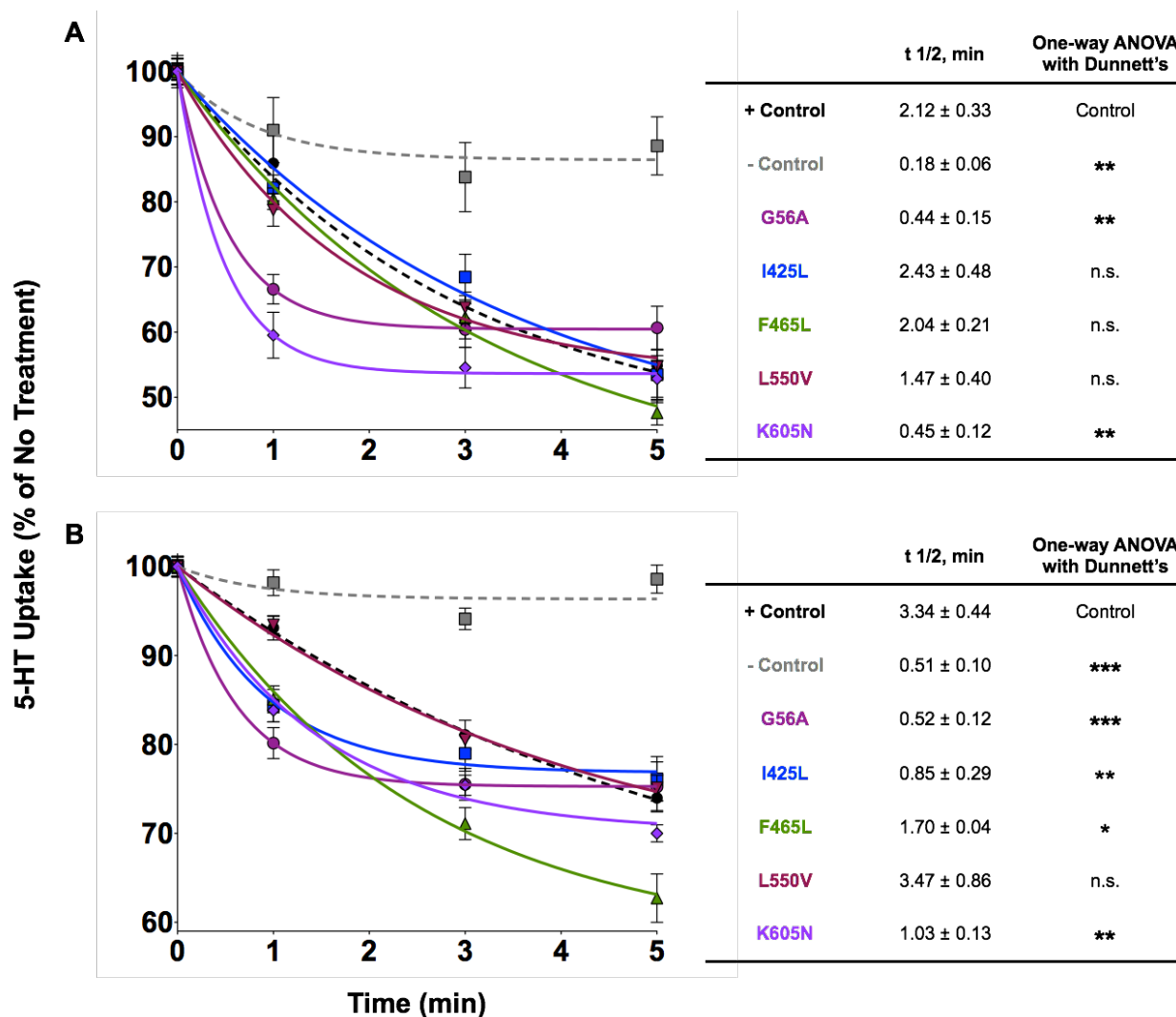


Figure 50. Cys-109 is more accessible to MTSET in sodium-free buffer in ASVs. HEK-GripTite cells plated at low- (a) or high-density (b) and transfected to express ASVs were treated with 1 mM MTSET in NMDG-Cl buffer for the indicated time. Following treatment, the cells were assayed for [³H]5-HT transport (50 nM for 5 min). Transport activity is plotted as a percent of untreated cells and the values represent the mean ± S.E. from three or more independent experiments. The t_{1/2} values are estimated from inactivation and analyzed with a one-way ANOVA followed by a post hoc Dunnett's test.

system, reactivity at Cys-109 was increased in the transmembrane domain ASV backgrounds I425L and F465L, but was unchanged from the positive control in the ASV background of L550V. Interestingly, MTSEA reactivity at Cys-277 was virtually identical between the ASV mutants and the positive control in NMDG⁺ buffered low- and high-density systems (Fig. 51a

and 51b, respectively, + *Control* is Cys-277/X5C and - *Control* is Ser-277/X5C). The similar MTSEA sensitivity is consistent with the transporters adopting a shared conformational state in the absence of Na⁺ that is not affected by the mutations. However, we cannot rule out the possibility that there are conformational changes in the ASVs that may not be proximal to or detected by the Cys-277 residue.

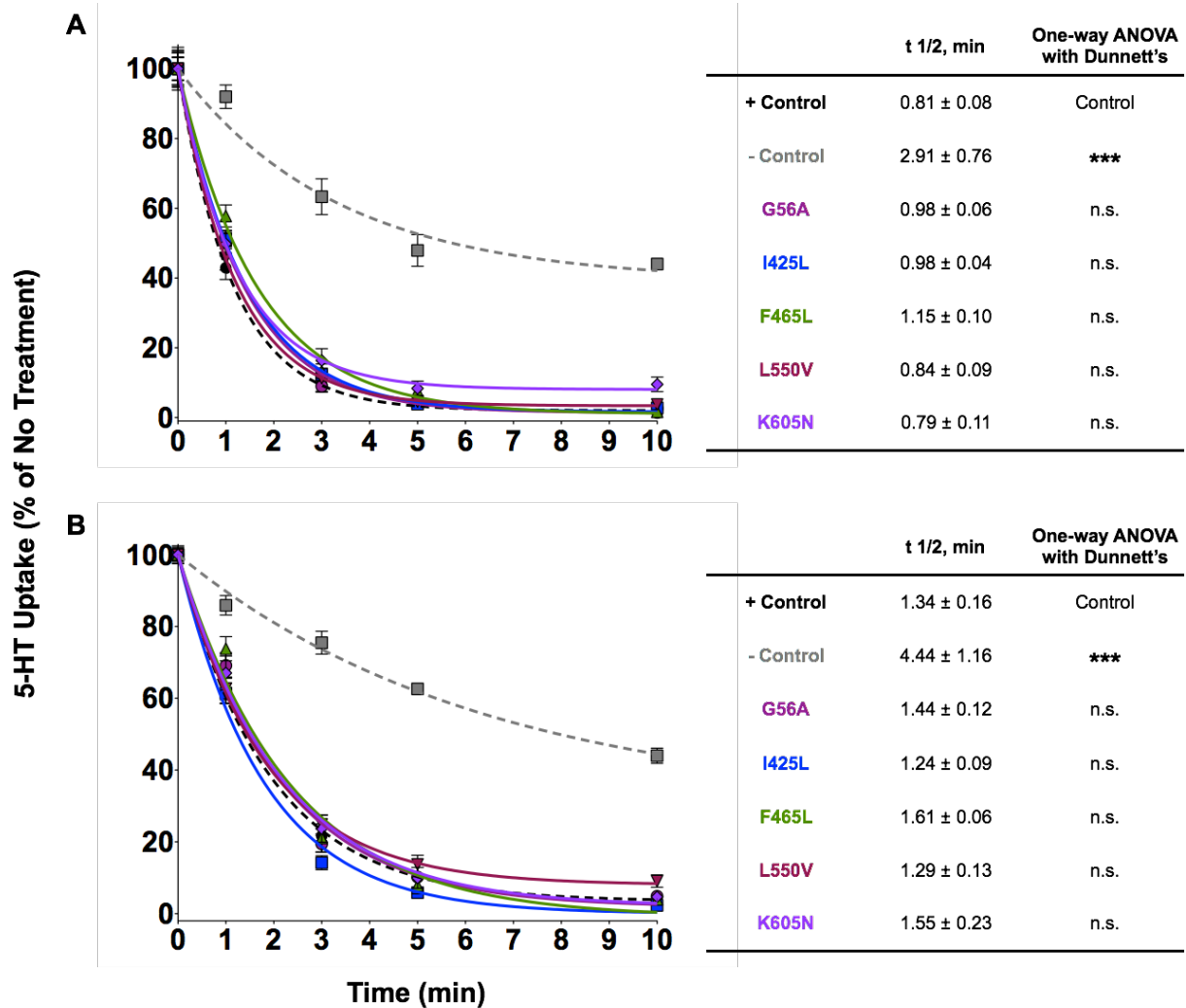


Figure 51. MTSEA reactivity at Cys-109 in sodium-free buffer is unaltered. HEK-GripTite cells plated at low- (a) or high-density (b) and transfected to express ASVs in the S277C/X5C background were treated with 2 mM MTSEA in NMDG-Cl buffer for the indicated time. Following treatment, the cells were assayed for [³H]5-HT transport (50 nM for 5 min). Transport activity is plotted as a percent of untreated cells and the values represent the mean ± S.E. from three or more independent experiments. The t ½ values are estimated from inactivation and analyzed with a one-way ANOVA followed by a post hoc Dunnett's test.

Effect of 5-HT and Cocaine on MTSEA Inactivation

In the presence of substrates, SERT undergoes multiple conformational changes while mediating substrate translocation (Jardetzky, 1966; Mitchell, 1990). Alternatively, antagonists can act by stabilizing occluded, extracellularly-facing, or intracellularly-facing conformations (Jacobs et al. 2007; Beuming et al. 2008; Schmitt, Rothman, and Reith 2013; Dahal et al. 2014; Wang, Penmatsa, and Gouaux 2015; Coleman, Green, and Gouaux 2016). We hypothesized that the ASVs may induce conformational changes that could become more evident with substrate or antagonist-bound SERT conformations. Therefore, we assessed how inactivation of transport by MTSEA was altered by preincubation with 5-HT or cocaine in the ASVs.

Addition of 5-HT decreases [³H]5-HT transport (Fig. 52, + *Control* is Cys-277/X5C and - *Control* is Ser-277/X5C), indicating that 5-HT increases the reactivity of MTSEA at Cys-277 (Zhang and Rudnick 2006; Jacobs et al. 2007). This result suggests that SERT accumulates in an inward-facing conformation when transporting 5-HT, thus increasing the accessibility of Cys-277 to MTSEA. In fact, a recent study showed that SERT will dwell in the inward-facing conformation longer before transitioning outward following addition of substrate, which is consistent with increased accessibility of Cys-277 (Zhang, Turk, and Rudnick 2016). Conversely, cocaine treatment yields an increase in [³H]5-HT transport (Fig. 52, + *Control*) resulting from a decrease in accessibility of Cys-277 to MTSEA, indicating cocaine induces a conformation that protects Cys-277 from MTSEA-induced transport inactivation. In the ASVs, accessibility of Cys-277 was unchanged after pretreatment with 5-HT compared to the positive control. Interestingly, cocaine protection from inactivation was observed with ASV F465L, but not with G56A, I425L, L550V, and K605N (Fig. 52). Importantly, these data are similar to those

highlighted in Fig. 49b, where the reactivity of MTSEA at Cys-277 was altered in ASVs G56A, I425L, L550V, and K605N, suggestive of a shared conformational change.

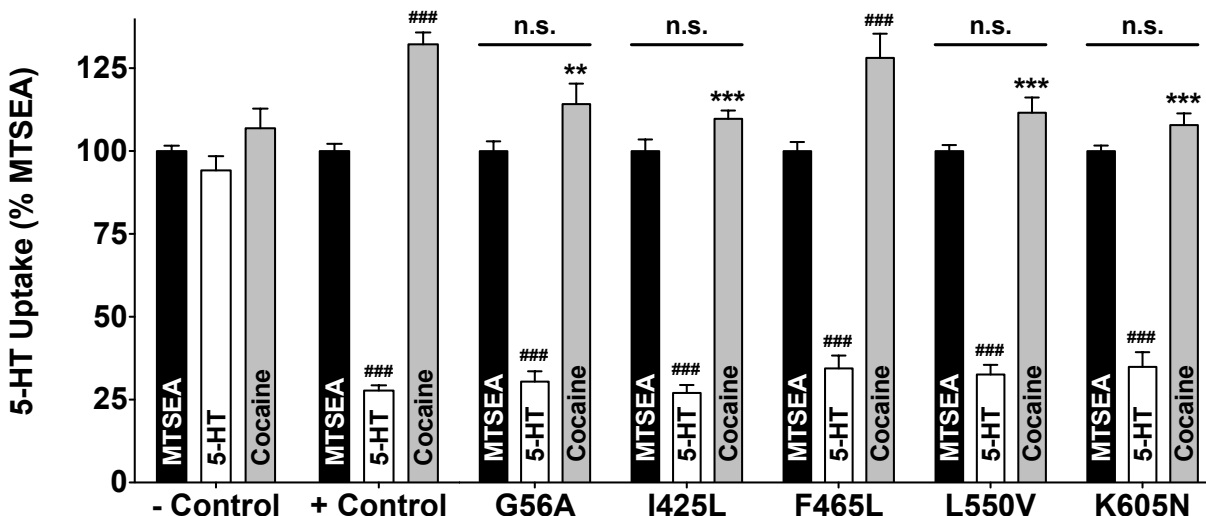


Figure 52. Cocaine does not protect Cys-277 from MTSEA inactivation in ASVs G56A, I425L, L550V, and K605N. HEK-GripTite cells transfected to express ASVs in the S277C/X5C background were pretreated with vehicle, 50 μ M 5-HT, or 50 μ M cocaine for 10 min before addition of 1 mM MTSEA in PBS/CM buffer for 10 min. After washing to remove unreacted MTSEA, remaining activity was assayed by [3 H]5-HT transport (50 nM for 5 min) and plotted as a percent of MTSEA-treated cells. ###, $p < 0.001$ - two-way ANOVA with Bonferroni post-hoc comparing treatments to MTSEA and **, $p < 0.01$; ***, $p < 0.001$ - two-way ANOVA with Bonferroni post-hoc comparing mutants to positive control. Data are the means \pm S.E. from three or more independent experiments.

PKG-mimicked SERT Phosphorylation Alters MTSEA Reactivity

The identification of Thr-276 in TM5 as the site of PKG-dependent phosphorylation (Ramamoorthy et al. 2007; Zhang et al. 2007) and the proximity of this residue to Cys-277 led us to question the impact of phosphorylation of Thr-276 on SERT conformation in ASV backgrounds. Thus, we engineered two backgrounds that would mimic hyper- (T276D) or de- (T276A) phosphorylated SERT. These mutants were evaluated for ability to transport 5-HT, the values from which were normalized to surface and total SERT expression to account for any changes in expression induced by the mutation, and assessed for conformational changes by testing for MTSEA reactivity at Cys-277.

[³H]5-HT transport in the T276D positive control increased ~600 fold by mimicking a hyperphosphorylated, PKG-stimulated transporter (Fig. 53, + Control is Cys-277/X5C), as PKG activation stimulates 5-HT transport (Miller and Hoffman 1994; Kilic, Murphy, and Rudnick 2003; Zhu et al. 2004). The T276A mutant however, which mimics dephosphorylated SERT, did not increase [³H]5-HT transport. In the ASVs, T276D increased [³H]5-HT transport in all mutant backgrounds, though not to the extent of the positive control, which may be the result of an already hyperphosphorylated transporter, whereas T276A in the ASVs only altered transport in mutant F465L (Fig. 53).

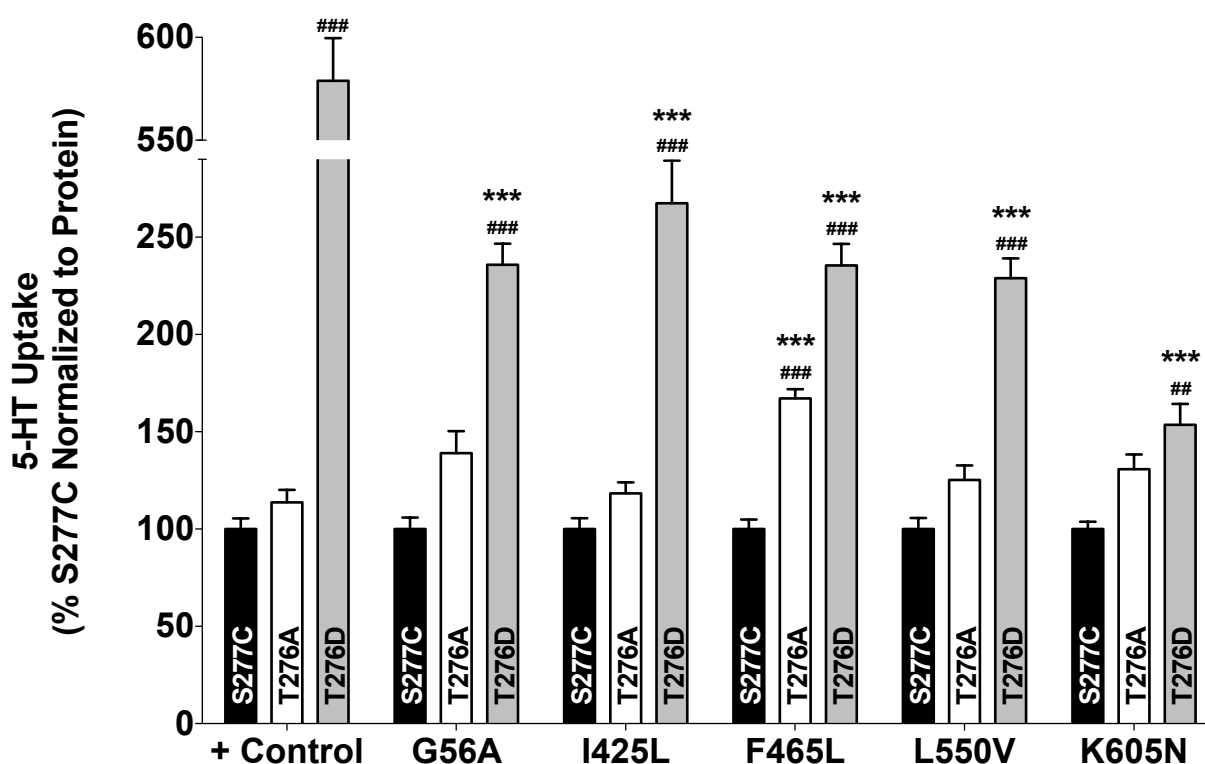


Figure 53. Transport is blunted in ASVs compared to control in the mimicked hyperphosphorylated T276D background. HEK-GripTite cells transfected to express ASVs in S277C/X5C PKG phosphorylation-dependent (S277C) or mimicked hyper- (T276D) and de- (T276A) phosphorylated backgrounds were assayed for transport activity by [³H]5-HT (50 nM for 5 min) and plotted as a percent of the S277C background following normalization to surface and total SERT expression. Values represent the mean \pm S.E. from three or more independent experiments. ##, $p < 0.01$; ###, $p < 0.001$ - two-way ANOVA with Bonferroni post-hoc comparing T276A and T276D backgrounds to S277C and ***, $p < 0.001$ - one-way ANOVA with Dunnett's post-hoc comparing mutants to positive control.

When challenged with MTSEA, [³H]5-HT transport is decreased in the T276D positive control pointing to a conformational change effected by the T276D mutation (Fig. 54, + *Control* is Cys-277/X5C). As phosphorylation by protein kinases is believed to occur at a site in an extended, not helical, conformation (Knighton et al. 1991; Bose et al. 2006; Goldsmith et al. 2007), these data and others suggest that the α -helix base of TM5 may unwind in order to support phosphorylation thereby increasing MTSEA reactivity at Cys-277 (Zhang et al. 2007; Zhang, Turk, and Rudnick 2016). In contrast, T276A results in an increase, or recovery, of [³H]5-HT transport, indicating protection of Cys-277 from MTSEA-induced inactivation.

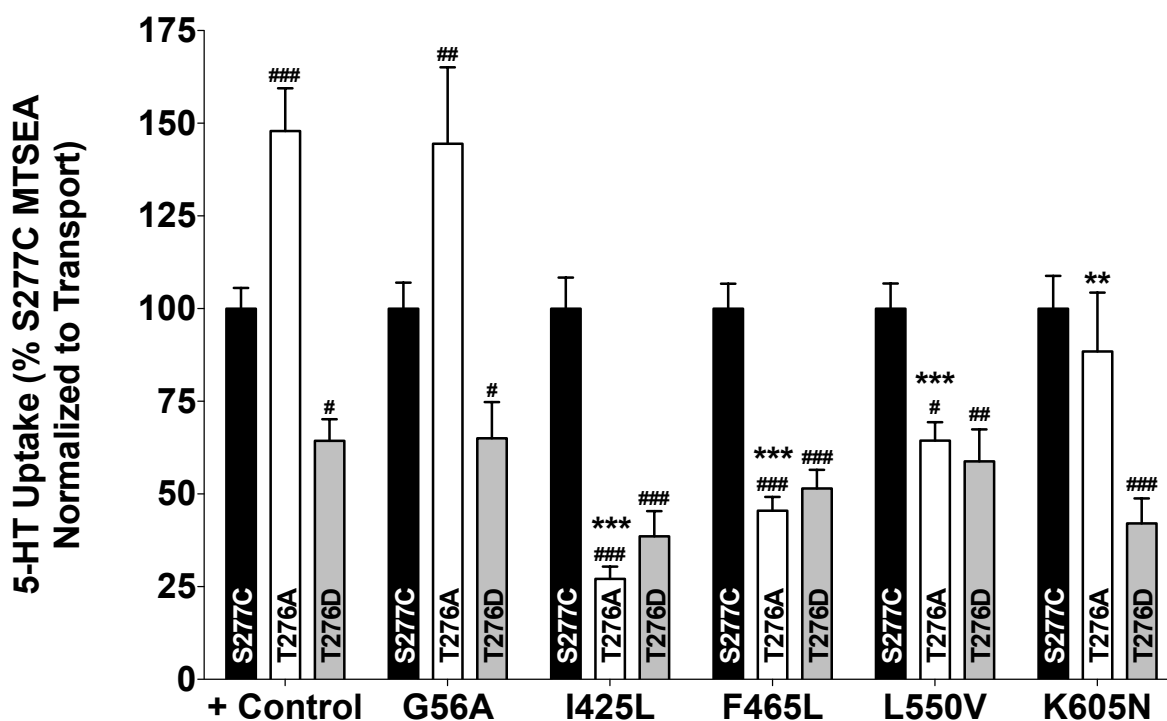


Figure 54. Accessibility of Cys-277 is altered in the ASVs compared to control in the mimicked dephosphorylated T276A background. HEK-GripTite cells transfected to express ASVs in S277C/X5C PKG phosphorylation-dependent (S277C) or mimicked hyper- (T276D) and de- (T276A) phosphorylated backgrounds were treated with 1 mM MTSEA in PBS/CM buffer for 10 min. Following treatment, cells were assayed for transport activity by [³H]5-HT (50 nM for 5 min) and plotted as a percent of the MTSEA-treated S277C background following normalization to baseline transport. Values represent the mean \pm S.E. from three or more independent experiments. #, $p < 0.05$; ##, $p < 0.01$; ###, $p < 0.001$ - two-way ANOVA with Bonferroni post-hoc comparing T276A and T276D backgrounds to S277C and **, $p < 0.01$; ***, $p < 0.001$ - one-way ANOVA with Dunnett's post-hoc comparing mutants to positive control.

Interestingly, addition of Asp-276 in the ASVs equally increased reactivity at Cys-277 compared to the positive control, as identified by decreased [³H]5-HT transport (Fig. 54), which suggests that a similar conformation is adopted in a mimicked hyperphosphorylated state. In contrast, addition of Ala-276 in the ASVs similarly decreased reactivity at Cys-277 compared to the positive control only in mutant G56A, as indicated by increased [³H]5-HT transport (Fig. 54), whereas reactivity was increased in ASVs I425L, F465L, and L550V, but unchanged in K605N.

Discussion

ASD is a complex neuropsychiatric disorder characterized by social, communication, and behavioral abnormalities. Previously, several rare, autism-associated SERT variants (ASVs) were identified in a genetic study of 120 families affected with ASD and, when considered together, correlated significantly with an elevated severity of rigid-compulsive behaviors (Tadevosyan-leyfer et al. 2003; Sutcliffe et al. 2005). Functional analyses of these variants indicated a shared increase in 5-HT transport relative to wild type hSERT through either increased catalytic activation or elevated surface density (Prasad et al. 2005; Prasad et al. 2009). Here, we extend analysis of the ASVs and reveal for the first time that ASVs G56A, I425L, F465L, L550V, and K605N induce changes in native SERT tertiary structure.

In physiologically buffered systems, MTSES reactivity was decreased at Cys-109 in ASVs G56A and K605N when cells were plated at a lower density, but the opposite was true in the presence of higher cell density, as the same ASVs increased the reactivity of MTSES at Cys-109. This discrepancy is likely explained by a change in cell-cell or protein-protein interactions that affect the accessibility of Cys-109 to MTSES. One possibility is the influence of membrane microdomains rich in cholesterol designated as lipid rafts. For example, we found that 5-HT transport was increased by ~40% in high cell density systems (data not shown) and, as identified

by Chang et al. (Chang et al. 2012; Rudnick et al. 2013), relaxation of the cytoskeletal-associated proteins tethering SERT to lipid rafts supports increased transport activity. As such, we propose that cell density affects insertion of SERT into lipid rafts through an, as yet, undefined mechanism and that accessibility of Cys-109 to MTSES is increased as a result of elevated transport activity associated with localization to untethered rafts. When Na^+ in the buffer was substituted with the larger, monovalent cation NMDG^+ , MTSET reactivity at Cys-109 was increased in ASVs G56A and K605N in both low and high cell density systems whereas an increase in reactivity at Cys-109 for variants I425L and F465L was only uncovered when tested in higher cell density.

Accessibility of Cys-277 to MTSEA in a physiological buffer was similarly decreased in ASVs G56A and K605N in a low-density system as well as in a high-density system, at which point a decrease in MTSEA reactivity was also observed with variants I425L and L550V. Interestingly, protection of Cys-277 by cocaine was identified only in the positive control and the ASV F465L whereas cocaine was unable to protect this site in variants G56A, I425L, L550V, and K605N, suggestive of a shared conformational change. Furthermore, replacement of Na^+ with the larger, monovalent cation NMDG^+ , which was recently shown to increase accessibility to Cys-277 by promoting an inward-facing conformation (Zhang, Turk, and Rudnick 2016), resulted in unchanged accessibility of Cys-277 to MTSEA in any ASV as compared to the positive control in both low and high cell density systems. These data suggest that addition of NMDG^+ promotes an inward-facing conformation that is similar between hSERT as the ASVs and that this conformation is adopted irrespective of cell density. In combination, the majority of conditions that tested accessibility of Cys-109 to MTS reagents identified an increase in reactivity whereas reactivity at Cys-277 is decreased. Collectively these findings suggest that the

ASVs G56A, F465L, and K605N alter SERT tertiary structure by increasing the amount of transporters in an outward-facing conformation (Fig. 55). Thus, the elevated transport capacity of ASVs may result from an increase in the number of transporters ready to accept substrate or through altered accessibility to a kinase or phosphatase that regulates surface expression.

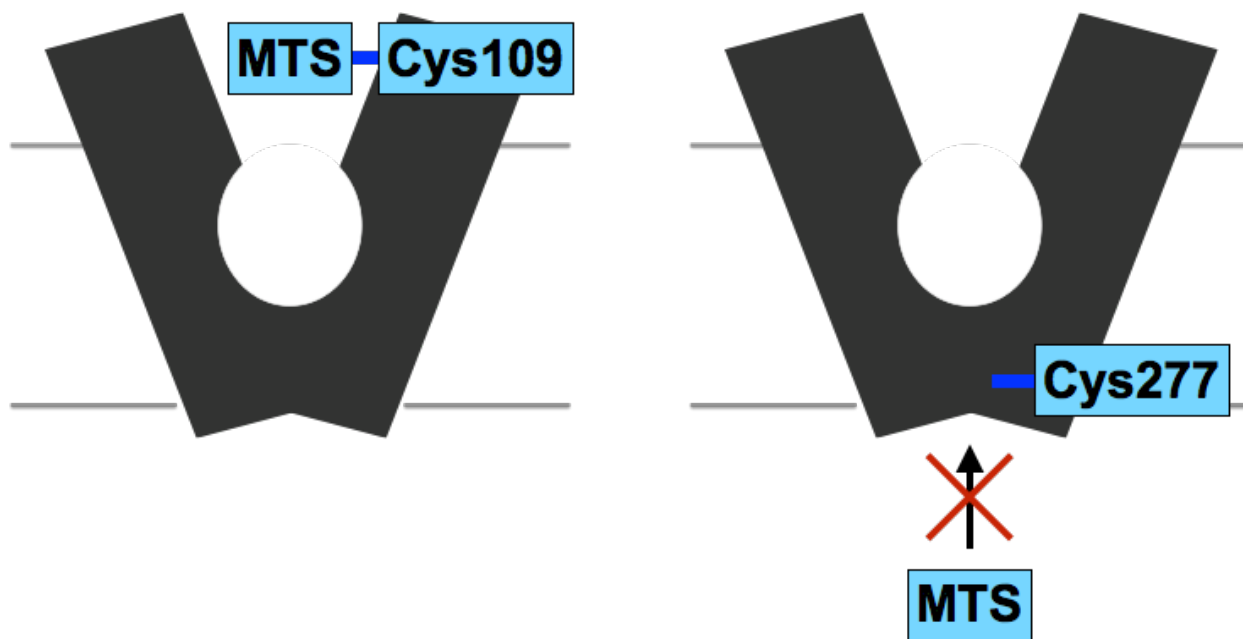


Figure 55. ASVs induce an outward-facing conformation. ASVs G56A, F465L, and K605N increase reactivity at Cys-109, but decrease reactivity at Cys-277, suggestive of an outward-facing conformation. These variants are in a conformation ready to accept substrate, which may explain the increase in 5-HT transport, or this conformational change may alter regulation on the cytoplasmic face by impacting protein-protein interactions.

Though we have established the ability of ASVs to impact tertiary structure, we have not yet identified a direct correlation between altered conformation and elevated 5-HT transport. As SERT function and cellular distribution are modified by interacting proteins, including protein kinases and phosphatases, a single nucleotide polymorphism at or near a site of interaction would certainly provide insight into the mechanism underlying modified SERT structure and function. To date, there are no known protein interactions that depend on the ASV residues analyzed here, though an ASV-induced change in SERT conformation may ultimately lead to modulation of a

protein binding site elsewhere in SERT. For example, Carneiro et al. identified a physical association between SERT and the integrin membrane receptor α IIB β 3 at a site in the C-terminus (Carneiro et al. 2008), genetic variation of which, like SERT, is associated with elevated whole blood 5-HT (Weiss et al. 2004; Weiss et al. 2005; Muller, Anacker, and Veenstra-VanderWeele 2016). Furthermore, a functional association exists as isoforms of integrin β 3 alter SERT transport activity, surface trafficking, and subcellular localization (Carneiro et al. 2008). Thus, based on the proposed C-terminal interaction of α IIB β 3 with SERT and the location of the ASV K605N on the C-terminus, it is plausible that the interactions stabilizing α IIB β 3 and SERT would be altered. This hypothesis and others will be assessed in our future studies in order to identify specific mechanisms linking the structural and functional effects observed in the ASVs.

REFERENCES

- Abramson, J., & Wright, E. M. (2009). Structure and function of Na(+)-symporters with inverted repeats. *Current Opinion in Structural Biology*, *19*(4), 425–432.
- Adkins, E. M., Samuvel, D. J., Fog, J. U., Eriksen, J., Jayanthi, L. D., Vaegter, C. B., ... Gether, U. (2007). Membrane mobility and microdomain association of the dopamine transporter studied with fluorescence correlation spectroscopy and fluorescence recovery after photobleaching. *Biochemistry*, *46*(37), 10484–10497.
- Agoston, G. E., Vaughan, R., Lever, J. R., Izenwasser, S., Terry, P. D., & Newman, A. H. (1997). A novel photoaffinity label for the dopamine transporter based on N-substituted 3 α -[bis(4'-fluorophenyl)methoxy]tropane. *Bioorganic & Medicinal Chemistry Letters*, *7*(23), 3027–3032.
- Agoston, G. E., Wu, J. H., Izenwasser, S., George, C., Katz, J., Kline, R. H., & Newman, A. H. (1997). Novel N-substituted 3 α -[bis(4'-fluorophenyl)methoxy]tropane analogues: selective ligands for the dopamine transporter. *Journal of Medicinal Chemistry*, *40*(26), 4329–4339.
- Agoston, G. E., Wu, J. H., Izenwasser, S., George, C., Katz, J., Kline, R. H., & Newman, A. H. (1997). Novel N-substituted 3 α -[bis(4'-fluorophenyl)methoxy]tropane analogues: selective ligands for the dopamine transporter. *Journal of Medicinal Chemistry*, *40*(26), 4329–4339.
- Amara, S. G., & Kuhar, M. J. (1993). Neurotransmitter Transporters: Recent Progress. *Annual Review of Neuroscience*, *16*(1), 73–93.
- Amara, S. G., & Sonders, M. S. (1998). Neurotransmitter transporters as molecular targets for addictive drugs. *Drug and Alcohol Dependence*, *51*(1-2), 87–96.
- American Psychiatric Association. (2013). *Diagnostic and statistical manual of mental disorders (5th ed.)*. American Psychiatric Publishing, Arlington, VA.
- Andersen, J., Kristensen, A. S., Bang-Andersen, B., & Strømgaard, K. (2009). Recent advances in the understanding of the interaction of antidepressant drugs with serotonin and norepinephrine transporters. *Chemical Communications*, (25), 3677–3692.
- Andersen, J., Taboureau, O., Hansen, K. B., Olsen, L., Egebjerg, J., Strømgaard, K., & Kristensen, A. S. (2009). Location of the antidepressant binding site in the serotonin transporter: importance of Ser-438 in recognition of citalopram and tricyclic antidepressants. *The Journal of Biological Chemistry*, *284*(15), 10276–10284.

- Anderson, G. M., Feibel, F. C., & Cohen, D. J. (1987). Determination of serotonin in whole blood, platelet-rich plasma, platelet-poor plasma and plasma ultrafiltrate. *Life Sciences*, *40*(11), 1063–1070.
- Androutsellis-Theotokis, A., Ghassemi, F., & Rudnick, G. (2001). A conformationally sensitive residue on the cytoplasmic surface of serotonin transporter. *The Journal of Biological Chemistry*, *276*(49), 45933–45938.
- Anguelova, M., Benkelfat, C., & Turecki, G. (2003). A systematic review of association studies investigating genes coding for serotonin receptors and the serotonin transporter: I. Affective disorders. *Molecular Psychiatry*, *8*(6), 574–591.
- Azima, H., & Vispo, R. H. (1958). IMIPRAMINE: A POTENT NEW ANTI-DEPRESSANT COMPOUND. *The American Journal of Psychiatry*, *115*(3), 245–246.
- Baganz, N. L., & Blakely, R. D. (2013a). A Dialogue between the Immune System and Brain, Spoken in the Language of Serotonin. *ACS Chemical Neuroscience*, *4*(1), 48–63.
- Baganz, N. L., & Blakely, R. D. (2013b). A Dialogue between the Immune System and Brain, Spoken in the Language of Serotonin. *ACS Chemical Neuroscience*, *4*(1), 48–63.
- Bailey, A., Le Couteur, A., Gottesman, I., Bolton, P., Simonoff, E., Yuzda, E., & Rutter, M. (1995). Autism as a strongly genetic disorder: evidence from a British twin study. *Psychological Medicine*, *25*(1), 63–77.
- Banala, A. K., Zhang, P., Plenge, P., Cyriac, G., Kopajtic, T., Katz, J. L., ... Newman, A. H. (2013). Design and synthesis of 1-(3-(dimethylamino)propyl)-1-(4-fluorophenyl)-1,3-dihydroisobenzofuran-5-carbonitrile (citalopram) analogues as novel probes for the serotonin transporter S1 and S2 binding sites. *Journal of Medicinal Chemistry*, *56*(23), 9709–9724.
- Barker, E. L., & Blakely, R. D. (1995). Norepinephrine and serotonin transporters: molecular targets of antidepressant drugs. *Psychopharmacology: The Fourth Generation of Progress*, *28*, 321–333.
- Barker, E. L., Moore, K. R., Rakhshan, F., & Blakely, R. D. (1999). Transmembrane domain I contributes to the permeation pathway for serotonin and ions in the serotonin transporter. *The Journal of Neuroscience: The Official Journal of the Society for Neuroscience*, *19*(12), 4705–4717.
- Barker, E. L., Perlman, M. A., Adkins, E. M., Houlihan, W. J., Pristupa, Z. B., Niznik, H. B., & Blakely, R. D. (1998). High affinity recognition of serotonin transporter antagonists defined by species-scanning mutagenesis. An aromatic residue in transmembrane domain I dictates species-selective recognition of citalopram and mazindol. *The Journal of Biological Chemistry*, *273*(31), 19459–19468.
- Baumann, M. H., Char, G. U., De Costa, B. R., Rice, K. C., & Rothman, R. B. (1994). GBR12909 attenuates cocaine-induced activation of mesolimbic dopamine neurons in the rat. *The Journal of Pharmacology and Experimental Therapeutics*, *271*(3), 1216–1222.

- Beaulieu, J.-M., & Gainetdinov, R. R. (2011). The physiology, signaling, and pharmacology of dopamine receptors. *Pharmacological Reviews*, *63*(1), 182–217.
- Bengel, D., Murphy, D. L., Andrews, A. M., Wichems, C. H., Feltner, D., Heils, A., ... Lesch, K.-P. (1998). Altered brain serotonin homeostasis and locomotor insensitivity to 3, 4-methylenedioxymethamphetamine (“Ecstasy”) in serotonin transporter-deficient mice. *Molecular Pharmacology*, *53*(4), 649–655.
- Berger, M., Gray, J. A., & Roth, B. L. (2009). The Expanded Biology of Serotonin. *Annual Review of Medicine*, *60*(1), 355–366.
- Bergman, J., Madras, B. K., Johnson, S. E., & Spealman, R. D. (1989). Effects of cocaine and related drugs in nonhuman primates. III. Self-administration by squirrel monkeys. *The Journal of Pharmacology and Experimental Therapeutics*, *251*(1), 150–155.
- Beuming, T., Kniazeff, J., Bergmann, M. L., Shi, L., Gracia, L., Raniszewska, K., ... Loland, C. J. (2008). The binding sites for cocaine and dopamine in the dopamine transporter overlap. *Nature Neuroscience*, *11*(7), 780–789.
- Beuming, T., Shi, L., Javitch, J. A., & Weinstein, H. (2006). A comprehensive structure-based alignment of prokaryotic and eukaryotic neurotransmitter/Na⁺ symporters (NSS) aids in the use of the LeuT structure to probe NSS structure and function. *Molecular Pharmacology*, *70*(5), 1630–1642.
- Biederman, J., & Spencer, T. (1999). Attention-deficit/hyperactivity disorder (ADHD) as a noradrenergic disorder. *Biological Psychiatry*, *46*(9), 1234–1242.
- Bisgaard, H., Larsen, M. A. B., Mazier, S., Beuming, T., Newman, A. H., Weinstein, H., ... Gether, U. (2011). The binding sites for benzotropines and dopamine in the dopamine transporter overlap. *Neuropharmacology*, *60*(1), 182–190.
- Björklund, A., & Dunnett, S. B. (2007). Fifty years of dopamine research. *Trends in Neurosciences*, *30*(5), 185–187.
- Blakely, R. D., & Edwards, R. H. (2012). Vesicular and plasma membrane transporters for neurotransmitters. *Cold Spring Harbor Perspectives in Biology*, *4*(2). <http://doi.org/10.1101/cshperspect.a005595>
- Bloch, M. H., Landeros-Weisenberger, A., Sen, S., Dombrowski, P., Kelmendi, B., Coric, V., ... Leckman, J. F. (2008). Association of the serotonin transporter polymorphism and obsessive-compulsive disorder: Systematic review. *American Journal of Medical Genetics. Part B, Neuropsychiatric Genetics: The Official Publication of the International Society of Psychiatric Genetics*, *147*(6), 850–858.
- Bohn, L. M., Xu, F., Gainetdinov, R. R., & Caron, M. G. (2000). Potentiated opioid analgesia in norepinephrine transporter knock-out mice. *The Journal of Neuroscience: The Official Journal of the Society for Neuroscience*, *20*(24), 9040–9045.

- Boja, J. W., Carroll, F. I., Vaughan, R. A., Kopajtic, T., & Kuhar, M. J. (1998). Multiple binding sites for [125I]RTI-121 and other cocaine analogs in rat frontal cerebral cortex. *Synapse*, 30(1), 9–17.
- Bose, R., Holbert, M. A., Pickin, K. A., & Cole, P. A. (2006). Protein tyrosine kinase-substrate interactions. *Current Opinion in Structural Biology*, 16(6), 668–675.
- Bossé, R., Fumagalli, F., Jaber, M., Giros, B., Gainetdinov, R. R., Wetsel, W. C., ... Caron, M. G. (1997). Anterior pituitary hypoplasia and dwarfism in mice lacking the dopamine transporter. *Neuron*, 19(1), 127–138.
- Boudker, O., & Verdon, G. (2010). Structural perspectives on secondary active transporters. *Trends in Pharmacological Sciences*, 31(9), 418–426.
- Bowton, E., Saunders, C., Erreger, K., Sakrikar, D., Matthies, H. J., Sen, N., ... Galli, A. (2010). Dysregulation of dopamine transporters via dopamine D2 autoreceptors triggers anomalous dopamine efflux associated with attention-deficit hyperactivity disorder. *The Journal of Neuroscience: The Official Journal of the Society for Neuroscience*, 30(17), 6048–6057.
- Bowton, E., Saunders, C., Reddy, I. A., Campbell, N. G., Hamilton, P. J., Henry, L. K., ... Galli, A. (2014). SLC6A3 coding variant Ala559Val found in two autism probands alters dopamine transporter function and trafficking. *Translational Psychiatry*, 4, e464.
- Bröer, S. (2006). The SLC6 orphans are forming a family of amino acid transporters. *Neurochemistry International*, 48(6-7), 559–567.
- Bröer, S., & Gether, U. (2012). The solute carrier 6 family of transporters. *British Journal of Pharmacology*, 167(2), 256–278.
- Brose, S. A., Baker, A. G., & Golovko, M. Y. (2013). A fast one-step extraction and UPLC-MS/MS analysis for E2/D 2 series prostaglandins and isoprostanes. *Lipids*, 48(4), 411–419.
- Brose, S. A., & Golovko, M. Y. (2013). Eicosanoid post-mortem induction in kidney tissue is prevented by microwave irradiation. *Prostaglandins, Leukotrienes, and Essential Fatty Acids*, 89(5), 313–318.
- Brose, S. A., Golovko, S. A., & Golovko, M. Y. (2016). Brain 2-Arachidonoylglycerol Levels Are Dramatically and Rapidly Increased Under Acute Ischemia-Injury Which Is Prevented by Microwave Irradiation. *Lipids*, 51(4), 487–495.
- Caplan, D. A., Subbotina, J. O., & Noskov, S. Y. (2008). Molecular mechanism of ion-ion and ion-substrate coupling in the Na⁺-dependent leucine transporter LeuT. *Biophysical Journal*, 95(10), 4613–4621.
- Carlsson, A. (1987). Perspectives on the discovery of central monoaminergic neurotransmission. *Annual Review of Neuroscience*, 10, 19–40.
- Carneiro, A. M. D., & Blakely, R. D. (2006). Serotonin-, protein kinase C-, and Hic-5-associated redistribution of the platelet serotonin transporter. *The Journal of Biological Chemistry*, 281(34), 24769–24780.

- Carneiro, A. M. D., Cook, E. H., Murphy, D. L., & Blakely, R. D. (2008). Interactions between integrin α IIb β 3 and the serotonin transporter regulate serotonin transport and platelet aggregation in mice and humans. *The Journal of Clinical Investigation*, 118(4), 1544–1552.
- Caron, M. G., & Gether, U. (2016). Structural biology: Antidepressants at work. *Nature*, 532(7599), 320–321.
- Carroll, F. I., Blough, B. E., Abraham, P., Mills, A. C., Holleman, J. A., Wolckenhauer, S. A., ... Forster, M. J. (2009). Synthesis and biological evaluation of bupropion analogues as potential pharmacotherapies for cocaine addiction. *Journal of Medicinal Chemistry*, 52(21), 6768–6781.
- Carroll, F. I., Gao, Y., Abraham, P., Lewin, A. H., Lew, R., Patel, A., ... Kuhar, M. J. (1992). Probes for the cocaine receptor. Potentially irreversible ligands for the dopamine transporter. *Journal of Medicinal Chemistry*, 35(10), 1813–1817.
- Carroll, F. I., Gao, Y. G., Rahman, M. A., Abraham, P., Parham, K., Lewin, A. H., ... Kuhar, M. J. (1991). Synthesis, ligand binding, QSAR, and CoMFA study of 3 beta-(p-substituted phenyl)tropane-2 beta-carboxylic acid methyl esters. *Journal of Medicinal Chemistry*, 34(9), 2719–2725.
- Carroll, F. I., Mascarella, S. W., Kuzemko, M. A., Gao, Y., Abraham, P., Lewin, A. H., ... Kuhar, M. J. (1994). Synthesis, ligand binding, and QSAR (CoMFA and classical) study of 3 beta-(3'-substituted phenyl)-, 3 beta-(4'-substituted phenyl)-, and 3 beta-(3',4'-disubstituted phenyl)tropane-2 beta-carboxylic acid methyl esters. *Journal of Medicinal Chemistry*, 37(18), 2865–2873.
- Cha, J. H., Zou, M.-F., Adkins, E. M., Rasmussen, S. G. F., Loland, C. J., Schoenenberger, B., ... Newman, A. H. (2005). Rhodamine-labeled 2beta-carbomethoxy-3beta-(3,4-dichlorophenyl)tropane analogues as high-affinity fluorescent probes for the dopamine transporter. *Journal of Medicinal Chemistry*, 48(24), 7513–7516.
- Chang, J. C., Tomlinson, I. D., Warnement, M. R., Ustione, A., Carneiro, A. M. D., Piston, D. W., ... Rosenthal, S. J. (2012). Single molecule analysis of serotonin transporter regulation using antagonist-conjugated quantum dots reveals restricted, p38 MAPK-dependent mobilization underlying uptake activation. *The Journal of Neuroscience: The Official Journal of the Society for Neuroscience*, 32(26), 8919–8929.
- Chemical Computing Group, Inc. (2012). *Molecular Operating Environment*, Chemical Computing Group Inc., Montreal, Quebec, Canada.
- Chen, F., Larsen, M. B., Sánchez, C., & Wiborg, O. (2005). The S-enantiomer of R,S-citalopram, increases inhibitor binding to the human serotonin transporter by an allosteric mechanism. Comparison with other serotonin transporter inhibitors. *European Neuropsychopharmacology: The Journal of the European College of Neuropsychopharmacology*, 15(2), 193–198.
- Cheng, M. H., & Bahar, I. (2015). Molecular Mechanism of Dopamine Transport by Human Dopamine Transporter. *Structure*, 23(11), 2171–2181.

- Cheng, M. H., Block, E., Hu, F., Cobanoglu, M. C., Sorkin, A., & Bahar, I. (2015). Insights into the Modulation of Dopamine Transporter Function by Amphetamine, Orphenadrine, and Cocaine Binding. *Frontiers in Neurology*, *6*, 134.
- Chen, J.-G., Liu-Chen, S., & Rudnick, G. (1997). External Cysteine Residues in the Serotonin Transporter†. *Biochemistry*, *36*(6), 1479–1486.
- Chen, J. G., Sachpatzidis, A., & Rudnick, G. (1997). The third transmembrane domain of the serotonin transporter contains residues associated with substrate and cocaine binding. *The Journal of Biological Chemistry*, *272*(45), 28321–28327.
- Chen, N.-H., Reith, M. E. A., & Quick, M. W. (2004). Synaptic uptake and beyond: the sodium- and chloride-dependent neurotransmitter transporter family SLC6. *Pflugers Archiv: European Journal of Physiology*, *447*(5), 519–531.
- Chen, N., & Reith, M. E. A. (2004). Interaction between dopamine and its transporter: role of intracellular sodium ions and membrane potential. *Journal of Neurochemistry*, *89*(3), 750–765.
- Chen, N., Vaughan, R. A., & Reith, M. E. (2001). The role of conserved tryptophan and acidic residues in the human dopamine transporter as characterized by site-directed mutagenesis. *Journal of Neurochemistry*, *77*(4), 1116–1127.
- Chen, N., Zhen, J., & Reith, M. E. A. (2004). Mutation of Trp84 and Asp313 of the dopamine transporter reveals similar mode of binding interaction for GBR12909 and benztropine as opposed to cocaine. *Journal of Neurochemistry*, *89*(4), 853–864.
- Chen, R., Daining, C. P., Sun, H., Fraser, R., Stokes, S. L., Leitges, M., & Gnegy, M. E. (2013). Protein kinase C β is a modulator of the dopamine D2 autoreceptor-activated trafficking of the dopamine transporter. *Journal of Neurochemistry*, *125*(5), 663–672.
- Chen, R., Han, D. D., & Gu, H. H. (2005). A triple mutation in the second transmembrane domain of mouse dopamine transporter markedly decreases sensitivity to cocaine and methylphenidate. *Journal of Neurochemistry*, *94*(2), 352–359.
- Chen, R., Tilley, M. R., Wei, H., Zhou, F., Zhou, F.-M., Ching, S., ... Gu, H. H. (2006). Abolished cocaine reward in mice with a cocaine-insensitive dopamine transporter. *Proceedings of the National Academy of Sciences of the United States of America*, *103*(24), 9333–9338.
- Chi, L., & Reith, M. E. A. (2003). Substrate-induced trafficking of the dopamine transporter in heterologously expressing cells and in rat striatal synaptosomal preparations. *The Journal of Pharmacology and Experimental Therapeutics*, *307*(2), 729–736.
- Cho, H. J., Meira-Lima, I., Cordeiro, Q., Michelon, L., Sham, P., Vallada, H., & Collier, D. A. (2005). Population-based and family-based studies on the serotonin transporter gene polymorphisms and bipolar disorder: a systematic review and meta-analysis. *Molecular Psychiatry*, *10*(8), 771–781.

- Choudhury, A., Dominguez, M., Puri, V., Sharma, D. K., Narita, K., Wheatley, C. L., ... Pagano, R. E. (2002). Rab proteins mediate Golgi transport of caveola-internalized glycosphingolipids and correct lipid trafficking in Niemann-Pick C cells. *The Journal of Clinical Investigation*, *109*(12), 1541–1550.
- Clarke, H., Flint, J., Attwood, A. S., & Munafò, M. R. (2010). Association of the 5-HTTLPR genotype and unipolar depression: a meta-analysis. *Psychological Medicine*, *40*(11), 1767–1778.
- Cline, E. J., Scheffel, U., Boja, J. W., Carroll, F. I., Katz, J. L., & Kuhar, M. J. (1992). Behavioral effects of novel cocaine analogs: a comparison with in vivo receptor binding potency. *The Journal of Pharmacology and Experimental Therapeutics*, *260*(3), 1174–1179.
- Coccaro, E. F. (1989). Central serotonin and impulsive aggression. *The British Journal of Psychiatry. Supplement*, *(8)*, 52–62.
- Coleman, J. A., Green, E. M., & Gouaux, E. (2016). X-ray structures and mechanism of the human serotonin transporter. *Nature*, *532*(7599), 334–339.
- Combs, S. A., DeLuca, S. L., DeLuca, S. H., Lemmon, G. H., Nannemann, D. P., Nguyen, E. D., ... Meiler, J. (2013). Small-molecule ligand docking into comparative models with Rosetta. *Nature Protocols*, *8*(7), 1277–1298.
- Cook, E. H., Jr, Courchesne, R., Lord, C., Cox, N. J., Yan, S., Lincoln, A., ... Leventhal, B. L. (1997). Evidence of linkage between the serotonin transporter and autistic disorder. *Molecular Psychiatry*, *2*(3), 247–250.
- Cook, E. H., & Leventhal, B. L. (1996). The serotonin system in autism. *Current Opinion in Pediatrics*, *8*(4), 348–354.
- Cordeiro, Q., Quirino, C., Jacqueline, S.-R., & Homero, V. (2010). Association between the SLC6A3 A1343G polymorphism and schizophrenia. *Arquivos de Neuro-Psiquiatria*, *68*(5), 716–719.
- Cremona, M. L., Matthies, H. J. G., Pau, K., Bowton, E., Speed, N., Lute, B. J., ... Yamamoto, A. (2011). Flotillin-1 is essential for PKC-triggered endocytosis and membrane microdomain localization of DAT. *Nature Neuroscience*, *14*(4), 469–477.
- Dahal, R. A., Pramod, A. B., Sharma, B., Krout, D., Foster, J. D., Cha, J. H., ... Henry, L. K. (2014). Computational and Biochemical Docking of the Irreversible Cocaine Analog RTI 82 Directly Demonstrates Ligand Positioning in the Dopamine Transporter Central Substrate-binding Site. *The Journal of Biological Chemistry*, *289*(43), 29712–29727.
- Darden, T., York, D., & Pedersen, L. (1993). Particle mesh Ewald: An $N \cdot \log(N)$ method for Ewald sums in large systems. *The Journal of Chemical Physics*, *98*(12), 10089–10092.
- Daws, L. C., Callaghan, P. D., Morón, J. A., Kahlig, K. M., Shippenberg, T. S., Javitch, J. A., & Galli, A. (2002). Cocaine increases dopamine uptake and cell surface expression of dopamine transporters. *Biochemical and Biophysical Research Communications*, *290*(5), 1545–1550.

- Daws, L. C., & Gould, G. G. (2011). Ontogeny and regulation of the serotonin transporter: Providing insights into human disorders. *Pharmacology & Therapeutics*, *131*(1), 61–79.
- DeFelice, L. J., & Galli, A. (1998). Electrophysiological analysis of transporter function. *Advances in Pharmacology*, *42*, 186–190.
- Delano W. L. (2013). *The PyMOL Molecular Graphics System*, Version 1.6, Schrödinger, LLC, New York.
- Desai, R. I., Kopajtic, T. A., Koffarnus, M., Newman, A. H., & Katz, J. L. (2005). Identification of a dopamine transporter ligand that blocks the stimulant effects of cocaine. *The Journal of Neuroscience: The Official Journal of the Society for Neuroscience*, *25*(8), 1889–1893.
- Du, L., Faludi, G., Palkovits, M., Bakish, D., & Hrdina, P. D. (2001). Serotonergic genes and suicidality. *Crisis*, *22*(2), 54–60.
- Du, L., Faludi, G., Palkovits, M., Demeter, E., Bakish, D., Lapierre, Y. D., ... Hrdina, P. D. (1999). Frequency of long allele in serotonin transporter gene is increased in depressed suicide victims. *Biological Psychiatry*, *46*(2), 196–201.
- Eiden, L. E., Schäfer, M. K.-H., Weihe, E., & Schütz, B. (2003). The vesicular amine transporter family (SLC18): amine/proton antiporters required for vesicular accumulation and regulated exocytotic secretion of monoamines and acetylcholine. *Pflügers Archiv*, *447*(5), 636–640.
- Eriksen, J., Bjørn-Yoshimoto, W. E., Jørgensen, T. N., Newman, A. H., & Gether, U. (2010). Postendocytic sorting of constitutively internalized dopamine transporter in cell lines and dopaminergic neurons. *The Journal of Biological Chemistry*, *285*(35), 27289–27301.
- Eriksen, J., Rasmussen, S. G. F., Rasmussen, T. N., Vaegter, C. B., Cha, J. H., Zou, M.-F., ... Gether, U. (2009). Visualization of dopamine transporter trafficking in live neurons by use of fluorescent cocaine analogs. *The Journal of Neuroscience: The Official Journal of the Society for Neuroscience*, *29*(21), 6794–6808.
- Eshleman, A. J., Carmolli, M., Cumbay, M., Martens, C. R., Neve, K. A., & Janowsky, A. (1999). Characteristics of drug interactions with recombinant biogenic amine transporters expressed in the same cell type. *The Journal of Pharmacology and Experimental Therapeutics*, *289*(2), 877–885.
- Eshleman, A. J., Henningsen, R. A., Neve, K. A., & Janowsky, A. (1994). Release of dopamine via the human transporter. *Molecular Pharmacology*, *45*(2), 312–316.
- Fabre, V., Beaufour, C., Evrard, A., Rioux, A., Hanoun, N., Lesch, K. P., ... Martres, M.-P. (2000). Altered expression and functions of serotonin 5-HT_{1A} and 5-HT_{1B} receptors in knock-out mice lacking the 5-HT transporter. *The European Journal of Neuroscience*, *12*(7), 2299–2310.
- Faham, S., Watanabe, A., Besserer, G. M., Cascio, D., Specht, A., Hirayama, B. A., ... Abramson, J. (2008). The crystal structure of a sodium galactose transporter reveals mechanistic insights into Na⁺/sugar symport. *Science*, *321*(5890), 810–814.

- Felts, B., Pramod, A. B., Sandtner, W., Burbach, N., Bulling, S., Sitte, H. H., & Henry, L. K. (2014). The Two Na⁺ Sites in the Human Serotonin Transporter Play Distinct Roles in the Ion Coupling and Electrogenicity of Transport. *The Journal of Biological Chemistry*, *289*(3), 1825–1840.
- Ferrer, J. V., & Javitch, J. A. (1998). Cocaine alters the accessibility of endogenous cysteines in putative extracellular and intracellular loops of the human dopamine transporter. *Proceedings of the National Academy of Sciences of the United States of America*, *95*(16), 9238–9243.
- Field, J. R., Henry, L. K., & Blakely, R. D. (2010). Transmembrane domain 6 of the human serotonin transporter contributes to an aqueously accessible binding pocket for serotonin and the psychostimulant 3,4-methylene dioxymethamphetamine. *The Journal of Biological Chemistry*, *285*(15), 11270–11280.
- Fog, J. U., Khoshbouei, H., Holy, M., Owens, W. A., Vaegter, C. B., Sen, N., ... Gether, U. (2006). Calmodulin kinase II interacts with the dopamine transporter C terminus to regulate amphetamine-induced reverse transport. *Neuron*, *51*(4), 417–429.
- Folk, G. E., Jr, & Long, J. P. (1988). Serotonin as a neurotransmitter: a review. *Comparative Biochemistry and Physiology. C, Comparative Pharmacology and Toxicology*, *91*(1), 251–257.
- Forrest, L. R., & Rudnick, G. (2009). The rocking bundle: a mechanism for ion-coupled solute flux by symmetrical transporters. *Physiology*, *24*, 377–386.
- Forrest, L. R., Tavoulari, S., Zhang, Y.-W., Rudnick, G., & Honig, B. (2007). Identification of a chloride ion binding site in Na⁺/Cl⁻-dependent transporters. *Proceedings of the National Academy of Sciences of the United States of America*, *104*(31), 12761–12766.
- Forrest, L. R., Zhang, Y.-W., Jacobs, M. T., Gesmonde, J., Xie, L., Honig, B. H., & Rudnick, G. (2008). Mechanism for alternating access in neurotransmitter transporters. *Proceedings of the National Academy of Sciences of the United States of America*, *105*(30), 10338–10343.
- Foster, J. D., Pananusorn, B., Cervinski, M. A., Holden, H. E., & Vaughan, R. A. (2003). Dopamine transporters are dephosphorylated in striatal homogenates and in vitro by protein phosphatase 1. *Brain Research. Molecular Brain Research*, *110*(1), 100–108.
- Foster, J. D., Pananusorn, B., & Vaughan, R. A. (2002). Dopamine transporters are phosphorylated on N-terminal serines in rat striatum. *The Journal of Biological Chemistry*, *277*(28), 25178–25186.
- Furman, C. A., Chen, R., Guptaroy, B., Zhang, M., Holz, R. W., & Gnegy, M. (2009). Dopamine and Amphetamine Rapidly Increase Dopamine Transporter Trafficking to the Surface: Live-Cell Imaging Using Total Internal Reflection Fluorescence Microscopy. *Journal of Neuroscience*, *29*(10), 3328–3336.

- Gabriele, S., Sacco, R., & Persico, A. M. (2014). Blood serotonin levels in autism spectrum disorder: a systematic review and meta-analysis. *European Neuropsychopharmacology: The Journal of the European College of Neuropsychopharmacology*, 24(6), 919–929.
- Gabriel, L. R., Wu, S., Kearney, P., Bellvé, K. D., Standley, C., Fogarty, K. E., & Melikian, H. E. (2013). Dopamine transporter endocytic trafficking in striatal dopaminergic neurons: differential dependence on dynamin and the actin cytoskeleton. *The Journal of Neuroscience: The Official Journal of the Society for Neuroscience*, 33(45), 17836–17846.
- Gabrielsen, M., Ravn, A. W., Kristiansen, K., & Sylte, I. (2012). Substrate binding and translocation of the serotonin transporter studied by docking and molecular dynamics simulations. *Journal of Molecular Modeling*, 18(3), 1073–1085.
- Gaffaney, J. D., Shetty, M., Felts, B., Pramod, A.-B., Foster, J. D., Henry, L. K., & Vaughan, R. A. (2014). Antagonist-induced conformational changes in dopamine transporter extracellular loop two involve residues in a potential salt bridge. *Neurochemistry International*, 73, 16–26.
- Gaffaney, J. D., & Vaughan, R. A. (2004). Uptake inhibitors but not substrates induce protease resistance in extracellular loop two of the dopamine transporter. *Molecular Pharmacology*, 65(3), 692–701.
- Gainetdinov, R. R., & Caron, M. G. (2003). MONOAMINE TRANSPORTERS: From Genes to Behavior. *Annual Review of Pharmacology and Toxicology*, 43(1), 261–284.
- Gainetdinov, R. R., Sotnikova, T. D., & Caron, M. G. (2002). Monoamine transporter pharmacology and mutant mice. *Trends in Pharmacological Sciences*, 23(8), 367–373.
- Gainetdinov, R. R., Wetsel, W. C., Jones, S. R., Levin, E. D., Jaber, M., & Caron, M. G. (1999). Role of serotonin in the paradoxical calming effect of psychostimulants on hyperactivity. *Science*, 283(5400), 397–401.
- Gershon, M. D. (2004). Review article: serotonin receptors and transporters -- roles in normal and abnormal gastrointestinal motility. *Alimentary Pharmacology & Therapeutics*, 20 Suppl 7, 3–14.
- Gershon, M. D. (2005). Nerves, reflexes, and the enteric nervous system: pathogenesis of the irritable bowel syndrome. *Journal of Clinical Gastroenterology*, 39(5 Suppl 3), S184–93.
- Gether, U., Andersen, P. H., Larsson, O. M., & Schousboe, A. (2006). Neurotransmitter transporters: molecular function of important drug targets. *Trends in Pharmacological Sciences*, 27(7), 375–383.
- Geurink, P. P., Prely, L. M., van der Marel, G. A., Bischoff, R., & Overkleeft, H. S. (2012). Photoaffinity labeling in activity-based protein profiling. *Topics in Current Chemistry*, 324, 85–113.
- Gillman, P. K. (2007). Tricyclic antidepressant pharmacology and therapeutic drug interactions updated. *British Journal of Pharmacology*, 151(6), 737–748.

- Giros, B., & Caron, M. G. (1993). Molecular characterization of the dopamine transporter. *Trends in Pharmacological Sciences*, *14*(2), 43–49.
- Giros, B., el Mestikawy, S., Godinot, N., Zheng, K., Han, H., Yang-Feng, T., & Caron, M. G. (1992). Cloning, pharmacological characterization, and chromosome assignment of the human dopamine transporter. *Molecular Pharmacology*, *42*(3), 383–390.
- Giros, B., Jaber, M., Jones, S. R., Wightman, R. M., & Caron, M. G. (1996). Hyperlocomotion and indifference to cocaine and amphetamine in mice lacking the dopamine transporter. *Nature*, *379*(6566), 606–612.
- Glatt, C. E., DeYoung, J. A., Delgado, S., Service, S. K., Giacomini, K. M., Edwards, R. H., ... Freimer, N. B. (2001). Screening a large reference sample to identify very low frequency sequence variants: comparisons between two genes. *Nature Genetics*, *27*(4), 435–438.
- Glowa, J. R., Wojnicki, F. H. E., Matecka, D., & Rice, K. C. (1995). Effects of dopamine reuptake inhibitors on food- and cocaine-maintained responding: II. Comparisons with other drugs and repeated administrations. *Experimental and Clinical Psychopharmacology*, *3*(3), 232–239.
- Goldsmith, E. J., Akella, R., Min, X., Zhou, T., & Humphreys, J. M. (2007). Substrate and docking interactions in serine/threonine protein kinases. *Chemical Reviews*, *107*(11), 5065–5081.
- Goodwin, J. S., Larson, G. A., Swant, J., Sen, N., Javitch, J. A., Zahniser, N. R., ... Khoshbouei, H. (2009). Amphetamine and methamphetamine differentially affect dopamine transporters in vitro and in vivo. *The Journal of Biological Chemistry*, *284*(5), 2978–2989.
- Gordon, E. M., Stollstorff, M., Devaney, J. M., Bean, S., & Vaidya, C. J. (2012). Effect of dopamine transporter genotype on intrinsic functional connectivity depends on cognitive state. *Cerebral Cortex*, *22*(9), 2182–2196.
- Grant, B. D., & Donaldson, J. G. (2009). Pathways and mechanisms of endocytic recycling. *Nature Reviews. Molecular Cell Biology*, *10*(9), 597–608.
- Grunhage, F., Schulze, T. G., Muller, D. J., Lanczik, M., Franzek, E., Albus, M., ... Others. (2000). Systematic screening for DNA sequence variation in the coding region of the human dopamine transporter gene. *Molecular Psychiatry*, *5*, 275–282.
- Gu, H. H., Wall, S., & Rudnick, G. (1996). Ion coupling stoichiometry for the norepinephrine transporter in membrane vesicles from stably transfected cells. *The Journal of Biological Chemistry*, *271*(12), 6911–6916.
- Gu, H., Wall, S. C., & Rudnick, G. (1994). Stable expression of biogenic amine transporters reveals differences in inhibitor sensitivity, kinetics, and ion dependence. *The Journal of Biological Chemistry*, *269*(10), 7124–7130.
- Haase, J., Killian, A. M., Magnani, F., & Williams, C. (2001). Regulation of the serotonin transporter by interacting proteins. *Biochemical Society Transactions*, *29*(Pt 6), 722–728.

- Hahn, M. K., & Blakely, R. D. (2007a). The functional impact of SLC6 transporter genetic variation. *Annual Review of Pharmacology and Toxicology*, *47*, 401–441.
- Hahn, M. K., & Blakely, R. D. (2007b). The functional impact of SLC6 transporter genetic variation. *Annual Review of Pharmacology and Toxicology*, *47*, 401–441.
- Hahn, M. K., Mazei-Robison, M. S., & Blakely, R. D. (2005). Single nucleotide polymorphisms in the human norepinephrine transporter gene affect expression, trafficking, antidepressant interaction, and protein kinase C regulation. *Molecular Pharmacology*, *68*(2), 457–466.
- Hahn, M. K., Robertson, D., & Blakely, R. D. (2003). A mutation in the human norepinephrine transporter gene (SLC6A2) associated with orthostatic intolerance disrupts surface expression of mutant and wild-type transporters. *The Journal of Neuroscience: The Official Journal of the Society for Neuroscience*, *23*(11), 4470–4478.
- Hahn, M. K., Steele, A., Couch, R. S., Stein, M. A., & Krueger, J. J. (2009). Novel and functional norepinephrine transporter protein variants identified in attention-deficit hyperactivity disorder. *Neuropharmacology*, *57*(7-8), 694–701.
- Halushka, M. K., Fan, J. B., Bentley, K., Hsie, L., Shen, N., Weder, A., ... Chakravarti, A. (1999). Patterns of single-nucleotide polymorphisms in candidate genes for blood-pressure homeostasis. *Nature Genetics*, *22*(3), 239–247.
- Hanley, H. G., Stahl, S. M., & Freedman, D. X. (1977). Hyperserotonemia and amine metabolites in autistic and retarded children. *Archives of General Psychiatry*, *34*(5), 521–531.
- Hansen, F. H., Skjørringe, T., Yasmineen, S., Arends, N. V., Sahai, M. A., Erreger, K., ... Gether, U. (2014). Missense dopamine transporter mutations associate with adult parkinsonism and ADHD. *The Journal of Clinical Investigation*, *124*(7), 3107–3120.
- Hastrup, H., Karlin, A., & Javitch, J. A. (2001). Symmetrical dimer of the human dopamine transporter revealed by cross-linking Cys-306 at the extracellular end of the sixth transmembrane segment. *Proceedings of the National Academy of Sciences of the United States of America*, *98*(18), 10055–10060.
- Hastrup, H., Sen, N., & Javitch, J. A. (2003). The human dopamine transporter forms a tetramer in the plasma membrane: cross-linking of a cysteine in the fourth transmembrane segment is sensitive to cocaine analogs. *The Journal of Biological Chemistry*, *278*(46), 45045–45048.
- Hediger, M. A. (Ed.). (2013). *Molecular aspects of medicine*, *34*(2-3), 95-752.
- Hediger, M. A., Romero, M. F., Peng, J.-B., Rolfs, A., Takanaga, H., & Bruford, E. A. (2003). The ABCs of solute carriers: physiological, pathological and therapeutic implications of human membrane transport proteins. *Pflügers Archiv*, *447*(5), 465–468.
- Heikkila, R. E., Cabbat, F. S., & Duvoisin, R. C. (1979). Motor activity and rotational behavior after analogs of cocaine: correlation with dopamine uptake blockade. *Communications in Psychopharmacology*, *3*(5), 285–290.

- Heils, A., Mössner, R., & Lesch, K. P. (1997). The human serotonin transporter gene polymorphism--basic research and clinical implications. *Journal of Neural Transmission*, *104*(10), 1005–1014.
- Heils, A., Teufel, A., Petri, S., Stöber, G., Riederer, P., Bengel, D., & Lesch, K. P. (1996). Allelic variation of human serotonin transporter gene expression. *Journal of Neurochemistry*, *66*(6), 2621–2624.
- Heim, C., & Nemeroff, C. B. (2001). The role of childhood trauma in the neurobiology of mood and anxiety disorders: preclinical and clinical studies. *Biological Psychiatry*, *49*(12), 1023–1039.
- He, L., Vasilidou, K., & Nebert, D. W. (2009). Analysis and update of the human solute carrier (SLC) gene superfamily. *Human Genomics*, *3*(2), 195–206.
- Henry, L. K., Adkins, E. M., Han, Q., & Blakely, R. D. (2003). Serotonin and cocaine-sensitive inactivation of human serotonin transporters by methanethiosulfonates targeted to transmembrane domain I. *The Journal of Biological Chemistry*, *278*(39), 37052–37063.
- Henry, L. K., Field, J. R., Adkins, E. M., Parnas, M. L., Vaughan, R. A., Zou, M.-F., ... Blakely, R. D. (2006). Tyr-95 and Ile-172 in transmembrane segments 1 and 3 of human serotonin transporters interact to establish high affinity recognition of antidepressants. *The Journal of Biological Chemistry*, *281*(4), 2012–2023.
- Henry, L. K., Iwamoto, H., Field, J. R., Kaufmann, K., Dawson, E. S., Jacobs, M. T., ... Blakely, R. D. (2011). A Conserved Asparagine Residue in Transmembrane Segment 1 (TM1) of Serotonin Transporter Dictates Chloride-coupled Neurotransmitter Transport. *The Journal of Neuroscience: The Official Journal of the Society for Neuroscience*, *28*(35), 30823–30836.
- Henry, L. K., Meiler, J., & Blakely, R. D. (2007). Bound to be different: neurotransmitter transporters meet their bacterial cousins. *Molecular Interventions*, *7*(6), 306–309.
- Hess, B., Bekker, H., Berendsen, H. J. C., Fraaije, J. G., & Others. (1997). LINCS: a linear constraint solver for molecular simulations. *Journal of Computational Chemistry*, *18*(12), 1463–1472.
- Hess, B., Kutzner, C., van der Spoel, D., & Lindahl, E. (2008). GROMACS 4: Algorithms for Highly Efficient, Load-Balanced, and Scalable Molecular Simulation. *Journal of Chemical Theory and Computation*, *4*(3), 435–447.
- Hill, E. R., Huang, X., Zhan, C.-G., Ivy Carroll, F., & Gu, H. H. (2011). Interaction of tyrosine 151 in norepinephrine transporter with the 2 β group of cocaine analog RTI-113. *Neuropharmacology*, *61*(1-2), 112–120.
- Hiranita, T., Soto, P. L., Newman, A. H., & Katz, J. L. (2009). Assessment of reinforcing effects of benzotropine analogs and their effects on cocaine self-administration in rats: comparisons with monoamine uptake inhibitors. *The Journal of Pharmacology and Experimental Therapeutics*, *329*(2), 677–686.

- Hollander, E., Phillips, A., Chaplin, W., Zagursky, K., Novotny, S., Wasserman, S., & Iyengar, R. (2004). A Placebo Controlled Crossover Trial of Liquid Fluoxetine on Repetitive Behaviors in Childhood and Adolescent Autism. *Neuropsychopharmacology: Official Publication of the American College of Neuropsychopharmacology*, 30(3), 582–589.
- Holmes, A., Murphy, D. L., & Crawley, J. N. (2003). Abnormal behavioral phenotypes of serotonin transporter knockout mice: parallels with human anxiety and depression. *Biological Psychiatry*, 54(10), 953–959.
- Holz, R. W., & Coyle, J. T. (1974). The Effects of Various Salts, Temperature, and the Alkaloids Veratridine and Batrachotoxin on the Uptake of [3H] Dopamine into Synaptosomes from Rat Striatum. *Molecular Pharmacology*, 10(5), 746–758.
- Hong, W. C., & Amara, S. G. (2013). Differential targeting of the dopamine transporter to recycling or degradative pathways during amphetamine- or PKC-regulated endocytosis in dopamine neurons. *The FASEB Journal*, 27(8), 2995–3007.
- Huang, X., Gu, H. H., & Zhan, C.-G. (2009). Mechanism for Cocaine Blocking the Transport of Dopamine: Insights from Molecular Modeling and Dynamics Simulations. *The Journal of Physical Chemistry. B*, 113(45), 15057–15066.
- Huang, X., & Zhan, C.-G. (2007). How dopamine transporter interacts with dopamine: insights from molecular modeling and simulation. *Biophysical Journal*, 93(10), 3627–3639.
- Huguet, G., Ey, E., & Bourgeron, T. (2013). The Genetic Landscapes of Autism Spectrum Disorders. *Annual Review of Genomics and Human Genetics*, 14(1), 191–213.
- Humphrey, W., Dalke, A., & Schulten, K. (1996). VMD: visual molecular dynamics. *Journal of Molecular Graphics*, 14(1), 33–8, 27–8.
- Indarte, M., Madura, J. D., & Surratt, C. K. (2008). Dopamine transporter comparative molecular modeling and binding site prediction using the LeuT(Aa) leucine transporter as a template. *Proteins*, 70(3), 1033–1046.
- Ingram, S. L., Prasad, B. M., & Amara, S. G. (2002). Dopamine transporter-mediated conductances increase excitability of midbrain dopamine neurons. *Nature Neuroscience*, 5(10), 971–978.
- Itokawa, M., Lin, Z., Cai, N.-S., Wu, C., Kitayama, S., Wang, J.-B., & Uhl, G. R. (2000). Dopamine Transporter Transmembrane Domain Polar Mutants: ΔG and $\Delta\Delta G$ Values Implicate Regions Important for Transporter Functions. *Molecular Pharmacology*, 57(6), 1093–1103.
- Iversen, L. (2000). Neurotransmitter transporters: fruitful targets for CNS drug discovery. *Molecular Psychiatry*, 5(4), 357–362.
- Iversen, L. L. (1971). Role of transmitter uptake mechanisms in synaptic neurotransmission. *British Journal of Pharmacology*, 41(4), 571–591.

- Iwasa, H., Kurabayashi, M., Nagai, R., Nakamura, Y., & Tanaka, T. (2001). Genetic variations in five genes involved in the excitement of cardiomyocytes. *Journal of Human Genetics*, 46(9), 549–552.
- Jaber, M., Jones, S., Giros, B., & Caron, M. G. (1997). The dopamine transporter: a crucial component regulating dopamine transmission. *Movement Disorders: Official Journal of the Movement Disorder Society*, 12(5), 629–633.
- Jaber, M., Robinson, S. W., Missale, C., & Caron, M. G. (1996). Dopamine receptors and brain function. *Neuropharmacology*, 35(11), 1503–1519.
- Jacob, G., Shannon, J. R., Costa, F., Furlan, R., Biaggioni, I., Mosqueda-Garcia, R., ... Robertson, D. (1999). Abnormal norepinephrine clearance and adrenergic receptor sensitivity in idiopathic orthostatic intolerance. *Circulation*, 99(13), 1706–1712.
- Jacobsen, J. P. R., Plenge, P., Sachs, B. D., Pehrson, A. L., Cajina, M., Du, Y., ... Caron, M. G. (2014). The interaction of escitalopram and R-citalopram at the human serotonin transporter investigated in the mouse. *Psychopharmacology*, 231(23), 4527–4540.
- Jacobs, M. T., Zhang, Y.-W., Campbell, S. D., & Rudnick, G. (2007). Ibogaine, a noncompetitive inhibitor of serotonin transport, acts by stabilizing the cytoplasm-facing state of the transporter. *The Journal of Biological Chemistry*, 282(40), 29441–29447.
- Jardetzky, O. (1966). Simple allosteric model for membrane pumps. *Nature*, 211(5052), 969–970.
- Jiang, T., Rong, Z., Peng, L., Chen, B., Xie, Y., Chen, C., ... Chen, H. (2010). Simultaneous determination of citalopram and its metabolite in human plasma by LC–MS/MS applied to pharmacokinetic study. *Journal of Chromatography B*, 878(5–6), 615–619.
- Jones, S. R., Gainetdinov, R. R., Jaber, M., Giros, B., Wightman, R. M., & Caron, M. G. (1998). Profound neuronal plasticity in response to inactivation of the dopamine transporter. *Proceedings of the National Academy of Sciences of the United States of America*, 95(7), 4029–4034.
- Just, H., Sitte, H. H., Schmid, J. A., Freissmuth, M., & Kudlacek, O. (2004). Identification of an additional interaction domain in transmembrane domains 11 and 12 that supports oligomer formation in the human serotonin transporter. *The Journal of Biological Chemistry*, 279(8), 6650–6657.
- Kahlig, K. M., Binda, F., Khoshbouei, H., Blakely, R. D., McMahon, D. G., Javitch, J. A., & Galli, A. (2005). Amphetamine induces dopamine efflux through a dopamine transporter channel. *Proceedings of the National Academy of Sciences of the United States of America*, 102(9), 3495–3500.
- Kahlig, K. M., & Galli, A. (2003). Regulation of dopamine transporter function and plasma membrane expression by dopamine, amphetamine, and cocaine. *European Journal of Pharmacology*, 479(1-3), 153–158.

- Kahlig, K. M., Javitch, J. A., & Galli, A. (2004). Amphetamine regulation of dopamine transport. Combined measurements of transporter currents and transporter imaging support the endocytosis of an active carrier. *The Journal of Biological Chemistry*, 279(10), 8966–8975.
- Kahlig, K. M., Lute, B. J., Wei, Y., Loland, C. J., Gether, U., Javitch, J. A., & Galli, A. (2006). Regulation of dopamine transporter trafficking by intracellular amphetamine. *Molecular Pharmacology*, 70(2), 542–548.
- Kaiser, C., & Setler, P. E. (1981). Antipsychotic agents. *Burger's Medicinal Chemistry*, 3, 859–980.
- Kalivas, P. W. (2007). Neurobiology of cocaine addiction: implications for new pharmacotherapy. *The American Journal on Addictions / American Academy of Psychiatrists in Alcoholism and Addictions*, 16(2), 71–78.
- Kanner, B. I., & Zomot, E. (2008). Sodium-coupled neurotransmitter transporters. *Chemical Reviews*, 108(5), 1654–1668.
- Katz, J. L., Agoston, G. E., Alling, K. L., Kline, R. H., Forster, M. J., Woolverton, W. L., ... Newman, A. H. (2001). Dopamine transporter binding without cocaine-like behavioral effects: synthesis and evaluation of benztrapine analogs alone and in combination with cocaine in rodents. *Psychopharmacology*, 154(4), 362–374.
- Katz, J. L., Izenwasser, S., & Terry, P. (2000). Relationships among dopamine transporter affinities and cocaine-like discriminative-stimulus effects. *Psychopharmacology*, 148(1), 90–98.
- Katz, J. L., Kopajtic, T. A., Agoston, G. E., & Newman, A. H. (2004). Effects of N-substituted analogs of benztrapine: diminished cocaine-like effects in dopamine transporter ligands. *The Journal of Pharmacology and Experimental Therapeutics*, 309(2), 650–660.
- Katz, J. L., Newman, A. H., & Izenwasser, S. (1997). Relations between heterogeneity of dopamine transporter binding and function and the behavioral pharmacology of cocaine. *Pharmacology, Biochemistry, and Behavior*, 57(3), 505–512.
- Kaufmann, K. W., Dawson, E. S., Henry, L. K., Field, J. R., Blakely, R. D., & Meiler, J. (2009). Structural determinants of species-selective substrate recognition in human and Drosophila serotonin transporters revealed through computational docking studies. *Proteins*, 74(3), 630–642.
- Kenna, G. A., Roder-Hanna, N., Leggio, L., Zywiak, W. H., Clifford, J., Edwards, S., ... Swift, R. M. (2012). Association of the 5-HTT gene-linked promoter region (5-HTTLPR) polymorphism with psychiatric disorders: review of psychopathology and pharmacotherapy. *Pharmacogenomics and Personalized Medicine*, 5, 19–35.
- Khoshbouei, H., Wang, H., Lechleiter, J. D., Javitch, J. A., & Galli, A. (2003). Amphetamine-induced dopamine efflux. A voltage-sensitive and intracellular Na⁺-dependent mechanism. *The Journal of Biological Chemistry*, 278(14), 12070–12077.

- Khoshbouei, H., Wang, H., Lechleiter, J. D., Javitch, J. A., & Galli, A. (2003). Amphetamine-induced Dopamine Efflux: A VOLTAGE-SENSITIVE AND INTRACELLULAR Na⁺-DEPENDENT MECHANISM. *The Journal of Biological Chemistry*, 278(14), 12070–12077.
- Kilic, F., Murphy, D. L., & Rudnick, G. (2003). A human serotonin transporter mutation causes constitutive activation of transport activity. *Molecular Pharmacology*, 64(2), 440–446.
- Kim, C.-H., Hahn, M. K., Joung, Y., Anderson, S. L., Steele, A. H., Mazei-Robinson, M. S., ... Kim, K.-S. (2006). A polymorphism in the norepinephrine transporter gene alters promoter activity and is associated with attention-deficit hyperactivity disorder. *Proceedings of the National Academy of Sciences of the United States of America*, 103(50), 19164–19169.
- Kim, J. H., & Lawrence, A. J. (2014). Drugs currently in Phase II clinical trials for cocaine addiction. *Expert Opinion on Investigational Drugs*, 23(8), 1105–1122.
- Kimmel, H. L., Negus, S. S., Wilcox, K. M., Ewing, S. B., Stehouwer, J., Goodman, M. M., ... Howell, L. L. (2008). Relationship between rate of drug uptake in brain and behavioral pharmacology of monoamine transporter inhibitors in rhesus monkeys. *Pharmacology, Biochemistry, and Behavior*, 90(3), 453–462.
- Kitayama, S., Shimada, S., Xu, H., Markham, L., Donovan, D. M., & Uhl, G. R. (1992). Dopamine transporter site-directed mutations differentially alter substrate transport and cocaine binding. *Proceedings of the National Academy of Sciences of the United States of America*, 89(16), 7782–7785.
- Kiyohara, C., & Yoshimasu, K. (2010). Association between major depressive disorder and a functional polymorphism of the 5-hydroxytryptamine (serotonin) transporter gene: a meta-analysis. *Psychiatric Genetics*, 20(2), 49–58.
- Klimek, V., Stockmeier, C., Overholser, J., Meltzer, H. Y., Kalka, S., Dilley, G., & Ordway, G. A. (1997). Reduced levels of norepinephrine transporters in the locus coeruleus in major depression. *The Journal of Neuroscience: The Official Journal of the Society for Neuroscience*, 17(21), 8451–8458.
- Knighton, D. R., Zheng, J. H., Ten Eyck, L. F., Ashford, V. A., Xuong, N. H., Taylor, S. S., & Sowadski, J. M. (1991). Crystal structure of the catalytic subunit of cyclic adenosine monophosphate-dependent protein kinase. *Science*, 253(5018), 407–414.
- Koldsø, H., Christiansen, A. B., Sinning, S., & Schiøtt, B. (2013). Comparative modeling of the human monoamine transporters: similarities in substrate binding. *ACS Chemical Neuroscience*, 4(2), 295–309.
- Koldsø, H., Noer, P., Grouleff, J., Autzen, H. E., Sinning, S., & Schiøtt, B. (2011). Unbiased simulations reveal the inward-facing conformation of the human serotonin transporter and Na⁺ ion release. *PLoS Computational Biology*, 7(10), e1002246.
- Koob, G. F., Sanna, P. P., & Bloom, F. E. (1998). Neuroscience of addiction. *Neuron*, 21(3), 467–476.

- Koob, G. F., & Volkow, N. D. (2010). Neurocircuitry of addiction. *Neuropsychopharmacology: Official Publication of the American College of Neuropsychopharmacology*, 35(1), 217–238.
- Kotzyba-Hibert, F., Kapfer, I., & Goeldner, M. (1995a). Recent trends in photoaffinity labeling. *Angewandte Chemie International Edition in English*, 34(12), 1296–1312.
- Kotzyba-Hibert, F., Kapfer, I., & Goeldner, M. (1995b). Recent trends in photoaffinity labeling. *Angewandte Chemie International Edition in English*, 34(12), 1296–1312.
- Krishnamurthy, H., & Gouaux, E. (2012). X-ray structures of LeuT in substrate-free outward-open and apo inward-open states. *Nature*, 481(7382), 469–474.
- Krishnamurthy, H., Piscitelli, C. L., & Gouaux, E. (2009). Unlocking the molecular secrets of sodium-coupled transporters. *Nature*, 459(7245), 347–355.
- Kristensen, A. S., Andersen, J., Jørgensen, T. N., Sørensen, L., Eriksen, J., Loland, C. J., ... Gether, U. (2011). SLC6 neurotransmitter transporters: structure, function, and regulation. *Pharmacological Reviews*, 63(3), 585–640.
- Kuhar, M. J., Ritz, M. C., & Boja, J. W. (1991). The dopamine hypothesis of the reinforcing properties of cocaine. *Trends in Neurosciences*, 14(7), 299–302.
- Kuhlman, B., Dantas, G., Ireton, G. C., Varani, G., Stoddard, B. L., & Baker, D. (2003). Design of a novel globular protein fold with atomic-level accuracy. *Science*, 302(5649), 1364–1368.
- Kuhn, R. (1958). The treatment of depressive states with G 22355 (imipramine hydrochloride). *The American Journal of Psychiatry*, 115(5), 459–464.
- Kumar, V., Yarravarapu, N., Lapinsky, D. J., Perley, D., Felts, B., Tomlinson, M. J., ... Newman, A. H. (2015). Novel Azido-Iodo Photoaffinity Ligands for the Human Serotonin Transporter Based on the Selective Serotonin Reuptake Inhibitor (S)-Citalopram. *Journal of Medicinal Chemistry*, 58(14), 5609–5619.
- Kurian, M. A., Li, Y., Zhen, J., Meyer, E., Hai, N., Christen, H.-J., ... Maher, E. R. (2011). Clinical and molecular characterisation of hereditary dopamine transporter deficiency syndrome: an observational cohort and experimental study. *Lancet Neurology*, 10(1), 54–62.
- Lacerda, A. E., Kuryshev, Y. A., Yan, G.-X., Waldo, A. L., & Brown, A. M. (2010). Vanoxerine: cellular mechanism of a new antiarrhythmic. *Journal of Cardiovascular Electrophysiology*, 21(3), 301–310.
- Larsen, M. B., Sonders, M. S., Mortensen, O. V., Larson, G. A., Zahniser, N. R., & Amara, S. G. (2011). Dopamine transport by the serotonin transporter: a mechanistically distinct mode of substrate translocation. *The Journal of Neuroscience: The Official Journal of the Society for Neuroscience*, 31(17), 6605–6615.

- La Sala, M. S., Hurtado, M. D., Brown, A. R., Bohórquez, D. V., Liddle, R. A., Herzog, H., ... Dotson, C. D. (2013). Modulation of taste responsiveness by the satiation hormone peptide YY. *FASEB Journal: Official Publication of the Federation of American Societies for Experimental Biology*, 27(12), 5022–5033.
- Lawal, H. O., & Krantz, D. E. (2013). SLC18: Vesicular neurotransmitter transporters for monoamines and acetylcholine. *Molecular Aspects of Medicine*, 34(2-3), 360–372.
- Leaver-Fay, A., Tyka, M., Lewis, S. M., Lange, O. F., Thompson, J., Jacak, R., ... Bradley, P. (2011). ROSETTA3: an object-oriented software suite for the simulation and design of macromolecules. *Methods in Enzymology*, 487, 545–574.
- Lee, S. H., Chang, M. Y., Lee, K. H., Park, B. S., Lee, Y. S., Chin, H. R., & Lee, Y. S. (2000). Importance of valine at position 152 for the substrate transport and 2beta-carbomethoxy-3beta-(4-fluorophenyl)tropane binding of dopamine transporter. *Molecular Pharmacology*, 57(5), 883–889.
- Lesch, K. P., Bengel, D., Heils, A., Sabol, S. Z., Greenberg, B. D., Petri, S., ... Murphy, D. L. (1996). Association of anxiety-related traits with a polymorphism in the serotonin transporter gene regulatory region. *Science*, 274(5292), 1527–1531.
- Lever, J. R., Carroll, F., Patel, A., Abraham, P., Boja, J., Lewin, A., & Lew, R. (1993). Radiosynthesis of a photoaffinity probe for the cocaine receptor of the dopamine transporter: 3 β -(p-chlorophenyl) tropan-2 β -carboxylic acid m-([125I]-iodo)-p-azidophenethyl ester ([125I]-RTI-82). *Journal of Labelled Compounds & Radiopharmaceuticals*, 33(12), 1131–1137.
- Lever, J. R., Zou, M.-F., Parnas, M. L., Duval, R. A., Wirtz, S. E., Justice, J. B., ... Newman, A. H. (2005). Radioiodinated azide and isothiocyanate derivatives of cocaine for irreversible labeling of dopamine transporters: synthesis and covalent binding studies. *Bioconjugate Chemistry*, 16(3), 644–649.
- Li, L.-B., Chen, N., Ramamoorthy, S., Chi, L., Cui, X.-N., Wang, L. C., & Reith, M. E. A. (2004). The role of N-glycosylation in function and surface trafficking of the human dopamine transporter. *The Journal of Biological Chemistry*, 279(20), 21012–21020.
- Lindsey, K. P., Wilcox, K. M., Votaw, J. R., Goodman, M. M., Plisson, C., Carroll, F. I., ... Howell, L. L. (2004). Effects of dopamine transporter inhibitors on cocaine self-administration in rhesus monkeys: relationship to transporter occupancy determined by positron emission tomography neuroimaging. *The Journal of Pharmacology and Experimental Therapeutics*, 309(3), 959–969.
- Lin, L., Yee, S. W., Kim, R. B., & Giacomini, K. M. (2015). SLC transporters as therapeutic targets: emerging opportunities. *Nature Reviews. Drug Discovery*, 14(8), 543–560.
- Lin, Z., & Uhl, G. R. (2002). Dopamine transporter mutants with cocaine resistance and normal dopamine uptake provide targets for cocaine antagonism. *Molecular Pharmacology*, 61(4), 885–891.

- Lin, Z., Wang, W., Kopajtic, T., Revay, R. S., & Uhl, G. R. (1999). Dopamine transporter: transmembrane phenylalanine mutations can selectively influence dopamine uptake and cocaine analog recognition. *Molecular Pharmacology*, *56*(2), 434–447.
- Lin, Z., Wang, W., & Uhl, G. R. (2000). Dopamine transporter tryptophan mutants highlight candidate dopamine- and cocaine-selective domains. *Molecular Pharmacology*, *58*(6), 1581–1592.
- Lodge, D. J., & Grace, A. A. (2011). Developmental pathology, dopamine, stress and schizophrenia. *International Journal of Developmental Neuroscience: The Official Journal of the International Society for Developmental Neuroscience*, *29*(3), 207–213.
- Loland, C. J., Desai, R. I., Zou, M.-F., Cao, J., Grundt, P., Gerstbrein, K., ... Gether, U. (2008). Relationship between conformational changes in the dopamine transporter and cocaine-like subjective effects of uptake inhibitors. *Molecular Pharmacology*, *73*(3), 813–823.
- Loland, C. J., Mereu, M., Okunola, O. M., Cao, J., Prisinzano, T. E., Mazier, S., ... Newman, A. H. (2012). R-modafinil (armodafinil): a unique dopamine uptake inhibitor and potential medication for psychostimulant abuse. *Biological Psychiatry*, *72*(5), 405–413.
- Lucki, I. (1998). The spectrum of behaviors influenced by serotonin. *Biological Psychiatry*, *44*(3), 151–162.
- Madras, B. K., Miller, G. M., & Fischman, A. J. (2002). The dopamine transporter: relevance to attention deficit hyperactivity disorder (ADHD). *Behavioural Brain Research*, *130*(1-2), 57–63.
- Madras, B. K., Pristupa, Z. B., Niznik, H. B., Liang, A. Y., Blundell, P., Gonzalez, M. D., & Meltzer, P. C. (1996). Nitrogen-based drugs are not essential for blockade of monoamine transporters. *Synapse*, *24*(4), 340–348.
- Madras, B. K., Spealman, R. D., Fahey, M. A., Neumeyer, J. L., Saha, J. K., & Milius, R. A. (1989). Cocaine receptors labeled by [³H]2 beta-carbomethoxy-3 beta-(4-fluorophenyl)tropane. *Molecular Pharmacology*, *36*(4), 518–524.
- Mandell, D. J., Coutsiaris, E. A., & Kortemme, T. (2009). Sub-angstrom accuracy in protein loop reconstruction by robotics-inspired conformational sampling. *Nature Methods*, *6*(8), 551–552.
- Mattis, J., Tye, K. M., Ferenczi, E. A., Ramakrishnan, C., O’Shea, D. J., Prakash, R., ... Deisseroth, K. (2012). Principles for applying optogenetic tools derived from direct comparative analysis of microbial opsins. *Nature Methods*, *9*(2), 159–172.
- Mazei-Robison, M. S., Bowton, E., Holy, M., Schmudermaier, M., Freissmuth, M., Sitte, H. H., ... Blakely, R. D. (2008). Anomalous dopamine release associated with a human dopamine transporter coding variant. *The Journal of Neuroscience: The Official Journal of the Society for Neuroscience*, *28*(28), 7040–7046.

- Mazei-Robison, M. S., Couch, R. S., Shelton, R. C., Stein, M. A., & Blakely, R. D. (2005). Sequence variation in the human dopamine transporter gene in children with attention deficit hyperactivity disorder. *Neuropharmacology*, *49*(6), 724–736.
- McElvain, J. S., & Schenk, J. O. (1992). A multisubstrate mechanism of striatal dopamine uptake and its inhibition by cocaine. *Biochemical Pharmacology*, *43*(10), 2189–2199.
- Meiergerd, S. M., Patterson, T. A., & Schenk, J. O. (1993). D2 receptors may modulate the function of the striatal transporter for dopamine: kinetic evidence from studies in vitro and in vivo. *Journal of Neurochemistry*, *61*(2), 764–767.
- Meiler, J., & Baker, D. (2006). ROSETTALIGAND: Protein--small molecule docking with full side-chain flexibility. *Proteins: Structure, Function, and Bioinformatics*, *65*(3), 538–548.
- Meltzer, P. C., Liang, A. Y., Blundell, P., Gonzalez, M. D., Chen, Z., George, C., & Madras, B. K. (1997). 2-Carbomethoxy-3-aryl-8-oxabicyclo[3.2.1]octanes: Potent Non-Nitrogen Inhibitors of Monoamine Transporters †. *Journal of Medicinal Chemistry*, *40*(17), 2661–2673.
- Merchant, B. A., & Madura, J. D. (2012). Insights from molecular dynamics: The binding site of cocaine in the dopamine transporter and permeation pathways of substrates in the leucine and dopamine transporters. *Journal of Molecular Graphics & Modelling*, *38*, 1–12.
- Miller, K. J., & Hoffman, B. J. (1994). Adenosine A3 receptors regulate serotonin transport via nitric oxide and cGMP. *The Journal of Biological Chemistry*, *269*(44), 27351–27356.
- Miranda, M., Wu, C. C., Sorkina, T., Korstjens, D. R., & Sorkin, A. (2005). Enhanced ubiquitylation and accelerated degradation of the dopamine transporter mediated by protein kinase C. *The Journal of Biological Chemistry*, *280*(42), 35617–35624.
- Missale, C., Castelletti, L., Govoni, S., Spano, P. F., Trabucchi, M., & Hanbauer, I. (1985). Dopamine uptake is differentially regulated in rat striatum and nucleus accumbens. *Journal of Neurochemistry*, *45*(1), 51–56.
- Mitchell, P. (1957). A general theory of membrane transport from studies of bacteria. *Nature*, *180*(4577), 134–136.
- Mitchell, P. (1990). Osmochemistry of solute translocation. *Research in Microbiology*, *141*(3), 286–289.
- Moore, R. Y., Halaris, A. E., & Jones, B. E. (1978). Serotonin neurons of the midbrain raphe: ascending projections. *The Journal of Comparative Neurology*, *180*(3), 417–438.
- Morón, J. A., Zakharova, I., Ferrer, J. V., Merrill, G. A., Hope, B., Lafer, E. M., ... Shippenberg, T. S. (2003). Mitogen-activated protein kinase regulates dopamine transporter surface expression and dopamine transport capacity. *The Journal of Neuroscience: The Official Journal of the Society for Neuroscience*, *23*(24), 8480–8488.
- Mortensen, O. V., & Amara, S. G. (2003). Dynamic regulation of the dopamine transporter. *European Journal of Pharmacology*, *479*(1-3), 159–170.

- Muller, C. L., Anacker, A. M. J., & Veenstra-VanderWeele, J. (2016). The serotonin system in autism spectrum disorder: From biomarker to animal models. *Neuroscience*, *321*, 24–41.
- Mundorf, M. L., Troyer, K. P., Hochstetler, S. E., Near, J. A., & Wightman, R. M. (2000). Vesicular Ca(2+) participates in the catalysis of exocytosis. *The Journal of Biological Chemistry*, *275*(13), 9136–9142.
- Murphy, D. L., Wichems, C., Andrews, A. M., Li, Q., Hamer, D., & Greenberg, B. D. (1999). CONSEQUENCES OF ENGINEERED AND SPONTANEOUS GENETIC ALTERATIONS OF THE 5-HT TRANSPORTER IN MICE, MEN, AND WOMEN. *Behavioural Pharmacology*, *10*, S65.
- Nakamura, M., Ueno, S., Sano, A., & Tanabe, H. (2000). The human serotonin transporter gene linked polymorphism (5-HTTLPR) shows ten novel allelic variants. *Molecular Psychiatry*, *5*(1), 32–38.
- Navaroli, D. M., Bellvé, K. D., Standley, C., Lifshitz, L. M., Cardia, J., Lambright, D., ... Corvera, S. (2012). Rabenosyn-5 defines the fate of the transferrin receptor following clathrin-mediated endocytosis. *Proceedings of the National Academy of Sciences of the United States of America*, *109*(8), E471–80.
- Nemeroff, C. B., & Owens, M. J. (2002). Treatment of mood disorders. *Nature Neuroscience*, *5 Suppl*, 1068–1070.
- Neubauer, H. A., Hansen, C. G., & Wiborg, O. (2006). Dissection of an allosteric mechanism on the serotonin transporter: a cross-species study. *Molecular Pharmacology*, *69*(4), 1242–1250.
- Newman, A. H., Allen, A. C., Izenwasser, S., & Katz, J. L. (1994). Novel 3 alpha-(diphenylmethoxy)tropane analogs: potent dopamine uptake inhibitors without cocaine-like behavioral profiles. *Journal of Medicinal Chemistry*, *37*(15), 2258–2261.
- Newman, A. H., & Katz, J. L. (2008). Atypical Dopamine Uptake Inhibitors that Provide Clues About Cocaine's Mechanism at the Dopamine Transporter. In *Transporters as Targets for Drugs* (pp. 95–129). Springer Berlin Heidelberg.
- Newman, A. H., Kline, R. H., Allen, A. C., Izenwasser, S., George, C., & Katz, J. L. (1995). Novel 4'-Substituted and 4',4"-Disubstituted 3.alpha.-(Diphenylmethoxy)tropane Analogs as Potent and Selective Dopamine Uptake Inhibitors. *Journal of Medicinal Chemistry*, *38*(20), 3933–3940.
- Newman, A. H., & Kulkarni, S. (2002). Probes for the dopamine transporter: New leads toward a cocaine-abuse therapeutic—A focus on analogues of benztropine and rimcazole. *Medicinal Research Reviews*, *22*(5), 429–464.
- Nieoullon, A. (2002). Dopamine and the regulation of cognition and attention. *Progress in Neurobiology*, *67*(1), 53–83.

- Ni, W., & Watts, S. W. (2006). 5-hydroxytryptamine in the cardiovascular system: focus on the serotonin transporter (SERT). *Clinical and Experimental Pharmacology & Physiology*, 33(7), 575–583.
- Obejero-Paz, C. A., Bruening-Wright, A., Kramer, J., Hawryluk, P., Tatalovic, M., Dittrich, H. C., & Brown, A. M. (2015). Quantitative Profiling of the Effects of Vanoxerine on Human Cardiac Ion Channels and its Application to Cardiac Risk. *Scientific Reports*, 5, 17623.
- Oreland, L., & Hallman, J. (1989). Blood platelets as a peripheral marker for the central serotonin system. *Nordisk Psykiatrisk Tidsskrift. Nordic Journal of Psychiatry*, 43(sup20), 43–51.
- Owens, M. J., Morgan, W. N., Plott, S. J., & Nemeroff, C. B. (1997). Neurotransmitter Receptor and Transporter Binding Profile of Antidepressants and Their Metabolites. *The Journal of Pharmacology and Experimental Therapeutics*, 283(3), 1305.
- Owens, M. J., & Nemeroff, C. B. (1994). Role of serotonin in the pathophysiology of depression: focus on the serotonin transporter. *Clinical Chemistry*, 40(2), 288–295.
- Ozaki, N., Goldman, D., Kaye, W. H., Plotnicov, K., Greenberg, B. D., Lappalainen, J., ... Murphy, D. L. (2003). Serotonin transporter missense mutation associated with a complex neuropsychiatric phenotype. *Molecular Psychiatry*, 8(11), 933–936.
- Pacholczyk, T., Blakely, R. D., & Amara, S. G. (1991). Expression Cloning of a Cocaine- and Antidepressant-Sensitive Human Noradrenaline Transporter. *Nature*, 350(6316), 350–354.
- Palmiter, R. D. (2008). Dopamine signaling in the dorsal striatum is essential for motivated behaviors: lessons from dopamine-deficient mice. *Annals of the New York Academy of Sciences*, 1129, 35–46.
- Parnas, M. L., Gaffaney, J. D., Zou, M. F., Lever, J. R., Newman, A. H., & Vaughan, R. A. (2008). Labeling of dopamine transporter transmembrane domain 1 with the tropane ligand N-[4-(4-azido-3-[125I]iodophenyl)butyl]-2beta-carbomethoxy-3beta-(4-chlorophenyl)tropane implicates proximity of cocaine and substrate active sites. *Molecular Pharmacology*, 73(4), 1141–1150.
- Penmatsa, A., Wang, K. H., & Gouaux, E. (2013). X-ray structure of dopamine transporter elucidates antidepressant mechanism. *Nature*, 503(7474), 85–90.
- Penmatsa, A., Wang, K. H., & Gouaux, E. (2015). X-ray structures of Drosophila dopamine transporter in complex with nisoxetine and reboxetine. *Nature Structural & Molecular Biology*, 22(6), 506–508.
- Piccini, J. P., Pritchett, E. L. C., Davison, B. A., Cotter, G., Wiener, L. E., Koch, G., ... Dittrich, H. C. (2016). Randomized, double-blind, placebo-controlled study to evaluate the safety and efficacy of a single oral dose of vanoxerine for the conversion of subjects with recent onset atrial fibrillation or flutter to normal sinus rhythm: RESTORE SR. *Heart Rhythm: The Official Journal of the Heart Rhythm Society*. <http://doi.org/10.1016/j.hrthm.2016.04.012>

- Piscitelli, C. L., & Gouaux, E. (2012). Insights into transport mechanism from LeuT engineered to transport tryptophan. *The EMBO Journal*, *31*(1), 228–235.
- Piscitelli, C. L., Krishnamurthy, H., & Gouaux, E. (2010). Neurotransmitter/sodium symporter orthologue LeuT has a single high-affinity substrate site. *Nature*, *468*(7327), 1129–1132.
- Plenge, P., Gether, U., & Rasmussen, S. G. (2007). Allosteric effects of R- and S-citalopram on the human 5-HT transporter: evidence for distinct high- and low-affinity binding sites. *European Journal of Pharmacology*, *567*(1-2), 1–9.
- Plenge, P., Shi, L., Beuming, T., Te, J., Newman, A. H., Weinstein, H., ... Loland, C. J. (2012). Steric hindrance mutagenesis in the conserved extracellular vestibule impedes allosteric binding of antidepressants to the serotonin transporter. *The Journal of Biological Chemistry*, *287*(47), 39316–39326.
- Pramod, A. B., Foster, J., Carvelli, L., & Henry, L. K. (2013). SLC6 transporters: structure, function, regulation, disease association and therapeutics. *Molecular Aspects of Medicine*, *34*(2-3), 197–219.
- Prasad, B. M., & Amara, S. G. (2001). The dopamine transporter in mesencephalic cultures is refractory to physiological changes in membrane voltage. *The Journal of Neuroscience: The Official Journal of the Society for Neuroscience*, *21*(19), 7561–7567.
- Prasad, H. C., Steiner, J. A., Sutcliffe, J. S., & Blakely, R. D. (2009). Enhanced activity of human serotonin transporter variants associated with autism. *Philosophical Transactions of the Royal Society of London. Series B, Biological Sciences*, *364*(1514), 163–173.
- Prasad, H. C., Zhu, C.-B., McCauley, J. L., Samuvel, D. J., Ramamoorthy, S., Shelton, R. C., ... Blakely, R. D. (2005). Human serotonin transporter variants display altered sensitivity to protein kinase G and p38 mitogen-activated protein kinase. *Proceedings of the National Academy of Sciences of the United States of America*, *102*(32), 11545–11550.
- Pristupa, Z. B., McConkey, F., Liu, F., Man, H. Y., Lee, F. J., Wang, Y. T., & Niznik, H. B. (1998). Protein kinase-mediated bidirectional trafficking and functional regulation of the human dopamine transporter. *Synapse*, *30*(1), 79–87.
- Qian, Y., Melikian, H. E., Rye, D. B., Levey, A. I., & Blakely, R. D. (1995). Identification and characterization of antidepressant-sensitive serotonin transporter proteins using site-specific antibodies. *The Journal of Neuroscience: The Official Journal of the Society for Neuroscience*, *15*(2), 1261–1274.
- QUACPAC (2011). *OpenEye Scientific Software*, Santa Fe, NM.
- Quick, M. W. (2003). Regulating the conducting states of a mammalian serotonin transporter. *Neuron*, *40*(3), 537–549.
- Quick, M., Winther, A.-M. L., Shi, L., Nissen, P., Weinstein, H., & Javitch, J. A. (2009). Binding of an octylglucoside detergent molecule in the second substrate (S2) site of LeuT establishes an inhibitor-bound conformation. *Proceedings of the National Academy of Sciences of the United States of America*, *106*(14), 5563–5568.

- Quick, M., Yano, H., Goldberg, N. R., Duan, L., Beuming, T., Shi, L., ... Javitch, J. A. (2006). State-dependent conformations of the translocation pathway in the tyrosine transporter Tyt1, a novel neurotransmitter: sodium symporter from *Fusobacterium nucleatum*. *The Journal of Biological Chemistry*, *281*(36), 26444–26454.
- Ralph, R. J., Paulus, M. P., Fumagalli, F., Caron, M. G., & Geyer, M. A. (2001). Prepulse inhibition deficits and perseverative motor patterns in dopamine transporter knock-out mice: differential effects of D1 and D2 receptor antagonists. *The Journal of Neuroscience: The Official Journal of the Society for Neuroscience*, *21*(1), 305–313.
- Ramamoorthy, S., Bauman, A. L., Moore, K. R., Han, H., Yang-Feng, T., Chang, A. S., ... Blakely, R. D. (1993). Antidepressant- and cocaine-sensitive human serotonin transporter: molecular cloning, expression, and chromosomal localization. *Proceedings of the National Academy of Sciences of the United States of America*, *90*(6), 2542–2546.
- Ramamoorthy, S., Cool, D. R., Mahesh, V. B., Leibach, F. H., Melikian, H. E., Blakely, R. D., & Ganapathy, V. (1993). Regulation of the human serotonin transporter. Cholera toxin-induced stimulation of serotonin uptake in human placental choriocarcinoma cells is accompanied by increased serotonin transporter mRNA levels and serotonin transporter-specific ligand binding. *The Journal of Biological Chemistry*, *268*(29), 21626–21631.
- Ramamoorthy, S., Giovanetti, E., Qian, Y., & Blakely, R. D. (1998). Phosphorylation and regulation of antidepressant-sensitive serotonin transporters. *The Journal of Biological Chemistry*, *273*(4), 2458–2466.
- Ramamoorthy, S., Samuvel, D. J., Buck, E. R., Rudnick, G., & Jayanthi, L. D. (2007). Phosphorylation of threonine residue 276 is required for acute regulation of serotonin transporter by cyclic GMP. *The Journal of Biological Chemistry*, *282*(16), 11639–11647.
- Ramamoorthy, S., Shippenberg, T. S., & Jayanthi, L. D. (2011). Regulation of monoamine transporters: Role of transporter phosphorylation. *Pharmacology & Therapeutics*, *129*(2), 220–238.
- Rao, A., Simmons, D., & Sorkin, A. (2011). Differential subcellular distribution of endosomal compartments and the dopamine transporter in dopaminergic neurons. *Molecular and Cellular Neurosciences*, *46*(1), 148-158.
- Rasmussen, S. G. F., & Gether, U. (2005). Purification and fluorescent labeling of the human serotonin transporter. *Biochemistry*, *44*(9), 3494–3505.
- Reith, M. E. A. (2002). *Neurotransmitter transporters: structure, function, and regulation*. Humana Press.
- Reith, M. E. A., Blough, B. E., Hong, W. C., Jones, K. T., Schmitt, K. C., Baumann, M. H., ... Katz, J. L. (2015). Behavioral, biological, and chemical perspectives on atypical agents targeting the dopamine transporter. *Drug and Alcohol Dependence*, *147*, 1–19.

- Reith, M. E., Berfield, J. L., Wang, L. C., Ferrer, J. V., & Javitch, J. A. (2001). The uptake inhibitors cocaine and benztropine differentially alter the conformation of the human dopamine transporter. *The Journal of Biological Chemistry*, 276(31), 29012–29018.
- Retz, W., Freitag, C. M., Retz-Junginger, P., Wenzler, D., Schneider, M., Kissling, C., ... Rösler, M. (2008). A functional serotonin transporter promoter gene polymorphism increases ADHD symptoms in delinquents: interaction with adverse childhood environment. *Psychiatry Research*, 158(2), 123–131.
- Rickhag, M., Owens, W. A., Winkler, M.-T., Strandfelt, K. N., Rathje, M., Sørensen, G., ... Gether, U. (2013). Membrane-permeable C-terminal dopamine transporter peptides attenuate amphetamine-evoked dopamine release. *The Journal of Biological Chemistry*, 288(38), 27534–27544.
- Ritz, M. C., Lamb, R. J., Goldberg, S. R., & Kuhar, M. J. (1987). Cocaine receptors on dopamine transporters are related to self-administration of cocaine. *Science*, 237(4819), 1219–1223.
- Robertson, D. (1999). The epidemic of orthostatic tachycardia and orthostatic intolerance. *The American Journal of the Medical Sciences*, 317(2), 75–77.
- Rothman, R. B. (1990). High affinity dopamine reuptake inhibitors as potential cocaine antagonists: a strategy for drug development. *Life Sciences*, 46(20), PL17–21.
- Rothman, R. B., & Baumann, M. H. (2003). Monoamine transporters and psychostimulant drugs. *European Journal of Pharmacology*, 479(1-3), 23–40.
- Rothman, R. B., Baumann, M. H., Prisinzano, T. E., & Newman, A. H. (2007). Dopamine transport inhibitors based on GBR12909 and benztropine as potential medications to treat cocaine addiction. *Biochemical Pharmacology*. <http://doi.org/10.1016/j.bcp.2007.08.007>
- Rothman, R. B., Baumann, M. H., Prisinzano, T. E., & Newman, A. H. (2008). Dopamine transport inhibitors based on GBR12909 and benztropine as potential medications to treat cocaine addiction. *Biochemical Pharmacology*, 75(1), 2–16.
- Rothman, R. B., Mele, A., Reid, A. A., Akunne, H. C., Greig, N., Thurkauf, A., ... Pert, A. (1991). GBR12909 antagonizes the ability of cocaine to elevate extracellular levels of dopamine. *Pharmacology, Biochemistry, and Behavior*, 40(2), 387–397.
- Rudnick, G. (1998). Bioenergetics of neurotransmitter transport. *Journal of Bioenergetics and Biomembranes*, 30(2), 173–185.
- Rudnick, G. (2006). Serotonin transporters--structure and function. *The Journal of Membrane Biology*, 213(2), 101–110.
- Rudnick, G., & Clark, J. (1993). From synapse to vesicle: the reuptake and storage of biogenic amine neurotransmitters. *Biochimica et Biophysica Acta*, 1144(3), 249–263.
- Rudnick, G., Krämer, R., Blakely, R. D., Murphy, D. L., & Verrey, F. (2013). The SLC6 transporters: perspectives on structure, functions, regulation, and models for transporter dysfunction. *Pflügers Archiv - European Journal of Physiology*, 466(1), 25–42.

- Runyon, S. P., & Carroll, F. I. (2008). Tropane-based dopamine transporter-uptake inhibitors. *Trudell ML SI (ed) Dopamine Transporters, Chemistry, Biology, and Pharmacology*. Wiley, New York, 125–170.
- Saha, K., Sambo, D., Richardson, B. D., Lin, L. M., Butler, B., Villarroel, L., & Khoshbouei, H. (2014). Intracellular methamphetamine prevents the dopamine-induced enhancement of neuronal firing. *The Journal of Biological Chemistry*, 289(32), 22246–22257.
- Sakrikar, D., Mazei-Robison, M. S., Mergy, M. A., Richtand, N. W., Han, Q., Hamilton, P. J., ... Blakely, R. D. (2012). Attention deficit/hyperactivity disorder-derived coding variation in the dopamine transporter disrupts microdomain targeting and trafficking regulation. *The Journal of Neuroscience: The Official Journal of the Society for Neuroscience*, 32(16), 5385–5397.
- Sánchez, C., & Hyttel, J. (1999). Comparison of the effects of antidepressants and their metabolites on reuptake of biogenic amines and on receptor binding. *Cellular and Molecular Neurobiology*, 19(4), 467–489.
- Sarker, S., Weissensteiner, R., Steiner, I., Sitte, H. H., Ecker, G. F., Freissmuth, M., & Sucić, S. (2010). The high-affinity binding site for tricyclic antidepressants resides in the outer vestibule of the serotonin transporter. *Molecular Pharmacology*, 78(6), 1026–1035.
- Sato, Y., Zhang, Y.-W., Androutsellis-Theotokis, A., & Rudnick, G. (2004). Analysis of transmembrane domain 2 of rat serotonin transporter by cysteine scanning mutagenesis. *The Journal of Biological Chemistry*, 279(22), 22926–22933.
- Saunders, C., Ferrer, J. V., Shi, L., Chen, J., Merrill, G., Lamb, M. E., ... Galli, A. (2000). Amphetamine-induced loss of human dopamine transporter activity: an internalization-dependent and cocaine-sensitive mechanism. *Proceedings of the National Academy of Sciences of the United States of America*, 97(12), 6850–6855.
- Schain, R. J., & Freedman, D. X. (1961). Studies on 5-hydroxyindole metabolism in autistic and other mentally retarded children. *The Journal of Pediatrics*, 58, 315–320.
- Schloss, P., & Henn, F. A. (2004). New insights into the mechanisms of antidepressant therapy. *Pharmacology & Therapeutics*, 102(1), 47–60.
- Schmitt, K. C., & Reith, M. E. A. (2010). Regulation of the dopamine transporter: aspects relevant to psychostimulant drugs of abuse. *Annals of the New York Academy of Sciences*, 1187, 316–340.
- Schmitt, K. C., & Reith, M. E. A. (2011). The atypical stimulant and nootropic modafinil interacts with the dopamine transporter in a different manner than classical cocaine-like inhibitors. *PloS One*, 6(10), e25790.
- Schmitt, K. C., Rothman, R. B., & Reith, M. E. A. (2013). Nonclassical pharmacology of the dopamine transporter: atypical inhibitors, allosteric modulators, and partial substrates. *The Journal of Pharmacology and Experimental Therapeutics*, 346(1), 2–10.

- Schmitt, K. C., Zhen, J., Kharkar, P., Mishra, M., Chen, N., Dutta, A. K., & Reith, M. E. A. (2008). Interaction of cocaine-, benztropine-, and GBR12909-like compounds with wild-type and mutant human dopamine transporters: molecular features that differentially determine antagonist-binding properties. *Journal of Neurochemistry*, *107*(4), 928–940.
- Schultz, W. (2007). Multiple dopamine functions at different time courses. *Annual Review of Neuroscience*, *30*, 259–288.
- Seeger, G., Schloss, P., & Schmidt, M. H. (2001). Functional polymorphism within the promotor of the serotonin transporter gene is associated with severe hyperkinetic disorders. *Molecular Psychiatry*, *6*(2), 235–238.
- Sen, N., Shi, L., Beuming, T., Weinstein, H., & Javitch, J. A. (2005). A pincer-like configuration of TM2 in the human dopamine transporter is responsible for indirect effects on cocaine binding. *Neuropharmacology*, *49*(6), 780–790.
- Serretti, A., Kato, M., De Ronchi, D., & Kinoshita, T. (2007). Meta-analysis of serotonin transporter gene promoter polymorphism (5-HTTLPR) association with selective serotonin reuptake inhibitor efficacy in depressed patients. *Molecular Psychiatry*, *12*(3), 247–257.
- Shannon, J. R., Flattem, N. L., Jordan, J., Jacob, G., Black, B. K., Biaggioni, I., ... Robertson, D. (2000). Clues to the origin of orthostatic intolerance: a genetic defect in the cocaine-and antidepressant sensitive norepinephrine transporter. *The New England Journal of Medicine*, *342*, 541–549.
- Shen, K., & Meyer, T. (1999). Dynamic control of CaMKII translocation and localization in hippocampal neurons by NMDA receptor stimulation. *Science*, *284*(5411), 162–166.
- Sherman, W., Day, T., Jacobson, M. P., Friesner, R. A., & Farid, R. (2006). Novel procedure for modeling ligand/receptor induced fit effects. *Journal of Medicinal Chemistry*, *49*(2), 534–553.
- Shih, J. C., Chen, K., & Ridd, M. J. (1998). Role of MAO A and B in neurotransmitter metabolism and behavior. *Polish Journal of Pharmacology*, *51*(1), 25–29.
- Shi, L., Quick, M., Zhao, Y., Weinstein, H., & Javitch, J. A. (2008). The mechanism of a neurotransmitter:sodium symporter--inward release of Na⁺ and substrate is triggered by substrate in a second binding site. *Molecular Cell*, *30*(6), 667–677.
- Shimada, S., Kitayama, S., Lin, C. L., Patel, A., Nanthakumar, E., Gregor, P., ... Uhl, G. (1991). Cloning and expression of a cocaine-sensitive dopamine transporter complementary DNA. *Science*, *254*(5031), 576–578.
- Singh, S. K. (2008). LeuT: a prokaryotic stepping stone on the way to a eukaryotic neurotransmitter transporter structure. *Channels*, *2*(5), 380–389.
- Singh, S. K., Piscitelli, C. L., Yamashita, A., & Gouaux, E. (2008). A competitive inhibitor traps LeuT in an open-to-out conformation. *Science*, *322*(5908), 1655–1661.

- Singh, S. K., Yamashita, A., & Gouaux, E. (2007). Antidepressant binding site in a bacterial homologue of neurotransmitter transporters. *Nature*, *448*(7156), 952–956.
- Sitte, H. H., Farhan, H., & Javitch, J. A. (2004). Sodium-dependent neurotransmitter transporters: oligomerization as a determinant of transporter function and trafficking. *Molecular Interventions*, *4*(1), 38–47.
- Sitte, H. H., Huck, S., Reither, H., Boehm, S., Singer, E. A., & Pifl, C. (1998). Carrier-mediated release, transport rates, and charge transfer induced by amphetamine, tyramine, and dopamine in mammalian cells transfected with the human dopamine transporter. *Journal of Neurochemistry*, *71*(3), 1289–1297.
- Sonders, M. S., Zhu, S. J., Zahniser, N. R., Kavanaugh, M. P., & Amara, S. G. (1997). Multiple ionic conductances of the human dopamine transporter: the actions of dopamine and psychostimulants. *The Journal of Neuroscience: The Official Journal of the Society for Neuroscience*, *17*(3), 960–974.
- Sorkina, T., Doolen, S., Galperin, E., Zahniser, N. R., & Sorkin, A. (2003). Oligomerization of dopamine transporters visualized in living cells by fluorescence resonance energy transfer microscopy. *The Journal of Biological Chemistry*, *278*(30), 28274–28283.
- Sorkina, T., Hoover, B. R., Zahniser, N. R., & Sorkin, A. (2005). Constitutive and protein kinase C-induced internalization of the dopamine transporter is mediated by a clathrin-dependent mechanism. *Traffic*, *6*(2), 157–170.
- Sorkina, T., Richards, T. L., Rao, A., Zahniser, N. R., & Sorkin, A. (2009). Negative Regulation of Dopamine Transporter Endocytosis by Membrane-Proximal N-Terminal Residues. *The Journal of Neuroscience: The Official Journal of the Society for Neuroscience*, *29*(5), 1361–1374.
- Spielewoy, C., Roubert, C., Hamon, M., Nosten-Bertrand, M., Betancur, C., & Giros, B. (2000). Behavioural disturbances associated with hyperdopaminergia in dopamine-transporter knockout mice. *Behavioural Pharmacology*, *11*(3-4), 279–290.
- Stahl, S. M. (1998). Mechanism of action of serotonin selective reuptake inhibitors: Serotonin receptors and pathways mediate therapeutic effects and side effects. *Journal of Affective Disorders*, *51*(3), 215–235.
- Stoops, W. W., Lile, J. A., Glaser, P. E. A., Hays, L. R., & Rush, C. R. (2012). Influence of acute bupropion pre-treatment on the effects of intranasal cocaine. *Addiction*, *107*(6), 1140–1147.
- Subach, F. V., Patterson, G. H., Manley, S., Gillette, J. M., Lippincott-Schwartz, J., & Verkhusha, V. V. (2009). Photoactivatable mCherry for high-resolution two-color fluorescence microscopy. *Nature Methods*, *6*(2), 153–159.
- Sulzer, D., Sonders, M. S., Poulsen, N. W., & Galli, A. (2005). Mechanisms of neurotransmitter release by amphetamines: a review. *Progress in Neurobiology*, *75*(6), 406–433.

- Sutcliffe, J. S., Delahanty, R. J., Prasad, H. C., McCauley, J. L., Han, Q., Jiang, L., ... Blakely, R. D. (2005). Allelic heterogeneity at the serotonin transporter locus (SLC6A4) confers susceptibility to autism and rigid-compulsive behaviors. *American Journal of Human Genetics*, 77(2), 265–279.
- Tadevosyan-leyfer, O., Dowd, M., Mankoski, R., Winklosky, B., Putnam, S., McGrath, L., ... Folstein, S. E. (2003). A Principal Components Analysis of the Autism Diagnostic Interview-Revised. *Journal of the American Academy of Child and Adolescent Psychiatry*, 42(7), 864–872.
- Tanda, G., Li, S. M., Mereu, M., Thomas, A. M., Ebbs, A. L., Chun, L. E., ... Katz, J. L. (2013). Relations between stimulation of mesolimbic dopamine and place conditioning in rats produced by cocaine or drugs that are tolerant to dopamine transporter conformational change. *Psychopharmacology*, 229(2), 307–321.
- Tanda, G., Newman, A. H., & Katz, J. L. (2009). Discovery of Drugs to Treat Cocaine Dependence: Behavioral and Neurochemical Effects of Atypical Dopamine Transport Inhibitors. In S.J. Enna and Michael Williams (Ed.), *Advances in Pharmacology* (Vol. Volume 57, pp. 253–289). Academic Press.
- Tang, W., Kang, J., Wu, X., Rampe, D., Wang, L., Shen, H., ... Garyantes, T. (2001). Development and evaluation of high throughput functional assay methods for HERG potassium channel. *Journal of Biomolecular Screening*, 6(5), 325–331.
- Tarnok, Z., Ronai, Z., Gervai, J., Kereszturi, E., Gadoros, J., Sasvari-Szekely, M., & Nemoda, Z. (2007). Dopaminergic candidate genes in Tourette syndrome: Association between tic severity and 3' UTR polymorphism of the dopamine transporter gene. *American Journal of Medical Genetics*, 144B(7), 900–905.
- Tate, C. G., Haase, J., Baker, C., Boorsma, M., Magnani, F., Vallis, Y., & Williams, D. C. (2003). Comparison of seven different heterologous protein expression systems for the production of the serotonin transporter. *Biochimica et Biophysica Acta*, 1610(1), 141–153.
- Tavoulari, S., Margheritis, E., Nagarajan, A., DeWitt, D. C., Zhang, Y.-W., Rosado, E., ... Rudnick, G. (2015). Two Na⁺ Sites Control Conformational Change in a Neurotransmitter Transporter Homolog. *The Journal of Biological Chemistry*, jbc.M115.692012.
- Tella, S. R. (1995). Effects of monoamine reuptake inhibitors on cocaine self-administration in rats. *Pharmacology, Biochemistry, and Behavior*, 51(4), 687–692.
- Thakur, G. A., Grizenko, N., Sengupta, S. M., Schmitz, N., & Joober, R. (2010). The 5-HTTLPR polymorphism of the serotonin transporter gene and short term behavioral response to methylphenidate in children with ADHD. *BMC Psychiatry*, 10, 50.
- Thapar, A., O'Donovan, M., & Owen, M. J. (2005). The genetics of attention deficit hyperactivity disorder. *Human Molecular Genetics*, 14 Spec No. 2, R275–82.

- Thompson, B. J., Jessen, T., Henry, L. K., Field, J. R., Gamble, K. L., Gresch, P. J., ... Blakely, R. D. (2011). Transgenic elimination of high-affinity antidepressant and cocaine sensitivity in the presynaptic serotonin transporter. *Proceedings of the National Academy of Sciences*, *108*(9), 3785–3790.
- Torres, G. E., & Amara, S. G. (2007). Glutamate and monoamine transporters: new visions of form and function. *Current Opinion in Neurobiology*, *17*(3), 304–312.
- Torres, G. E., Gainetdinov, R. R., & Caron, M. G. (2003). Plasma membrane monoamine transporters: structure, regulation and function. *Nature Reviews. Neuroscience*, *4*(1), 13–25.
- Uhl, G. R., & Lin, Z. (2003). The top 20 dopamine transporter mutants: structure–function relationships and cocaine actions. *European Journal of Pharmacology*, *479*(1–3), 71–82.
- Ukairo, O. T., Bondi, C. D., Newman, A. H., Kulkarni, S. S., Kozikowski, A. P., Pan, S., & Surratt, C. K. (2005). Recognition of benztropine by the dopamine transporter (DAT) differs from that of the classical dopamine uptake inhibitors cocaine, methylphenidate, and mazindol as a function of a DAT transmembrane 1 aspartic acid residue. *The Journal of Pharmacology and Experimental Therapeutics*, *314*(2), 575–583.
- Vaughan, R. A. (1995). Photoaffinity-labeled ligand binding domains on dopamine transporters identified by peptide mapping. *Molecular Pharmacology*, *47*(5), 956–964.
- Vaughan, R. A., Agoston, G. E., Lever, J. R., & Newman, A. H. (1999). Differential binding of tropane-based photoaffinity ligands on the dopamine transporter. *The Journal of Neuroscience: The Official Journal of the Society for Neuroscience*, *19*(2), 630–636.
- Vaughan, R. A., & Foster, J. D. (2013). Mechanisms of dopamine transporter regulation in normal and disease states. *Trends in Pharmacological Sciences*, *34*(9), 489–496.
- Vaughan, R. A., Gaffaney, J. D., Lever, J. R., Reith, M. E., & Dutta, A. K. (2001). Dual incorporation of photoaffinity ligands on dopamine transporters implicates proximity of labeled domains. *Molecular Pharmacology*, *59*(5), 1157–1164.
- Vaughan, R. A., & Kuhar, M. J. (1996). Dopamine transporter ligand binding domains. Structural and functional properties revealed by limited proteolysis. *The Journal of Biological Chemistry*, *271*(35), 21672–21680.
- Vaughan, R. A., Sakrikar, D. S., Parnas, M. L., Adkins, S., Foster, J. D., Duval, R. A., ... Hauck-Newman, A. (2007). Localization of cocaine analog [125I]RTI 82 irreversible binding to transmembrane domain 6 of the dopamine transporter. *The Journal of Biological Chemistry*, *282*(12), 8915–8925.
- Vaughan, R. A., Uhl, G., & Kuhar, M. J. (1993). Recognition of dopamine transporters by antipeptide antibodies. *Molecular and Cellular Neurosciences*, *4*(2), 209–215.
- Veenstra-VanderWeele, J., & Blakely, R. D. (2012). Networking in autism: leveraging genetic, biomarker and model system findings in the search for new treatments. *Neuropsychopharmacology: Official Publication of the American College of Neuropsychopharmacology*, *37*(1), 196–212.

- Veenstra-VanderWeele, J., Muller, C. L., Iwamoto, H., Sauer, J. E., Owens, W. A., Shah, C. R., ... Blakely, R. D. (2012). Autism gene variant causes hyperserotonemia, serotonin receptor hypersensitivity, social impairment and repetitive behavior. *Proceedings of the National Academy of Sciences of the United States of America*, *109*(14), 5469–5474.
- Velasquez, J. C., Goeden, N., Herod, S. M., & Bonnin, A. (2016). Maternal Pharmacokinetics and Fetal Disposition of (±)-Citalopram during Mouse Pregnancy. *ACS Chemical Neuroscience*. <http://doi.org/10.1021/acschemneuro.5b00287>
- Velázquez-Sánchez, C., Ferragud, A., Murga, J., Cardá, M., & Canales, J. J. (2010). The high affinity dopamine uptake inhibitor, JHW 007, blocks cocaine-induced reward, locomotor stimulation and sensitization. *European Neuropsychopharmacology: The Journal of the European College of Neuropsychopharmacology*, *20*(7), 501–508.
- Vernier, P., Moret, F., Callier, S., Snappyan, M., Wersinger, C., & Sidhu, A. (2004). The degeneration of dopamine neurons in Parkinson's disease: insights from embryology and evolution of the mesostriatocortical system. *Annals of the New York Academy of Sciences*, *1035*, 231–249.
- Vocci, F. J., Acri, J., & Elkashef, A. (2005). Medication development for addictive disorders: the state of the science. *The American Journal of Psychiatry*, *162*(8), 1432–1440.
- Volkow, N. D., Wang, G. J., Fowler, J. S., Gatley, S. J., Ding, Y. S., Logan, J., ... Lieberman, J. (1996). Relationship between psychostimulant-induced“ high” and dopamine transporter occupancy. *Proceedings of the National Academy of Sciences*, *93*(19), 10388–10392.
- Vosburg, S. K., Hart, C. L., Haney, M., Rubin, E., & Foltin, R. W. (2010). Modafinil does not serve as a reinforcer in cocaine abusers. *Drug and Alcohol Dependence*, *106*(2-3), 233–236.
- Wall, S. C., Innis, R. B., & Rudnick, G. (1993). Binding of the cocaine analog 2 beta-carbomethoxy-3 beta-(4-[125I]iodophenyl)tropane to serotonin and dopamine transporters: different ionic requirements for substrate and 2 beta-carbomethoxy-3 beta-(4-[125I]iodophenyl)tropane binding. *Molecular Pharmacology*, *43*(2), 264–270.
- Wang, H., Elferich, J., & Gouaux, E. (2012). Structures of LeuT in bicelles define conformation and substrate binding in a membrane-like context. *Nature Structural & Molecular Biology*, *19*(2), 212–219.
- Wang, H., Goehring, A., Wang, K. H., Penmatsa, A., Ressler, R., & Gouaux, E. (2013). Structural basis for action by diverse antidepressants on biogenic amine transporters. *Nature*, *503*(7474), 141–145.
- Wang, K. H., Penmatsa, A., & Gouaux, E. (2015). Neurotransmitter and psychostimulant recognition by the dopamine transporter. *Nature*, *521*(7552), 322–327.
- Watanabe, A., Choe, S., Chaptal, V., Rosenberg, J. M., Wright, E. M., Grabe, M., & Abramson, J. (2010). The mechanism of sodium and substrate release from the binding pocket of vSGLT. *Nature*, *468*(7326), 988–991.

- Weiss, L. A., Abney, M., Cook, E. H., Jr, & Ober, C. (2005). Sex-specific genetic architecture of whole blood serotonin levels. *American Journal of Human Genetics*, 76(1), 33–41.
- Weiss, L. A., Veenstra-Vanderweele, J., Newman, D. L., Kim, S.-J., Dytch, H., McPeck, M. S., ... Abney, M. (2004). Genome-wide association study identifies ITGB3 as a QTL for whole blood serotonin. *European Journal of Human Genetics: EJHG*, 12(11), 949–954.
- Wei, Y., Williams, J. M., Dipace, C., Sung, U., Javitch, J. A., Galli, A., & Saunders, C. (2007). Dopamine transporter activity mediates amphetamine-induced inhibition of Akt through a Ca²⁺/calmodulin-dependent kinase II-dependent mechanism. *Molecular Pharmacology*, 71(3), 835–842.
- Wilbrandt, W., & Rosenberg, T. (1961). The concept of carrier transport and its corollaries in pharmacology. *Pharmacological Reviews*, 13, 109–183.
- Wisor, J. P., Nishino, S., Sora, I., Uhl, G. H., Mignot, E., & Edgar, D. M. (2001). Dopaminergic role in stimulant-induced wakefulness. *The Journal of Neuroscience: The Official Journal of the Society for Neuroscience*, 21(5), 1787–1794.
- Wolters, J. P., & Hellstrom, W. J. G. (2006). Current concepts in ejaculatory dysfunction. *Reviews in Urology*, 8 Suppl 4, S18–25.
- Wong, D. T., & Bymaster, F. P. (1995). Development of antidepressant drugs. Fluoxetine (Prozac) and other selective serotonin uptake inhibitors. *Advances in Experimental Medicine and Biology*, 363, 77–95.
- Wong, D. T., & Bymaster, F. P. (2002). Dual serotonin and noradrenaline uptake inhibitor class of antidepressants potential for greater efficacy or just hype? *Progress in Drug Research. Fortschritte Der Arzneimittelforschung. Progres Des Recherches Pharmaceutiques*, 58, 169–222.
- Wong, M.-L., & Licinio, J. (2001). Research and Treatment Approaches to Depression. *Nature Reviews. Neuroscience*, 2(5), 343–351.
- Woodward, J. J., Wilcox, R. E., Leslie, S. W., & Riffée, W. H. (1986). Dopamine uptake during fast-phase endogenous dopamine release from mouse striatal synaptosomes. *Neuroscience Letters*, 71(1), 106–112.
- Wu, X., & Gu, H. H. (2003). Cocaine affinity decreased by mutations of aromatic residue phenylalanine 105 in the transmembrane domain 2 of dopamine transporter. *Molecular Pharmacology*, 63(3), 653–658.
- Xu, F., Gainetdinov, R. R., Wetsel, W. C., Jones, S. R., Bohn, L. M., Miller, G. W., ... Caron, M. G. (2000). Mice lacking the norepinephrine transporter are supersensitive to psychostimulants. *Nature Neuroscience*, 3(5), 465–471.
- Yamashita, A., Singh, S. K., Kawate, T., Jin, Y., & Gouaux, E. (2005). Crystal structure of a bacterial homologue of Na⁺/Cl⁻-dependent neurotransmitter transporters. *Nature*, 437(7056), 215–223.

- Yubero-Lahoz, S., Robledo, P., Farré, M., & de la Torre, R. (2013). Platelet SERT as a peripheral biomarker of serotonergic neurotransmission in the central nervous system. *Current Medicinal Chemistry*, *20*(11), 1382–1396.
- Zahniser, N. R., & Sorkin, A. (2004). Rapid regulation of the dopamine transporter: role in stimulant addiction? *Neuropharmacology*, *47 Suppl 1*, 80–91.
- Zahniser, N. R., & Sorkin, A. (2009). Trafficking of dopamine transporters in psychostimulant actions. *Seminars in Cell & Developmental Biology*, *20*(4), 411–417.
- Zdravkovic, I., Zhao, C., Lev, B., Cuervo, J. E., & Noskov, S. Y. (2012). Atomistic models of ion and solute transport by the sodium-dependent secondary active transporters. *Biochimica et Biophysica Acta*, *1818*(2), 337–347.
- Zhan, C.-G., Deng, S.-X., Skiba, J. G., Hayes, B. A., Tschampel, S. M., Shields, G. C., & Landry, D. W. (2005). First-principle studies of intermolecular and intramolecular catalysis of protonated cocaine. *Journal of Computational Chemistry*, *26*(10), 980–986.
- Zhang, F., Vierock, J., Yizhar, O., Fenno, L. E., Tsunoda, S., Kianianmomeni, A., ... Deisseroth, K. (2011). The microbial opsin family of optogenetic tools. *Cell*, *147*(7), 1446–1457.
- Zhang, Y.-W., Gesmonde, J., Ramamoorthy, S., & Rudnick, G. (2007). Serotonin transporter phosphorylation by cGMP-dependent protein kinase is altered by a mutation associated with obsessive compulsive disorder. *The Journal of Neuroscience: The Official Journal of the Society for Neuroscience*, *27*(40), 10878–10886.
- Zhang, Y.-W., & Rudnick, G. (2006). The cytoplasmic substrate permeation pathway of serotonin transporter. *The Journal of Biological Chemistry*, *281*(47), 36213–36220.
- Zhang, Y.-W., Turk, B. E., & Rudnick, G. (2016). Control of serotonin transporter phosphorylation by conformational state. *Proceedings of the National Academy of Sciences of the United States of America*. <http://doi.org/10.1073/pnas.1603282113>
- Zhao, C., Stolzenberg, S., Gracia, L., Weinstein, H., Noskov, S., & Shi, L. (2012). Ion-controlled conformational dynamics in the outward-open transition from an occluded state of LeuT. *Biophysical Journal*, *103*(5), 878–888.
- Zhao, Y., Terry, D. S., Shi, L., Quick, M., Weinstein, H., Blanchard, S. C., & Javitch, J. A. (2011). Substrate-modulated gating dynamics in a Na⁺-coupled neurotransmitter transporter homologue. *Nature*, *474*(7349), 109–113.
- Zhong, H., Hansen, K. B., Boyle, N. J., Han, K., Muske, G., Huang, X., ... Sánchez, C. (2009). An allosteric binding site at the human serotonin transporter mediates the inhibition of escitalopram by R-citalopram: Kinetic binding studies with the ALI/VFL-SI/TT mutant. *Neuroscience Letters*, *462*(3), 207–212.
- Zhou, Z., Zhen, J., Karpowich, N. K., Goetz, R. M., Law, C. J., Reith, M. E. A., & Wang, D.-N. (2007). LeuT-desipramine structure reveals how antidepressants block neurotransmitter reuptake. *Science*, *317*(5843), 1390–1393.

- Zhou, Z., Zhen, J., Karpowich, N. K., Law, C. J., Reith, M. E. A., & Wang, D.-N. (2009). Antidepressant specificity of serotonin transporter suggested by three LeuT-SSRI structures. *Nature Structural & Molecular Biology*, *16*(6), 652–657.
- Zhu, C.-B., Blakely, R. D., & Hewlett, W. A. (2006). The proinflammatory cytokines interleukin-1beta and tumor necrosis factor-alpha activate serotonin transporters. *Neuropsychopharmacology: Official Publication of the American College of Neuropsychopharmacology*, *31*(10), 2121–2131.
- Zhu, C.-B., Hewlett, W. A., Feoktistov, I., Biaggioni, I., & Blakely, R. D. (2004). Adenosine receptor, protein kinase G, and p38 mitogen-activated protein kinase-dependent up-regulation of serotonin transporters involves both transporter trafficking and activation. *Molecular Pharmacology*, *65*(6), 1462–1474.
- Zoete, V., Cuendet, M. A., Grosdidier, A., & Michielin, O. (2011). SwissParam: a fast force field generation tool for small organic molecules. *Journal of Computational Chemistry*, *32*(11), 2359–2368.
- Zomot, E., Bendahan, A., Quick, M., Zhao, Y., Javitch, J. A., & Kanner, B. I. (2007). Mechanism of chloride interaction with neurotransmitter:sodium symporters. *Nature*, *449*(7163), 726–730.
- Zou, M. F., Kopajtic, T., Katz, J. L., Wirtz, S., Justice, J. B., Jr, & Newman, A. H. (2001). Novel tropane-based irreversible ligands for the dopamine transporter. *Journal of Medicinal Chemistry*, *44*(25), 4453–4461.